



The University of
Nottingham

UNITED KINGDOM • CHINA • MALAYSIA

**DISCRETE ELEMENT MODELLING OF
CONE PENETRATION TESTING IN
GRANULAR MATERIALS**

By

Omar Falagush

M.Sc, B.Sc

Thesis submitted to the University of Nottingham for the
degree of Doctor of Philosophy

December 2013

To my parents

ABSTRACT

Cone penetration testing (CPT) is one of the most versatile devices for *in situ* soil testing. With minimal disturbance to the ground, it provides information about soil classification and geotechnical parameters. Several researchers have used different numerical techniques such as strain path methods and finite element methods to study CPT problems. The Discrete Element Method (DEM) is a useful alternative tool for studying cone penetration problems because of its ability to provide micro mechanical insight into the behaviour of granular materials and cone penetration resistance.

This study uses three-dimensional DEM to simulate the cone penetration testing of granular materials in a calibration chamber. Due to the geometric symmetry of this study a 90° segment of the calibration chamber and the cone penetrometer was initially considered followed by a 30° segment to allow for the simulation of smaller particle sizes and to reduce computational time. This research proposes a new particle refinement method, similar to the mesh refinement of finite-element modelling, in the sense that a large number of small particles were brought into contact with the cone tip, while the large particles were distanced further away from the cone, to reduce computational time effectively. Using a radius expansion method for sample preparation and assigning a constant mass to each particle in the sample was found to reduce computational time significantly with little influence on tip resistance.

The effects of initial sample conditions and particle friction coefficient were found to have an important influence on the tip resistance. In addition, prohibiting particle rotation was found to increase tip resistance significantly compared to when the particles were permitted to rotate freely. Particle shape in this study was simulated by replacing the spheres with simple two-ball clumps and was found to have an important effect on the tip resistance.

DEM simulations of biaxial tests were conducted to investigate the effect of initial sample conditions, particle shape and particle friction coefficient on the stress-strain behaviour of granular materials. All the above mentioned parameters were found to have a significant effect on the stress-strain behaviour of granular materials. Biaxial test simulations were also conducted to obtain basic granular material properties to derive analytical CPT solutions from continuum mechanics principles. Some of the DEM simulation results were found to be in good agreement with the analytical solutions that used a combined cylindrical-spherical cavity expansion method.

Particle crushing was simulated during the cone penetration tests by replacing a broken particle with two new equi-sized smaller particles with mass conserved. The results showed considerable reduction in the tip resistance for the crushing model compared to the non-crushing model and this reduction increased as the confining stress increased.

ACKNOWLEDGEMENTS

First of all, all praise and thanks to my God (Allah) for what I have achieved in my life. I would like to extend my deepest thanks to my supervisors Professor Glenn McDowell and Professor Hai-Sui Yu, for their assistance during the length of this thesis. I appreciate their valuable discussions, encouragement, patience and advice throughout this research. Their guidance and supervision are gratefully acknowledged.

I would like also to thank all the colleagues and friends for the valuable discussion and the enjoyable time during my study. Special thanks are given to Dr. Jean-Francois Ferellec for his help in DEM simulation in this project. A great thank goes to the Libyan government for providing me the financial support during my study.

Finally, I would like to thank my father: Alsanusi, my mother: Khadeja, my wife: Soad and my children: Rehab, Noralden, Taiba and Zeyad for their constant support, love and encouragement through my study.

TABLE OF CONTENTS

ABSTRACT.....	II
ACKNOWLEDGEMENTS.....	IV
TABLE OF CONTENTS.....	V
NOTATION.....	IX
CHAPTER 1 INTRODUCTION.....	1
1.1 Background	1
1.2 Aims and Objectives	3
1.3 Outline of Thesis	4
CHAPTER 2 LITERATURE REVIEW.....	7
2.1 Cone Penetration Test	7
2.1.1 Historical background	7
2.1.2 General description of CPT and CPTU.....	10
2.1.3 Role of CPT in site investigation	11
2.1.4 CPT equipment	12
2.1.5 CPT test procedure.....	14
2.1.6 Presentation of results	18
2.1.7 Interpretation of CPT data.....	20
2.2 Centrifuge Test.....	30
2.2.1 Introduction.....	30
2.2.2 Factors affecting penetration resistance	31
2.3 Calibration Chamber Test	37
2.3.1 Introduction.....	37
2.3.2 Chamber size and boundary effects	40

2.3.3	Experimental calibration chamber	42
2.4	Particle crushing	49
2.4.1	Introduction	49
2.4.2	Compression of a single particle	51
2.4.3	Weibull statistics applied to soil particle strength.....	54
2.4.4	Yielding of granular materials	55
2.5	Conclusions	59
CHAPTER 3 DISCRETE ELEMENT MODELLING OF GRANULAR		
MATERIAL.....		
		61
3.1	Introduction	61
3.2	Discrete Element Method.....	62
3.3	The PFC ^{3D} Particle-Flow Model	63
3.3.1	Introduction	63
3.3.2	Calculation Cycle	65
3.3.3	Contact constitutive model.....	72
3.3.4	Clump logic.....	78
3.4	Effect of particle properties	82
3.4.1	Particle shape	82
3.4.2	Particle rotation	89
3.4.3	Particle friction coefficient.....	91
3.5	Examples of DEM applications.....	94
3.5.1	DEM of particle flow	94
3.5.2	DEM of cemented sand.....	96
3.5.3	DEM of railway ballast	100
3.6	Conclusions	106
CHAPTER 4 DISCRETE ELEMENT MODELLING OF CPT IN A		
CALIBRATION CHAMBER.....		
		107
4.1	Introduction	107
4.2	Modelling procedure and sample preparation	108
4.3	Results of feasibility simulations	112
4.4	Particle refinement method	115
4.4.1	Application of a 90° Chamber segment	117

4.4.2	Application of a 30° Chamber segment	120
4.5	Effect of particle shape	124
4.5.1	Application of a 90° Chamber segment	125
4.5.2	Application of a 30° Chamber segment	127
4.6	Effect of radius expansion method	128
4.7	Effect of constant particle mass	130
4.8	Other factors affecting DEM simulations	134
4.8.1	Effect of initial sample porosity	135
4.8.2	Effect of mean effective stress	136
4.8.3	Effect of particle friction coefficient	138
4.8.4	Effect of particle rotation	141
4.8.5	Effect of clump shape	143
4.9	Contact force distributions	146
4.10	Displacement vector distributions	147
4.11	Conclusions	151
CHAPTER 5 DISCRETE ELEMENT MODELLING OF BIAXIAL TEST		154
5.1	Introduction	154
5.2	Modelling procedure and sample preparation	156
5.3	Influence of initial sample porosity	160
5.4	Influence of confining stress	164
5.5	Influence of particle shape	166
5.6	Influence of particle friction coefficient	170
5.6.1	Spheres	170
5.6.2	Two-ball clumps	173
5.7	Conclusions	175
CHAPTER 6 ANALYTICAL SOLUTION OF THE CPT AND COMPARISON WITH THE DEM SIMULATIONS		176
6.1	Introduction	176
6.2	Cavity expansion method	177
6.3	Combined cylindrical-spherical cavity expansion method	181
6.4	DEM simulation of biaxial and CPT tests	184

6.5	Analytical solution for CPT using a combined cylindrical-spherical cavity expansion method.....	187
6.5.1	The procedure for obtaining an analytical CPT solution	188
6.5.2	Results and discussion	188
6.5.3	Comparison of DEM results and analytical solutions.....	193
6.6	Conclusions	195
CHAPTER 7 DISCRETE ELEMENT MODELLING OF PARTICLE		
CRUSHING.....		
7.1	Introduction	196
7.2	Modelling procedure	197
7.3	Results and discussion.....	202
7.4	Conclusions	216
CHAPTER 8 CONCLUSIONS AND SUGGESTIONS FOR FUTURE		
RESEARCH.....		
8.1	Summary and Conclusions	218
8.2	Suggestions for Further Research.....	221
REFERENCES.....		
APPENDIX.....		

NOTATION

A_c	Cone projected area
A_s	Surface area of friction sleeve
b	Material constant
B	Cone diameter
B_q	Pore pressure ratio
B/d_{50}	Cone diameter to mean grain size ratio
$\frac{c}{a}$	Relative size of the plastic zone
CPT	Cone Penetration Test
$CPTU$	Cone Penetration Test with pore water pressure measurement
CU	Coefficient of Uniformity
DEM	Discrete Element Method
d	Particle size (diameter)
d_0	Initial particle size
d_{50}	Median particle size
D_R	Relative density
D_c	Container diameter
D_c/B	Container to cone diameter ratio

e_{max}	Maximum void ratio
e_{min}	Minimum void ratio
E	Young's modulus
f_s	Friction sleeve
f_t	sleeve friction corrected for pore pressure effects
F	Force
F_c	Total force acting on the friction sleeve
F_f	Diametral fracture force applied
F_i	Contact force vector
F_i^n	Normal contact force vector
F_i^s	Shear contact force vector
F_c^n	Normal contact bond strength
F_c^s	Shear contact bond strength
g	Earth's gravity
G	Shear modulus
H	Chamber height
\dot{H}_i	Angular momentum of the particle
I_{rr}	Reduced rigidity index
I_s	Rigidity index
K_0	Stress ratio

k_n	Normal stiffness
k_s	Shear stiffness
m	Mass of a ball
m	Weibull modulus
n	Porosity
M_i	Resultant moment
N	Test acceleration level at the surface of the specimen
N_q	Cone factor in sand
p'_0	Initial mean effective stress
p'	Mean effective stress
P'_{lc}	Effective cylindrical cavity limit pressure
$P_s(V)$	Survival probability of block of particles
q	Octahedral shear stress in a particle
q_0	value of octahedral shear stress for a particular particle size such that 37% of particles are stronger
q_c	Cone tip resistance
$q_{c,cc}$	Tip resistance obtained in the chamber
$q_{c,field}$	Tip resistance obtained in the field
q_t	cone resistance corrected for pore pressure effects
Q	Normalised tip resistance

Q_c	Total force acting on the cone
R_f	Friction ratio
R_s	Radius of the surface of the specimen from the central axis of the centrifuge
S/B	Side boundary effect ratio
u	Pore water pressure
u_o	In situ equilibrium pore pressure
u_1	On the cone pore pressure
u_2	Behind the cone pore pressure
u_3	Behind the friction sleeve pore pressure
Z	Normalised penetration depth
Z_m	Model penetration depth
Z_{pc}	Corrected prototype depth
Δt	Time step
Δu	Excess pore pressure
σ	Characteristic tensile stress induced within the particle
σ_1	Major principal stress in a particle
σ_2	Intermediate principal stress in a particle
σ_3	Minor principal stress in a particle
σ_f	Tensile stress at failure

σ'_{h0}	Initial horizontal effective stress
σ_{v0}	In situ total vertical stress
σ'_{v0}	Initial vertical effective stress
σ_v	Total vertical stress
σ'_v	Effective vertical stress
ϕ	Soil friction angle
μ	Friction coefficient
ρ	Material density
δ	Angle of bedding plane to the principal stress direction
ε_v	Average volumetric strain
$\delta\varepsilon_1$	Maximum principal strain increments
$\delta\varepsilon_3$	Minimum principal strain increments
$\delta\varepsilon_v$	Volumetric strain increments
$\delta\gamma$	Shear strain increments
ψ	Soil dilation angle
ν	Poisson's ratio

CHAPTER 1

INTRODUCTION

1.1 Background

The use of *in situ* soil testing to determine parameters and engineering properties of soil has increased significantly in recent years. There is no doubt that geotechnical engineers are more likely to use *in situ* soil tests to determine soil parameters required in geotechnical design. This is especially true for soils that are difficult to sample, such as clean sand or soft clay. Moreover, *in situ* tests are usually less expensive and less time consuming compared to laboratory tests. Historically the impact of *in situ* tests has been significant and they continue to play a key role in characterising engineering properties of soils; for example, the cone penetration test (CPT), standard penetration test (SPT), self-boring pressuremeter test (SBPMT), cone pressuremeter test (CPMT) and flat dilatometer test (DMT).

The Cone Penetration Test (CPT) is an *in situ* testing method used in geotechnical engineering for soil classification and estimation of soil parameters, such as undrained shear strength, friction angle and overconsolidation ratio. The acceptance of the cone penetration test as a major tool in *in situ* testing has increased significantly because of its output repeatability and reliability. The test method consists of pushing a series of rods, housed in a cone tip at the base, into the ground at a controlled rate (usually 20 mm/s), and measuring continuously or at selected depth intervals, the penetration resistance of the cone, the local friction resistance on

a friction sleeve and pore pressure in the vicinity of the cone and sleeve. These measurements are then used to obtain information about site stratigraphy and soil classification.

The first Dutch cone penetration test was made at the Rijkwaterstaat (Department of Public Works) in Holland (Barentsen, 1936). According to Broms and Flodin (1988) the first electric cone penetrometer was developed in Berlin during the Second World War. A conventional electrical piezometer that could also measure pore pressure was developed by the Norwegian Geotechnical Institute (NGI) (Lunne et al., 1997).

Cone penetration problems are typically analysed by theoretical methods including bearing capacity theory (Durgunoglu and Mitchell, 1975) and cavity expansion methods (Yu and Mitchell, 1996; Yu and Mitchell, 1998), numerical analyses including strain path methods (Baligh, 1985) and finite element methods (De Borst and Vermeer, 1982), experiments including centrifuge tests (Bolton and Gui, 1993) and calibration chamber tests (Houlsby and Hitchman, 1988). Calibration chamber tests are mostly used to obtain correlations between cone resistance and engineering properties of sandy soil.

The discrete element method (DEM) is an alternative tool for interpreting the penetration mechanism of the cone penetration test. The method provides insight into mechanical behaviour of granular material at both micro and macro level. DEM was first developed by Cundall (1971) for rock mechanics and has since been increasingly implemented to simulate the mechanical behaviour of granular materials (Cundall and Strack, 1979; Ting et al., 1989; Rothenburg and Bathurst, 1992).

Few studies have been carried out on DEM simulations of CPT in granular materials. Huang and Ma (1994) showed using DEM simulation for deep penetration that both the penetration mechanism and soil dilatancy in a granular material are affected by the soil's loading history. Jiang et al. (2006) used a two-dimensional DEM model to study the plane-strain penetration mechanism in granular material. Their results showed some important qualitative insight for the penetration mechanism. Arroyo et al. (2011) built a virtual calibration chamber to simulate cone penetration tests in sand using a three-dimensional DEM model. The simulation results were in good quantitative agreement with experimental tests. In a similar vein, this project uses three-dimensional discrete element modelling to simulate cone penetration testing of granular materials in a calibration chamber.

1.2 Aims and Objectives

Simulations of a CPT using discrete element modelling poses a real challenge with regards to the computational time involved especially where the full scale geometry of the cone and realistic sand-sized particles are used as the model inputs. The main aim of this study was to attempt to simulate cone penetration testing using a realistic cone size with DEM and real sand-sized particles to obtain micro mechanical insight into the behaviour of the material. To this end, the objectives of this thesis were as follows:

1. To use a suitable particle model in DEM to study cone penetration testing in a granular material comprising real sand-sized particles, with acceptable computational time.

2. To study the effect of parameters such as initial sample conditions and particle friction coefficient on cone tip resistance.
3. To investigate the effect of particle shape on cone tip resistance using different shapes of simple two-ball clumps.
4. To conduct DEM simulations of biaxial tests to investigate the mechanical behaviour of granular material and to obtain continuum parameters for an analytical cavity expansion analysis of CPT.
5. To compare the tip resistance results of DEM simulations with those predicted using cavity expansion theory based on continuum mechanics.
6. To investigate the effect of particle crushing on the DEM tip resistance results during cone penetration tests.

It is important to state that the objective of this study is not to model a single piece of experimental data, but rather to examine the effects of various micro parameters on the macroscopic behaviour of granular material under cone penetration test.

1.3 Outline of Thesis

The thesis is divided into eight chapters. A brief layout of this thesis is given below.

Chapter 1 introduces the thesis, and briefly presents the purpose and main objectives of this study.

Chapter 2 presents a literature review of three main areas. First, the cone penetration test is described and a brief review of its development, applications as well as the interpretation of CPT results is given. Cone penetration tests in a centrifuge are then introduced and a review of the factors affecting tip resistance is presented. The

calibration chamber test is also presented and a brief review of the results obtained from tests in the experimental calibration chamber is introduced.

Chapter 3 describes the discrete element method theory including the principle of numerical modelling using PFC^{3D} program. The underlying concepts and functions of PFC^{3D}, the effect of particle properties and examples of PFC^{3D} applications in simulating soil behaviour are also presented.

In Chapter 4, PFC^{3D} is used to simulate cone penetration tests of granular materials in a calibration chamber. A novel technique of particle refinement is implemented in the simulations to reduce computational time, whereby small particle sizes are generated next to the cone penetrometer and larger particles further away. The effects of different particle parameters such as initial sample conditions, particle friction coefficient and particle shape on tip resistance are investigated.

In Chapter 5, PFC^{3D} is used to simulate biaxial tests to investigate the mechanical behaviour of granular materials with the aim of obtaining continuum parameters for an analytical cavity expansion solution of CPT.

In Chapter 6, the cavity expansion method is briefly reviewed and the CPT simulation solution using DEM is compared with the CPT analytical solution that uses a combined cylindrical-spherical cavity expansion method. Some CPT results using cavity expansion method are explained and the comparison is presented.

In Chapter 7, DEM simulations of particle crushing using spherical fragments with conservation of mass are studied and their effect on the tip resistance results is investigated.

In Chapter 8, conclusions on the work undertaken in this research are presented and recommendations for possible future work are given.

CHAPTER 2

LITERATURE REVIEW

2.1 Cone Penetration Test

The Cone Penetration Test (CPT) is an *in situ* testing method used to determine various geotechnical parameters. The repeatability and reliability of the cone penetration test has increased its acceptance as a prevailing choice amongst *in situ* testing techniques. The testing method consists of a series of rods having a cone tip at the base with area of 10 cm^2 and 60° tip apex angle. The cone tip and the series of rods are driven into the ground at a controlled rate (usually 20 mm/s), and measuring continuously or at selected depth intervals the penetration resistance of the cone, the local friction resistance on a friction sleeve and pore pressure in the vicinity of the cone and sleeve.

2.1.1 Historical background

The cone penetration test was developed in the early 1930s as a geological tool for stratigraphic purposes. In 1932 Barentsen made the first Dutch cone penetrometer at the Rijkwaterstaat (Department of Public Works) in Holland. A gas pipe with internal diameter of 19mm housed a steel rod with 15mm diameter capable of moving up and down within it was used. The entire assembly including the external pipe and the internal rod with its 10cm^2 , 60° angled cone (see Figure 2.1), were hand-driven (Barentsen, 1936). The maximum depth of penetration achieved was 10-12m and the penetration resistance was recorded on a manometer.

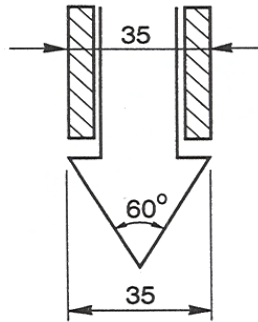


Figure 2.1 Old type Dutch cone (Sanglerat, 1972)

The Dutch static cone penetration test was further improved by adding an “adhesion jacket” above the cone (see Figure 2.2) (Begemann, 1953; Begemann, 1969).

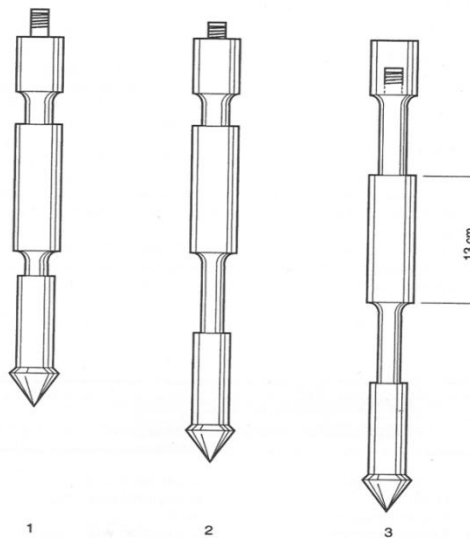


Figure 2.2 Begemann type cone with friction sleeve (Sanglerat, 1972)

With this, it was possible to measure the local skin friction in addition to cone resistance. Measurements of the aforementioned parameters were made at 0.2m intervals, although in some instances the interval was reduced to 0.1m. Begemann (1965) was also the first to propose that the friction ratio (sleeve friction/cone resistance) could be used to classify soil layers in terms of soil type (see Figure 2.3).

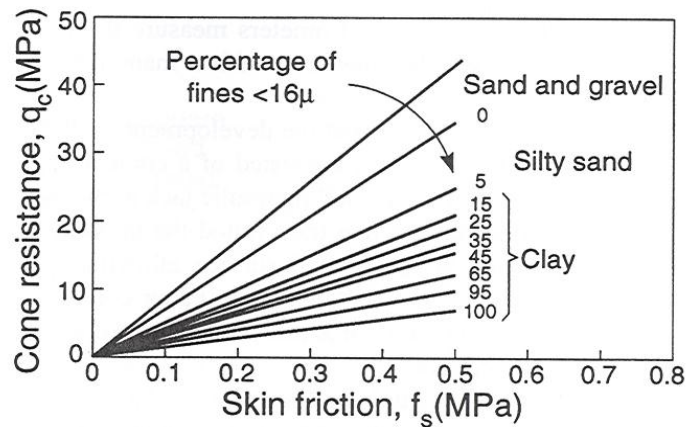


Figure 2.3 Soil classification from cone resistance and sleeve friction readings (Begemann, 1965)

The first electric cone penetrometer is thought to have been developed in Berlin during the Second World War (Broms and Flodin, 1988). In 1965, however, an electric friction cone penetrometer (depicted Figure 2.4) was developed by Fugro with the assistance of the Dutch State Research Institute. Later, a conventional electrical piezometer that could also measure pore pressure was developed by the Norwegian Geotechnical Institute (NGI) (Lunne et al., 1997). Significant studies in the development of the cone penetrometer were also made in the Netherlands (Broms and Flodin, 1988). In addition, cone penetrometer research was progressed in Canada by Campanella and his students (Campanella et al., 1983; Robertson and Campanella, 1983a; Robertson and Campanella, 1983b; Robertson and Campanella, 1986; Robertson et al., 1986; Robertson and Wride, 1998; Robertson, 2009), as well as by many other geotechnical researchers around the world.

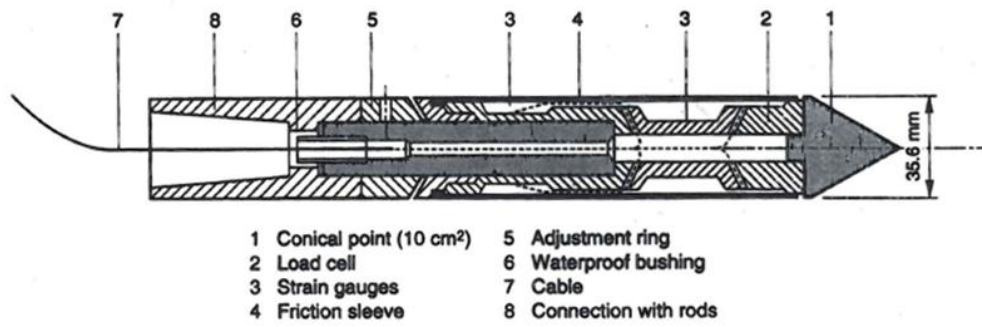


Figure 2.4 The Fugro electrical friction cone (de Ruiter, 1971)

2.1.2 General description of CPT and CPTU

In the Electric Cone Penetration Test (CPT) and the Cone Penetration Test which allows for pore water pressure measurements, (i.e. a piezocone test or CPTU), a cone attached to the end of a series of rods is pushed into the ground at a constant rate and continuous or intermittent measurements are obtained from the resistance to the penetration of the cone penetrometer. An annotated diagram depicting the salient elements of cone penetrometer is shown in Figure 2.5.

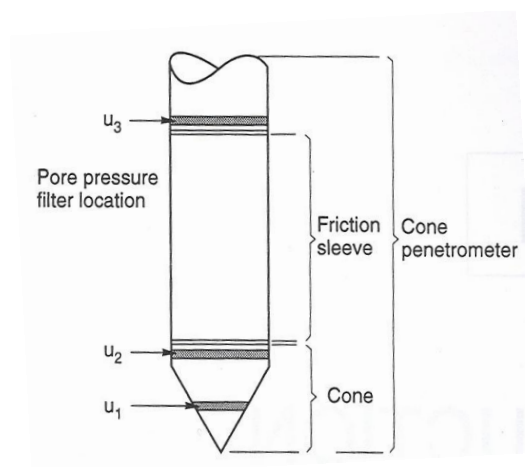


Figure 2.5 Terminology for cone penetrometers (Lunne et al., 1997)

The total force acting on the cone Q_c divided by the cone projected area A_c , gives a cone resistance q_c . The total force acting on the friction sleeve F_c divided by the surface area of friction sleeve A_s , gives the local side friction f_s . In the piezocone penetrometer, pore pressure is typically measured at the three positions shown in Figure 2.5 as u_1 , u_2 or u_3 corresponding to measurements on the cone, behind the cone and behind the friction sleeve respectively. Existing CPT systems can be divided into three main groups namely: mechanical cone penetrometers, electric cone penetrometers and piezocone penetrometers. A cone penetrometer with 10 cm^2 base area cone having an apex angle of 60° is accepted as the recommended standard penetrometer and is specified in the International Reference Test Procedure (ISSMFE, 1989).

2.1.3 Role of CPT in site investigation

The CPT, piezocone (CPTU) and seismic (SCPT/SCPTU) have the highest applicability for soils because they provide a proximate continuous profile and are much more cost-effective. The three main applications of the CPT in the site investigation process are identified as (Lunne et al., 1997):

- 1) To establish sub-surface stratigraphy and identify materials present.
- 2) To estimate geotechnical parameters.
- 3) To give results for direct geotechnical design.

Furthermore, the CPT can give guidance on what subsequent tests to perform, in that it helps to identify critical areas or strata requiring further *in situ* testing or sampling. The CPT can also be implemented alone for design if the geology is uniform and well understood and if predictions based on CPT results have been locally verified and correlated with structure performance. It is however general practice for the CPT

to be used in conjunction with other site investigation techniques for one or more of the following reasons:

- to identify soil type
- to verify local correlations
- to provide a complete information where interpretation of CPT data is difficult due to soil problems or partial drainage conditions
- to assess the effects of future changes in soil loading which are not documented by the CPT

The CPT has the following advantages over the other *in situ* soil testing:

- Fast and gives continuous data
- Repeatable and reliable penetration data (not operator-dependent)
- Economical and productive

Disadvantages of CPT are:

- Requires skilled people for operating
- No soil sample can be obtained during a CPT
- Penetration can be hindered in gravel or cemented layers

2.1.4 CPT equipment

The two main components of CPT equipment are a cone penetrometer and pushing equipment. Cone penetrometers come in a different range of sizes. The 10cm² and 15cm² probes are the most common and are specified in most standards. Figure 2.6 shows cone sizes ranging from a mini-cone of 2cm² to a large cone of 40cm².



Figure 2.6 Range of CPT probes (from left: 2 cm², 10 cm², 15 cm², 40 cm²) (Robertson and Cabal, 2010)

Nowadays many additional sensors and/or measurements have been added to the basic repertoire of the cone penetrometer, for instance: temperature, electrical conductivity, inclination, pressuremeter and seismic wave velocity measurements. Readings obtained from electronic measuring devices during penetration are usually recorded automatically and stored on a computer which is connected to the cone penetrometer by electric cable. Specialised or bespoke trucks are normally used as the main cone pushing equipment to derive cone penetrometers into the ground. They usually consist of hydraulic jacking and reaction systems. The thrust capacity needed for cone testing normally varies between 10 and 20 tonnes with the power for the hydraulic jacking system usually supplied from the truck's engine. Figure 2.7 shows the CPT truck of Nottingham Centre for Geomechanics (NCG).



Figure 2.7 CPT truck of Nottingham Centre for Geomechanics (NCG)

2.1.5 CPT test procedure

In order to obtain accurate results from field operations that utilise electric cone penetrometers, well-qualified operators and good technical back-up facilities for calibration and maintenance of the equipment are required. During the testing process it is advised that any deviation from the IRTP (ISSMFE, 1989) or other chosen standard be reported (Lunne et al., 1997). The following points outline the CPT test procedure:

- ***Pre-drilling***

In the case of penetration testing in fills or hard soils, it may be necessary to pre-drill in order to avoid overloading or damaging the cone penetrometer. Fills with hard soil like stones should always be pre-bored. In some situations it may also be necessary to use a casing. However in other specific instances, pre-forming a hole through the overlying problematic material using a solid steel dummy probe with a diameter slightly larger than the cone penetrometer is preferred to pre-drilling.

- *Verticality*

The pushing system should be set up so as to achieve a push direction as near to vertical as possible. The deviation of the initial pushing direction from the vertical should not exceed 2° . The axis of the push rods should also coincide with the thrust direction. The pushing rods should also be checked for straightness according to the IRTP (ISSMFE, 1989). The last two considerations: verticality of the pushing system and straightness of the rods, are aimed at reducing the likelihood of the penetrometer deviating from its vertical path, except when caused to do so as a result of impacting hard inclusions.

The majority of electric cone penetrometers today have simple slope sensors incorporated in their design to provide a measure of the non-vertically of the sounding (pushing). This is particularly useful to avoid potential damage to equipment arising from sudden deflection. The maximum depth for which the use of a slope sensor can be disregarded depends on the acceptable error in recorded depth without any obstructions. However, for most CPT tests the maximum depth recommended without a slope sensor, over which negligible error in recorded depth can be assumed is about 15m. For soundings deeper than about 15m it is advisable to keep a running record of the measured inclinations to allow corrections to be made to the depth of penetration. The effect of verticality on depth of penetration is shown graphically in Figure 2.8.

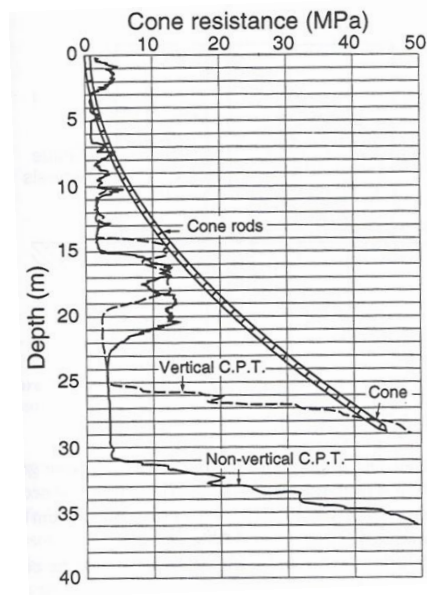


Figure 2.8 Effect of verticality on measured depth (Bruzzi and Battaglio, 1987)

- **Reference measurements**

The majority of modern electric cone penetrometers have been shown to exhibit high degrees of accuracy and repeatability. However, tests with cone penetrometers have also shown that the zero load output of the sensors can be sensitive to external changes (for example, in temperature). In view of this, it is therefore recommended that reference measurements of the sensors at zero loads be recorded before and after each sounding. The reference measurements should be applied when the penetrometer has almost the same temperature as the ground. It is particularly important when testing in soft soils that reference measurements are recorded when temperature equilibrium is achieved between the penetrometer and ground. To ensure that the penetrometer and ground temperatures are closer, the probe can be placed either in the ground or in a container of water and allowed to stabilize at the ambient temperature.

- ***Rate of penetration***

The prescribed rate of penetration for a CPT should be 20 mm/s \pm 5 mm/s (ISSMFE, 1989). However, when a piezocone is used, the relevant guideline states that the range of penetration rates should be reduced.

- ***Interval of readings***

Electric cone penetrometers give continuous analogue data which can be converted by most systems to digital format at predetermined intervals. The IRTTP (ISSMFE, 1989) recommends that the depth interval between readings shall be no more than 200mm. This interval is rather large considering most systems have the capability to collect data at intervals of 10-50mm. However, the desired interval depends on project type. For example, projects that require information concerning very thin strata may require data to be collected at close intervals or continuously in analogue form.

- ***Depth measurements***

Several systems are available for depth measurement during a CPT. The most common ones are either based on a depth wheel concept or a cable drive. The system utilised should be referenced to the ground surface or a stable platform. The depth of cone penetration can be determined to within an accuracy of \pm 100mm, relative to the ground surface or other fixed reference point, with a resolution of better than 10mm (ISSMFE, 1989). Care should be taken if the system used is not independent of the thrust machine as it may be subject to movement during cone penetration.

2.1.6 Presentation of results

The final presentation of the CPT and CPTU data in the field should contain both measured and derived parameters.

Measured parameters

The measured parameters q_c , f_s and u should be plotted on one sheet. At any one site all profiles should be presented to a common set of scales. The following are the scales recommended by IRTP (ISSMFE, 1989):

- depth scale: vertical axis, 1 unit length for 1 m
- cone resistance q_c : horizontal axis the same unit length for 2 MPa
- sleeve friction f_s : horizontal axis the same unit length for 50 kPa
- pore water pressure u : horizontal axis the same unit length for 20 kPa

Figure 2.9 is an example of the implementation of the above-mentioned recommendations.

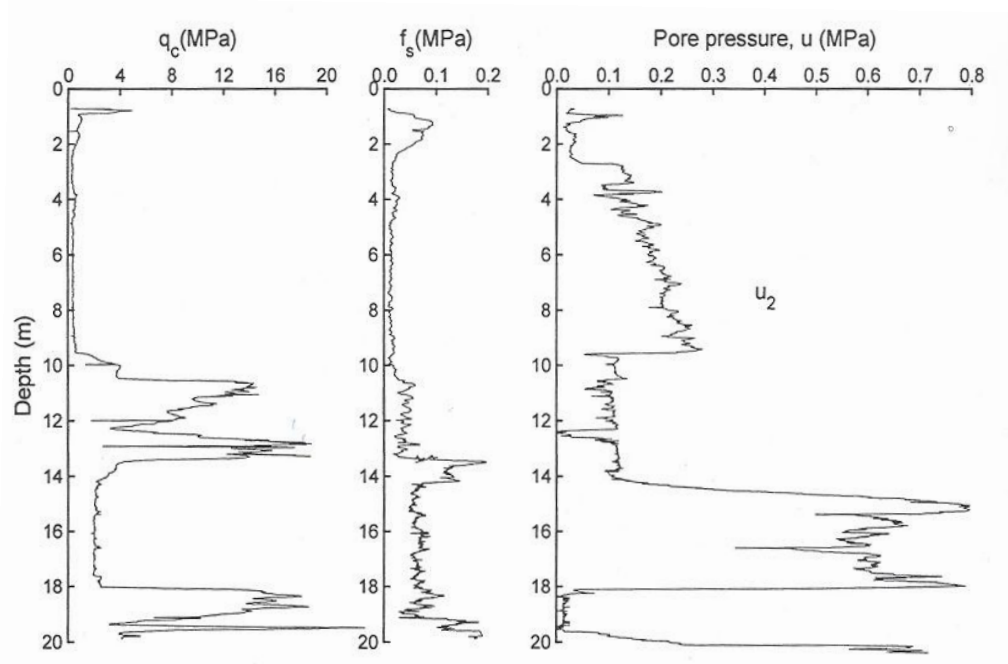


Figure 2.9 Data presented in accordance to the Recommended Test Procedure (Lunne et al., 1997)

Derived parameters

The following parameters should be derived and plotted when possible:

- q_t is the cone resistance corrected for pore pressure effects
- f_t is the sleeve friction corrected for pore pressure effects, only valid when pore pressures have been measured at both ends of the friction sleeve
- R_f is the friction ratio, usually in %, which can be calculated by using either uncorrected parameters (q_c, f_s) or corrected parameters (q_t, f_t)

$$R_f = \frac{f_s}{q_c} \quad 2.1$$

Or ideally

$$R_f = \frac{f_t}{q_t} \quad 2.2$$

Or more typically

$$R_f = \frac{f_s}{q_t} \quad 2.3$$

- B_q is the pore pressure ratio

$$B_q = \frac{\Delta u}{q_t - \sigma_{vo}} \quad 2.4$$

where

Δu is the excess pore pressure ($u - u_o$)

u_o is the *in situ* equilibrium pore water pressure

σ_{vo} is the *in situ* total vertical stress

Figure 2.10 gives an example of plotting derived parameters.

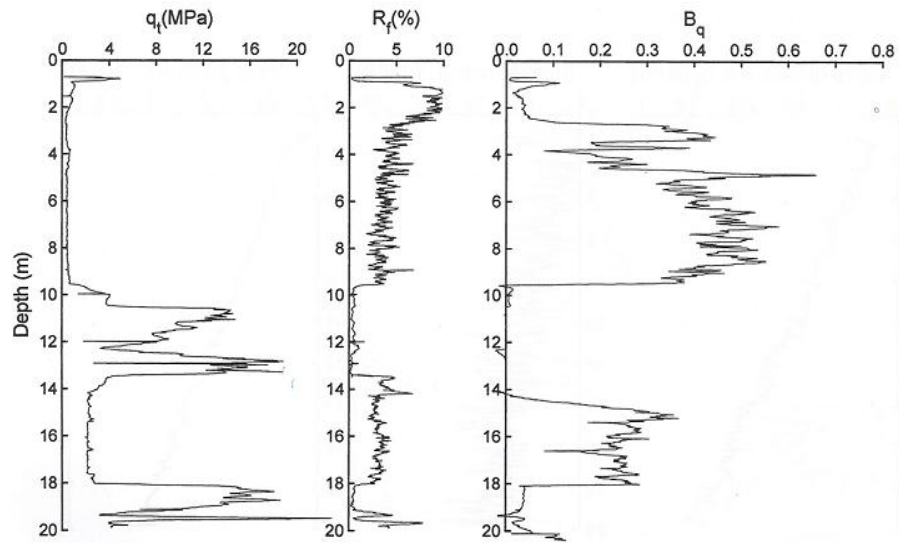


Figure 2.10 Example of plotting derived parameters from Figure 2.9 (Lunne et al., 1997)

2.1.7 Interpretation of CPT data

Over the last few decades, cone penetration testing has been considered one of the most widely used *in situ* testing equipment for determining soil profiles and soil properties. Its use was bolstered by the development of empirical correlations and soil classification charts (Robertson, 1986; Lunne et al., 1997; Mitchell and Brandon, 1998). Soil stratigraphy and soil classification are described as follows:

Soil stratigraphy

Continuous monitoring of pore pressure during CPT testing can improve the identification of soil stratigraphy. Figure 2.11 shows the excellent profiling capability of the piezocone. The pore pressure recorded varies in response to the soil type being penetrated in the immediate area of the pore pressure sensing element as follows:

- soft to medium stiff clays result in very high pore pressures

- very stiff overconsolidated clays result in very low or negative pore pressures
- very dense fine or silty sands result in very low or negative pore pressures
- contractive silts result in high positive pore pressures

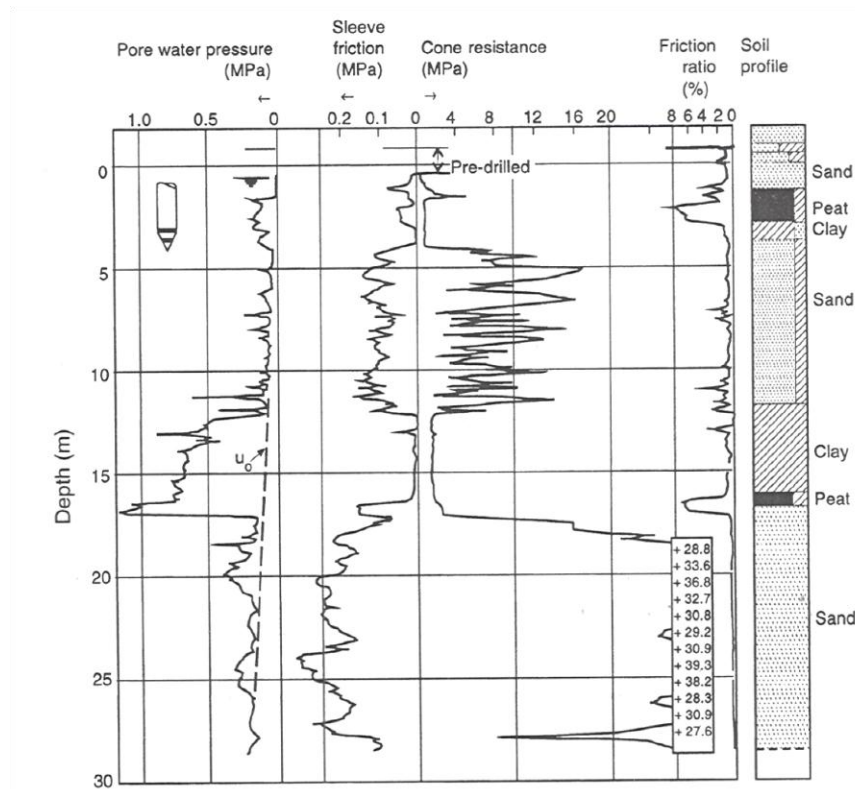


Figure 2.11 Example CPTU results showing excellent profiling capacity (Zuidberg et al., 1982)

Soil classification

The most comprehensive work on soil classification using electric CPT data was introduced as seen in Figure 2.12 (Douglas and Olsen, 1981). The chart shows that sandy soils tend to possess high cone resistance and a low friction ratio, whereas the vice versa is observed for soft clay soils. Furthermore, organic soils such as peat are indicated as having very low cone resistance and a very high friction ratio. Soils with low cone resistance and low friction ratio fall in the sensitive soils category, whilst soils that possess high horizontal stresses - i.e. high overconsolidation ratio (OCR) have been noted to have higher cone resistance and friction ratio.

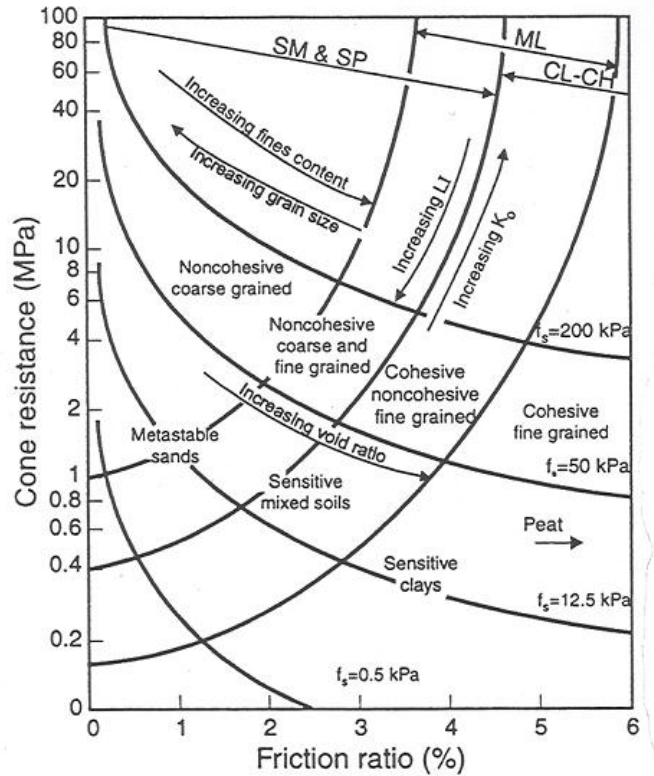


Figure 2.12 CPT soil behaviour type classification charts (Douglas and Olsen, 1981)

Cone penetration problems are mainly analysed by the following methods.

Bearing capacity method

The bearing capacity method was one of the first methods used for analysing the cone penetration test, which when applied to CPT, assumes cone resistance to be equal to the collapse load of a deep circular foundation in soil. Bearing capacity solution for deep cone penetration problems by Durgunoglu and Mitchell (1975) is relatively simple, in that it can be implemented easily by a practitioner familiar with bearing capacity calculations. However, Yu and Mitchell (1998) have pointed out that bearing capacity theory applied to cone penetration modelling in sand does not account for soil stiffness and volume change. In the solution of Durgunoglu and Mitchell (1975) a failure mechanism was used to derive a plane strain solution first (i.e. for wedge penetration). Following this, an empirical shape factor was applied to

account for axisymmetric geometry of typical cone penetration problems. When the soil-cone interface friction angle is half of the soil friction angle, the solution (Durgunoglu and Mitchell, 1975) may be expressed by the following equation:

$$N_q = \frac{q'_c}{\sigma'_{v0}} = 0.194 \exp^{(7.63 \tan \phi)} \quad 2.5$$

where N_q is the cone factor in sand and ϕ is the drained soil friction angle.

Cavity expansion method

Analysis of the cone penetration test using the cavity expansion approach was first introduced by Bishop et al. (1945) after they noticed that the pressure required to create a deep hole in an elastic-plastic medium is proportional to that necessary to expand a cavity of the same volume under the same conditions. Yu and Mitchell (1996) and (1998) also proposed that cone tip resistance could be related with (mainly spherical) cavity limit pressures and developed theoretical (analytical or numerical) limit pressure solutions for cavity expansion in soils. Further detail concerning the cavity expansion method is presented in Chapter 6.

Strain path method

For deep penetration problems, experimental results have shown that soil deformations as a result penetration of piles or penetrometers are similar even when the properties of the soils are different (Vesic, 1963). Ladanyi (1963) proposed that soil stresses could be calculated if the strain path of the soil around the cavity is reproduced in a suitable laboratory test. These ideas lead to the suggestion (Baligh, 1985) that deep steady penetration problems in soil are basically strain-controlled, and that the accompanied deformations are not sensitive to the material properties. In

addition, Baligh (1985) argued that as a result of kinematic constraints present in deep foundation studies, soil deformations can be only determined with a logical degree of accuracy from kinematic considerations. This approximate analytical approach is known as the "strain path method". A kinematic model known as the "simple cone model" was presented by Levadoux and Baligh (1986). This model can be used as the initial deformation field for a strain path method. The idea of a simple cone model originates from fluid mechanics where the velocity field for expanding a spherical cavity is the same as the velocity field of a point source at a fixed position in a fluid at rest. The aim of the simple cone model is to recreate the approximate penetrometer geometry through a combination of sources and sinks in a uniform flow field. Sagaseta et al. (1998) extended the method to analyse penetration problems at shallow depths.

The strain path method is considered to be better than the cavity expansion theory as it applies the two dimensional nature of the CPT penetration mechanism. However, the strain path method has not been entirely embraced as its equations of equilibrium are not completely satisfied in the sense that they only provide an approximate solution. Furthermore, the strain path method has only been proven for cone penetration analysis of undrained clays.

Finite element method

The finite element method is utilised in the analysis of cone penetration and pile driving problems. Some of the earlier finite element models in this regard (De Borst and Vermeer, 1982; Griffiths, 1982) considered the problem of undrained clay by investigating small strain deformations using elasto-perfectly plastic models.

Furthermore, results for large strain deformation in cohesive materials have been offered (Budhu and Wu, 1992).

The problem of deep penetration in sand was first presented by modelling sand as a Mohr-Coulomb material (Willson, 1985). The first large strain deformation of the penetration in frictional materials was introduced by Cividini and Gioda (1988). They explained the similarity of cavity expansion to the soil penetration process through a finite element model. They also emphasised the importance of changing boundary condition at the cone tip.

Susila and Hryciw (2003) used an updated Lagrangian large strain formulation and auto-adaptive remeshing technique to model cone penetration in normally consolidated sand. Specifically, the technique was utilised to treat the very large deformation of the mesh surrounding the cone tip. Their results showed the distribution of resistance along the cone sleeve to be non-uniform overall, although it was significantly lower closer to the cone tip and it became uniformly higher along the sleeve. Huang et al. (2004) implemented a large strain (updated Lagrangian) finite element method to model the cone penetration test in sand. They treated the cone as a rigid body and the soil was assumed to be an elastic-perfectly-plastic continuum obeying the Mohr-Coulomb criterion. They also carried out parametric studies to investigate the effect of pressure level, shear modulus, soil internal friction angle and dilation angle on cone resistance and the plastic zone around the cone. Numerical results of these studies showed a reasonable agreement compared to the correlations based on cavity expansion theory.

Although the studies of Susila and Hryciw (2003) and Huang et al.(2004) appear to capture the geometric aspects of the cone penetration problem of sand; they fail to satisfactorily capture the material behaviour. In spite of strides made in recent years to study the cone penetration mechanism using the finite element method, a common limitation is observed, in that the results of finite element method have not been verified or compared with experimental results (e. g. of a calibration chamber) or field data. Furthermore, no particular approach has received general acceptance for interpreting the CPT, even for clay. For instance, some studies have indicated that better predictions of cone penetration testing in undrained clay may be obtained if specific analytical and numerical methods are combined (Teh and Houlsby, 1991; Salgado et al., 1997; Abu-Farsakh et al., 2003).

Discrete element method

The discrete element method (DEM) is an alternative tool that has been utilised for interpreting the cone penetration mechanism. It was developed by Cundall and Strack (1979), and is based on discrete mechanics. This numerical analysis method utilises basic constitutive laws at interparticle contacts and can provide the macro and micro-scopic response of a particle assembly subjected to loading. Few DEM simulations of CPT studies have been carried out on granular materials. Huang and Ma (1994) were among the first to implement DEM for the simulation of deep penetration in sand with respect to the material's loading history. Their results showed that both the penetration mechanism and soil dilatancy in a granular material are affected by its loading history.

Focussing on the effect of soil–penetrometer interface friction (tip–soil friction), Jiang et al. (2006) used a two-dimensional (2D) DEM model in a manner similar to

the centrifuge modelling of CPT in granular materials to study the plane-strain penetration mechanism in granular material. The material used in their simulations comprised disks with an average grain diameter of 2.925mm. Assuming geometric symmetry of their model, only half of the ground and penetrometer were considered in their simulations. The final ground (for penetration) consisted of 10000 particles with a planar void ratio of about 0.24, and depth and width of $16R$ and $17.5R$, respectively, where R represents half the width of the penetrometer. The multi-layer under compaction method used to generate the ground was derived after Jiang et al. (2003). Figure 2.13 illustrates the generated ground and boundary conditions for the DEM simulations.

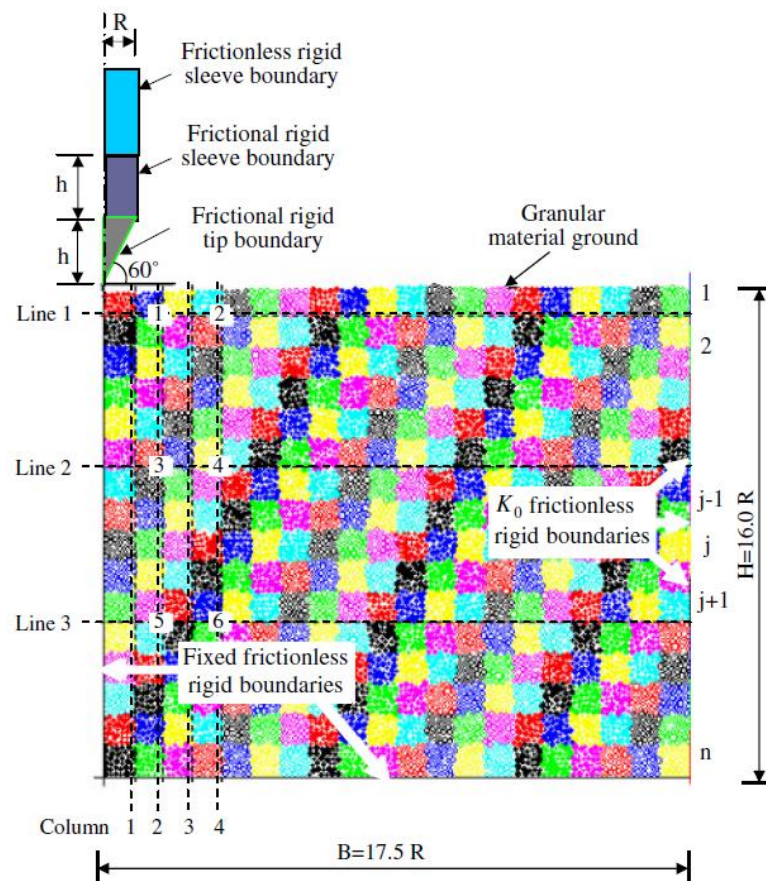


Figure 2.13 Boundary conditions and observance positions in the DEM analyses (Jiang et al., 2006)

After the granular ground was generated, Jiang et al. conducted two DEM penetration tests applying different tip–soil frictions. The penetration mechanism during cone penetration was assessed via the monitoring of tip resistance, deformation pattern, displacement paths, velocity vector distributions and stress field for each penetration test. The results showed that tip resistance increases with increasing penetration depth and increasing tip–soil friction. It was also shown that penetration leads to high gradients of displacement and velocity fields near the penetrometer. Lastly it was observed that during penetration, the soil stresses near the penetrometer increased from their initial values to higher peak stresses, which subsequently became constant at values which were slightly higher than the stresses upon initiating penetration. Although qualitative insight was gained, the limitations of 2D DEM simulations prevent quantitative comparisons with physical tests. For example, using 2D DEM simulation, Deluzarche and Cambou (2006) pointed out that the difference in the contact geometry means that contact model parameters used in a 2D DEM model cannot be directly related to the material properties of real 3D particles.

Arroyo et al. (2011) built a virtual calibration chamber to simulate cone penetration tests in sand using a three-dimensional (3D) DEM model. The particles were represented by single spheres which were prohibited from rotating to enable the rotational resistance of non-spherical particles to be modelled. The simulation results were compared to experimental tests conducted in Ticino sand (Jamiolkowski et al., 2004). The particles used in the DEM models scaled to 50 times larger than the Ticino sand, such that a median particle size d_{50} of 26.5mm with a cone diameter B of 71.2mm was necessary to achieve an appropriate number of particles in contact with

the cone tip. The results showed that under isotropic boundary stresses, their numerical results demonstrated good quantitative agreement with the predictions of experimentally derived empirical equations for Ticino sand. Figure 2.14 shows the calibration chamber and cone penetrometer used in the DEM model.

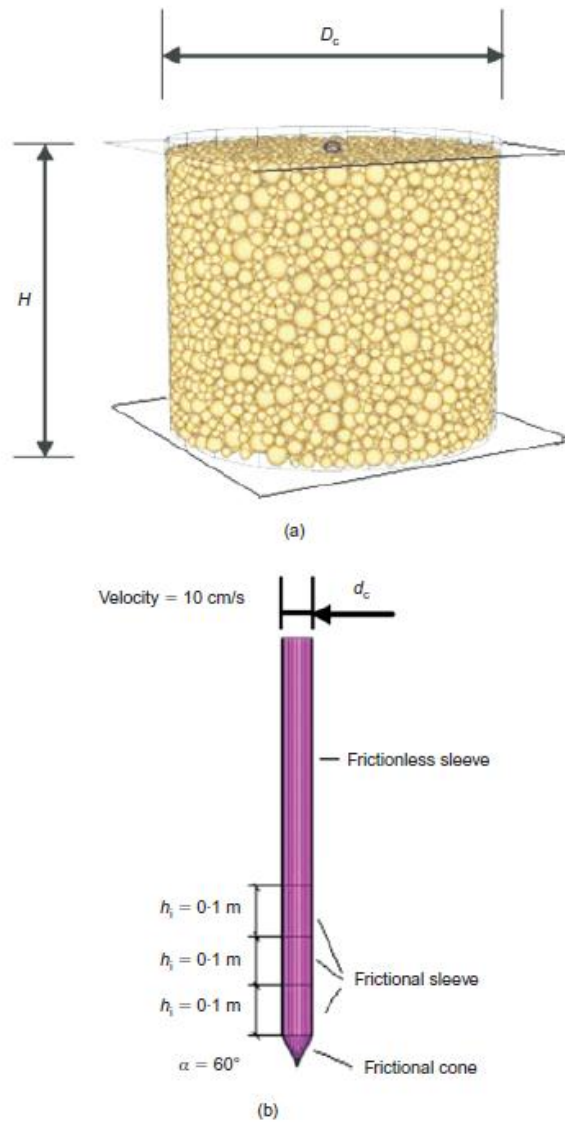


Figure 2.14 View of the DEM model components with indication of the main relevant dimensions: (a) calibration chamber; (b) cone (Arroyo et al., 2011)

2.2 Centrifuge Test

2.2.1 Introduction

The centrifuge test is a fundamental tool available to the geotechnical engineer for the study and analysis of design problems using geotechnical materials. In the centrifuge, a model can be tested and the results then extrapolated to a prototype situation. Centrifuges have been widely used in modelling geotechnical problems due to their favourable costs and their ability to predict foundation behaviour from a soil specimen of known parameters without the delay associated with conducting full-scale tests. The most significant advantage of the centrifuge is its ability to replicate the stress levels equivalent to those encountered *in situ*. There are two main exploitations of a CPT in the centrifuge:

- To check the uniformity or repeatability of the sample
- To obtain some absolute measure of the continuous in-flight strength profile of the sample

In the laboratory, the centrifuge model can be prepared in a plane strain or axisymmetric strong-box or just a simple tub and then instrumented and transferred carefully to the centrifuge for testing. Figure 2.15 shows the assembled package of a CPT centrifuge test.

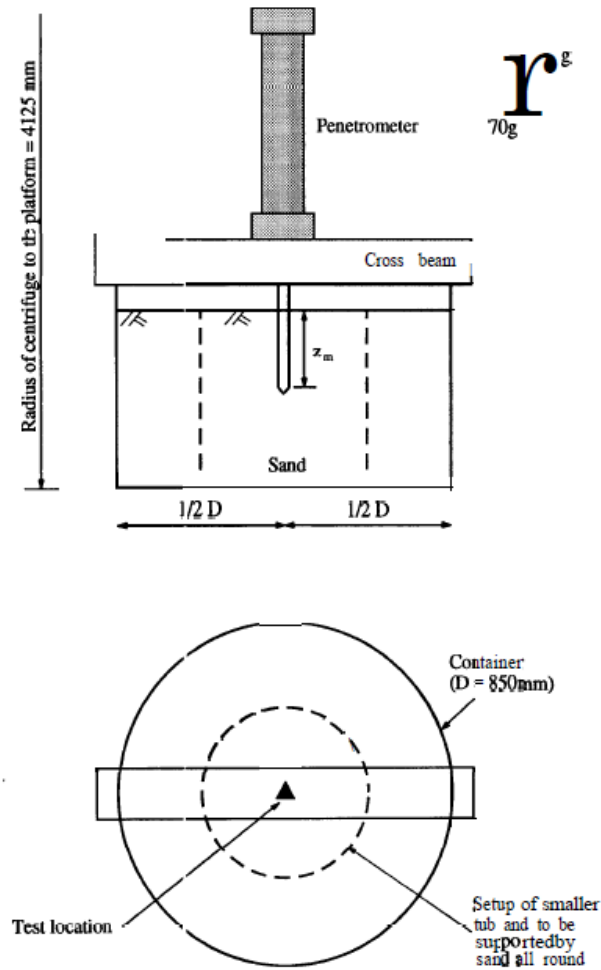


Figure 2.15 Schematic of centrifuge package (Bolton and Gui, 1993)

2.2.2 Factors affecting penetration resistance

Several factors such as container size, particle size, stress level and penetration rate have been found to affect the results of CPT in centrifuge modelling (Bolton and Gui, 1993; Gui et al., 1998; Bolton et al., 1999).

Container size effect

CPTs in containers of different diameters were conducted in a centrifuge to study the effect of the container-to-cone diameter ratio D/B (Bolton et al., 1999). For a CPT having a 10mm diameter cone, two containers of 850mm and 210mm diameters were

used, while for 12mm and 11.3mm diameter cones, containers of 530mm and 100mm diameter were used respectively. The consequence of this was a range of D/B ratios, from 8.85 to 85. From Figure 2.16 it can be seen that there is no obvious increase in Q for the test done with $D/B = 44$ and $D/B = 85$. However, Q is higher for the test carried out in the container with $D/B = 21$ and is significantly higher for $D/B = 8.85$.

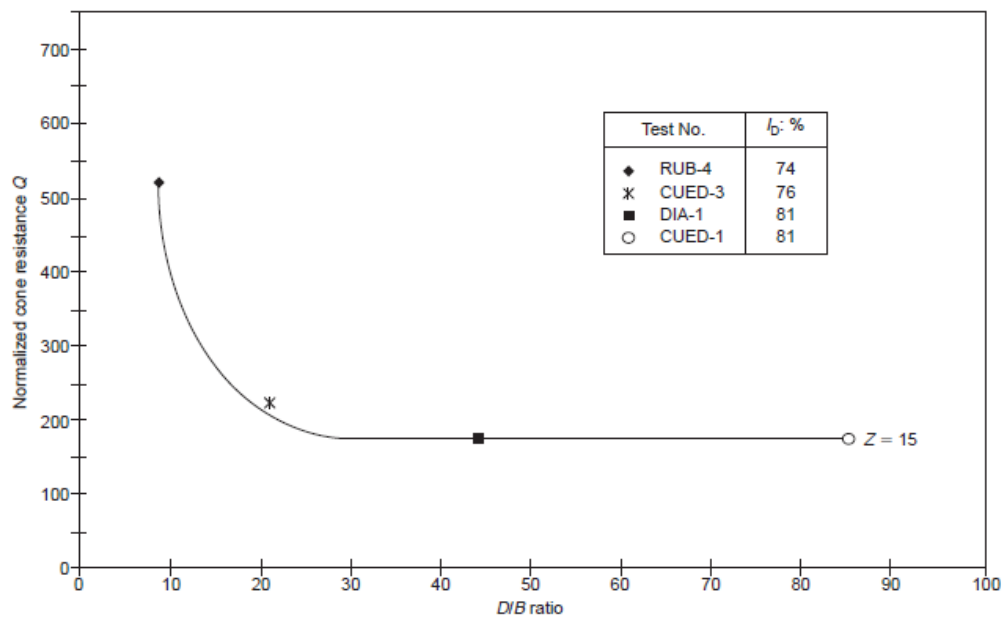


Figure 2.16 Effect of D/B ratio (Bolton et al., 1999)

Side boundary effect

A circular container with diameter of 530mm was used to study the side boundary effect S/B on CPT results in centrifuge modelling (Bolton et al., 1999). Two dense specimens, with relative densities of 81% and 80% were prepared and using a cone penetrometer which could be moved in flight, three CPTs were conducted for each specimen. For the first specimen, the penetrometer targeted the centre of the specimen (point C), and then the quarter-points of the container (A and E) as shown in Figure 2.17. For the second specimen, the first and second penetration tests were

performed at the quarter-points (A and E), and the final test at the centre of the specimen (point C). Figure 2.17 shows the results of these tests, which indicate no significant deviation in Q , for both $S/B=11$ and $S/B=22$. Furthermore, it is evident that the sequence of penetration had no clear effect on the measured cone resistance.

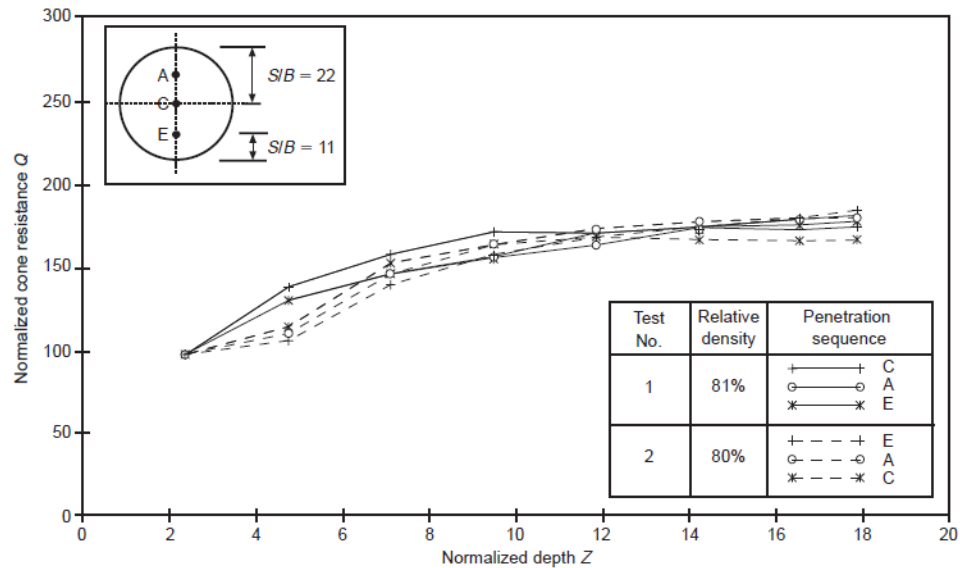
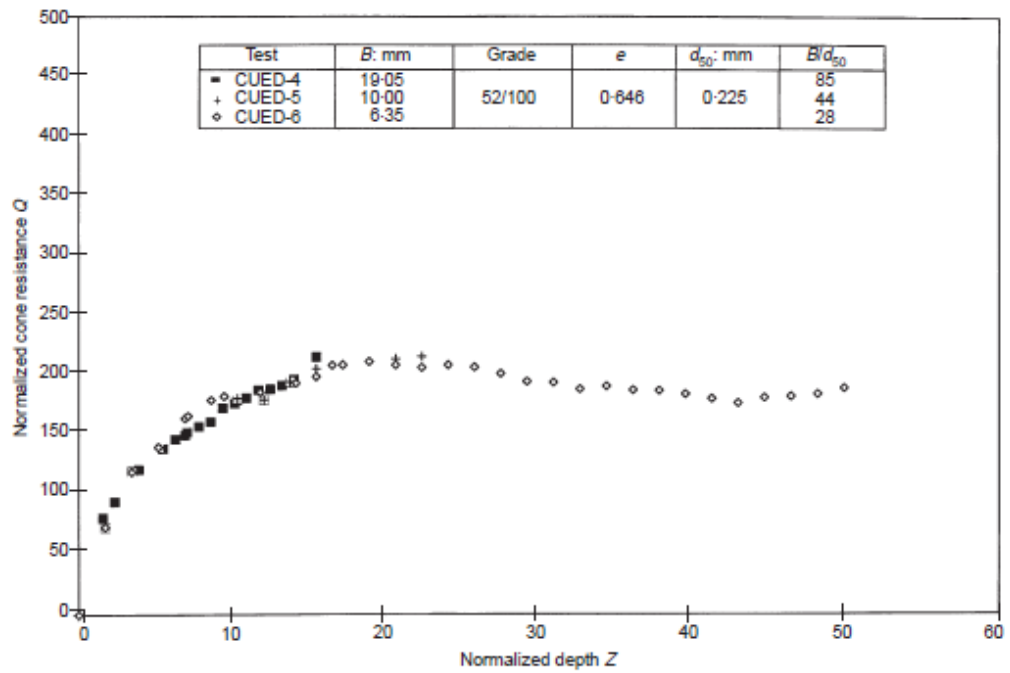


Figure 2.17 Effect of S/B ratio for a circular container (Bolton et al., 1999)

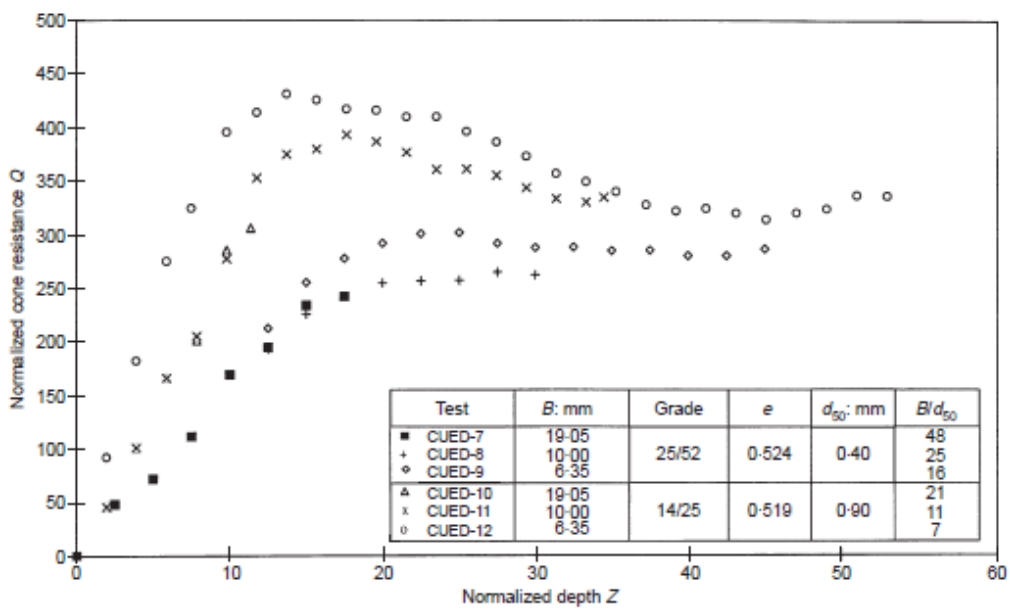
Particle size effect

Leighton Buzzard sand was used by Bolton and Gui (1993) to study the effect of the ratio of cone diameter to the mean grain size B/d_{50} . Figure 2.18a shows their plot of normalized cone resistance Q against the normalized depth Z for cones of different diameters for fine sand of identical relative densities. It can be seen that there is little variation of Q with depth as a result of varying the sand's particle size except when the cone was in close proximity to the base of the test container. It can therefore be concluded that the soil particle size does not affect the CPT result for values of the B/d_{50} in the range 28 to 85.

In similar plots Figure 2.18b for medium and coarse Leighton Buzzard sand, it is shown that between $B/d_{50}=25$ and 48 there is little variation in Q , although some divergence in Q is noted from $B/d_{50}=16$. For the coarse sand, comparatively higher Q values are generally evident with only marginal change noted when B/d_{50} was reduced from 21 to 11. However, a further reduction of B/d_{50} to 7 appears to elicit an increase in penetration resistance, especially at shallow depths. It therefore follows that some extra resistance is to be expected if the B/d_{50} ratio is allowed to fall below about 20 or thereabouts.



(a)



(b)

Figure 2.18 Grain size effects in Leighton Buzzard sand: (a) fine particles; (b) medium and coarse particles (Bolton et al., 1999)

Stress level effect

The stress level effect is often investigated by plotting Q against Z while holding B/d_{50} constant, for a particular soil of a particular density but for different acceleration ratios N . Bolton et al., (1999) conducted three CPTs applying the same boundary conditions at three elevated g levels $40g$, $70g$ and $125g$. All the tests were conducted using a cone diameter of 11.3mm and samples with relative density of 96%. From Figure 2.19 it can be seen that as the stresses increase, Q values decrease, thought most likely to be due to the increased tendency for crushing in the absence of any evidence to attribute the decrease to side friction. However, the importance of separately accounting for the effects of crushing and relative density cannot be ignored as has been demonstrated by Jamiolkowski et al. (1985) for deep probes.

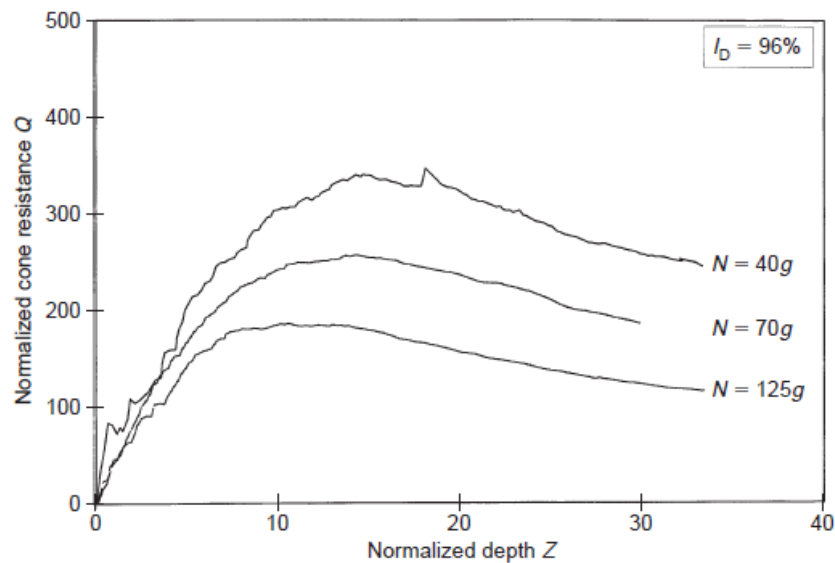


Figure 2.19 Effect of stress level (Bolton et al., 1999)

Penetration rate effect

To investigate the effect of CPT penetration rate by centrifuge modelling, five dense samples were prepared in a 400mm diameter chamber (Gui et al., 1998). Using a

11.3mm diameter cone, a single CPT was conducted at the centre of each sample. Penetration rates of 2.5 and 20mm/sec were applied to each sample. Figure 2.20 shows that there is no much difference in Q as a result of varying the penetration rate.

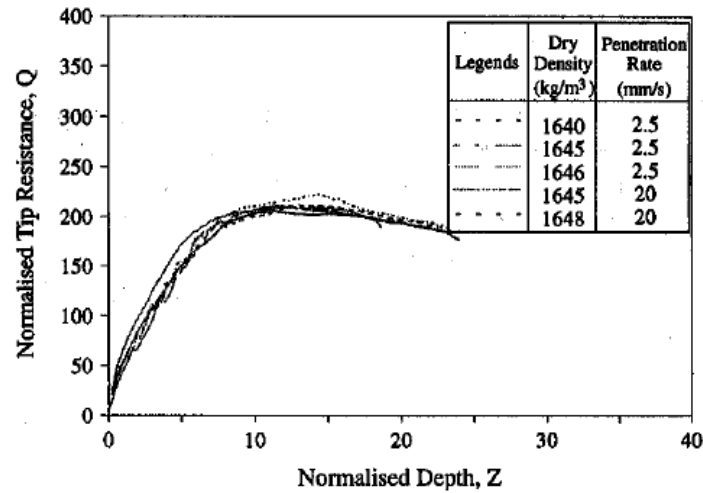


Figure 2.20 Effect of rate of penetration (Gui et al., 1998)

2.3 Calibration Chamber Test

2.3.1 Introduction

Calibration chamber testing has been shown to be a very useful technique for the calibration of *in situ* testing tools utilised in cohesionless materials (Parkin and Lunne, 1982; Salgado et al., 1998; Huang and Hsu, 2004). CPT tests conducted in a calibration chamber typically involve sample preparation in a laboratory, sample consolidation to a desired stress level, and then the undertaking of the CPT test for a specified set of boundary conditions. Each CPT test gives a value of q_c , which can be related to the initial density and stress level experienced in the chamber. A relation between q_c , density and stresses can be obtained by carrying out a number

of tests that cover a range of densities and stresses. The present general practice is to interpret the properties of a soil by comparing CPT data obtained *in situ* to the calibration chamber CPT results for the same soil.

Many calibration chambers have been built, for example, in the USA (Holden, 1971; Villet and Mitchell, 1981), Australia (Chapman, 1974), the UK (Fahey, 1980), Norway (Parkin and Lunne, 1982) and Italy (Bellotti et al., 1982). In the last few years the use of calibration chambers for testing sands has increased, as has their configuration and/or setup of the tests. Variations noted to date typically relate to chamber dimensions, boundary conditions, deposition procedure and capability to handle saturated specimens. According to a statistical study conducted by Ghionna and Jamiolkowski (1991), there were 19 calibration chambers in the world as of 1991. Table 2.1 summarises the geographical locations of all known existing calibration chambers in the world (Hsu and Huang, 1999).

Table 2.1 Current calibration chambers in the world (Hsu and Huang, 1999)

Calibration chamber (Owner and location)	Specimen diameter (m)	Specimen height (m)	Boundary conditions		
			Radial	Bottom	Top
Country Roads Board, Australia	0.76	0.91	Flexible	Cushion	Rigid
University of Florida, U.S.A.	1.20	1.20	Flexible	Cushion	Rigid
Monash University, Australia	1.20	1.80	Flexible	Cushion	Rigid
Norwegian Geotechnical Institute	1.20	1.50	Flexible	Cushion	Rigid
ENEL-CRIS, Milano, Italy	1.20	1.50	Flexible	Cushion	Rigid
ISMES, Bergamo, Italy	1.20	1.50	Flexible	Cushion	Rigid
University of California, Berkeley, U.S.A.	0.76	0.80	Flexible	Rigid	Rigid
University of Texas at Austin, U.S.A.	Cube 2.1x2.1x2.1		Flexible	Flexible	Flexible
University of Houston, U.S.A.	0.76	2.54	Flexible	Cushion	Cushion
North Carolina State University, U.S.A.	0.94	1.00	Flexible	Rigid	Rigid
Louisiana State University, U.S.A.	0.55	0.80	Flexible	Flexible	Rigid
Golder Associates, Calgary, Canada	1.40	1.00	Flexible	Rigid	Cushion
Virginia Polytechnic Institute and State University, U.S.A.	1.50	1.50	Flexible	Rigid	Rigid
University of Grenoble, France	1.20	1.50	Flexible	Cushion	Cushion
Oxford University, U.K.	0.90	1.10	Flexible	Cushion	Rigid
University of Tokyo, Japan	0.90	1.10	Flexible	Rigid	Rigid
University of Sheffield, U.K.	0.79	1.00	Flexible	Rigid	Flexible
Cornell University, U.S.A.	2.10	2.90	Flexible	Rigid	Rigid
Waterways Experiment Station, U.S.A.	0.80-3.00	Variable	Flexible	Rigid	Rigid
National Chiao-Tung University, Taiwan	0.51	0.76	Flexible	Rigid	Rigid
National Chiao-Tung University, Taiwan	0.79	1.60	Flexible	Flexible	Flexible

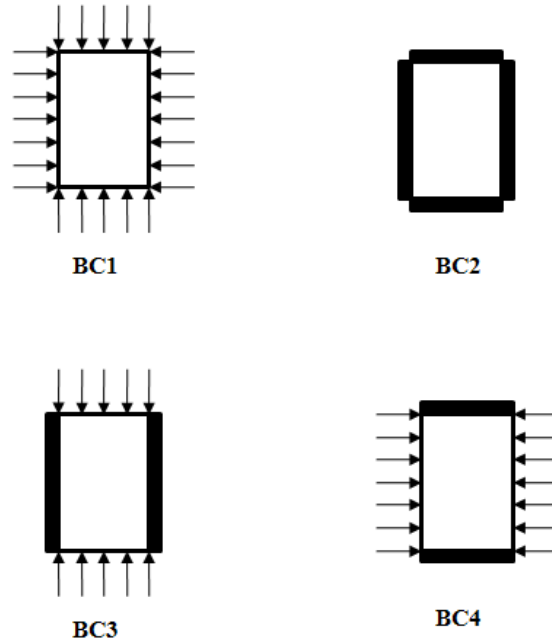
The use of a calibration chamber test and the subsequent interpretation of its results offers several advantages summarized as follows (Schnaid, 1990):

- The reproducible samples are, to some extent, similar in structure to natural deposits formed by sedimentation.
- Samples are homogeneous and the test is repeatable for a wide range of relative densities.
- Vertical and horizontal stresses applied on the samples can be controlled accurately.
- Stress and strain history of the samples can be simulated.

On the other hand the most significant disadvantage is the problem of limited chamber size which poses significant boundary effect concerns.

2.3.2 Chamber size and boundary effects

It is well known that the tip resistance value measured during the test is influenced by the boundary conditions subjected to the sample (Parkin and Lunne, 1982; Bellotti et al., 1982; Been et al., 1987; Salgado, 1993; Huang and Hsu, 2005). Figure 2.21 shows four different variations of boundary conditions that can be applied in a calibration chamber. The differences between the four types of boundary conditions shown relate to the nature of the stresses and/or displacements at the top, bottom and lateral sample boundaries. However, none of the four different boundary conditions described in Figure 2.21 simulate real field conditions perfectly. To reduce this discrepancy, researchers have often suggested the use of larger calibration chambers.



- BC1 (Constant stresses on lateral, top and bottom boundaries)
 BC2 (No displacement on lateral, top and bottom boundaries)
 BC3 (No displacement on lateral boundary, constant stresses on top and bottom boundaries)
 BC4 (Constant stresses on lateral boundary, no displacement on top and bottom boundaries)

Figure 2.21 Boundary conditions in a conventional calibration chamber test (Salgado et al., 1998)

Been et al. (1988) showed that boundary conditions at the top and bottom of a chamber specimen have little effect on CPT test results. Furthermore, Parkin (1988) proposed that of the four boundary conditions shown in Figure 2.21, BC1 and BC3 are the most important boundary conditions that affected CPT results. In a study (Parkin and Lunne, 1982) two different calibration chamber and penetrometer sizes were used. Their results showed that for loose sands, chamber size and boundary conditions do not have a significant effect on cone resistance. In contrast, for dense sands those effects were found to be considerable. Lunne and Christophersen (1983), referring to their chamber test results for Hokksund sand, determined that when the chamber to cone diameter ratio is 50, the difference in tip resistance obtained in the chamber compared to the field is small.

Jamiolkowski et al. (1985) presented an expression to relate the tip resistance obtained in a calibration chamber to the tip resistance in the field.

$$q_{c,field} = q_{c,cc} \left(1 + \frac{0.2(D_R\% - 30)}{60} \right) \quad 2.6$$

where

$q_{c,cc}$ is the experimental value of tip resistance measured in a calibration chamber

D_R is the relative density

$q_{c,field}$ is the corrected tip resistance expected to be measured in the field for a sand with the same relative density and *in situ* stresses as in the calibration chamber

When the above equation was applied to loose sand with a relative density of 30%, the results were found to be close to that obtained in the field with the effect of the calibration chamber size proving insignificant. However, by increasing the relative density of the sample in the chamber, the size effect is likely to be more significant. The above equation is valid for a cone penetrometer with a projected cone area of 10cm^2 pushed in a 1.2m diameter chamber, and is based on the experimental data obtained from calibration chamber test for a sample subjected to the BC1 boundary condition.

2.3.3 Experimental calibration chamber

This section describes the experimental calibration chamber (Schnaid, 1990) for Leighton Buzzard sand which has been used as a benchmark in this study for comparison to numerical models presented in a later chapter. A general description

of the calibration chamber components, test procedure, sample preparation, soil properties and the tip resistance results are presented as follows:

Calibration chamber

Schnaid's large triaxial calibration chamber was designed and built in Oxford University to calibrate a cone-pressurometer testing device. Figure 2.22 shows the lay-out of the apparatus developed.

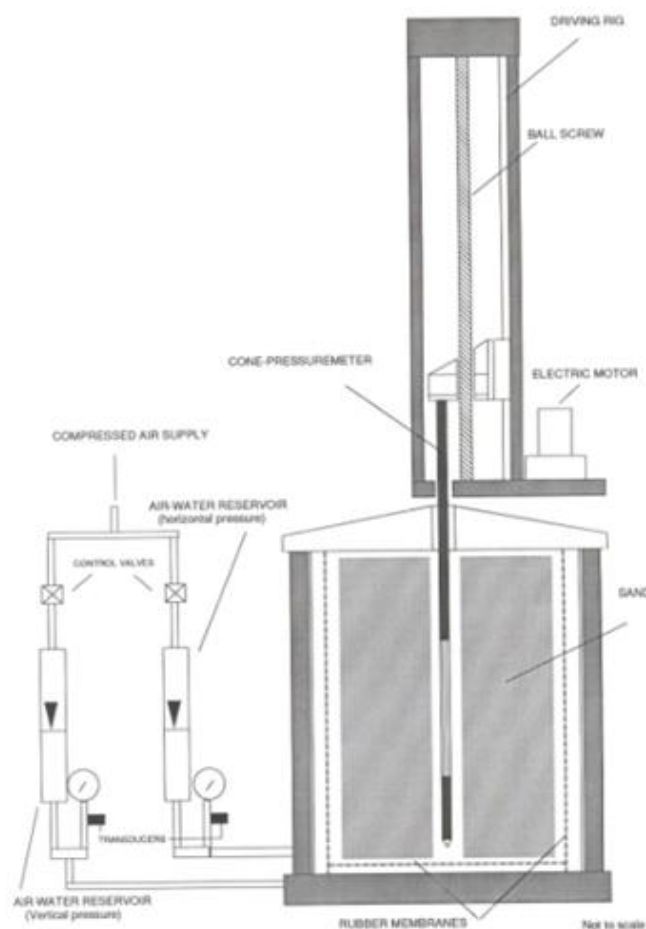


Figure 2.22 Schematic diagram of Oxford University calibration chamber (Schnaid, 1990)

The chamber is capable of housing and testing a cylindrical sand sample with diameter and height of 1.0m and 1.5m respectively. Samples tested are confined laterally and at the bottom surface by a flexible rubber membrane, which is used to

apply horizontal stress (laterally) and vertical stress (at the bottom) via water pressure. The top of the sample is confined by a rigid plate. To measure and control pressures during testing, two independent but identical pressurization systems are used, one for the horizontal stress and the other for the vertical stress. A change in the system's air pressure is induced using a self-relieving valve resulting in an air-water interface system. The interface allows water to be used to transmit stresses to the soil sample and also regulates pressure fluctuations arising from variations in volume experienced by the sample during a test.

Cone penetrometer testing device

As this study is only concerned with tip resistance results, only the cone component of the CPT assembly is considered. A standard 60°, 10cm² electric cone penetrometer is used to measure cone tip resistance. However, if required, sleeve friction and pore pressure measurements (in the case of a piezocone), can also be made.

Testing procedure

A rigid cylindrical mould is used to form a cylindrical sample inside a membrane walled chamber. A hopper with perforated plates and diffuser sieves is used to pour sand continuously in the chamber until it is slightly proud of the chamber. The sand surface is then levelled and the membrane gathered and connected to a vacuum supply. The sample is kept cylindrical by applying a vacuum pressure of 10kPa (± 5 kPa). A little vacuum is also applied to the annular space between the lateral flexible membrane and the chamber wall to pull the rubber membrane back to the chamber wall to enable the rigid former to be easily removed. The annular space behind the lateral membrane is then filled with water and the sample vacuum released to enable the boundary of the cylindrical sample to be supported by the

water. After the top surface of the sample is levelled precisely the top plate is fixed to the chamber body. The sample is confined independently horizontally and vertically by opening the chamber valves and controlling the self-relieving valves on the pressurization panel. Cone penetrometer tests can then be carried out at constant horizontal and vertical stresses. This is done by pushing the cone penetrometer into the chamber at a speed of 20mm/sec (± 5 mm/sec), and continuous recordings taken for cone tip resistance, penetration depth and horizontal vertical stresses.

Sample preparation

Preparation of the sand sample via raining deposition appears to be the most satisfactory technique as it not only results in reasonably homogeneous samples with intended densities but it also simulates soil fabric similar to that found in natural deposits formed by sedimentation (Oda et al., 1978; Bellotti et al., 1982). The method is applied by raining sand continuously from a cylindrical hopper placed above the chamber. Two shutter plates perforated in exactly the same way are placed at the base of the hopper and sand is jetted through the holes and separated into a uniform rain by diffuser sieves.

According to Kolbuszewski (1948), the ratio of a sample poured from a hopper is dependent on the intensity of the flow and the fall height of the sand. The raining deposition technique can be applied in the calibration chamber to obtain dense, medium and loose sand samples. This is achievable using a combination of different shutter plate sizes and diffuser sieves. The density of each sample is calculated at the end of each test by weighing the sand in the chamber and dividing its weight by the volume of the sample.

Soil properties

Leighton Buzzard sand fraction B was used as the standard granular soil in the calibration chamber. It has a specific gravity of 2.65 with graded particles passing between the British Standard sieves No. 14 and No. 25 as shown by Figure 2.23. It can be seen that the sand is very uniform (Coefficient of Uniformity $CU = 1.3$) and the mean grain size d_{50} is 0.8mm. The single particles are mostly quartz minerals with subangular to subrounded shapes. The maximum void ratio $e_{max}=0.774$ and the minimum void ratio $e_{min}=0.479$ can be achieved depending on the relative density of the samples to be tested.

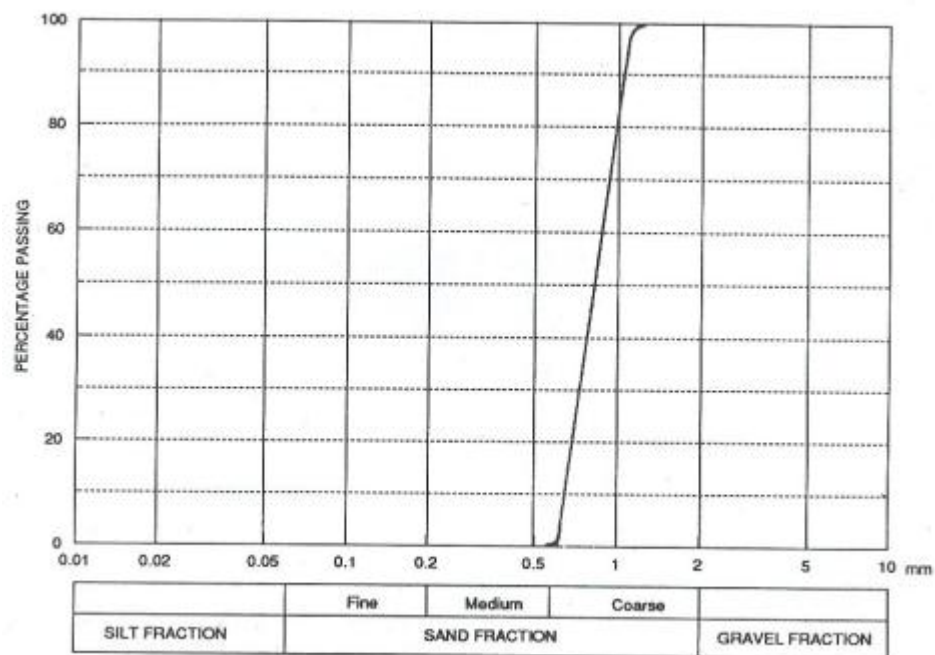


Figure 2.23 Particle size distributions (Schnaid, 1990)

Cone penetrometer testing results

After the sand has been stressed to the desired condition, the cone pressuremeter is pushed into the sample at a standard penetration rate of 20mm/s. Cone resistance and penetration depth is then measured every half second to plot profile of cone

resistance against depth. Schnaid (1990) investigated the influence of relative density and stress level on the cone tip resistance. Figure 2.24 shows the influence of relative density on q_c for tests carried out under identical stress conditions of mean effective stress $p'=100\text{kPa}$ and stress ratio $K_0=1.0$, while Figure 2.25 shows the influence of mean effective stress on q_c for tests performed at the same stress ratio ($K_0=0.5$) and approximately equal relative densities (from 62% to 68%). The plots indicate that the cone tip resistance increases with increasing density and increasing mean effective stress. Both behaviours have been studied in depth by researchers with calibration chambers and it has been consistently shown that relative density and mean effective stress are the most significant variables affecting the cone tip resistance (Schmertmann, 1976; Villet and Mitchell, 1981; Baldi et al., 1982; Baldi et al., 1986).

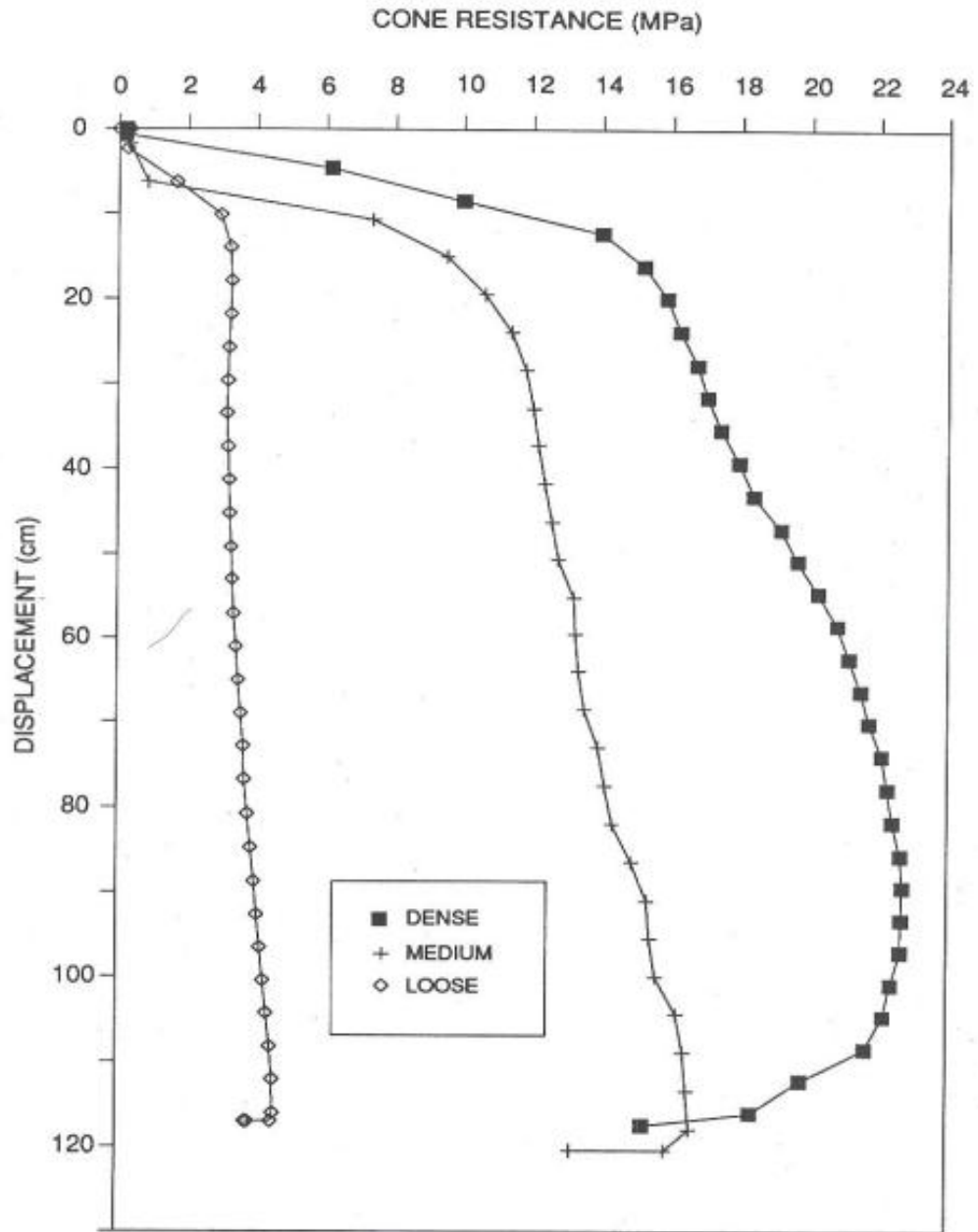


Figure 2.24 Influence of relative density on a profile of cone tip resistance against depth (Schnaid, 1990)

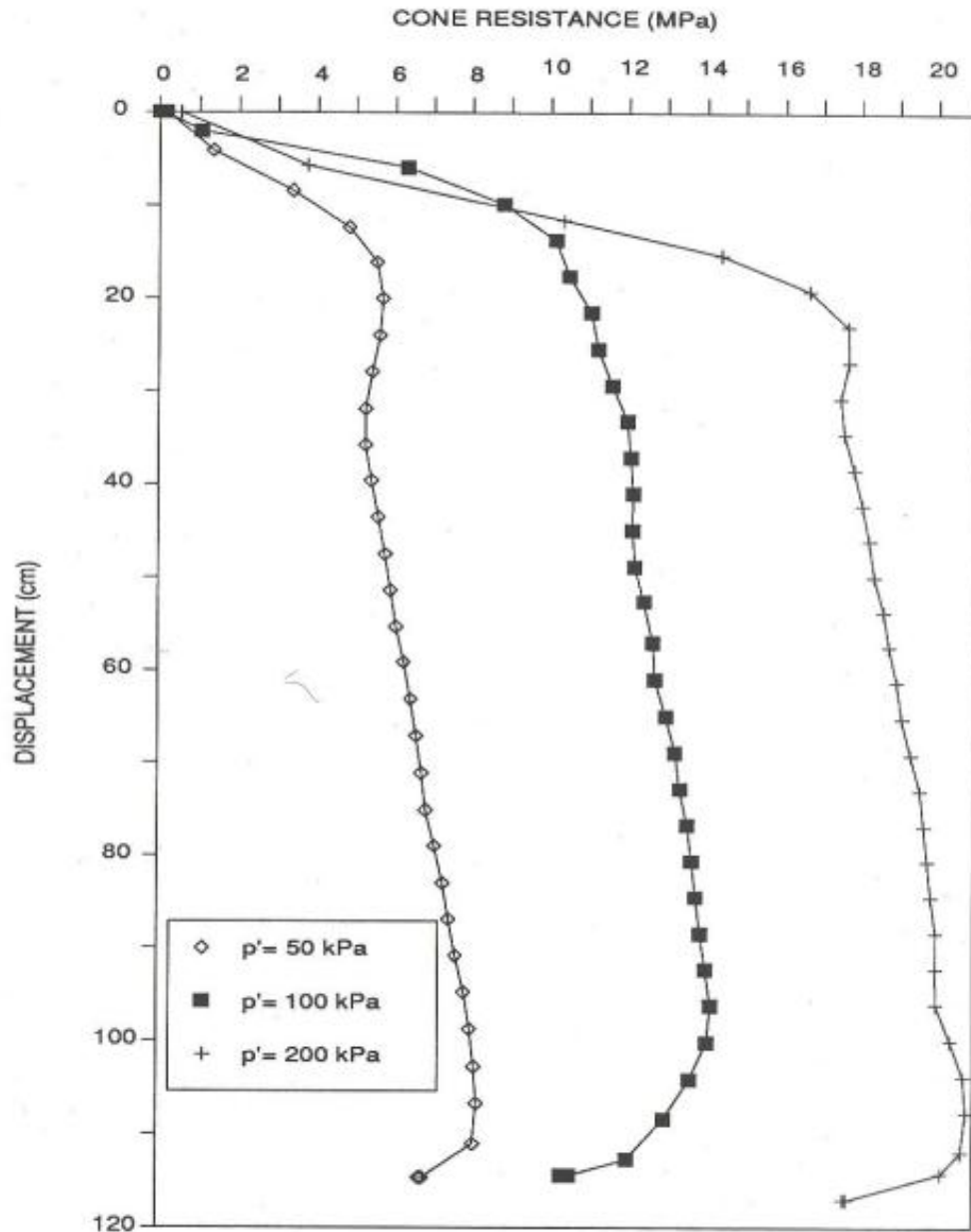


Figure 2.25 Influence of mean effective stress on a profile of cone tip resistance against depth (Schnaid, 1990)

2.4 Particle crushing

2.4.1 Introduction

Particle crushing is a relatively recent addition to the body of knowledge on granular materials and has attracted considerable interest amongst geotechnical researchers.

The survival probability of a particle in an aggregate assembly subjected to one-dimensional compression is determined by the applied macroscopic stress, size of the particle and a coordination number, which is the number of contacts with neighbouring particles (McDowell et al., 1996). Increasing the applied macroscopic stress would increase the average induced tensile stress in the particle, and consequently increase the probability of particle fracture. Soil particle strength in itself is a variable parameter because of the randomness of particle internal flaw sizes. Large particles tend to contain considerably more and larger internal flaws and thus exhibit a lower average tensile strength compared to smaller particles. It therefore follows on that the breakage probability of a particle will be less for smaller sized particles. Similarly, the breakage probability of a particle is reduced when the coordination number is increased. This occurs because the induced tensile stress in a particle diminishes as a result of the compressive stresses generated due to an increased interaction between constituent particles.

The tensile strength of a soil particle can be obtained by compressing the particle between two flat platens. McDowell and Amon (2000) found that the average strength and variation in strengths of soil particles is consistent with Weibull statistics (Weibull, 1951). McDowell and Bolton (1998) suggested that yielding of an aggregate subjected to one-dimensional compression was due to the onset of particle breakage and suggested that the yield stress of an aggregate should be proportional to the average tensile strength of the constituent particles.

2.4.2 Compression of a single particle

Particle fracture is known to be an important parameter affecting the behaviour of crushable soils. Investigating a range of particle sizes, Lee (1992) diametrically compressed individual particles of Leighton Buzzard sand, oolitic limestone and carboniferous limestone between flat platens as illustrated in Figure 2.26.

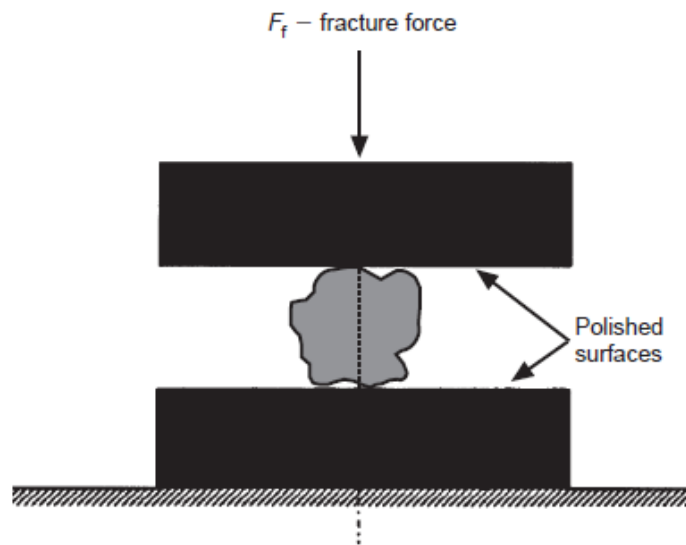


Figure 2.26 Particle tensile strength test set-up (Lee, 1992)

Lee also used a method similar to the Brazilian test, traditionally used to determine the tensile strength of concrete and calculated the tensile strength of the particles by applying the equation:

$$\sigma_f = \frac{F_f}{d^2} \quad 2.7$$

where:

σ_f is the tensile stress at failure

F_f is the diametral fracture force applied

d is the particle size

Lee (1992) introduced a typical result of this kind of crushing test by plotting force against deformation as shown in Figure 2.27.

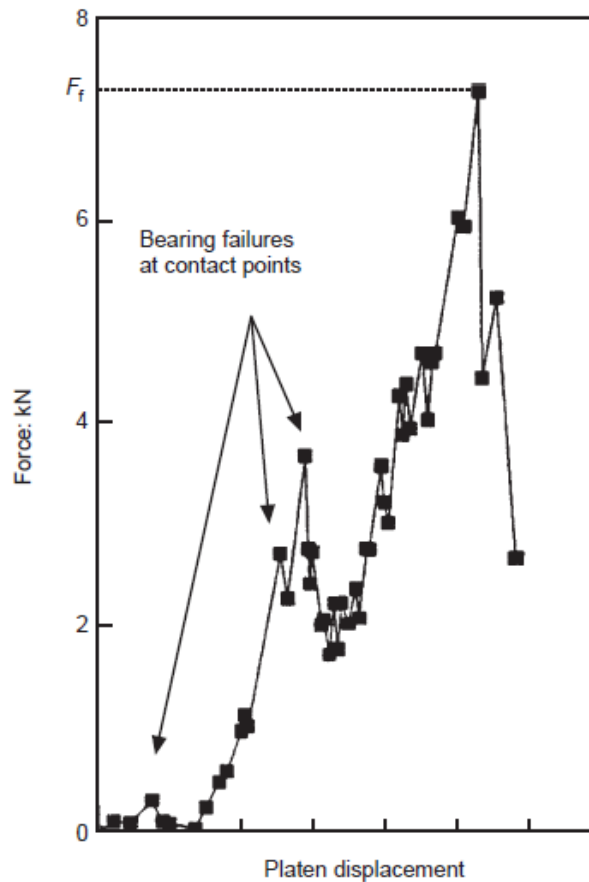


Figure 2.27 Typical plot of force against deformation for a typical particle(Lee, 1992)

Some initial peaks can be observed in the plotted curve above corresponding to the fracturing of asperities and rounding of the particle as small corners are broken off. In addition, it is evident that the initial small peaks are followed by a maximum peak corresponding to the maximum load and a major fracture along the loading axis where the particle split into two or more parts. As such, the tensile strength of the particle is determined using the maximum peak load. Figure 2.28 illustrates the mean tensile strength σ_f as a function of the average particle size d . It was found that the data presented could be expressed by the relation:

$$\sigma_f \propto d^b$$

2.8

where typical values of b are given as -0.357, -0.343 and -0.420 for Leighton Buzzard sand, oolitic limestone and carboniferous limestone, respectively.

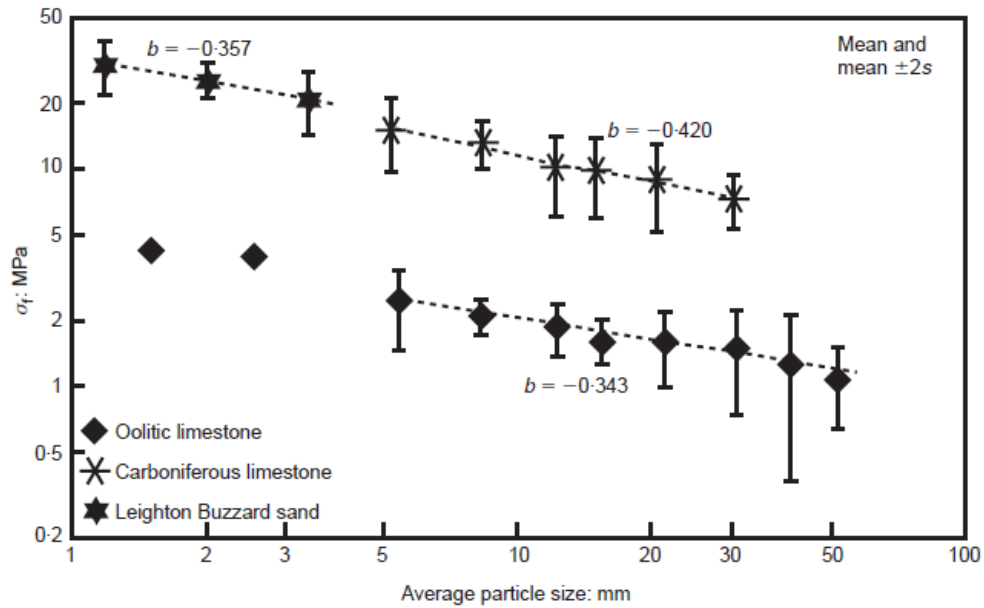


Figure 2.28 Results of mean tensile strength for single particle crushing tests (Lee, 1992)

McDowell and Bolton (1998) defined a general characteristic tensile stress σ as:

$$\sigma = \frac{F}{d^2} \quad 2.9$$

where:

F is the force applied

d is the particle size

σ is the characteristic tensile stress induced within the particle

2.4.3 Weibull statistics applied to soil particle strength

The Weibull (1951) distribution approach is widely adopted for analysing the breakage of disordered material and has been particularly implemented for analysing the variation in strength of ceramics. The simplicity of the Weibull statistics lies in its conformance to a “weakest link” model for which the failure of one element in a larger block of interconnected identical elements results in the failure of the entire block. Weibull proposed that for a volume V , under an applied tensile stress σ , the survival probability $P_s(V)$ of the block is given by:

$$P_s(V) = \exp \left[-\frac{V}{V_0} \left(\frac{\sigma}{\sigma_0} \right)^m \right] \quad 2.10$$

where V_0 is a reference volume of the material such that:

$$P_s(V_0) = \exp \left[-\left(\frac{\sigma}{\sigma_0} \right)^m \right] \quad 2.11$$

The stress σ_0 is the value of stress for a sample of volume V_0 whereby 37% of tested samples survive, and m is the Weibull modulus, which decreases with increasing variability in strength, as illustrated in Figure 2.29. When $\sigma = 0$, all the samples survive and $P_s(V_0) = 1$. Also, as the tensile stress σ increases, more samples fail and $P_s(V_0)$ decreases. For large stresses $\sigma \rightarrow \infty$, all the samples fail and $P_s(V_0) \rightarrow 0$.

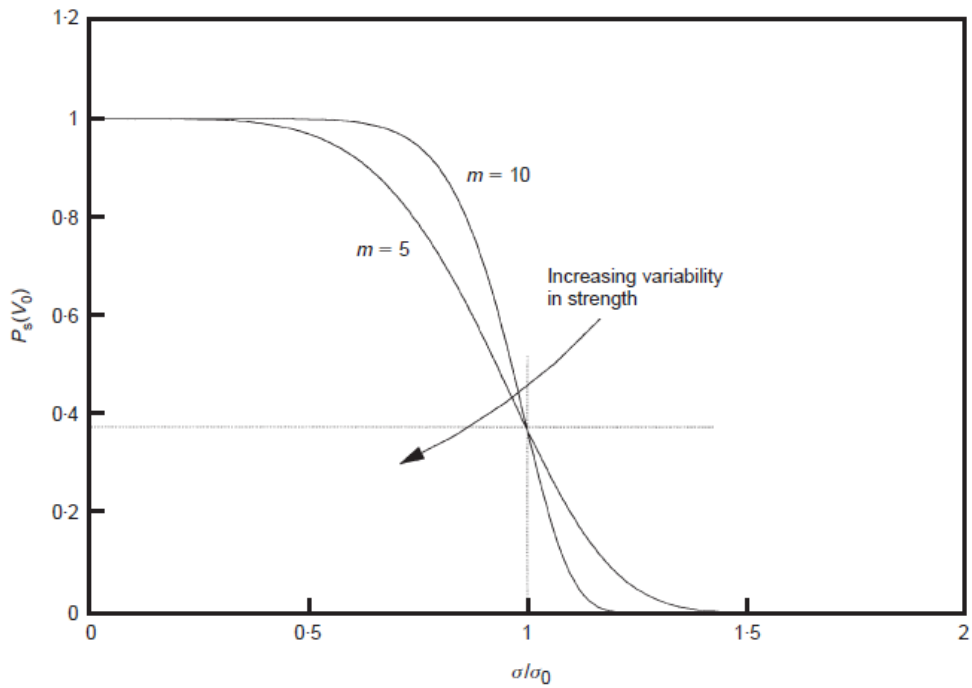


Figure 2.29 Weibull distribution of strengths

McDowell and Bolton (1998) showed that it is possible to derive the following expression if bulk fracture occurs (as opposed to surface fracture):

$$\sigma_0 \propto d^{-3/m} \quad 2.12$$

This expression is equivalent to Equation 2.8. Furthermore, for values of m between 5 and 10 lie in the range of Lee's data for rock particles in Figure 2.28.

2.4.4 Yielding of granular materials

McDowell and Bolton (1998) studied the micro mechanics of soils subjected to one-dimensional compression. They found that at low stresses, the behaviour of soils subjected to one-dimensional compression is quasi-elastic and small irrecoverable deformations may occur because of particle rearrangement. However, at high stresses further compaction cannot be occurred due to particle rearrangement alone. Hence,

they suggested that particle fracture is necessary for further compaction beyond yielding, which is known to be a point where major plastic deformation starts.

In addition, McDowell and Bolton (1998) noted that not all particles are loaded in the same way. However, it may be assumed that all particles will finally be in the path of the columns of strong force that transmit the macroscopic stress. Using discrete element method numerical simulations, Cundall and Strack (1979) showed that the applied major principal stress was transmitted through columns of strong force as shown in Figure 2.30.

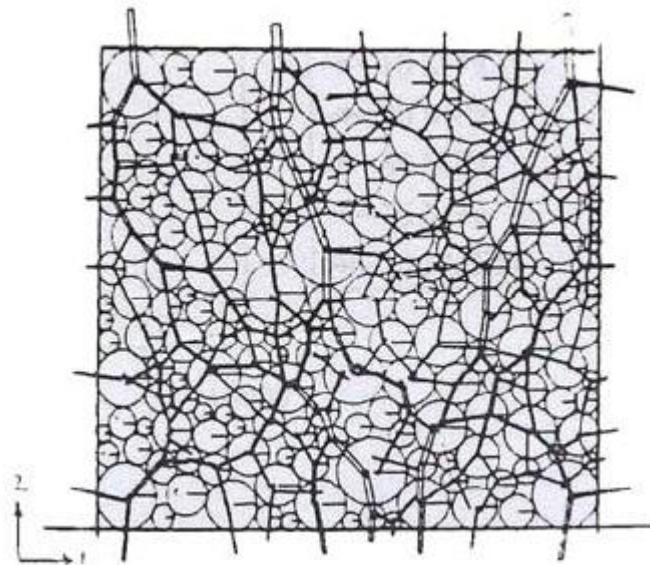


Figure 2.30 Discrete element simulation of array of photoelastic discs (Cundall and Strack, 1979)

McDowell & Bolton (1998) proposed that the yield stress must be proportional to the average tensile strength of the particles when it measured by crushing between flat platens. They defined yield stress as a value of macroscopic stress which causes maximum rate of particle breakage under increasing stress.

McDowell (2002) described one-dimensional compression tests on densely compacted silica sand of different uniformly-graded samples. The initial voids ratio was almost the same for each aggregate, as all particles had similar angularity and compacted in the same way to maximum density. Figure 2.31 shows the test results and it can be seen that the stress level in the yielding region depends on the initial particle size and increases with reducing particle size.

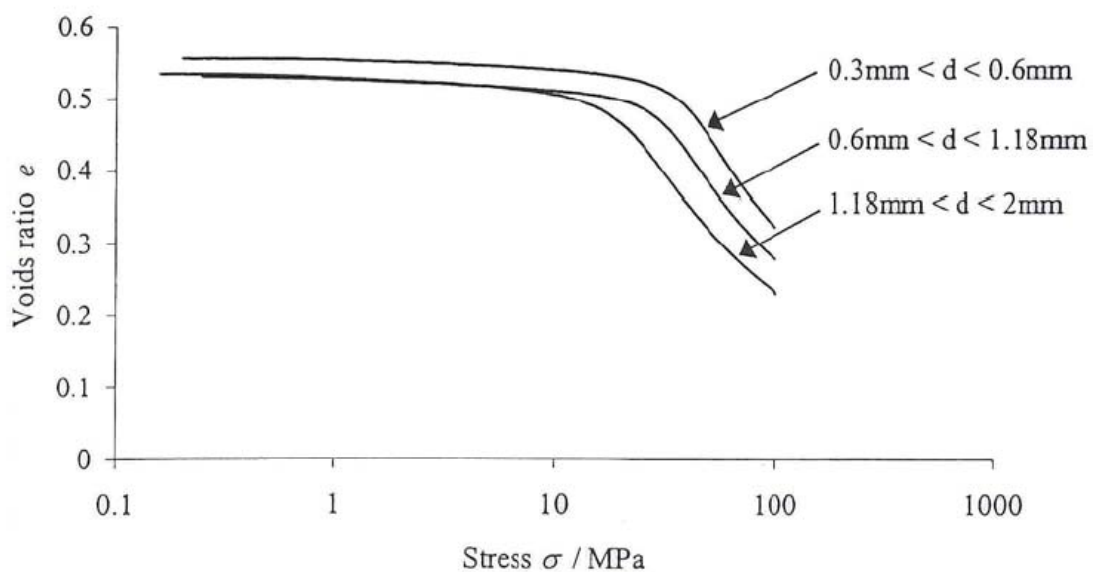


Figure 2.31 Compression plots for different uniform gradings of sand (McDowell, 2002)

McDowell (2002) described that the major principal stress applied was only transmitted through two or three columns of strong force for a group of approximately 12 particles wide. In order to predict the yield stress of the aggregate as 1/4 of the 37% tensile strength of the constituent particles in the aggregate, McDowell (2002) used a simple estimation that the characteristic stress induced in the particles forming the columns of strong force should be four times the applied macroscopic stress. The results were shown in Figure 2.32 and it can be seen that the yield stress was predicted fairly well and this further strengthens the suggestion made

by McDowell and Bolton (1998) that yield stress should be proportional to the tensile strength of the individual particles.

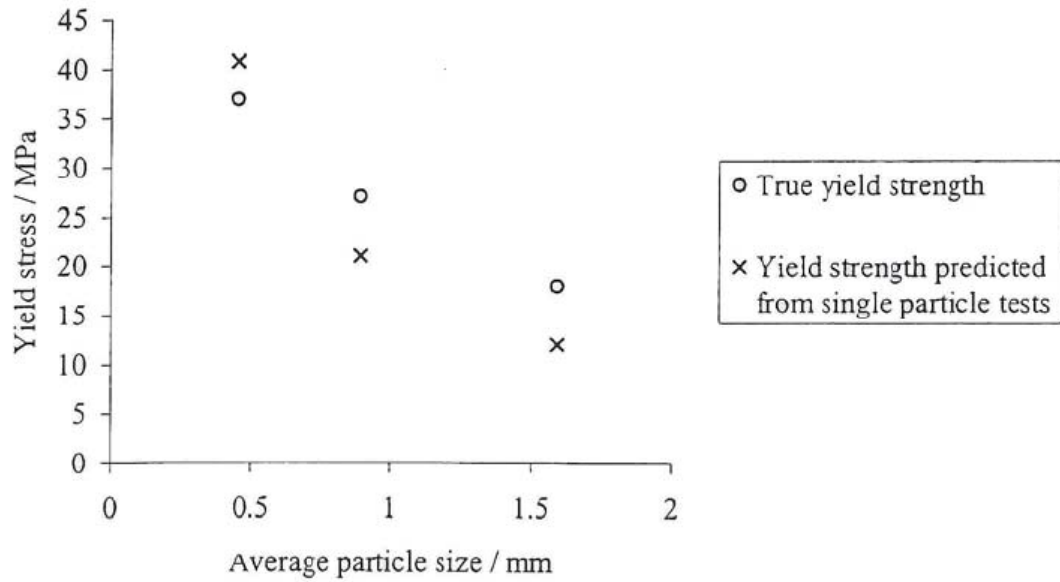


Figure 2.32 Yield stress predicted from single particle crushing tests, assuming yield stress = (37% tensile strength)/4 (McDowell, 2002)

2.5 Conclusions

CPT is a well established *in situ* soil test in geotechnical engineering because of its ability to measure data continuously and the repeatability it offers at a relatively low cost. The CPT has also been proven a useful *in situ* tool for soil classification and the determination of soil stratigraphy and soil properties. Cone penetration problems are mainly analysed using bearing capacity, strain path, cavity expansion, finite element and discrete element methods.

Centrifuge tests have been shown by several researchers to be a useful means of modelling geotechnical problems. Results from the centrifuge testing of CPT models are generally extrapolated to a prototype situation. Centrifuges are a less expensive and quicker means of undertaking full-scale tests and this makes them an attractive option. Several factors have been found to affect the penetration resistance in centrifuge modelling such as container size, particle size, stress level and penetration rate.

Calibration chamber testing has also been shown to be a useful experimental or empirical way to interpret results of cone penetration tests in sand. It offers several advantages such as the ability to replicate homogeneous samples for a wide range of relative densities as well as the accurate control of the vertical and horizontal stresses applied to the samples being tested. However, the calibration chamber's limited size has been reported as a problem because of the boundary conditions imposed on the sample being tested. The large calibration chamber utilised by Schnaid (1990) was used as a benchmark for comparison to the numerical models utilised in this study. The general characteristics of the calibration chamber including the test procedure,

sample preparation and soil properties have been described. Several tests undertaken using this calibration chamber to ascertain the influence of relative density and stress level on the cone tip resistance have shown that increasing one or both of the aforementioned parameters results in an increased cone tip resistance.

The key difference between the calibration chamber and centrifuge is that in the calibration chamber test the effect of the overburden pressure can be simulated by applying vertical and horizontal stresses on the boundaries, whereas in the centrifuge test the overburden pressure can be simulated by applying weight on a pressurised bladder fixed at the sample's surface. However, the effect of stress gradient due to the self-weight of the soil cannot be simulated in the calibration chamber but can be simulated in the centrifuge.

Particle crushing is an important issue in many geotechnical engineering applications, such as cone penetration testing and pile driving. Particle crushing is controlled by several factors such as, the applied macroscopic stress, size of the particle and the coordination number. For a single particle compressed diametrically between flat platens, the average strength and variation in strengths of soil particles is follow a Weibull distribution. Experimental results have also shown that for oedometer tests on sands, the yield stress is approximately proportional to the average tensile strength of the constituent particles.

CHAPTER 3

DISCRETE ELEMENT MODELLING OF GRANULAR MATERIAL

3.1 Introduction

Granular materials are made up of many distinct solid particles of various shapes and sizes. They can behave differently from other conventional states of matter: solids, liquid, or gas. They exhibit very complex behaviour under different loading and unloading conditions making it difficult to obtain generalised constitutive relationships. Cundall and Strack (1979) showed that the Discrete Element Method (DEM) provides a way to understand the mechanical properties of granular material at both microscopic and macroscopic level. Discrete element modelling is a numerical method which was developed to compute the motion of a large number of particles of micron-scale size and above, and describe the mechanical behaviour of assemblies of discs and spheres respectively in two and three dimensions.

Today DEM is widely accepted as an effective method for addressing engineering problems in granular and discontinuous materials, especially in granular flows, powder mechanics, and rock mechanics. The stress-strain behaviour of granular material with microstructural consideration can be determined from properties of inter-particle contacts. Discrete element modelling is also a useful method for

investigating features which are difficult to measure in laboratory tests for instance, particle displacement and contact forces.

3.2 Discrete Element Method

The discrete element method is designed to investigate problems in engineering and applied science that show gross discontinuous behaviour. The examples of engineering problems are many, for instance solid flow in hoppers, flow in pneumatic conveying and in geo-engineering for analysing stability of underground mine openings. These examples show that discontinuous behaviour is difficult to simulate by the conventional continuum-based computer modelling methods such as finite element method. DEM is a useful complement to continuum methods. It is a time stepping simulation of the dynamics of individual particles or a cluster of particles. The discrete element method was first developed by Cundall (1971) for rock mechanics problems and then increasingly applied to simulate the mechanical behaviour of granular materials (Cundall and Strack, 1979; Ting et al., 1989; Rothenburg and Bathurst, 1992).

Due to improving computer technology, DEM is becoming an important method in many scientific fields and is playing a greater role in industry. For instance, it is applied in the mining industry to simulate industrial particle flows (Cleary, 2000), in chemical engineering to simulate segregation phenomena in systems consisting of particles of different sizes (Hoomans et al., 2000) and to study the fabric and structure of granular materials under loading, and for developing constitutive relations for soil using disks and spheres (Oner, 1984; Zhang and Cundall, 1986; Bathurst and Rothenburg, 1988).

The interaction of particles is modelled contact by contact and the motion of the particles is modelled particle by particle. Cundall and Hart (1992) presented a summary of the fundamental aspects of the discrete element method and highlighted the scope of the method, which allows finite displacement and rotations of discrete bodies, including complete detachment and recognizing new contacts automatically as the calculation progresses.

The contact forces and displacements of a stressed assembly of particles in the DEM simulation are determined by tracing the movements of the individual particles. The movements and the interactions of the particles are considered to be a dynamic process resulting from the propagation of disturbances through the particle system caused by specified walls, particle motions and body forces. The dynamic process of a particle assembly is treated by using an explicit time-stepping scheme in which it is assumed that the velocities and accelerations are constant within each timestep. Damping is an important parameter in the DEM calculation as the movements of granular materials particles are permanent. Failure to consider damping in any particle system would lead to the generation of kinetic energy within the system and subsequent simple harmonic motion around the equilibrium position. Consequently, damping serves to dissipate the kinetic energy from the system.

3.3 The PFC^{3D} Particle-Flow Model

3.3.1 Introduction

PFC^{3D} is a general particle-flow model which simulates the movement and interaction of spherical particles by the distinct element method (DEM), as presented by Cundall and Strack (1979). PFC^{3D} is designed to be an efficient tool to simulate

complicated problems in solid mechanics and granular materials. Newton's second law is applied as the principle for the motion of each particle caused by the contact and body forces acting upon it. Meanwhile a force-displacement law is applied to update the contact force caused by the relative motion at each contact. PFC^{3D} allows particles to be bonded together at their contact point to model more complex behaviour. However, the bonds created break when the inter particle forces (i.e. tensile, shear or moment) acting on any bond exceeds the bond strength. It is also possible to create arbitrary shape particles when two or more particles overlap, such that each group of particles acts as an autonomous object using clump logic. Particles within a clump may overlap to any extent, and each clump behaves as a rigid body with deformable boundaries and, therefore, can be used as a super-particle of general shape.

The particle-flow model PFC^{3D} provides the following assumptions:

1. The particles in the model are treated as rigid bodies.
2. The contacts happen over a vanishingly small area (as a point).
3. A soft-contact is assumed to occur at particle contact areas wherein the rigid particles are allowed to overlap one another at contact points.
4. The magnitude of the overlap is related to the contact force using the force-displacement law and all overlaps are small compared to individual particle sizes.
5. Bonds can form at contacts between particles.
6. All particles are spheres, and arbitrary shaped super-particles can be created using the clump. Each clump consists of a set of overlapping spheres, and acts as a rigid body with a deformable boundary.

PFC^{3D} can model stress-strain behaviour of granular materials using the movement and interaction of rigid spherical particles based on the DEM. The PFC^{3D} particle-flow model contains “balls” and “walls”. Walls are used in the application of velocity boundary conditions to assemblies of balls to simulate compaction and confinement. The balls and walls interact with one another via the forces that arise at contacts. The timestep calculation is automatic and changes during the simulation in accordance to the number of contacts around each particle and the instantaneous stiffness values and masses.

3.3.2 Calculation Cycle

The repeated application of the law of motion to each particle, a force-displacement law to each contact and a constant updating of wall positions are required in the calculation cycle in PFC^{3D}. Contacts exist between two balls or between a ball and a wall, which form and break automatically during the course of a simulation. Figure 3.1 shows the calculation cycle. It can be seen that at the start of each timestep, from the known particle and wall positions the set of contacts is updated. After that the force-displacement law is applied to each contact to update the contact forces based on the relative motion between the two entities at the contact and the contact constitutive model. Then, the law of motion is applied to each particle to update its velocity and position based on the resultant force and moment arising from the contact forces and any forces acting on the particle. Furthermore, the wall positions are updated based on the specified wall velocities. The force-displacement law and the law of motion are described in the following subsections.

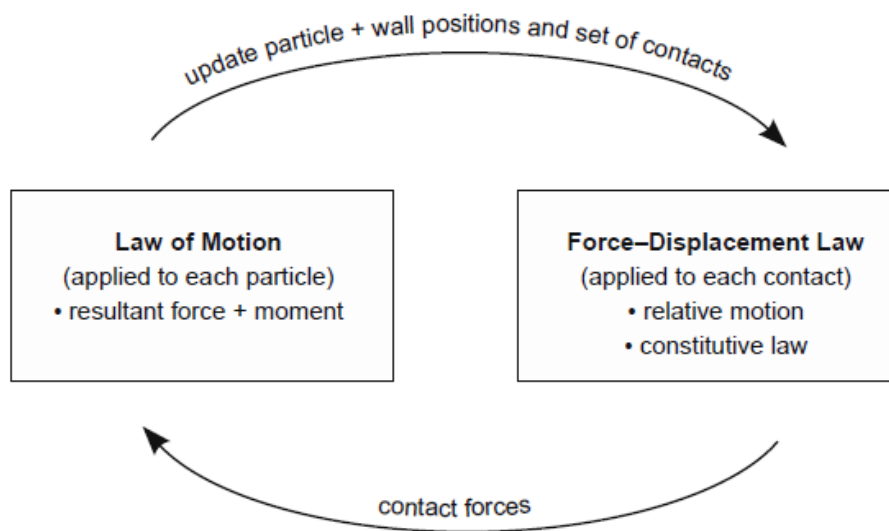


Figure 3.1 The calculation cycle in PFC3D (Itasca, 2003)

Force-Displacement Law

The force-displacement law relates the relative displacement between two entities at a contact to the contact force acting on the entities. There are two types of contacts: ball-ball and ball-wall. Figure 3.2 illustrates a ball-ball contact, the contact between two spheres labelled A and B.

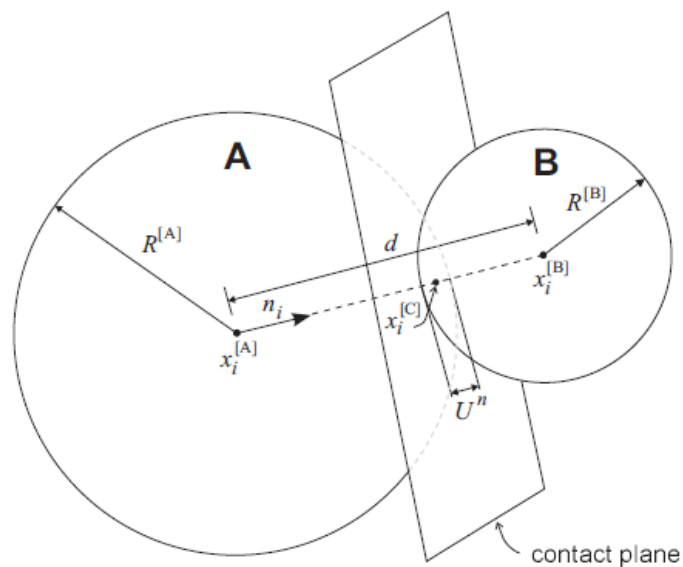


Figure 3.2 Notation used to describe ball-ball contact (Itasca, 2003)

Figure 3.3 shows a ball-wall contact, the contact between a sphere and a wall, labelled b and w .

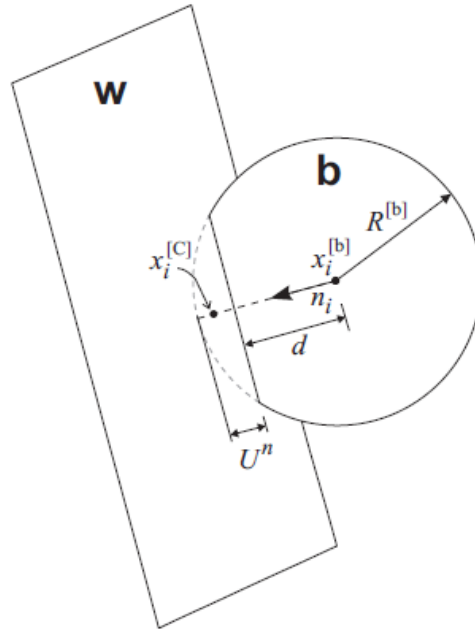


Figure 3.3 Notation used to describe ball-wall contact (Itasca, 2003)

In these figures:

n_i is the unit normal that defines the contact plane

d is the distance between the ball centres in ball-ball contact, and the distance between the ball centre and the wall in ball-wall contact

$x_i^{[A]}$, $x_i^{[B]}$ and $x_i^{[b]}$ are the position vectors of the centres of balls A and B

U^n is the overlap of the two entities, and is given by:

$$U^n = R^{[A]} + R^{[B]} - d \quad \text{for (ball-ball)} \quad 3.1$$

$$U^n = R^{[b]} - d \quad \text{for (ball-wall)} \quad 3.2$$

$x_i^{[C]}$ is the location of the contact point, and is given by:

$$x_i^{[C]} = x_i^{[A]} + (R^{[A]} - \frac{1}{2}U^n)n_i \quad \text{for (ball-ball)} \quad 3.3$$

$$x_i^{[C]} = x_i^{[b]} + (R^{[b]} - \frac{1}{2}U^n)n_i \quad \text{for (ball-wall)} \quad 3.4$$

The contact force vector F_i can be resolved into normal and shear components with respect to the contact plane as

$$F_i = F_i^n + F_i^s \quad 3.5$$

where F_i^n and F_i^s are the normal and shear component vectors, respectively.

The normal contact force vector is calculated by:

$$F_i^n = K^n U^n n_i \quad 3.6$$

where K^n is the value of normal stiffness [force/displacement] at the contact and the current contact-stiffness model is used to determine this value.

The shear contact force is determined incrementally. When the contact is created, the total shear contact force is initialized to zero. Each subsequent relative shear-displacement increment results in an increment of elastic shear force that is added to

the current value. Given that the shear contact force vector F_i^S is stored as a vector in global coordinates, therefore it must also be updated to account for contact motion. F_i^S is updated by computing two rotations:

$\{F_i^S\}_{rot.1}$ is about the line common to the old and new contact planes.

$\{F_i^S\}_{rot.2}$ is about the new normal direction.

The shear component of the contact displacement-increment vector occurring over a time step of Δt is calculated by

$$\Delta U_i^S = V_i^S \Delta t \quad 3.7$$

The shear elastic force-increment vector is calculated by

$$\Delta F_i^S = -k^S \Delta U_i^S \quad 3.8$$

where k^S is the shear stiffness (also tangent modulus) [force/displacement] at the contact and it can be determined by the current contact stiffness model. Finally, the new shear contact force is obtained by adding the old shear force vector existing at the start of the timestep to the shear elastic force-increment vector.

$$F_i^S = \{F_i^S\}_{rot.2} + \Delta F_i^S \quad 3.9$$

Law of Motion

The resultant force and moment vectors acting on a single rigid particle are used to determine the motion of this particle which can be described in terms of the translational motion of a point in the particle and the rotational motion of the particle. The equations of motion can be expressed as two vector equations, which relate the resultant force to the translational motion and the resultant moment to the rotational motion. The equations of motion can be written in the vector form as follows:

$$F_i = m(\ddot{x}_i - g_i) \quad \text{translational motion} \quad 3.10$$

$$M_i = \dot{H}_i \quad \text{rotational motion} \quad 3.11$$

where

F_i is the sum of all externally applied forces acting on the particle

m is the total mass of the particle

g_i is the body force acceleration vector

M_i is the resultant moment acting on the particle

\dot{H}_i is the angular momentum of the particle

In the case of a spherical particle of radius R , whose mass is distributed uniformly throughout its volume, the centre of mass coincides with the sphere centre. Thus, Equation 3.11 can be simplified and referred to the global-axis system

$$M_i = I\dot{\omega}_i = \left(\frac{2}{5}mR^2\right)\dot{\omega}_i \quad \text{rotational motion} \quad 3.12$$

where

I is the moment of inertia of the particle

$\dot{\omega}_i$ is the angular acceleration of the particle

The Equations of motion (3.10) and (3.12) are integrated using a centered finite difference procedure involving a timestep of Δt . The quantities \dot{x}_i and ω_i are calculated at the mid-intervals of $t \pm n\Delta t/2$, and the other quantities $x_i, \ddot{x}_i, \dot{\omega}_i, F_i$ and M_i are calculated at the primary intervals of $t \pm n\Delta t$. The translational and rotational accelerations at time t are described by the following expressions in terms of the velocity values at mid-intervals:

$$\ddot{x}_i^{(t)} = \frac{1}{\Delta t} \left(\dot{x}_i^{(t+\frac{\Delta t}{2})} - \dot{x}_i^{(t-\frac{\Delta t}{2})} \right) \quad 3.13$$

$$\dot{\omega}_i^{(t)} = \frac{1}{\Delta t} \left(\omega_i^{(t+\frac{\Delta t}{2})} - \omega_i^{(t-\frac{\Delta t}{2})} \right) \quad 3.14$$

By substituting Equations (3.13) and (3.14) into Equations (3.10) and (3.12) and solving for the velocities at time $t+\Delta t/2$ result in expressions obtained as:

$$\dot{x}_i^{(t+\Delta t/2)} = \dot{x}_i^{(t-\Delta t/2)} + \left(\frac{F_i^{(t)}}{m} + g_i \right) \Delta t \quad 3.15$$

$$\omega_i^{(t+\Delta t/2)} = \omega_i^{(t-\Delta t/2)} + \left(\frac{M_i^{(t)}}{I} \right) \Delta t \quad 3.16$$

Finally, the velocities in Equations (3.15) and (3.16) are used to update the position of the particle centre as follows:

$$x_i^{(t+\Delta t)} = x_i^{(t)} + \dot{x}_i^{(t+\Delta t/2)} \Delta t \quad 3.17$$

Overall, given the values of $\dot{x}_i^{(t-\Delta t/2)}$, $\omega_i^{(t-\Delta t/2)}$, $x_i^{(t)}$, $F_i^{(t)}$ and $M_i^{(t)}$ Equations (3.15) and (3.16) are used to obtain $\dot{x}_i^{(t+\Delta t/2)}$ and $\omega_i^{(t+\Delta t/2)}$. Then, Equation (3.17) is used to calculate $x_i^{(t+\Delta t)}$. By applying the force-displacement law, the values of $F_i^{(t+\Delta t)}$, $M_i^{(t+\Delta t)}$ are obtained and used in the next cycle.

3.3.3 Contact constitutive model

The overall constitutive behaviour of a material is simulated in PFC^{3D} by implementing a simple constitutive model at each contact. The constitutive model acting at a particular contact comprises: a stiffness model, a slip model and a bonding model. These three models are described in the following subsections.

Contact-stiffness model

The contact-stiffness model provides the relative displacement via a force-displacement law. The linear contact model is defined by the normal stiffness k_n and shear stiffness k_s between two contacts and assumes that the stiffness of the two contacting entities A and B act in series. The contact normal and shear stiffness for the linear contact model are given by:

$$k^n = \frac{k_n^{[A]} k_n^{[B]}}{k_n^{[A]} + k_n^{[B]}} \quad 3.18$$

$$k^s = \frac{k_s^{[A]} k_s^{[B]}}{k_s^{[A]} + k_s^{[B]}} \quad 3.19$$

where the superscripts [A] and [B] denote the two entities in contact.

The slip model

The slip model is an essential property of the two entities in contact. It provides no normal strength in tension and allows slip to happen by limiting the shear force. The model describes the constitutive behaviour for particle contact taking place at a point. It is defined by the friction coefficient at the contact μ (dimensionless), where μ is taken to be the minimum friction coefficient of the two contacting entities. Both the normal and shear contact forces are set to zero when the overlap is less than or equal to zero. The contact is checked for slip conditions by calculating the maximum allowable shear contact force

$$F_{max}^s = \mu |F_i^n| \quad 3.20$$

If $|F_i^s| > F_{max}^s$, then slip is allowed to occur during the next calculation cycle by setting the magnitude of F_i^s via

$$F_i^s \leftarrow F_i^s (F_{max}^s / |F_i^s|) \quad 3.21$$

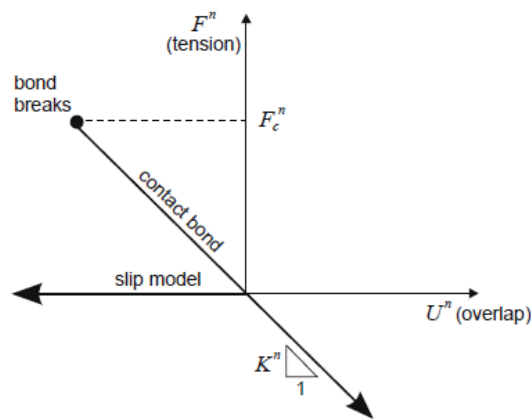
The bonding models

PFC^{3D} allows particles to be bonded together at contacts. There are two bonding models: (a) contact-bond model and (b) parallel-bond model. Both types of bonds may be active at the same time. Nevertheless, the presence of a contact bond inactivates the slip model. The bonds can be envisioned as a piece of glue joining the two particles. Once a bond is formed at a contact between two particles, the contact continues to exist until the bond is broken. Only one particle may be bonded to another one, and a particle may not be bonded to a wall.

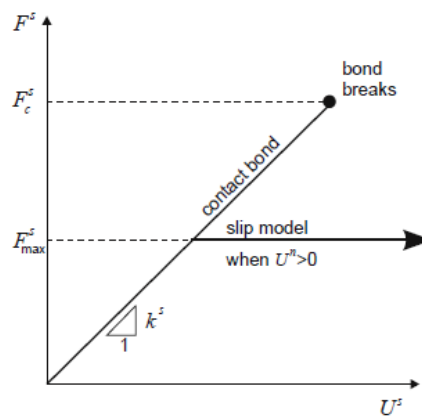
(a) The contact-bond model

The contact bond can be visualized as a pair of elastic springs with constant normal and shear stiffnesses acting at the contact point. These two springs have specified shear and tensile normal strengths. The magnitude of the shear contact force is limited by the shear contact bond strength. Contact bonds also allow tensile forces to develop at a contact. The magnitude of the tensile normal contact force is limited by the normal contact bond strength.

A contact bond comprises a normal contact bond strength F_c^n and a shear contact bond strength F_c^s . If the magnitude of the tensile normal contact force equals or exceeds the normal contact bond strength, the bond breaks. If the magnitude of the shear contact force equals or exceeds the shear contact bond strength, the bond breaks. The constitutive behaviour relating the normal and shear components of contact force and relative displacement for particle contact occurring at a point is illustrated in Figure 3.4.



(a) normal component of contact force



(b) shear component of contact force

Figure 3.4 Constitutive behaviour for contact occurring at a point (Itasca, 2003)

(b) The parallel –bond model

The parallel-bond model describes the constitutive behaviour of a finite-sized piece of cementation material deposited between two balls. Parallel bonds can transmit both forces and moments between particles. A parallel bond can be envisioned as a set of elastic springs with constant normal and shear stiffnesses, uniformly distributed over a circular disk lying on the contact plane and centered at the contact point. The constitutive behaviour of the parallel bond is shown in Figure 3.5. Relative motion at the contact causes a force and a moment to develop within the bond material as a result of the parallel-bond stiffnesses. The parallel bond breaks when either of normal and shear maximum stresses exceeds the parallel bond strength. The total force and moment associated with the parallel bond are denoted by \overline{F}_i and \overline{M}_i with the convention that this force and moment represent the action of the bond on sphere B of Figure 3.5. Each of these vectors can be resolved into normal and shear components with respect to the contact plane as

$$\overline{F}_i = \overline{F}_i^n + \overline{F}_i^s \quad 3.22$$

$$\overline{M}_i = \overline{M}_i^n + \overline{M}_i^s \quad 3.23$$

where \overline{F}_i^n , \overline{M}_i^n and \overline{F}_i^s , \overline{M}_i^s denote the normal and shear component vectors, respectively. These vectors are shown in Figure 3.5.

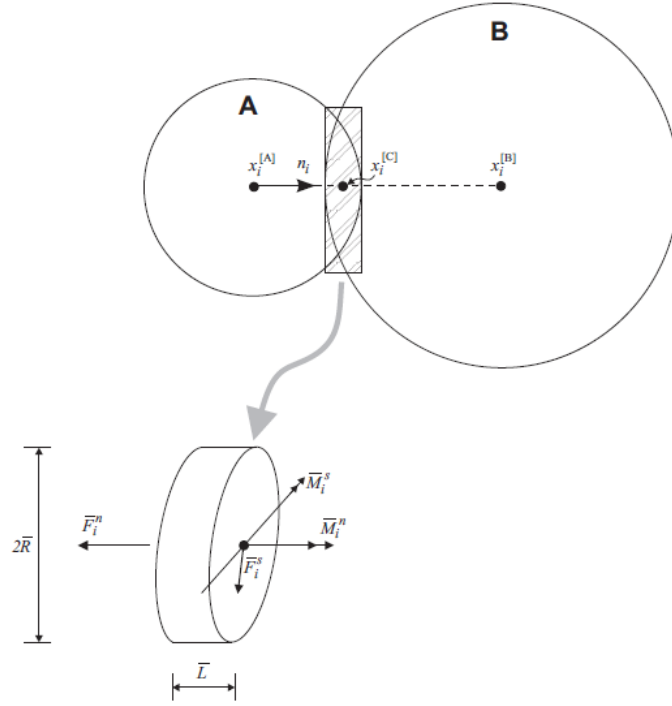


Figure 3.5 Parallel bond depicted as a cylinder of cementations material (Itasca, 2003)

where the parallel bond is depicted as a cylinder of elastic material, the normal component vectors can be expressed in terms of the scalar values \bar{F}^n and \bar{M}^n via

$$\bar{F}_i^n = (\bar{F}_j n_j) n_i = \bar{F}^n n_i \quad 3.24$$

$$\bar{M}_i^n = (\bar{M}_j n_j) n_i = \bar{M}^n n_i \quad 3.25$$

The maximum tensile and shear stresses acting on the bond periphery can be calculated by

$$\sigma_{max} = \frac{-\bar{F}^n}{A} + \frac{|\bar{M}_i^s|}{I} \bar{R} \quad 3.26$$

$$\tau_{max} = \frac{|\bar{F}_i^s|}{A} + \frac{|\bar{M}^n|}{J} \bar{R} \quad 3.27$$

where

A is the area of the bond disk

J is the polar moment of inertia of the disk cross-section

I is the moment of inertia of the disk cross-section about an axis through the contact point

R is the radius of the bond disc. The value of these parameters can be calculated as:

$$A = \pi \bar{R}^2 \quad 3.28$$

$$J = \frac{1}{2} \pi \bar{R}^4 \quad 3.29$$

$$I = \frac{1}{4} \pi \bar{R}^4 \quad 3.30$$

3.3.4 Clump logic

A clump is defined as a single entity of overlapping balls and behaves as a rigid body, whereas the balls comprising the clump remain at a fixed distance from each other. Contacts internal to the clump are ignored during the calculation cycle, resulting in a saving of computer time compared to a similar calculation in which all contacts are active. Particles within a clump may overlap to any extent and contact

forces are not generated between these particles. However, any contact forces that exist when the clump is created or when a particle is added to the clump will be preserved unchanged during cycling. Thus, a clump acts as a rigid body (with a deformable boundary) that will not break apart, regardless of the forces acting upon it. In this sense, a clump differs from a group of particles that are bonded to one another (agglomerate).

Mass Properties of a Clump

The mass properties of a clump are defined by the following equations:

$$m = \sum_{P=1}^{N_P} m^{[P]} \quad 3.31$$

$$x_i^{[G]} = \frac{1}{m} \sum_{P=1}^{N_P} m^{[P]} x_i^{[P]} \quad 3.32$$

$$I_{ii} = \sum_{P=1}^{N_P} \left\{ m^{[P]} (x_j^{[P]} - x_j^{[G]}) (x_j^{[P]} - x_j^{[G]}) + \frac{2}{5} m^{[P]} R^{[P]} R^{[P]} \right\} \quad 3.33$$

$$I_{ij} = \sum_{P=1}^{N_P} \left\{ m^{[P]} (x_i^{[P]} - x_j^{[G]}) (x_j^{[P]} - x_j^{[G]}) \right\} ; (j \neq i) \quad 3.34$$

For a general clump comprised of N_P balls, which has mass $m^{[P]}$, radius $R^{[P]}$ and centroid location $x^{[P]}$. The basic mass properties of a clump are: m is the total mass,

$x_i^{[G]}$ is the location of the centre of mass of clump and $I_{ii} - I_{ij}$ are the moments and products of inertia.

Full Equations of Motion for a Clump

The motion of a clump is calculated by the resultant force and moment vectors acting upon it. Clump motion can be described in terms of the translational motion of a point in the clump and the rotational motion of the entire clump.

The equation for translational motion can be expressed in the vector form

$$F_i = m (\ddot{x}_i - g_i) \quad \text{translational motion} \quad 3.35$$

where F_i is the resultant force, the sum of all externally-applied forces acting on the clump and g_i is the body force acceleration vector arising from gravity loading. The resultant force is calculated by

$$F_i = \sum_{P=1}^{N_P} \left(\tilde{F}_i^{[P]} + \sum_{C=1}^{N_C} F_i^{[P,C]} \right) \quad 3.36$$

where $\tilde{F}_i^{[P]}$ is the externally-applied force acting on particle (P), and $F_i^{[P,C]}$ is the force acting on particle (P) at contact (C). The equation for rotational motion can be written in the vector form

$$M_i = \dot{H}_i \quad \text{rotational motion} \quad 3.37$$

where M_i is the resultant moment about the centre of mass, and \dot{H}_i is the time rate-of-change of the angular momentum of the clump. The resultant moment in Equation (3.37) is calculated by

$$M_i = \sum_{p=1}^{N_p} \left\{ \tilde{M}_i^{[P]} + \epsilon_{ijk} (x_j^{[P]} - x_j^{[G]}) F_k^{[P]} + \sum_{c=1}^{N_c} \epsilon_{ijk} (x_j^{[c]} - x_j^{[p]}) F_k^{[p,c]} \right\} \quad 3.38$$

where $\tilde{M}_i^{[P]}$ is the externally-applied moment acting on particle (P), $F_k^{[P]}$ is the resultant force acting on particle (P) at its centroid, and $F_k^{[p,c]}$ is the force acting on particle (P) at contact (C).

Equation (3.37) is referred to a local coordinate system that is attached to the clump at its centre of mass. Therefore, for this system, the time rate-of-change of the angular momentum can be written as

$$\dot{H}_i = \alpha_i I_{ii} - \alpha_i + \epsilon_{ijk} \omega_j (\omega_k I_{kk} - \omega_l I_{kl}); (j \neq i, l \neq k) \quad 3.39$$

where $\alpha_i = \dot{\omega}_i$

3.4 Effect of particle properties

DEM has been proven to be an excellent tool for investigation of the macroscopic response of a material from a microscopic perspective owing to its potential for revealing micromechanical details. The effects of micro-properties on the granular material behaviour are very important and DEM provides a useful tool for researching this case.

3.4.1 Particle shape

The early and now most common type of DEM models used disks and spheres in 2D and 3D respectively (Cundall and Strack, 1979; Cundall, 1988a). These shapes are popular as their particles are easy to identify when in contact, and the ease of calculation of resulting contact point geometries and overlap. A large number of problems can be modelled using the 3D DEM in practical situations. As natural grains (like sands and gravels) have irregular shapes, DEM simulations require similar shapes. A sample containing non-spherical particles provides more interlocking and better moment resistance.

Ting et al. (1989) showed that the prohibition of the particle rotation to mimic the particle roughness was the key factor controlling the strength and deformation. Bardet and Proubet (1992) implemented cylindrical particles in a two-dimensional simulation to investigate shear bands in granular soils. They found the influence of particle rotation within shear bands validates the use of micropolar models and the thickness of shear bands is strongly influenced by the model parameters controlling the micropolar effects. Santamarina and Cho (2004) clarified that the particle size

and shape reflect the composition of material and play a significant role in soil behaviour. They showed that the three principal scales in particle shape: sphericity, angularity and roughness are very important parameters to determine the characteristic of soil behaviour.

A new method of representing non-spherical, smooth-surfaced, axisymmetrical particles constructed of overlapping spheres in discrete element modelling has been presented by Favier et al. (1999). The Multi-element particle model is constructed of spheres whose centres are located on the axis of symmetry. Consider two particles, each comprising two spherical elements with identical diameters, contacting at point c as shown in Figure 3.6. The global position of each particle is determined at its centroid by its global position vector $r_{p(G)}$. The relative position vector between the particle centroid and the centre of an element sphere d_{ps} is defined a priori because the position of each sphere within a particle is determined in advance.

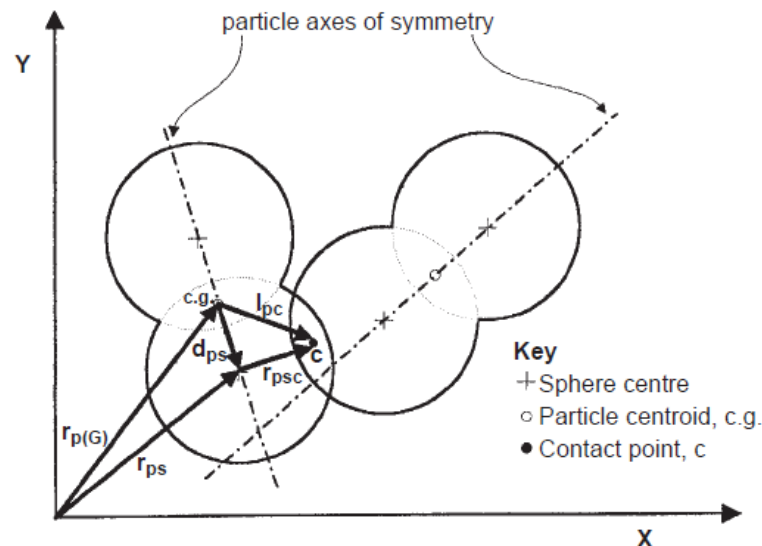


Figure 3.6 Schematic of contact between two multi-element axis-symmetrical particles, each comprising two element spheres of the same diameter (Favier et al., 1999)

Figure 3.7 shows how to transfer the force between the element spheres and particles.

The total moment for the centre of an element sphere due to tangential forces is

$$M_{t_{ps}} = \sum_{c=1}^C (r_{psc} \times f_{t_{psc}}) \quad 3.40$$

where $f_{t_{psc}}$ is the tangential component of the contact force at contact point c and C is the total number of contact points on each sphere at the current timestep, as shown in Figure 3.7a. Each element sphere resultant contact force is

$$f_{ps} = \sum_{c=1}^C f_{pcs} \quad 3.41$$

Figure 3.7b shows that this force is transferred to the centre of each element sphere. The moments generated by force acting on the centre of each element sphere which do not pass through the centroid of the particle are then added to the moment of the tangential forces, giving the total moment acting on the particle, as shown in Figure 3.7c.

$$M_P = \sum_{S=1}^S [(d_{PS} * f_{PS}) + M_{t_{PS}}] \quad 3.42$$

$$M_P = \sum_{S=1}^S \left[(d_{PS} * f_{PS}) + \sum_{C=1}^C (r_{PSC} * f_{t_{PSC}}) \right] \quad 3.43$$

where S is total number of element spheres in the particle.

The total out-of-balance force acting on the particle is the vectorial summation of resultant contact forces acting on its element spheres:

$$f_p = \sum_{S=1}^S f_{ps} \quad 3.44$$

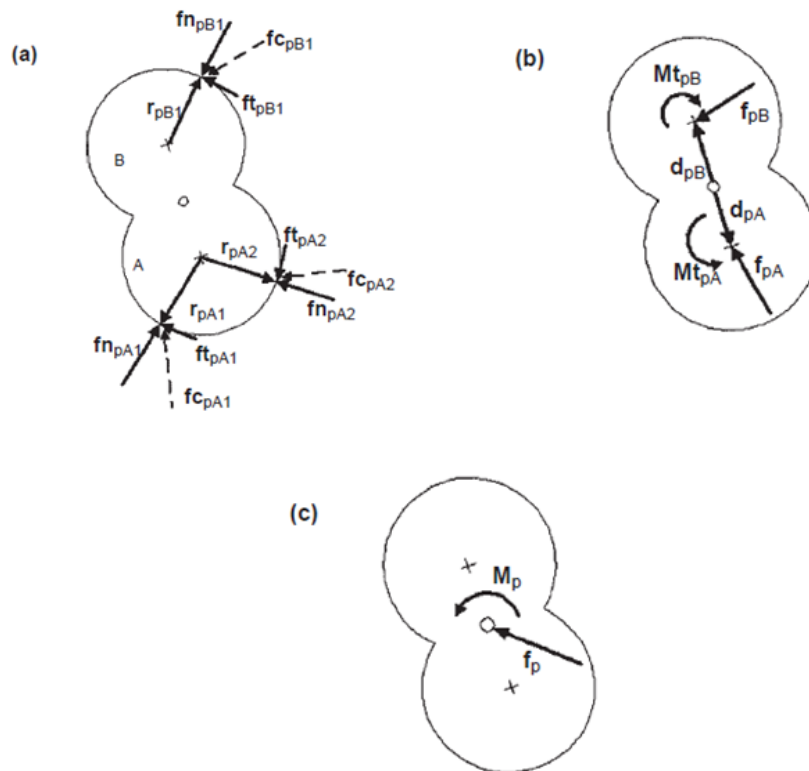


Figure 3.7 Method of transfer of force acting on element spheres to the centroid of a particle (Favier et al., 1999)

Once the total force and moment on the particle have been determined, Newton's second law is used to calculate the translational and rotational acceleration of the particle (Favier et al., 1999). Figure 3.8a illustrates the three arbitrary particle reference points A_1 , A_2 and A_3 in the co-ordinate frame. The position vectors of these

reference points have to be linearly independent. The new inertia tensor can be visualised by the inertia ellipsoid whose major axes are coincident with the principal axes of inertia as seen in Figure 3.8b and the total applied moment on a particle is transformed from global co-ordinate to the local co-ordinate system during each timestep (Favier et al., 1999). The non-spherical particle is represented by this multi-sphere method by using overlapping spheres. The advantages of using spheres to represent a particle are the computational speed and accuracy of contact detection, which should make the method comparable in computational efficiency to alternative schemes for representing non-spherical particles.

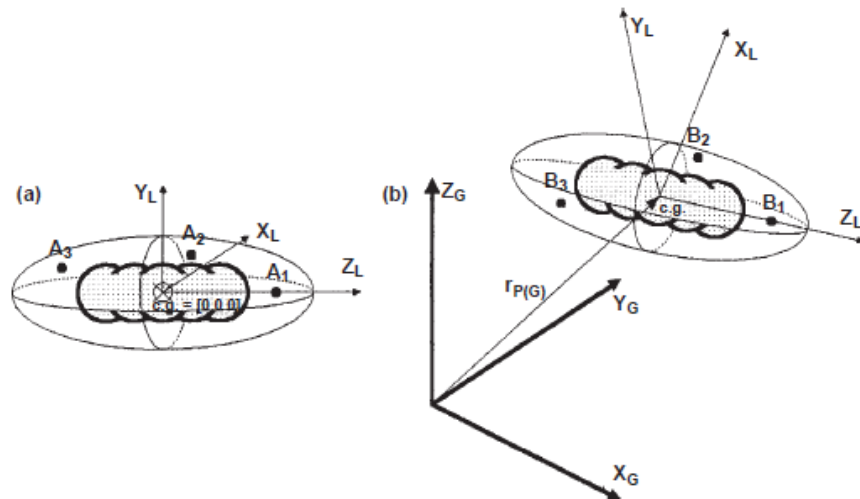


Figure 3.8 Characteristic inertial ellipsoid for a particle (a) during particle generation with arbitrary reference points A_1 , A_2 and A_3 and (b) during transformation of local rotation acceleration to the global co-ordinate system showing rotated reference points B_1 , B_2 and B_3 (Favier et al., 1999)

Several researchers have implemented elliptical particles to simulate particle shape. Rothenburg and Bathurst (1992) investigated the results of numerical simulation using elliptical particles. The peak friction angle and the volumetric dilation of the

assembly were found to be close to the real sand when the elliptical particle was used.

Lin and Ng (1997) used random arrays of elastic ellipsoidal particles in a three-dimensional discrete element model. A new numerical model (computer code ELLIPSE3D) was developed in this study. The numerical results show that particle shape has a significant effect on shear strength, deformation behaviour and fabric statistics of particle arrays. It demonstrated that using non-spherical particles in the discrete element model improves the accuracy of the simulations of granular materials. Ting et al. (1995) produced an extensive investigation of elliptical particles. The results indicate that DEM using two dimensional elliptical particles produces a mechanical behaviour which is similar both quantitatively and qualitatively to the behaviour of real granular materials.

In order to investigate the effect of the particle shape on the shearing resistance and dilation behaviour, Ni (2003) modelled each particle as two spheres bonded together with a high strength parallel bond, as shown in Figure 3.9. The bond was act as a column of elastic glue between the two spheres. The numerical results showed that the deformation and shear strength behaviour of the assembly are a function of the particle shape factor defined as $(R+r)/R$. The peak and ultimate shear strength and the overall dilation of the simulated sample increased with increasing shape factor. However, the degree of particle rotation decreased significantly with increasing particle shape factor.

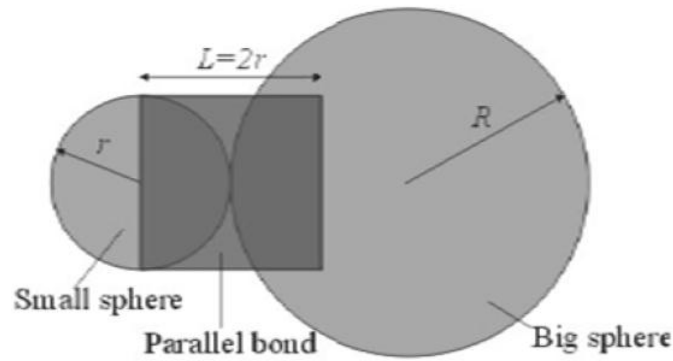


Figure 3.9 Schematic illustration of a bonded particle (Ni, 2003)

Geng (2010) investigated the influence of particle shape using particles of two-ball clumps to simulate the biaxial test and cavity expansion. The simulation results showed that the sample of clumps gives a larger peak stress and higher ultimate stress in the biaxial test and a higher cavity pressure in cavity expansion test than the sample of spheres and compared qualitatively well with experimental results.

Since modelling particle shape is important in DEM simulations, several researchers have focussed on the representation of the actual shape of real granular materials. Railway ballast behaviour was simulated by several researchers (Norman and Selig, 1983; McDowell et al., 2005; Hossain et al., 2007). Lim and McDowell (2005) studied the effect of particle shape by using clumps with simple cubes of 8 spheres to simulate railway ballast in box tests. The results showed that the eight-ball clumps give much more realistic behaviour compared with spheres and this was due to particle interlocking.

Lu and McDowell (2007) addressed the effect of the shape of railway ballast on their behaviour. Spheres and clumps were implemented in their simulations to represent

railway ballast particles. They developed a method of generating clumps close to real ballast shapes. Balls were generated in selected directions to model real ballast shape. In order to form the edges of the clumps, additional balls were generated to link up the furthest balls of adjacent directions. They noted that the interlocking provided by the clumps of the developed method gives a much more realistic load deformation response than the spheres and that the behaviour was closer to the real ballast behaviour obtained from experimental results.

3.4.2 Particle rotation

Particle rotation is known to have a substantial influence on the behaviour of granular materials. Smooth spheres or disks provide no resistance to rotation at the contact points, while real soil particles present resistance to rotation at the contact points. Ting et al. (1989) used two dimensional disks to simulate laboratory tests. Their results show that two-dimensional DEM can simulate realistic nonlinear, stress history-dependent soil behaviour appropriately when the rotation of the particle is restrained. Belheine et al. (2009) presented a 3D spherical discrete model with rolling resistance in order to take into account the roughness of grains. Rolling resistance means that a moment may be transferred between the discrete elements via the contacts, and that moment resists particle rotation. The rolling which occurs during shear displacement is decreased. The results showed that the larger the value of the applied rolling resistance, the higher the resulting peak stress.

Iwashita and Oda (1998) introduced a modified distinct element method (MDEM), where rotational resistance to rolling for each particle was one of the factors controlling the strength and dilatancy of granular materials. They suggested that

rotational resistance should be activated at contact points in the discrete element modelling. They used MDEM to investigate the effect of rolling restriction. In convention of the MDEM, an additional set of springs, dash pots, no-tension joint, and a shear slider were added at each contact. Any moment M_i (Figure 3.10) is balanced by two rolling resistance sources provided by an elastic spring and a dash pot and limited by a sliding criterion.

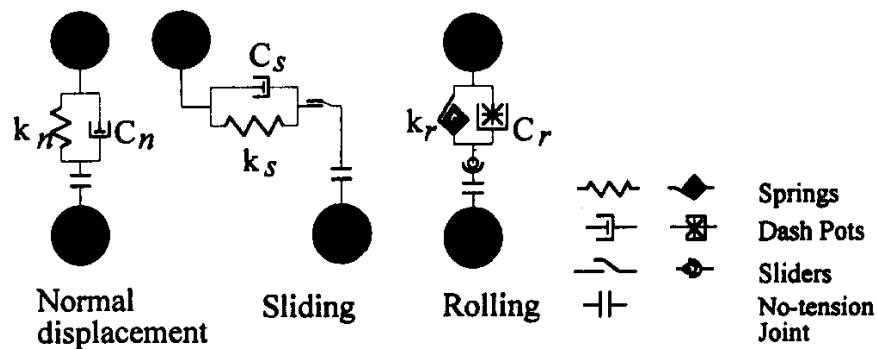


Figure 3.10 Contact Model in MDEM (Iwashita and Oda, 1998)

Three biaxial tests were conducted to investigate the effect of rolling resistance on the microstructure developed in shear bands. Figure 3.11 shows the results of stress ratio and volumetric strain against axial strain. The curve of rolling resistance test simulation lies between the curves of free-rolling test and no-rolling test simulations. It is noted that higher peak and ultimate shear strength were observed by prohibiting the particle rotation, compared to simulations that allowed particle rotation. They noted that the shear bands developed well when the particle rolling resistance is considered in DEM. In addition, the high gradient of particle rotation along the shear band boundaries can be reproduced, in a manner quite similar to those of natural granular soils, when the rolling resistance at contacts is considered.

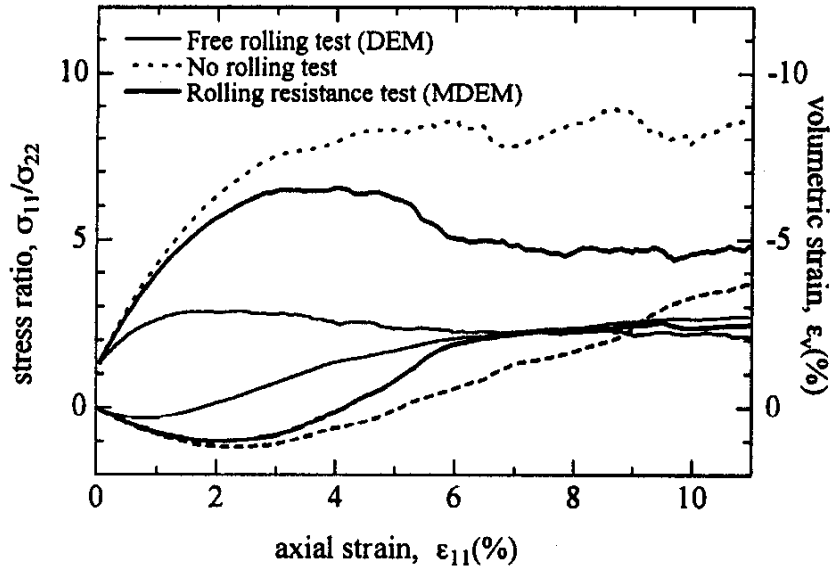


Figure 3.11 Stress ratio and volumetric strain with axial strain relationships in three numerical simulation tests (Iwashita and Oda, 1998)

3.4.3 Particle friction coefficient

Many researchers have demonstrated that particle friction coefficient has a significant effect on the deformation behaviour of granular materials. The relationship between the interparticle friction and shear strength was examined using results from experimental triaxial tests (Bishop, 1954). Skinner (1969) studied the influence of using different values of interparticle friction on the shearing strength of a random assembly of spherical particles. The results show that the particle rolling controlled the volumetric change of the sample when the interparticle friction was high, and the particle sliding controlled the volumetric change of the sample when the interparticle friction was low. The shear strength value depends on both particles rolling and sliding.

A DEM study was conducted to investigate the macro and micro mechanical responses of granular materials with variation of interparticle friction (Sazzad and

Islam, 2008). The results showed that interparticle friction has a significant influence on the stress-strain dilative response and that higher value of interparticle friction gives larger macroscopic strength and dilation of the assembly.

DEM simulations of biaxial tests were carried out on samples with different particle friction coefficients ranging from 0.3 to 0.9 to investigate the effect of particle friction on the stress-strain behaviour (Geng, 2010). The results (Figure 3.12) showed that interparticle friction has an important effect on the peak axial stress, as well as the overall sample dilation at the end of shear. The peak axial stress of each stress-strain curve increases with increasing friction coefficient. The volumetric dilation increases when the friction coefficient increases.

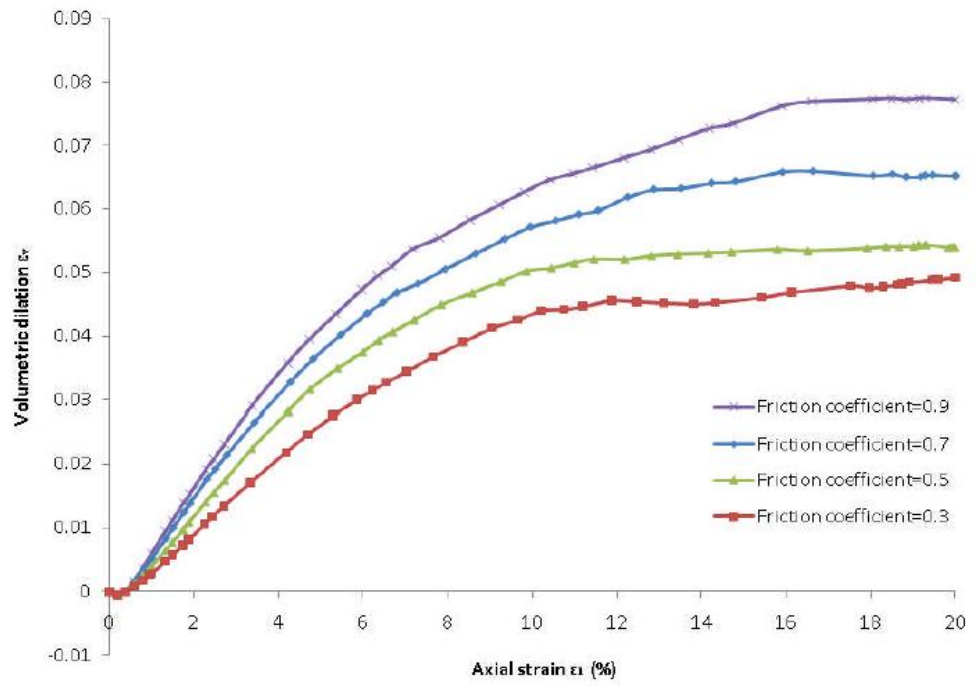
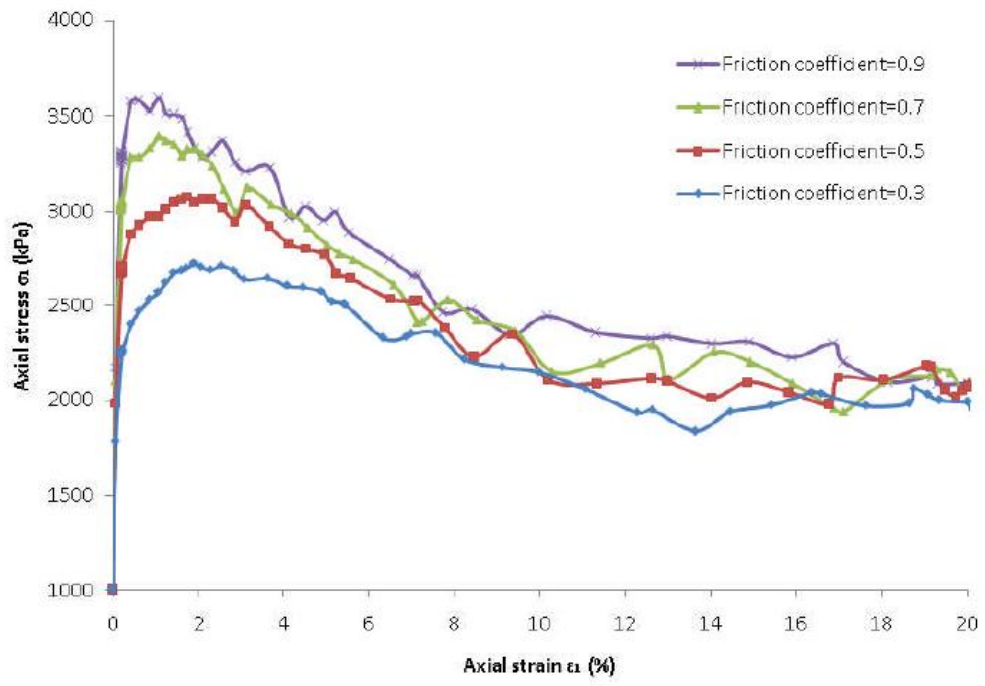


Figure 3.12 Axial stress against axial strain and volumetric dilation against axial strain of the samples with various particle friction coefficients (Geng, 2010)

3.5 Examples of DEM applications

There are two main motivations to apply DEM in geotechnical engineering. First, in applying boundary condition problems, discrete element methods are simpler to simulate large deformation problems than continuum-mechanics-based analysis tools. DEM simulations can also capture mechanisms such as arching or erosion that are a result of the characteristics of the granular material. DEM is also used as a tool in basic research. DEM simulation can be used to investigate the material behaviour at a much more detailed scale than can be monitored even in a high quality laboratory test. In conventional experimental soil mechanics assumptions about the fundamental mechanisms that are responsible for the highly complex response of soil can be proposed. A DEM model allows the exploration of the inner micromechanics of soil behaviour to confirm or reject these assumptions. This section will give some examples of applications in geotechnical engineering which make use of DEM.

3.5.1 DEM of particle flow

Recently, discrete element modelling has been widely used to model granular material flow in hoppers, chutes and belt conveyers (Zhang and Vu-Quoc, 2000; Li et al., 2009; McDowell et al., 2011).

McDowell et al. (2011) for example used three-dimensional (3D) DEM simulations to model the flow of pebbles in a chute. The pebbles were simulated using spheres and, alternatively, ellipsoid-shaped four-ball clumps. To model the experiments, the same number of particles (spheres or clumps) were randomly generated in a taller chute and then allowed them to fall free and come to rest at the base of the chute as illustrated in Figure 3.13a. After the sample came to equilibrium, the particles whose

centre positions were next to the defined positions of the 20 marked pebbles in the experiments were chosen to be marked in the simulation as seen in Figure 3.13b (in the experiment 20 pebbles were coloured red so that they can easily be tracked during the flow, they placed in five columns next to the side wall and 100 mm distant along the length of the chute). Horizontal and vertical gravity were applied at the same time to achieve the same angle of inclination of gravity to the bottom wall of the chute as in the laboratory experiments (Figure 3.13).

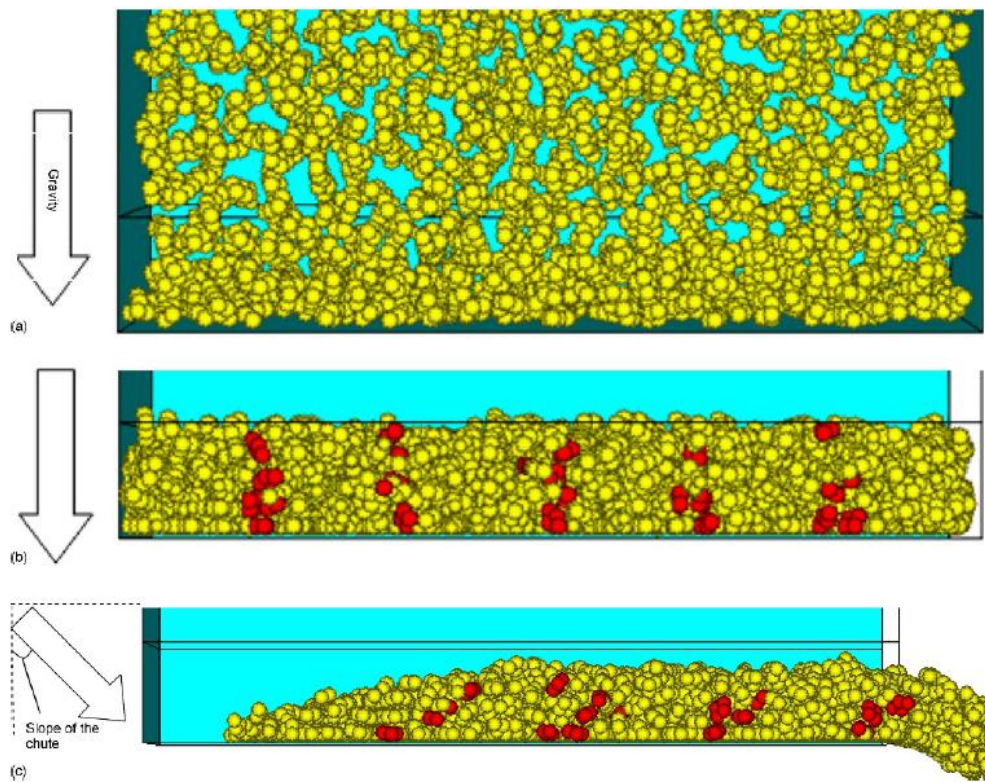


Figure 3.13 DEM simulation of chute filling and flow, with gravity applied at the same angle to the bottom wall as for the chute in the laboratory experiments (McDowel et al., 2011)

The results showed that using spheres gave a poor agreement compared with experimental data. However, the velocity profiles for tracked pebbles and clearance times of clumps were in good agreement with the experimental results. The work

shows that it is possible to simulate the flow of irregular shaped particles in three dimensions when shape and particle parameters were selected precisely.

3.5.2 DEM of cemented sand

Cemented sands are commonly found in nature, for example, in aged sedimentary deposits. Natural cementation initiates from different sources, for instance, from the precipitation of calcite, silica, iron oxides, and even clays (Santamarina et al., 2001; Mitchell and Soga, 2005). Cemented soils can also be produced artificially by mixing with cement or chemicals. Experimental results showed that cementation by Portland cement have an important effect on soil properties (i.e., increasing strength and changing the volumetric response from contraction to dilation) (Clough et al., 1981; Abdulla and Kioussis, 1997; Schnaid et al., 2001).

Numerical simulations using two-dimensional (2D) DEM were carried out on Portland-cement sand by Wang and Leung (2008) to understand the associated fundamental mechanisms of this behaviour. A numerical sample was formed by combining three kinds of particles (sand particles, cementing particles and membrane particles) as illustrated in Figure 3.14. The sand particles were generated according to the grain-size distribution of Ottawa 20–30 sand. The radii were scaled up 1.25 times to reduce the total number of particles used in the simulations and hence the calculation time.

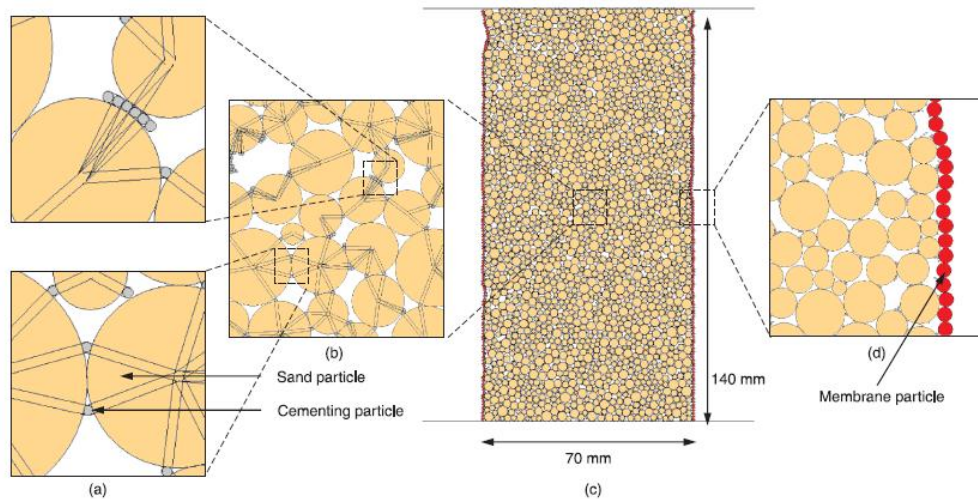


Figure 3.14 Characteristics of the numerical specimen: (a) special arrangements of the cementing particles; (b) parallel bonds between cementing particles and sand grains; (c) specimen used in the biaxial tests; (d) membrane particles (Wang and Leung, 2008)

The cementing particles and the sand particles were arranged in a special way as shown in detail in Figure 3.14a. Tiny particles were used to simulate the cementing particles and deposited around the contacts of the large soil particles. This arrangement was similar to the real formation method of cementation. In the experiments, the cement content was calculated by the weight ratio. The same way was used in the simulations by converting the weight ratio to a volume ratio or area ratio. This area ratio was then used to control the number of cementing particles in the simulations for different cement contents. The contact model between the cementing particles and the sand particles was regulated by adopting the parallel-bond model in the simulations as indicated in Figure 3.14b. The parallel-bond was considered broken when the normal or shear force exceeded the maximum resistance strength. The flexible membrane was simulated by a series of small same-sized particles as illustrated in Figure 3.14d. These particles were connected by a strong and flexible contact bond, therefore, moment cannot be transmitted and the

membrane-particle string behaves similar to the rubber membrane used in the triaxial tests.

After the sand particle packing was achieved, the cementing particles were positioned following the process demonstrated in Figure 3.15.

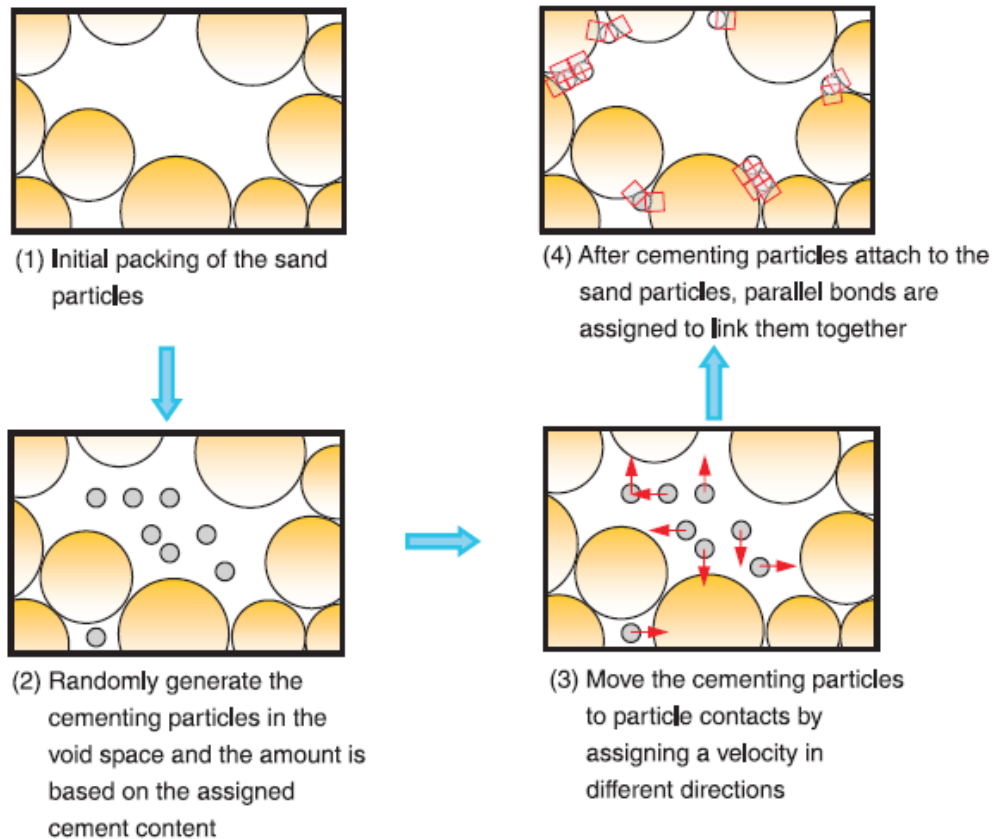


Figure 3.15 Procedures for positioning the cementing particles. Note that the size of the cementing particles is enlarged for better presentation (Wang and Leung, 2008)

Similar conditions implemented to the physical sample were reproduced in the compression biaxial test simulations. The top and bottom walls were simulated with a rigid frictionless wall. The bottom wall was fixed in position, and the axial loading was applied by the top wall. The stress, strain, and overall void ratio were monitored during the simulation test.

The results showed that stress–strain relationship similar to the experimental results was obtained from the Portland cement sand simulations as seen in Figure 3.16. The strength development, peak strength, and strain-softening response became more visible when the cement content was higher.

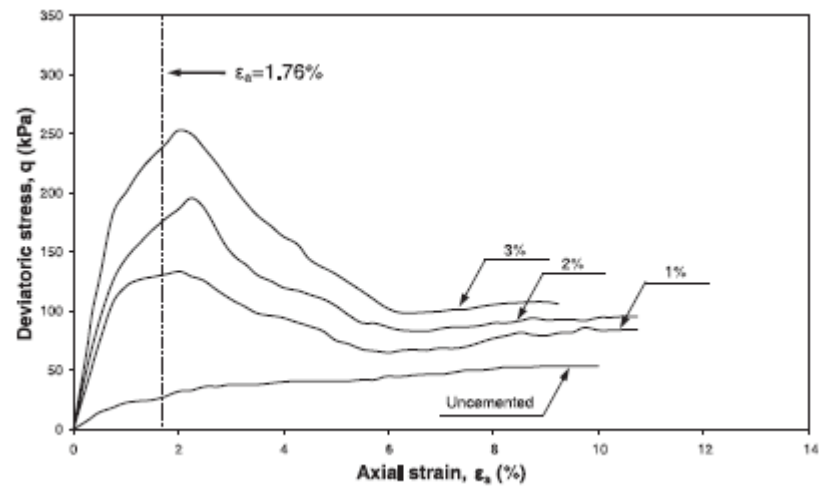


Figure 3.16 Stress–strain relationships of Portland cement sand obtained from the biaxial-test simulations under 50 kPa confining pressure (Wang and Leung, 2008)

Figure 3.17 shows results similar to the experimental observations. Simulation results illustrated that cementation can effectively change the volumetric response from contraction to dilation, and such a change was increased with increasing cement content.

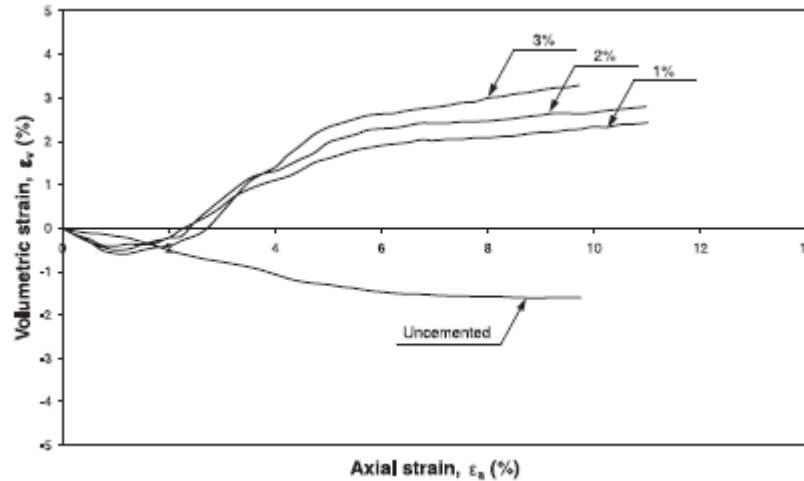


Figure 3.17 Volumetric responses of biaxial-test simulations on Portland cement sand under 50 kPa confining pressure (Wang and Leung, 2008)

Additionally, the simulation results showed that all the particles together in the bonding network shared the load and many micro force-chains associated with cementation were generated. In contrast to uncemented sand, a more stable and strong force-chain network exposed to smaller force or stress concentrations was formed in the cemented sand.

3.5.3 DEM of railway ballast

In general, railway ballast consists of large, angular particles of typical size 40mm. The complex behaviour of ballast has been studied by several researchers using laboratory and *in situ* tests. However, due to the restrictions of the experimental tests to monitor the ballast particle response precisely, the true nature of the deformation and mechanism of degradation are still not fully clear. Railway ballast is an interesting discrete or discontinuous material in geomechanics and has attracted interest from DEM researchers. Several researchers have described simulations of ballast (Lu and McDowell, 2007; Lu and McDowell, 2010; Hossain et al., 2007).

Lu and McDowell (2010) for example used a three-dimensional (3D) DEM simulation to model the mechanical behaviour of railway ballast under static and cyclic conditions. The particle model used in the simulations was the ten-ball triangular clump with eight asperities shown in Figure 3.18a. The dimensions of the model samples were approximately 300 mm in diameter and 600 mm high, with each sample containing 618 particles (a particle being a ten-ball triangular clump with eight asperities). The diameter of each of the ten balls in the clump was 16.33 mm, and each asperity was 6 mm. A sample with 618 particles of ten-ball triangular clumps under 120 kPa confining pressure before loading is shown in Figure 3.18b.

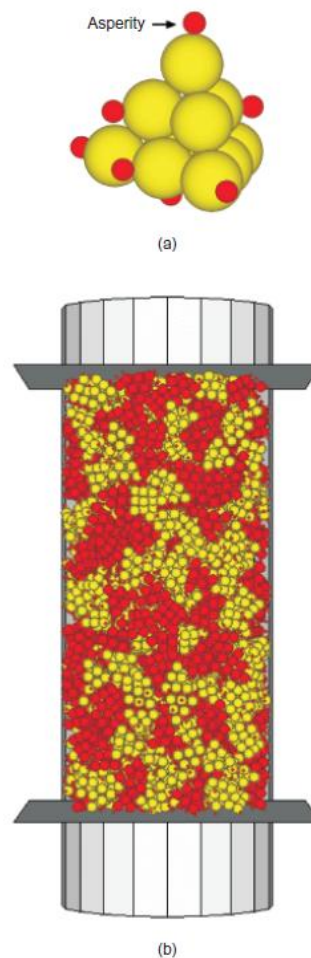


Figure 3.18 DEM model: (a) ten-ball triangular clump with eight small balls (asperities) bonded as a ballast particle model and (b) assembly of ten-ball triangular clumps with eight small balls (asperities) bonded in the triaxial cell (Lu and McDowell, 2010)

A weak parallel bond was used to model the interlocking and breaking of very small asperities. For larger asperities the interlocking and fracture was modelled by bonding eight small balls to the clump. After the assembly generation process was finished, an artificial isotropic compression was applied to all walls by means of servo-control to achieve the required stress condition. In the monotonic triaxial test simulations, and following Indraratna et al. (1998), monotonic loading was applied to each sample on both the top and bottom walls with a constant speed of 0.02 m/s until axial strain reached 0.2. For the cyclic triaxial test simulations, the servo-control was implemented to both the top and bottom walls to sustain the required loading. The details of the simulation procedure can be found in Lu and McDowell (2008) and fully presented by Lu (2008).

The results showed that, as seen in Figure 3.19, when asperity abrasion was modelled and under different confining pressures both the stress–strain behaviour and volumetric response were simulated successfully using breakable assemblies. The breakable assembly in which asperity abrasion leads to a higher number of contacts and dilatancy was more oppressed provides better agreement with experimental results.

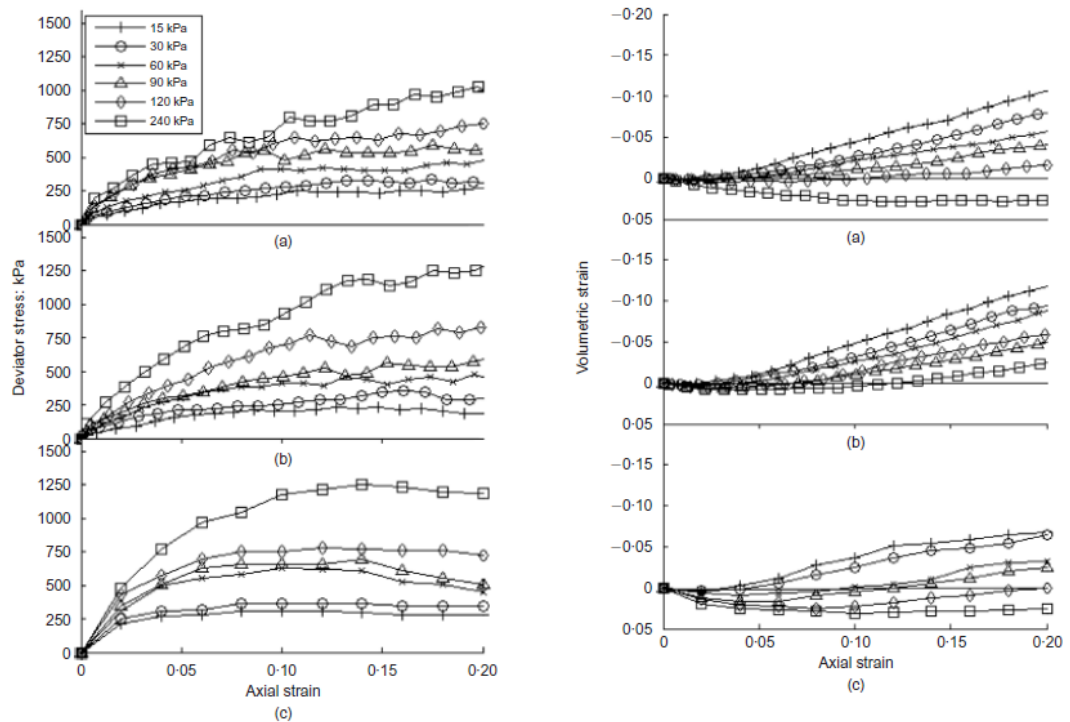


Figure 3.19 Results of deviator stress & volumetric strain against axial strain under a range of confining pressures: (a) using breakable assemblies; (b) using unbreakable assemblies; and (c) experimental results by (Indraratna et al., 1998) (Lu and McDowell, 2010)

Different cyclic loading conditions (maximum deviatoric stresses and confining pressures) were also applied to the breakable assemblies. Figure 3.20 and Figure 3.21 respectively show the experimental and simulation results. After few cycles, the simulated assemblies stabilised more rapidly than the real ballast. Compared with the experimental data, under different loading conditions the same DEM model produces a similar order of magnitude of permanent axial strain. For assemblies with low confining pressure and high maximum deviator stress, higher dilation results in the simulations. Under different loading conditions the number of broken asperities showed a similar pattern to the ballast breakage index in the experimental results.

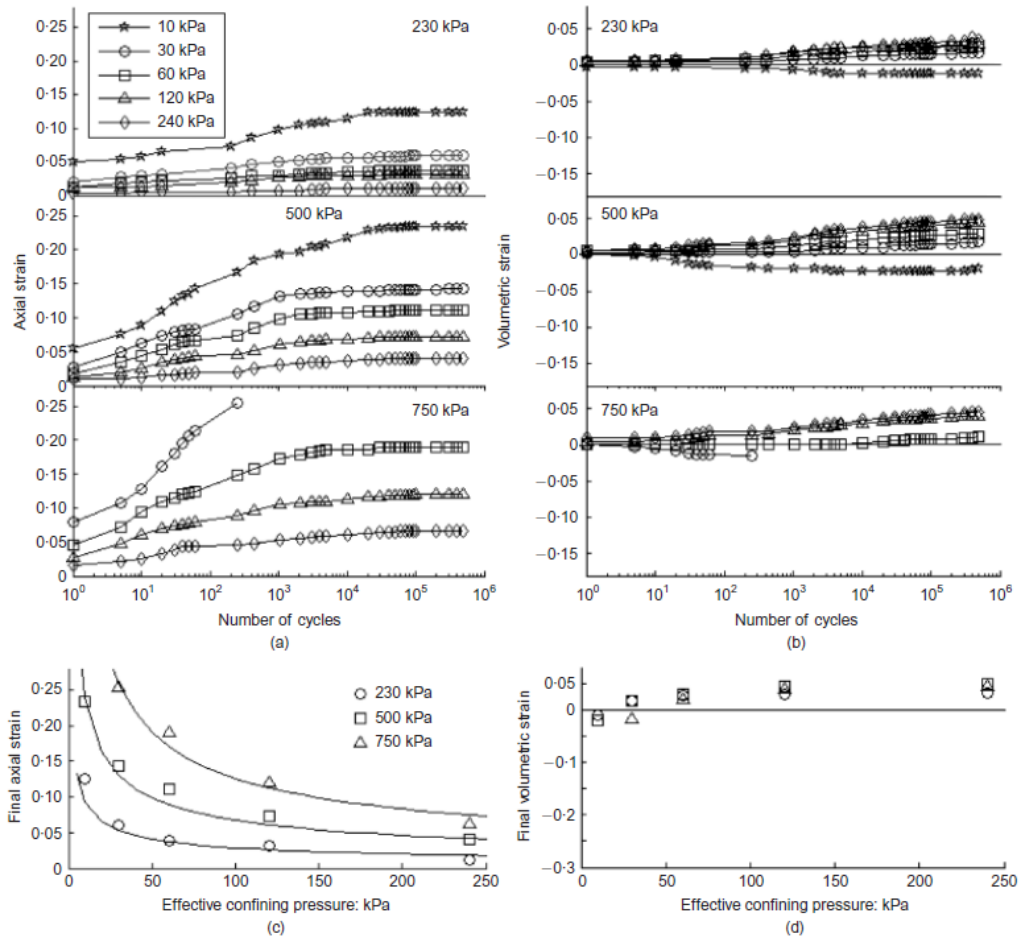


Figure 3.20 Experimental results under cyclic loading: (a) axial strain as a function of the number of cycles; (b) volumetric strain as a function of cycles; (c) final axial strain after 500 000 cycles; (d) final volumetric strain after 500 000 cycles (Lackenby et al., 2007)

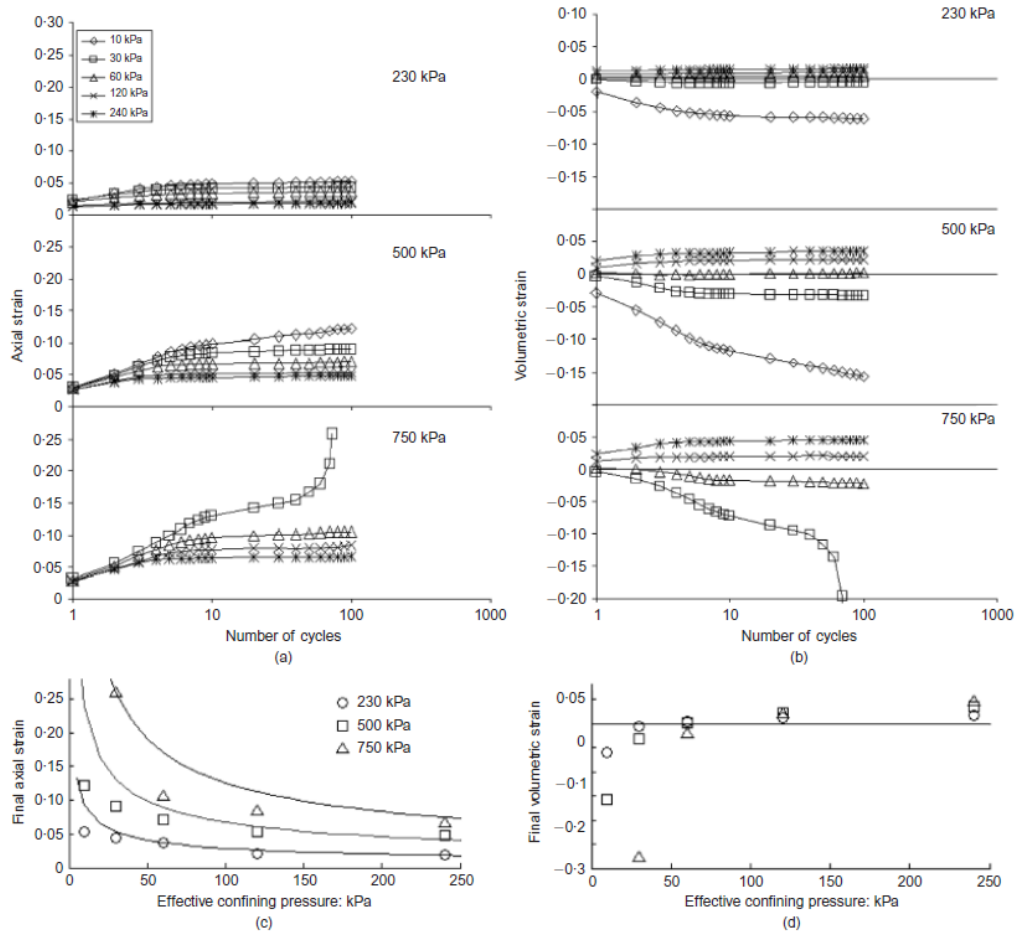


Figure 3.21 Simulation results under cyclic loading: (a) axial strain as a function of the number of cycles; (b) volumetric strain as a function of cycles; (c) final axial strain after 100 cycles; (d) final volumetric strain after 100 cycles (Lu and McDowell, 2010)

Additionally, the simulation results showed that the cyclic degradation behaviour was controlled by asperity fracture (i.e. the fracture of small angular protuberances), which were simulated by bonding small balls to the clumps. Overall, the behaviour of real ballast in terms of axial and volumetric strain and degradation under both monotonic and cyclic loading were able to be captured by DEM simulations.

3.6 Conclusions

DEM has been widely applied to simulate granular material behaviour. It is a useful tool for fundamental research into the behaviour of granular materials. The main concepts and general mathematical backgrounds of DEM and PFC^{3D} have been presented. Some specific features in PFC^{3D} have been described. The most powerful way of modelling assemblies of discs and spheres is by numerical techniques. It is more flexible in application than analytical modelling and has the merit over physical modelling that any data are accessible at any stage of the test. The main drawback of the DEM is its enormous computational expense. Enough particles are required to ensure a representative sample and sufficient number of contacts.

DEM permits the investigation of the particle properties which cannot be obtained using continuum mechanics: for instance, interparticle friction and contact force distribution. Due to easy rolling of disks or spheres, the strength of an assembly of spheres or disks is very low. Therefore, a clump of complex particle shape or artificial restraint applied to the rotation of disks or spheres have been used to address this problem. The behaviour of granular materials in DEM is affected by many particle parameters including particle shape, particle rotation and friction coefficient. Examples of DEM applications such as particle flow, cemented sand and railway ballast were presented to show the versatility of the technique.

CHAPTER 4

DISCRETE ELEMENT MODELLING OF CPT IN A CALIBRATION CHAMBER

4.1 Introduction

This chapter describes the CPT simulation of granular materials in a calibration chamber using the discrete element method (DEM). Huang and Ma (1994), Calvetti et al. (2005) and Jiang et al. (2006) all used DEM in the study of two-dimensional (2D) models of cone penetration tests. Although qualitative insight was gained, the limitations of their disc-based models prevented quantitative comparisons with physical tests. Moreover the kinematic constraints of two-dimensional simulations are completely different from three-dimensional (3D) simulations and real granular material. Research to date has seen the use of other numerical techniques in addition to DEM for CPT modelling. For example, Susila and Hryciw (2003) used finite element modelling to simulate CPTs in normally consolidated sand and found the results to agree very well with earlier analytical and experimental studies. Ahmadi et al. (2005) also used the finite difference method to evaluate cone tip resistance in sand. By comparing predicted numerical values of cone tip resistance with published experimental measurements from calibration chamber tests, they found the error band between predicted and measured values to be $\pm 25\%$. Using a 3D DEM model, Arroyo et al. (2011) built a virtual calibration chamber to simulate cone penetration tests in sand with particles that were represented by single spheres which were

prohibited from rotating. They deduced that under isotropic boundary stresses, the numerical results showed good quantitative agreement with the predictions of the empirical equations based on the physical results. The reported good agreement between DEM and experimental results can be attributed to the prohibition of particle rotation in the DEM model. However, particle size scaling is not recommended as it decreases the ratio between cone diameter and median particle size (B/d_{50}), thereby decreasing the number of particles in contact with the cone tip and consequently creating large voids around the cone tip.

This research will focus on the use of PFC^{3D} to present a new particle refinement method, similar to mesh refinement in finite-element modelling (Dolbow and Belytschko, 1999; Sukumar and Belytschko, 2000), in the sense that a large number of small particles were brought into contact with the cone tip, while large particles were distanced further away from the cone, to reduce computational time.

4.2 Modelling procedure and sample preparation

Cone penetration tests in a calibration chamber were conducted using the discrete element modelling PFC^{3D} program version 3.00 (Itasca, 2003). All simulations were carried out using a computer with an Intel Core Quad CPU at 3 GHz and with 3 GB RAM. The particles were either spherical in shape or clumps of two balls and could rotate freely. For simplicity, a linear–elastic contact law was selected. Due to the geometric symmetry of sample-penetrometer setup, only a quarter of the sample and penetrometer was initially considered to reduce computational time. The experimental data (Schnaid, 1990) for Leighton Buzzard sand was used as a benchmark for comparison to the numerical model and to ascertain the suitability of

the model parameters. Table 4.1 shows the dimensions and boundary conditions for both the experimental and the optimum numerical calibration chambers.

Table 4.1 Dimensions and boundary conditions of experimental and numerical calibration chambers

Setting	Units	Experimental calibration chamber	Numerical calibration chamber
Chamber width (D)	(mm)	1000	300
Chamber height (H)	(mm)	1500	100
Cone diameter (B)	(mm)	36	18
Particles size (d_{50})	(mm)	0.8	1.0
Vertical and horizontal stresses	(kPa)	100	300
(D_c/B) ratio	-	27.78	16.67
(B/d_{50}) ratio	-	45	18

The numerical chamber was prepared by generating five finite walls to serve as sample boundaries to confine the particles during generating and equilibrium. The walls were outer cylindrical wall, two vertical planar walls at 90° to each other and the top and bottom planar walls. All the walls were kept frictionless. After the chamber walls were generated, the sample particles were prepared using a deposition and compaction method. The spheres were generated in a taller cylinder at random coordinates within the specified chamber boundaries and allowed to fall under gravity. To accelerate the deposition and to achieve the desired sample height (100mm), the particles were compressed by moving the top wall downward. The sample was then allowed to attain equilibrium. Figure 4.1 shows the final sample in a 90° segment of calibration chamber.

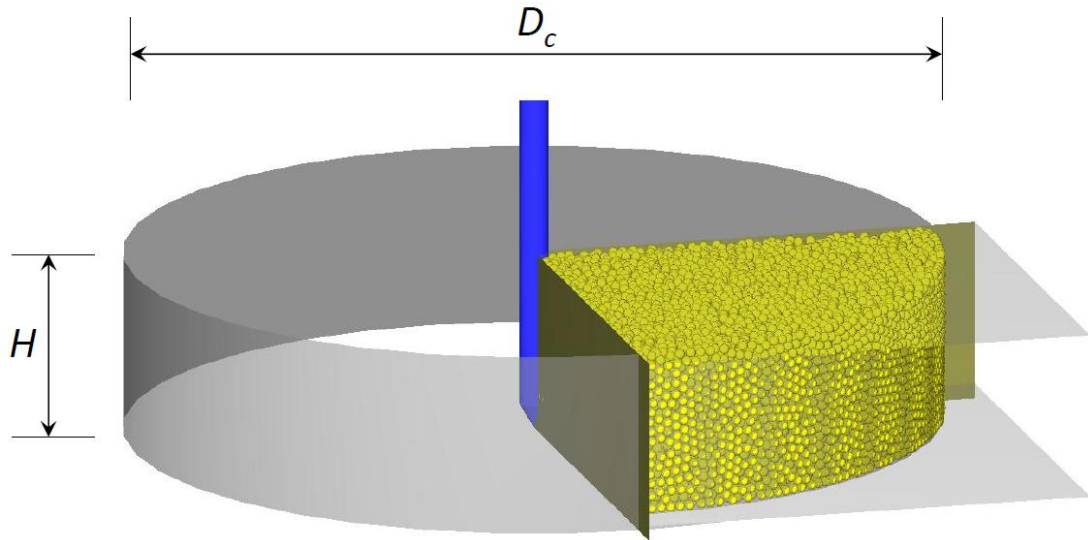


Figure 4.1 Sample of one particle size in a 90° segment of calibration chamber

Table 4.2 shows the particle and wall properties maintained for all the simulations.

Table 4.2 The particle and wall properties for DEM simulations

Input parameter	Value
Particle and wall normal stiffness (k_n)	$5 \times 10^5 \text{N/m}$
Particle and wall shear stiffness (k_s)	$5 \times 10^5 \text{N/m}$
Particle density	2650kg/m^3
Particle friction coefficient	0.5
Frictional tip cone coefficient of friction	0.5
Frictional sleeve coefficient of friction	0.5
Chamber wall coefficient of friction	0

After the sample was generated, a constant stress boundary condition (BC1) was applied and this was maintained during cone penetration. This was facilitated by subjecting the sample to an isotropic compressive stress of 300kPa using a servo-control mechanism (see Appendix) such that the bottom wall and the cylindrical wall experienced vertical stress and horizontal stress respectively. Over the duration of the

simulation the top wall and the two vertical walls remained fixed in place. The stresses on all three non-servo-controlled walls were found to be approximately 300kPa before and during the penetration.

Along with three rigid walls, the cone penetrometer used in the simulation had a diameter B of 18mm and an apex angle of 60° . The walls are described below and shown in Figure 4.2:

1. A conical frictional wall with an inclination to the X-axis of 60° to simulate a penetrometer tip
2. A vertical frictional wall to simulate the penetrometer sleeve. The frictional sleeve has effectively the same height (h) as the penetrometer tip
3. A vertical frictionless wall to simulate the upper penetrometer sleeve. With this, the height of the frictionless sleeve depends upon the target penetration depth of the simulation.

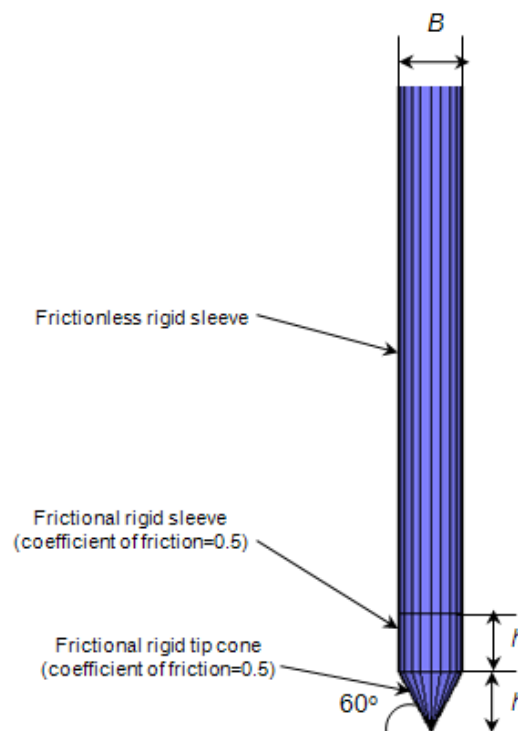


Figure 4.2 Boundary conditions for cone penetrometer

The values of normal stiffness, shear stiffness and friction coefficient for the cone penetrometer were as defined earlier in Table 4.2. The penetrometer was pushed downwards into the sample at the standard rate of 20mm/sec used in calibration chambers and the field (ISSMFE, 1989); this has also been shown to be acceptable in DEM - for example, applying a velocity of 10mm/sec or 30mm/sec does not affect the tip resistance results significantly.

4.3 Results of feasibility simulations

An initial simulation was conducted using the same dimensions and boundary conditions as the experimental chamber (Table 4.1) which meant only large particles could be used. In order to achieve an acceptable computational duration, a sample containing 12880 (30mm diameter size) particles with an initial porosity of 0.37 was used. Figure 4.3 shows the cone tip resistance q_c obtained from this simulation to be very noisy and exhibiting high variability. The source of the noise in the penetration curve is due to particle size effects, as very few 30mm particles (typically 2) were actually in contact with the cone tip, or the cone is in a void ($q_c = 0$ MPa).

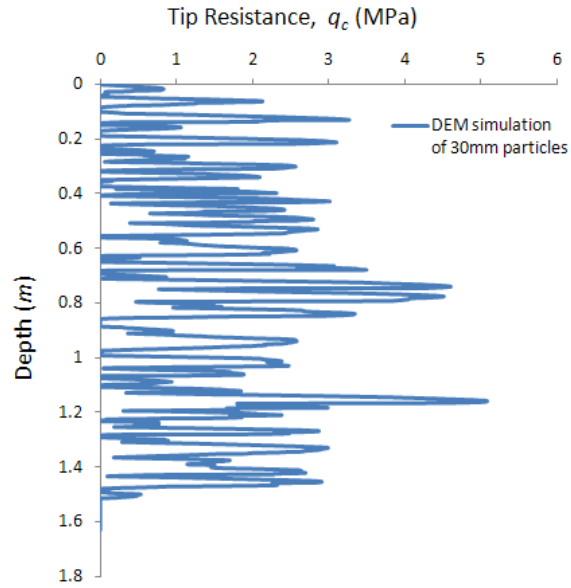


Figure 4.3 Tip resistance results of 30mm particles

To facilitate the use of smaller particles to simulate the behaviour of real sand in the numerical model, the chamber width D_c and the cone diameter B were reduced while maintaining a similar ratio of D_c/B as for an experimental chamber for the following reasons:

- a) To increase the ratio of cone diameter to particle diameter B/d_{50} to a more realistic value with a more realistic value of d_{50}
- b) To ensure that, during penetration, the cone tip remained in contact with an acceptable number of particles

As the chamber height H was also reduced when the parameters for using smaller sized particles were being determined, it was considered important to investigate the effect of this on tip resistance. Three simulations were conducted using equal chamber widths of 500mm and varying chamber heights. The particle sizes and initial porosity for all three samples were 8mm and 0.37 respectively. Figure 4.4 shows the plot of cone tip resistance q_c against depth for the different chamber heights examined. It can be seen that there is little difference in the ultimate q_c for H

= 200, 100 and 70mm; that is the ultimate q_c for $H = 200$ mm is about 1.75MPa and this value increased to about 2MPa for $H = 100$ mm and $H = 70$ mm. Consequently, a decision was made to use a chamber height of 100mm for all the subsequent simulations, as this height resulted in a more acceptable computational time without affecting tip resistance too much.

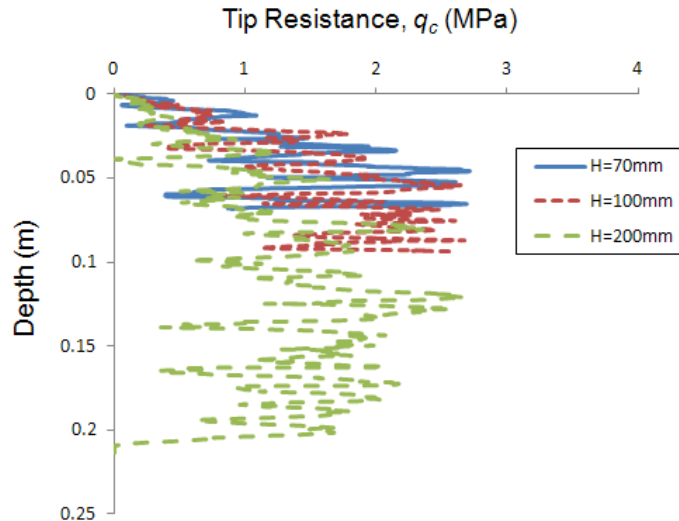


Figure 4.4 Effect of reducing chamber height on tip resistance values

Similarly, to investigate the effect of chamber width on tip resistance, three simulations were conducted using equal chamber heights of 100mm but varying D_c/B ratios. The particle diameter and initial porosity in all three samples were 6mm and 0.37 respectively. Figure 4.5 shows the plot of cone tip resistance q_c against depth for the different D_c/B ratios considered. It can be seen that the ultimate value of q_c for $D_c/B = 27.78$ and 16.67 is almost the same (about 2MPa) whereas it is smaller for $D_c/B = 11.11$ (about 1.5MPa). Therefore, it was decided that the chamber with $D_c/B = 16.67$ would be used in the simulations, as this ratio gave a more reasonable computational time without affecting tip resistance too much. Consequently, all models for the simulations undertaken in this study thereafter had $D_c = 300$ mm, $B = 18$ mm and $H = 100$ mm.

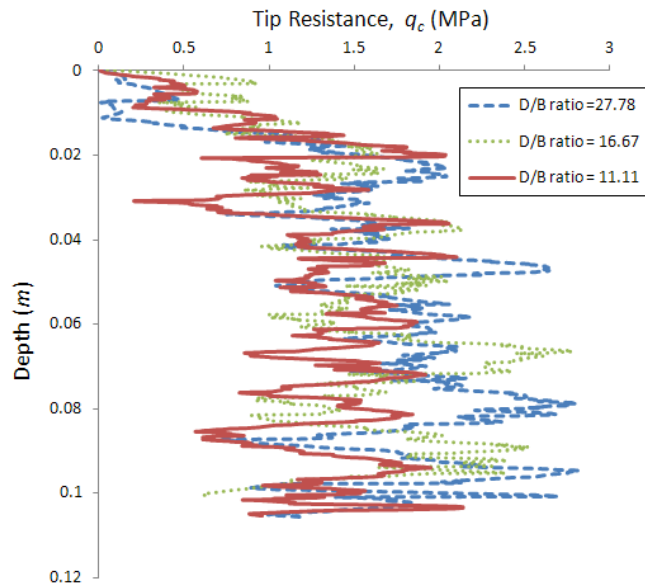


Figure 4.5 Effect of D_c/B ratios on tip resistance values

It should be noted that this study was not an attempt to model real materials but to ascertain the possibility of simulating CPT using a realistic cone size with DEM in an aggregate comprising sand-sized grains, and thereby gain micro-mechanical insight into the behaviour of the material. To this effect, it is acknowledged that limitations with respect to the model size and the particle size are chosen to give acceptable computational limits without introducing significant geometry of the numerical model.

4.4 Particle refinement method

In order to increase the number of small particles in contact with the cone tip, a Particle Refinement Method (PRM) was used, whereby small particles were generated nearer the cone penetrometer and larger particles further away. Table 4.3 provides a summary of particle and geometrical configurations as well computational time for all the particle refinement method simulations.

Table 4.3 Summary of geometry and computational time for all PRM simulations

Simulation	Sample preparation method	Particle mass	Model angle (degrees)	Number of zones	Zone external radius (mm)	Zone particle size (mm)	Number of particles	Number of particles in contact with cone tip	Average model run (days)
A	Compaction	Variable	90	1	150	6	9700	8	4
B	Compaction	Variable	90	2	75,150	6,12	3550	8	2
C	Compaction	Variable	90	3	75,95,150	6,9,12	3900	8	2
D	Compaction	Variable	30	3	75,95,150	2,3,4	33600	14	30
E	Compaction	Variable	30	3	75,95,150	6,9,12	1300	8	1
F	Compaction	Variable	30	2	75,150	2,4	30800	14	27
G	Compaction	Variable	90	1	150	2c-6	9700	5	7
H	Compaction	Variable	30	3	75,95,150	2c-2,3,4	33600	8	50
I	R.E	Variable	30	3	75,95,150	2,3,4	34700	14	7
J	R.E	Constant	30	3	75,95,150	2,3,4	34700	14	3
K	R.E	Constant	30	5	20,35,50,65,150	1,1.5,2,3,4	37050	52	5
L	R.E	Constant	30	5	20,35,50,65,150	1,1.5,2,3,4	37050	52	5
M	R.E	Constant	30	5	20,35,50,65,150	1,1.5,2,3,4	37050	52	5
N	R.E	Constant	30	5	20,35,50,65,150	1,1.5,2,3,4	37050	52	5
O	R.E	Constant	30	5	20,35,50,65,150	1,1.5,2,3,4	37050	52	5
P	R.E	Constant	30	5	20,35,50,65,150	1,1.5,2,3,4	37050	52	5
Q	R.E	Constant	30	5	20,35,50,65,150	1,1.5,2,3,4	37050	52	5
R	R.E	Constant	30	5	20,35,50,65,150	1,1.5,2,3,4	37050	52	5
S	R.E	Constant	30	5	20,35,50,65,150	2c-1,1.5,2,3,4	37050	52	10
T	R.E	Constant	30	5	20,35,50,65,150	2c-1,1.5,2,3,4	37050	52	10
U	R.E	Constant	30	5	20,35,50,65,150	2c-1,1.5,2,3,4	37050	52	10
V	R.E	Constant	30	5	20,35,50,65,150	1,1.5,2,3,4	37050	52	5
W	R.E	Constant	30	5	20,35,50,65,150	2c-1,1.5,2,3,4	37050	52	10
X	R.E	Constant	30	5	20,35,50,65,150	2c-1,1.5,2,3,4	37050	52	10
Y	R.E	Constant	30	5	20,35,50,65,150	2c-1,1.5,2,3,4	37050	52	10
Z	R.E	Constant	30	5	20,35,50,65,150	2c-1,1.5,2,3,4	37050	52	10

2c = a two-ball clump of the same volume as a single sphere.

R.E = Radius Expansion.

4.4.1 Application of a 90° Chamber segment

Following the sample preparation process described earlier, an additional cylindrical frictionless wall was generated as an interface between the small and large particles to separate them during the deposition and compression process. The dividing wall was then deleted and the particles allowed to attain equilibrium. An isotropic compressive stress of 300kPa was then applied to the side cylindrical wall and to the bottom wall using a servo-control mechanism (see Appendix). The final sample is shown in Figure 4.6.

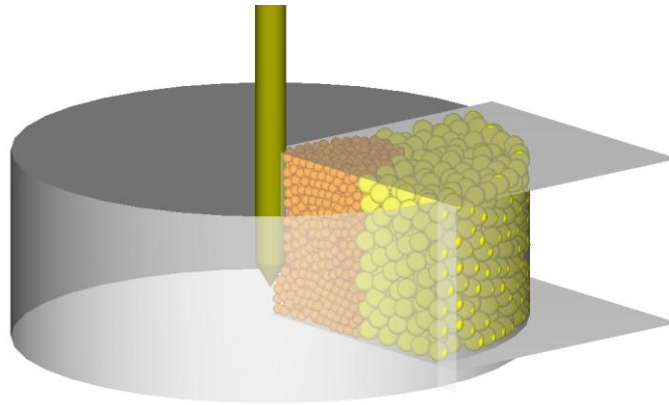


Figure 4.6 Particle refinement in a 90° segment of the calibration Chamber

To examine the effect of the particle refinement method on the cone tip resistance, simulations of models having the same initial porosity of 0.37 were performed with a sample comprising 6mm particles filling the entire chamber (simulation A) and then with a sample comprising 6mm and 12mm particles filling the entire chamber (simulation B). The 6mm particles were deposited to fill the half of the chamber nearest to the cone (up to a radius of 75mm) while the 12mm particles were further away. A compressive stress of 300kPa was then applied laterally and upwards to the cylindrical and the bottom walls respectively. It should be noted that stresses on the

remaining three walls not controlled by the servo were calculated before and during penetration. The stresses on all three non-servo-controlled walls were found to be approximately 300kPa before and during the penetration.

Figure 4.7 shows a comparison of the tip resistance results for the two different sample simulations, where it is evident that at shallow depths (0-0.06m) the tip resistance for the two-sized sample is much lower than the single-sized sample. This is believed to be caused by large voids in the boundary of 6mm and the 12mm particles, permitting easy migration of the 6mm particles into the void space and therefore resulting in a low cone tip resistance. Figure 4.8 shows the migration of the 6mm particles from the initial dividing boundary into the void spaces of the 12mm particles.

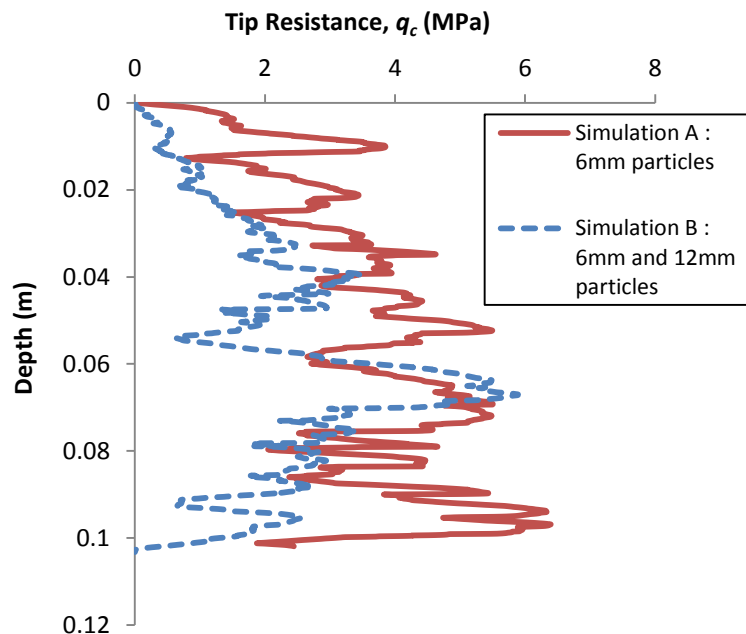


Figure 4.7 Tip resistance results for simulations A and B

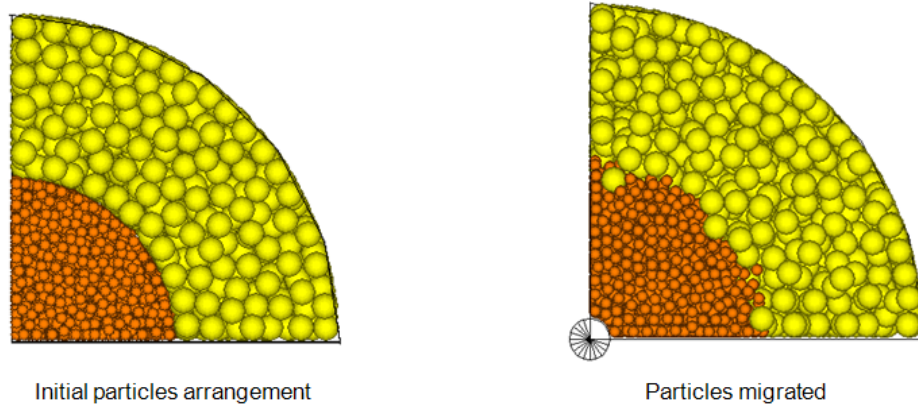


Figure 4.8 Migration of particles through the initial separating boundary for simulation B

To further address the problem of particle migration and to verify that the large voids at the boundary of the 6mm particles and the 12mm particles were responsible for the observed behaviour, a filter was placed at the interface between the two particle sizes. At half radius, that is 75mm from the cone, the chamber was filled with the 6mm spheres followed by a 20mm ‘filter’ of 9mm particles. The remaining 55mm radius was then filled with 12mm diameter particles (simulation C). Figure 4.9 shows a comparison of the resulting tip resistances for the single sized sample of 6mm particles and sample containing 6, 9 and 12mm particles. It can be seen that the addition of the filter provided a much better approximation to the tip resistance obtained using only 6mm spheres. Additionally, Figure 4.10 shows particle migration as a result of introducing a filter between the 6mm and 12mm particles. This suggests that using the filter zone was effective in preventing the small-sized particles migrating into the void spaces of the larger ones.

It was therefore decided that a 3-tiered sample comprising three zones of different particle sizes would be used to decrease computational time and at the same time maintain a near equivalent tip resistance to a sample comprising only small particles.

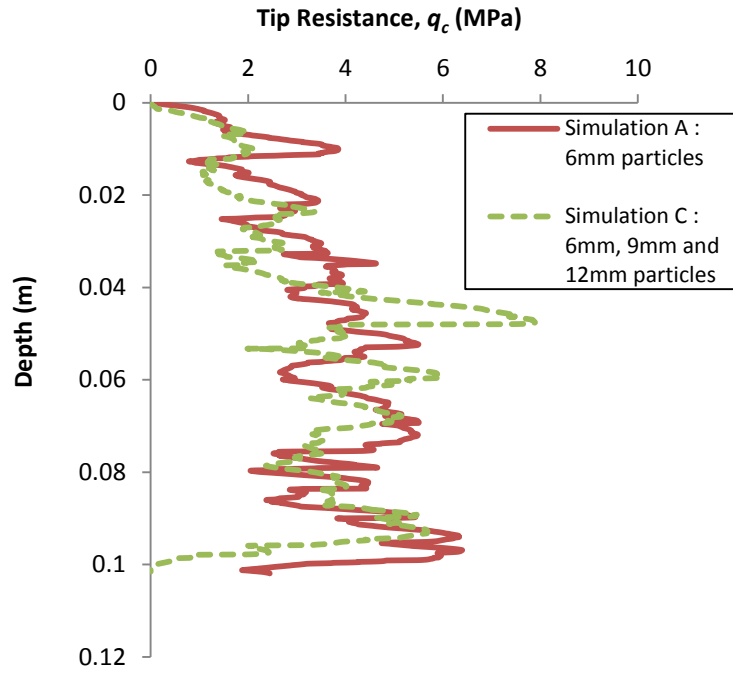


Figure 4.9 Tip resistance results for simulations A and C

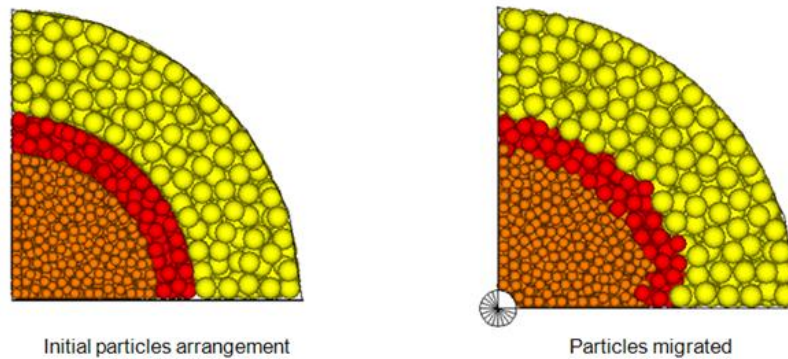


Figure 4.10 Migration of particles through the initial boundaries for simulation C

4.4.2 Application of a 30° Chamber segment

After giving further consideration to a real sand particle size, the 6mm sand-sized particle near the cone was still considered to be too large, and it was thought that a smaller-sized particle would be more appropriate. However, to simulate a sample

comprising smaller sized particles, for example, 2mm, near the cone in a 90° segment would have required a large number of particles which would have lengthened the computational time unacceptably. Consequently, a 30° segment of the calibration chamber was modelled to reduce the number of particles and thus the computational time, as shown in Figure 4.11.

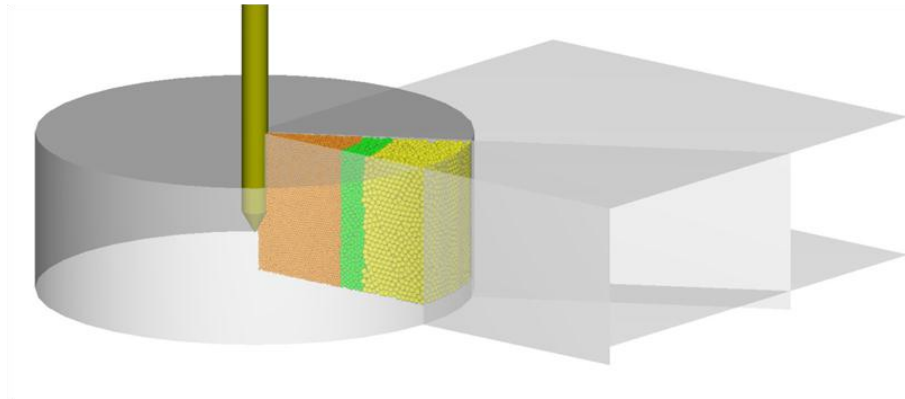


Figure 4.11 Particle refinement method of three particle sizes in a 30° segment of the calibration chamber

The sample for simulation D as per Figure 4.11 was generated by filling half (75mm, radially) of the 30° chamber segment with 2mm particles followed by a 20mm thick band of 3mm particles. The remaining 55mm was filled with 4mm particles. The number of 2mm particles in contact with the cone tip in the 30° segment of the calibration chamber was typically around 14 during the simulation whereas typically only about 7 particles were in contact with the cone when 6mm particles and a 90° segment of the calibration chamber was utilised. Figure 4.12 shows the effect of the new particle configuration on particle migration at the initial dividing boundaries for simulation D.

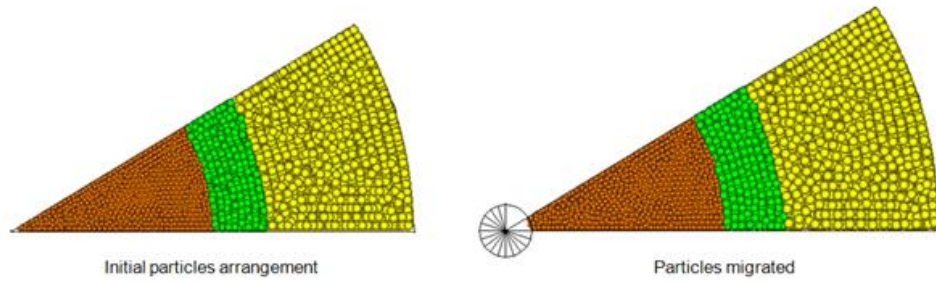


Figure 4.12 Migration of particles through the initial dividing boundaries for simulation D

Additionally, Figure 4.13 is a comparison of the tip resistance results for simulations A and D. Here, it can be seen that using 2mm spheres increased the ultimate tip resistance to about 6MPa compared with about 4MPa for 6mm spheres, albeit for a smaller chamber segment.

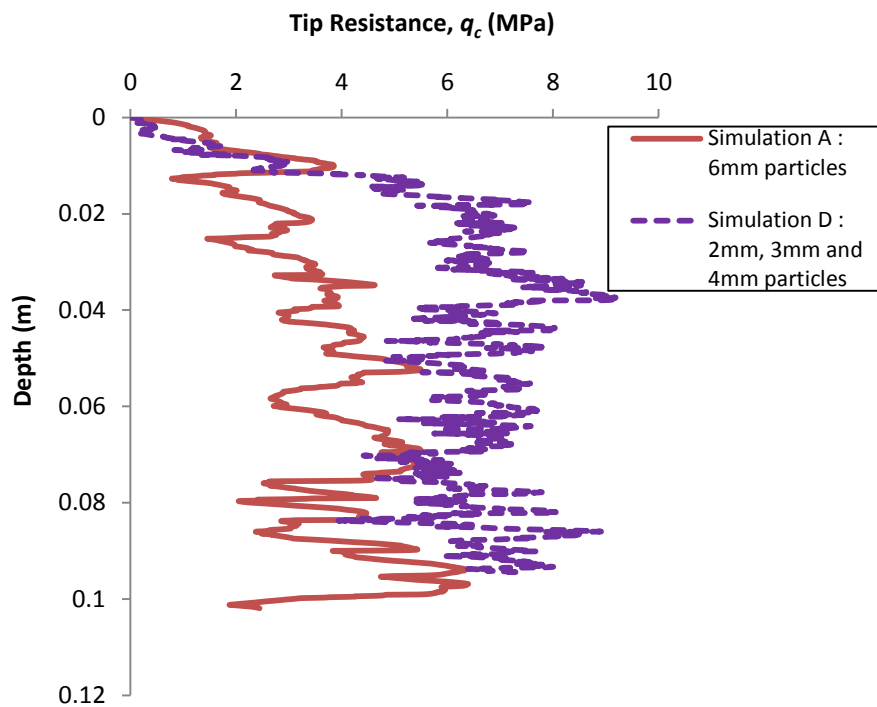


Figure 4.13 Tip resistance results for simulations A and D

Using a smaller segment chamber would not be appropriate for large particle sizes. Figure 4.14 illustrates the particle refinement process for simulation E (which is for a 30° segment of calibration chamber) would not be suitable for the 6mm particles and

12mm particles with the filter of 9mm particles. From Figure 4.14 it is evident that the segment angle of 30° is too narrow for the placement of the 6mm particles under the cone tip and would not guarantee sustained contact with it.

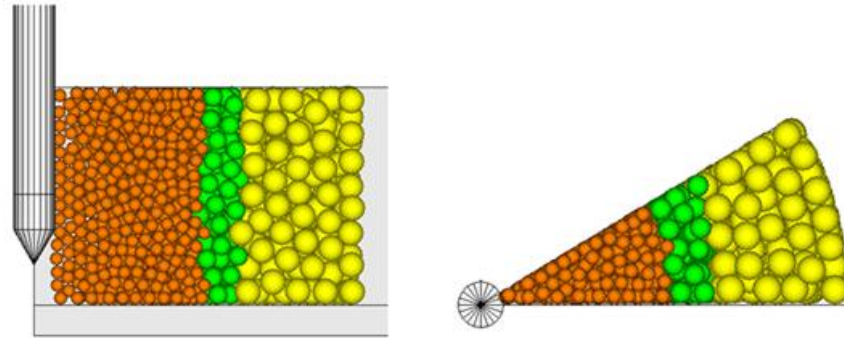


Figure 4.14 Particle refinement for simulation E

This is confirmed further in Figure 4.15 which shows the tip resistance results for simulation E. It is therefore only logical that the 30° segment comprising 2, 3 and 4mm particles should be compared with the 90° segment comprising bigger particles.

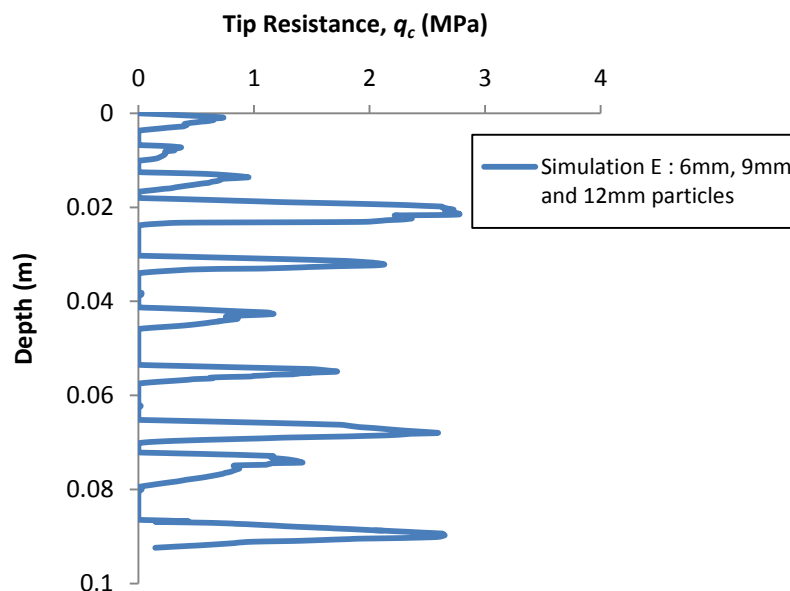


Figure 4.15 Tip resistance results for simulations E

To demonstrate the usefulness of the 3-tier particle refinement method, simulation F was conducted wherein the 3mm sphere filter layer described in simulation D was removed and replaced with 4mm spheres. The outcome of the substitution is shown in Figure 4.16, where it is seen that at shallow depths (0-0.06m) the tip resistance for simulation F was generally much lower than simulation D.

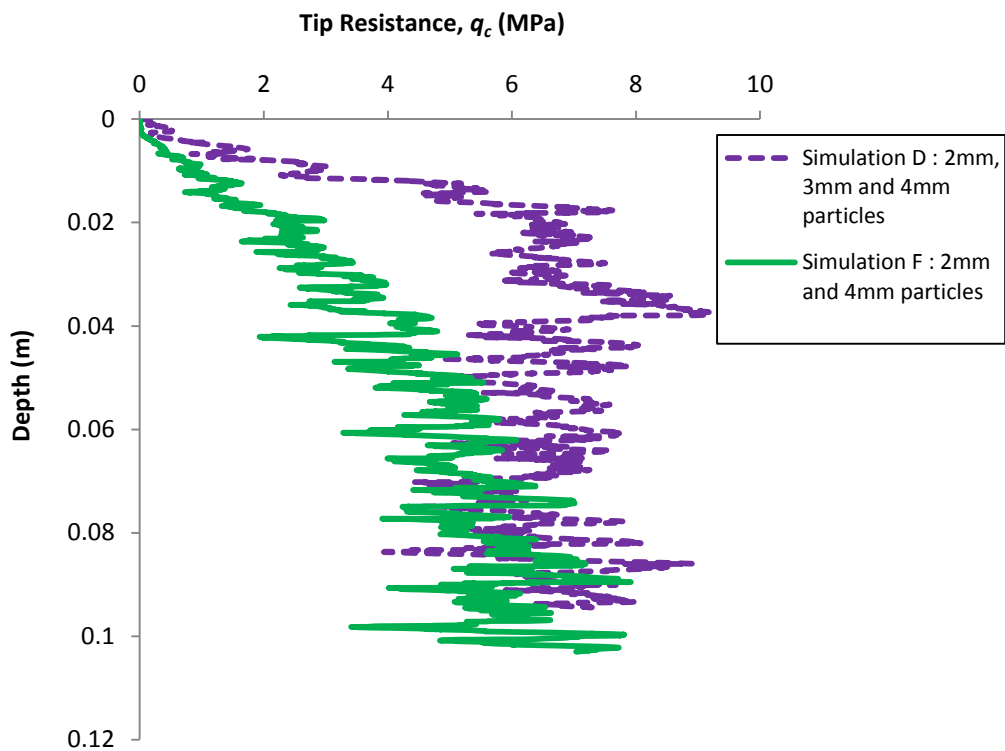


Figure 4.16 Tip resistance results for simulations D and F

4.5 Effect of particle shape

The effect of particle shape on the mechanical behaviour of granular materials has been investigated by several researchers (Ting et al., 1989; Ng and Dobry, 1992; Ni, 2003). Ting et al. (1989) showed that prohibiting particle rotation to mimic the particle roughness was effective in controlling the strength and deformation. Ni (2003) modelled each particle as two spheres bonded together with a high strength

parallel bond to investigate the effect of the particle shape on the shearing resistance and dilation behaviour. The numerical results showed that the deformation and shear strength behaviour of the sample are a function of the particle shape factor. However, simply using spheres to represent each grain is not sufficient to mimic granular materials comprising angular particles. This is because they do not have the same 3D particle kinematics as non-spherical particles. Consequently, in this investigation non-spherical clumps were utilised to ascertain the effect of particle shape on tip resistance.

A clump is defined as a single entity of overlapping balls behaving as a rigid body and with the balls constituting the clump maintained at a fixed distance from each other. The clump used in this study had a volume equivalent to the parent sphere as in previous simulations. During calculations the internal overlapping contacts are ignored, in order to save computational time compared to a similar calculation in which all contacts are active. Thus, a clump acts as a rigid body (with a deformable boundary) that will not break apart, regardless of the forces acting upon it. In this way, a clump differs from a group of particles bounded to one another. Clump logic was described in Section 3.3.4 of Chapter 3.

4.5.1 Application of a 90° Chamber segment

Two simulations were carried out in a 90° segment of the calibration chamber to investigate the effect of particle shape on tip resistance. The first simulation comprised only 6mm single spheres (simulation A). In the second simulation the 6mm spheres were replaced with simple two-ball clumps (Figure 4.17) having the same volume as the parent spheres (simulation G). The shape of the clump is such

that the two overlapping spheres are of equal size. Both spheres have a radius $R = 2.52\text{mm}$ and such that the centre of each is on the surface of the other. All the clumps were given a random orientation within the sample before compression and samples were generated following the same procedure described earlier.

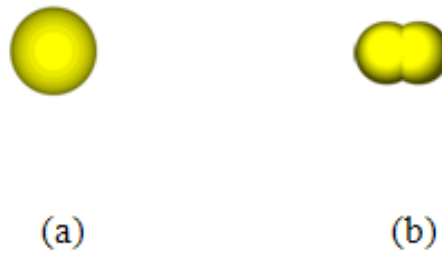


Figure 4.17(a) Single sphere (b) Two-ball clump of equivalent volume

Figure 4.18 shows a comparison of the tip resistance results for the 6mm single spheres and the 6mm two-ball clumps. It can be seen that the ultimate tip resistance increased three fold for the two-ball clumps to about 12MPa compared to 4MPa of the single spheres. This indicates that particle shape contributes significantly to the cone tip resistance. The difference in the response of the sample of spheres compared to that of the clumps can be attributed to the interlocking of the three-dimensional clumps and the increased rolling resistance of the particles.

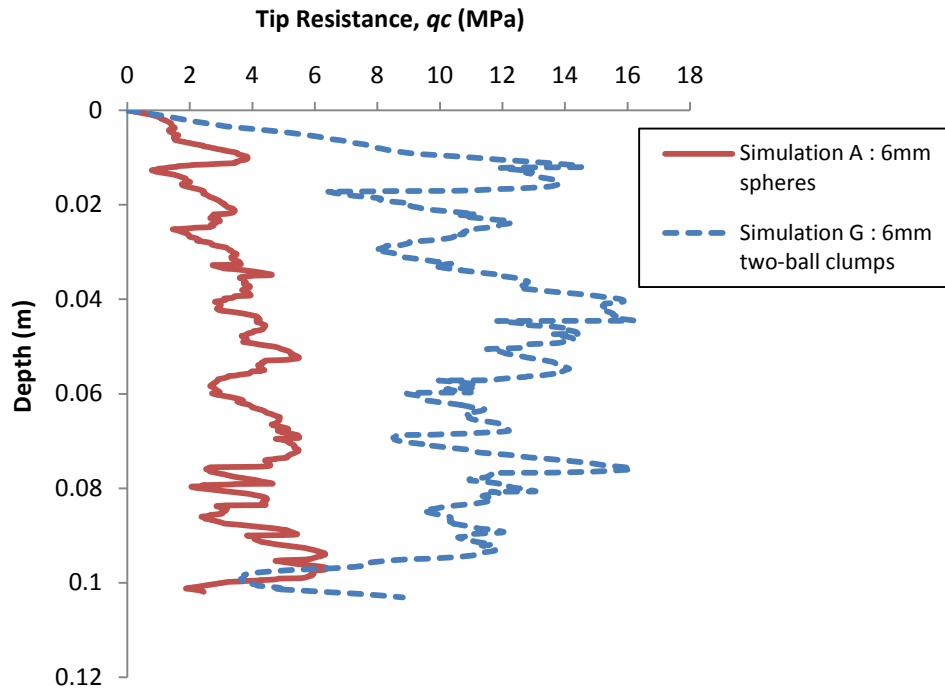


Figure 4.18 Effect of particle shape on tip resistance for simulations A and G

4.5.2 Application of a 30° Chamber segment

For a refined sample, for example that comprising 2, 3 and 4mm sized particles in a 30° segment, replacing all the spheres with two-ball clumps would have effectively doubled the number of balls to be simulated and led to a longer computational time. Therefore, to reduce the computational time involved, only the 2mm spheres were replaced by two-ball clumps (see Figure 4.17) of equivalent volume. The zones of the sample comprising 3mm and 4mm spheres were allowed to maintain their original configuration.

Figure 4.19 shows tip resistances resulting from simulation D (2, 3 and 4mm spheres) and simulation H, which was the refined sample comprising 2mm two-ball clumps, 3 and 4mm spheres. It can be seen that the ultimate tip resistance was almost

increased to 14MPa from about 6MPa as a result of substituting the 2mm spheres with 2mm two-ball clumps placed in next to the cone.

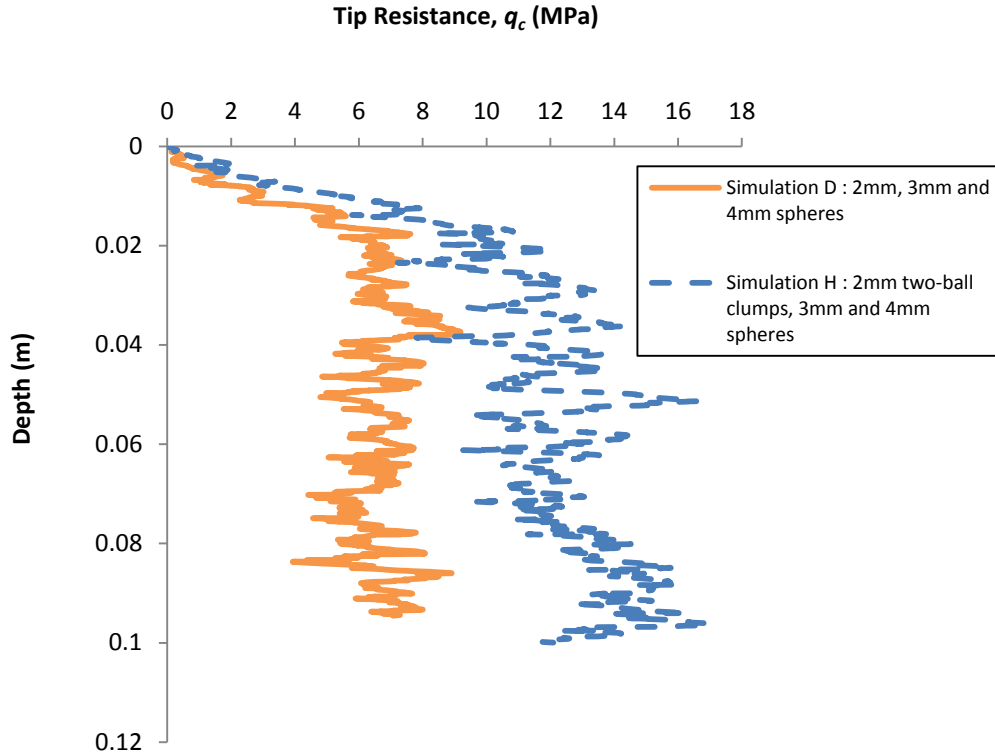


Figure 4.19 Effect of particle shape on cone tip resistance for simulations D and H

4.6 Effect of radius expansion method

In all the previous simulations conducted, the sample preparation involved deposition and compaction method, which was found to increase the computational time of the simulations significantly. Consequently, a radius expansion method (Itasca, 2003; Belheine et al., 2009; Arroyo et al., 2011) was employed as an alternative means of achieving the required initial sample. In this method a specified number of particles located at random coordinates were placed within a given space of walls boundary. Particles were initially generated with small radii (10 times smaller than original particle size) and then expanded gradually in 5 steps by multiplying the particle radii

by a factor of 10 to achieve the target particle radius. This was necessary to ensure that the particles did not overlap with one another or with a wall (or defined boundary). After the particle radii were expanded, a series of calculation cycles was applied until the system reached equilibrium. During the process, gravity was set to zero to ensure that the sample remained isotropic. The particle and wall properties were maintained as in the previous simulations that had used the deposition and compaction method.

To investigate the effect of using the radius expansion method on simulation time and tip resistance, two samples were prepared using the compaction method (simulation D) and the radius expansion method (simulation I) respectively. Both samples comprised the identical particle configuration of 2, 3 and 4mm spheres and also had the same initial porosity of 0.37. An isotropic compressive stress of 300kPa was applied to the two samples after preparing them and during the penetration. It is evident from Figure 4.20 that the ultimate tip resistance resulting from the two simulations were almost the same at about 7MPa. The main difference between the two methods relates mainly to the time it took to simulate both cases. While the sample prepared by deposition and compaction method needed 30 days for complete simulation, the sample prepared by the radius expansion method required only 7 days, illustrating the usefulness of the radius expansion method in saving computational time.

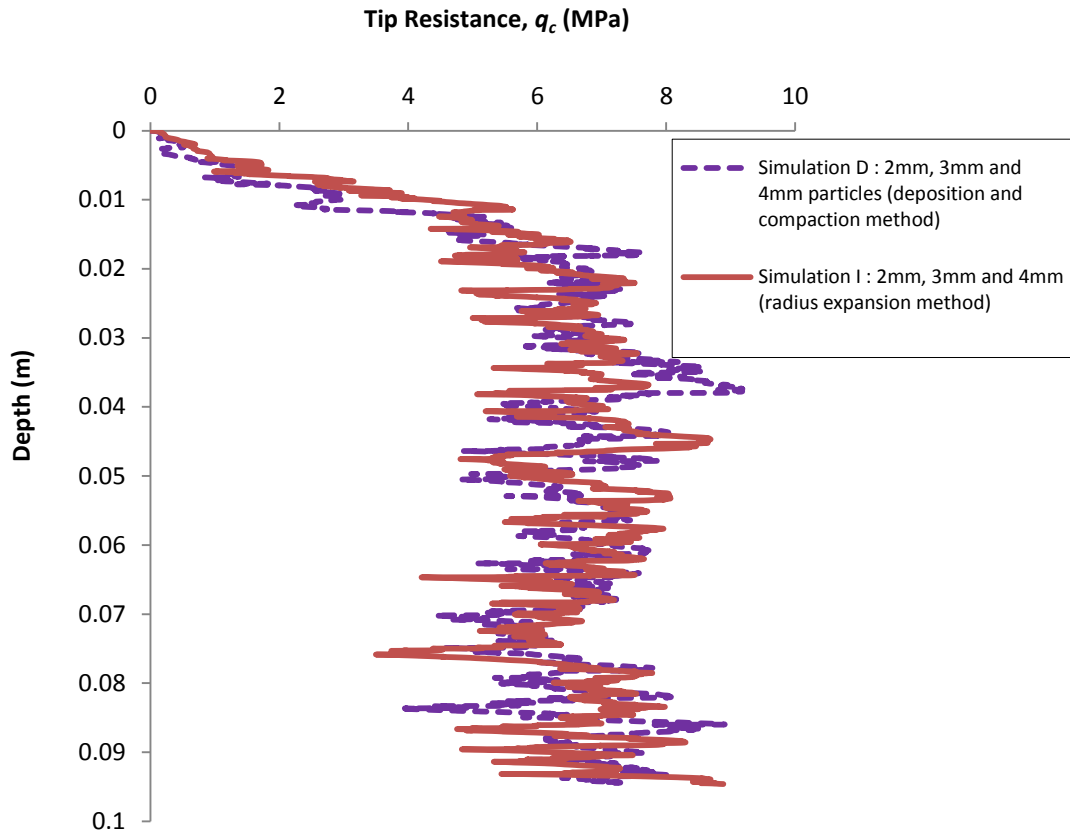


Figure 4.20 Tip resistance results for simulations D and I

4.7 Effect of constant particle mass

The use of constant mass was considered due to the need to simulate even smaller particle size next to the cone penetrometer and hence increase the number of particles in contact with the cone tip area. The time increment over which the velocity and displacement of the particles are integrated from their accelerations using Newton's second law is called time step. The critical time step is a function of the smallest particle mass and reducing the particle size at constant specific gravity and constant particle density next to the cone reduces the time step. This means that the smallest particle size controls the time step and can lead to computational inefficiency. Consequently, each particle size in each zone was given a constant mass in order to

reduce the computation time, given that the simulations were quasi-static in nature and gravity was not important under the boundary stresses applied in these simulations.

The effect of using constant mass on computation time and tip resistance was examined by preparing two samples, both of which utilised the radius expansion method, but had variable particle mass (i.e. constant density - simulation I) and constant particle mass (simulation J) respectively. Both samples had the same 2, 3 and 4mm spheres configuration and an initial porosity 0.37. Additionally, they were subjected to an isotropic compressive stress of 300kPa. The results of the simulations, shown in Figure 4.21 indicate that the two samples have almost equal ultimate tip resistances of about 7MPa. Again the primary difference lay in the simulation times, in that it took 7 days to complete the simulation when the sample was prepared using variable mass particles, whereas the simulation prepared using particles of constant mass took only 3 days.

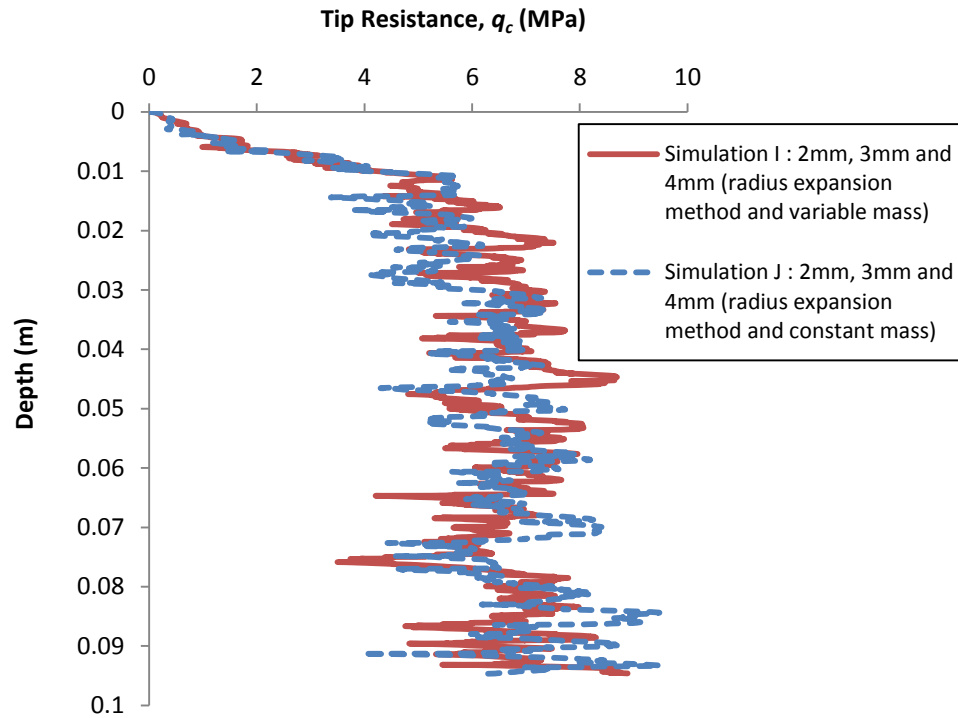


Figure 4.21 Tip resistance results for simulations I and J

It can be deduced from Figure 4.21 that using particles of constant mass had little effect on the tip resistance comparing with particles of variable mass. Therefore, a simulation comprising five particle zones: 1, 1.5, 2, 3 and 4mm diameter spheres, with size increasing with distance from the cone was performed (simulation K), with the aim of introducing even smaller particles next to the cone. The sample which had an initial porosity of 0.37 and subjected to isotropic compression stress of 300kPa is depicted in Figure 4.22. The number of 1mm particles in contact with the cone tip was typically around 52 during the simulation whereas typically only around 14 particles were in contact with the cone when 2mm particles were generated next to the cone.

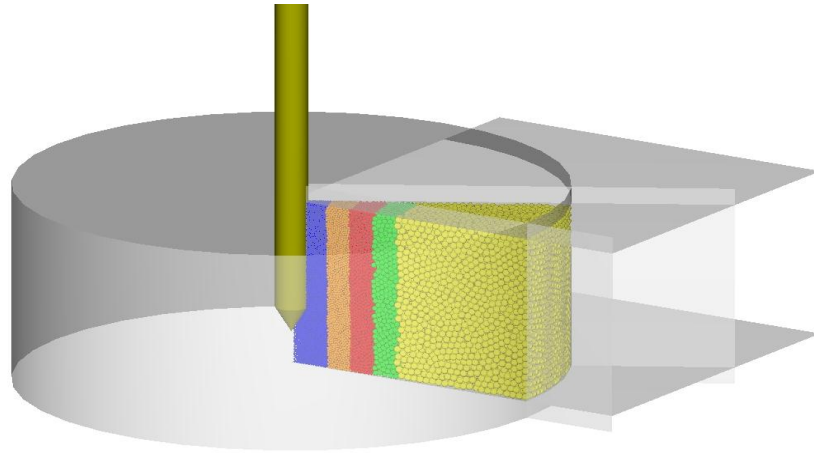


Figure 4.22 Sample of five particle sizes in a 30° segment of the calibration chamber

Figure 4.23 compares the tip resistances of simulation K with simulation J and it is evident that at shallower depths especially, the tip resistance for simulation K was higher than that of simulation J. In addition, using the smaller particles next to the cone leads to less fluctuation in the tip resistance, which is desirable for CPT modelling in sand and making comparisons with available data (Schnaid, 1990). Therefore, a sample comprising five particle zones : 1, 1.5, 2, 3 and 4mm diameter spheres (simulation K) is used in all the subsequent simulations as it provides a large number of small particle size next to the cone penetrometer and lower computational time.

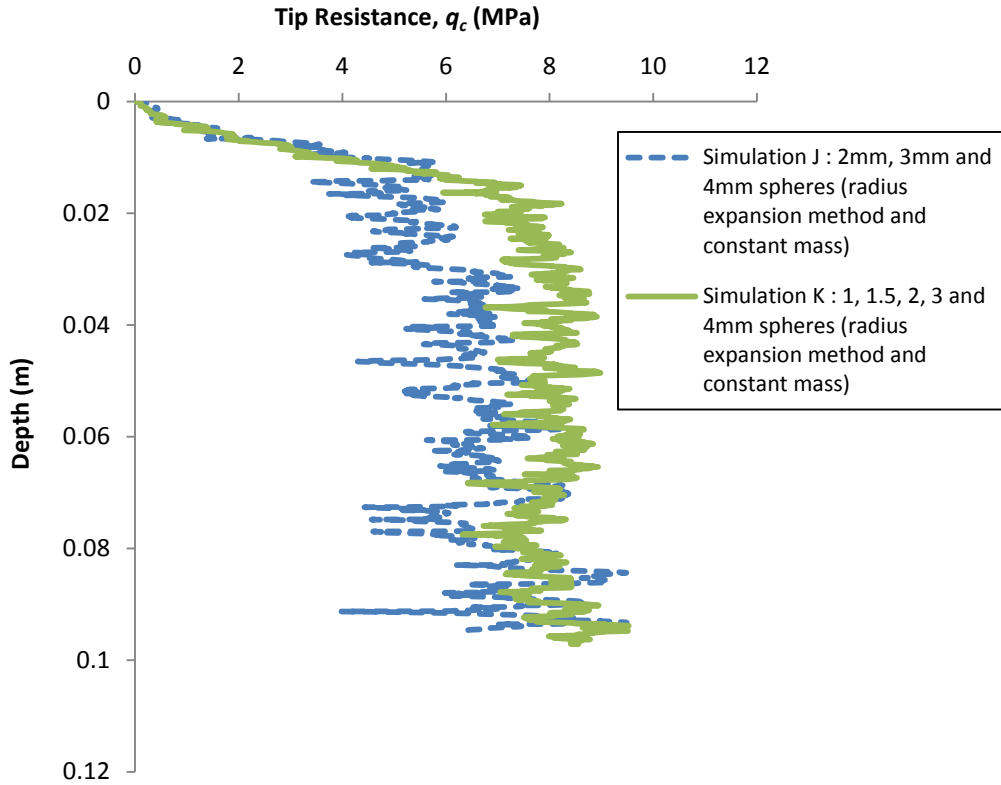


Figure 4.23 Tip resistance results for simulations J and K

4.8 Other factors affecting DEM simulations

Many researchers have shown that cone tip resistance is affected by initial sample porosity and mean effective stress (Schmertmann, 1976; Villet and Mitchell, 1981; Baldi et al., 1982; Baldi et al., 1986). Other factors found to have an important effect on the behaviour of granular materials and consequently tip resistance are particle friction coefficient (Lee and Seed, 1967; Schanz and Vermeer, 1996) and particle rotation (Belheine et al., 2009). These factors will now be investigated using the same numerical model as in simulation K (see Table 4.3).

4.8.1 Effect of initial sample porosity

To investigate the effect of initial sample porosity on the tip resistance results three simulations (K, L and M) were conducted by applying alternative particle friction coefficients of 0, 0.2 and 0.5. The friction coefficients were assigned to these values during particle generation and isotropic compaction of 300kPa to control the sample porosities, resulting in initial porosities of the three samples of 0.37, 0.39 and 0.42 respectively.

During the process of sample generation, the particles interlocking and forming the internal structure of the sample are directly affected by the particle frictional coefficient. Hence any variation in the particle friction coefficient during sample generation results in a different arrangement of the internal structure and hence different sample porosities at equilibrium. Therefore, using a small particle friction coefficient during sample generation permitting inter-particle sliding would result in a dense specimen. On the other hand, using a large particle friction coefficient would lead to resistance to inter-particle sliding and thus a very loose specimen could be generated.

The friction coefficient of the first two samples was reset to 0.5 after isotropic compaction was completed and before pushing the cone. All the samples were then subjected to an isotropic stress of 300kPa. The influence of varying initial porosity on cone tip resistance is shown in Figure 4.24. It is evident from a comparison of the simulations that a reduction in the initial porosity has led to an increase in ultimate tip resistance. The ultimate tip resistance has reduced from 8MPa for the sample with initial porosity 0.37 to about 4MPa for the sample with initial porosity 0.39 and has reduced further to about 2MPa for the sample with initial porosity 0.42.

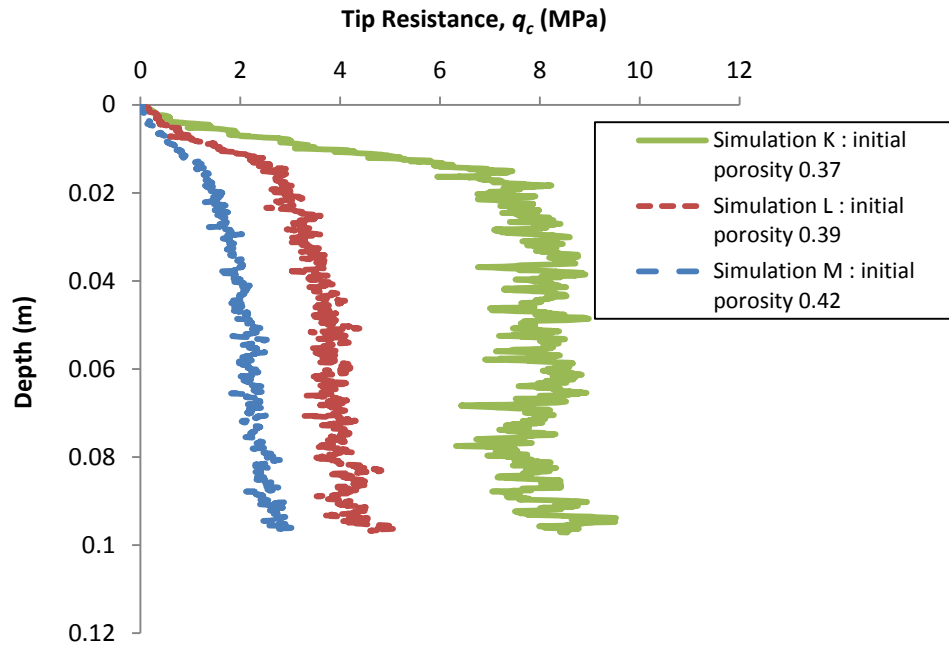


Figure 4.24 Influence of initial porosity on tip resistance

4.8.2 Effect of mean effective stress

To examine the effect of mean effective stress on the tip resistance results, three simulations (N, O and K) comprising samples with the same initial porosity of 0.37 and varying mean effective stresses 100kPa, 200kPa and 300kPa respectively were performed. Figure 4.25 shows that increasing the mean effective stresses resulted in progressively larger values of ultimate tip resistance. Whereas, the ultimate tip resistance was about 3MPa when the mean effective stress was 100kPa, this value increased to about 6MPa for a mean effective stress of 200kPa and increased further to about 8.5MPa when the mean effective stress was 300kPa.

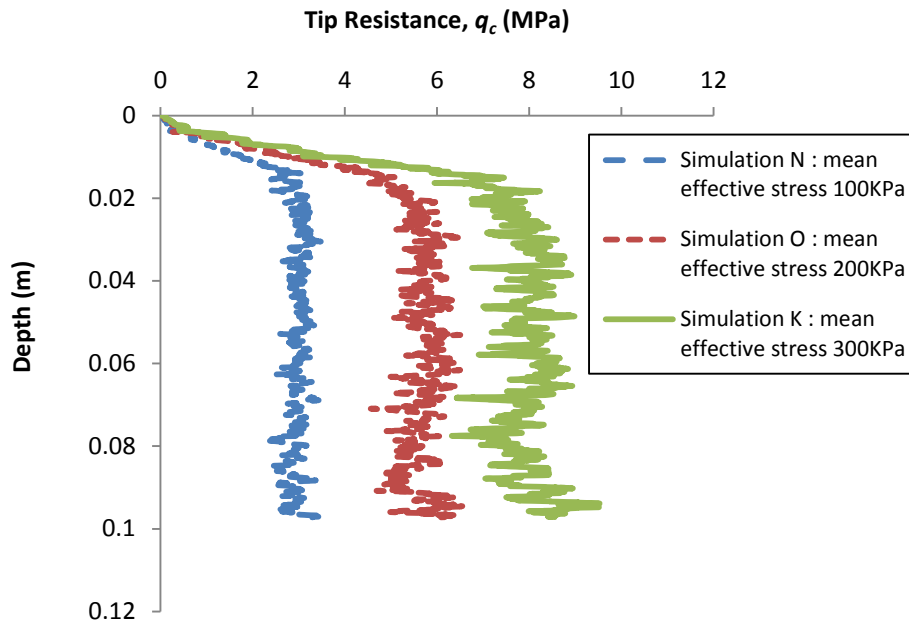


Figure 4.25 Influence of mean effective stress on tip resistance, q_c

It should be noted that when the tip resistance in the three simulations normalised by the initial horizontal stress q_c/σ_{ho} , gives approximately the same value for the three simulations which is about 30 as shown in Figure 4.26.

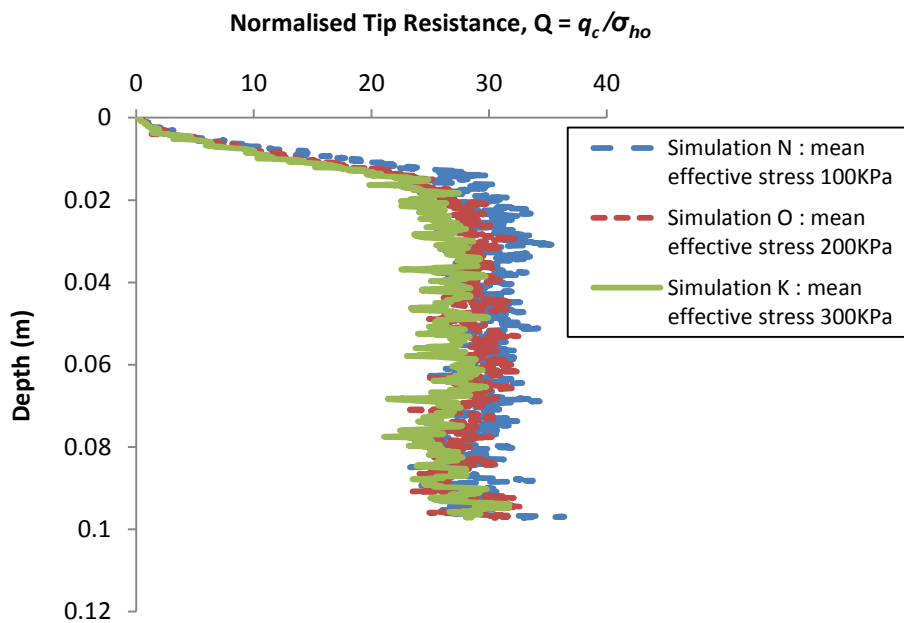


Figure 4.26 Influence of mean effective stress on normalised tip resistance, $Q = q_c/\sigma_{ho}$

4.8.3 Effect of particle friction coefficient

The particle friction coefficient has been reported to have an important influence on the deformation behaviour of a soil (Lee and Seed, 1967; Schanz and Vermeer, 1996). In this section, the effect of particle friction coefficient on the cone resistance was investigated using spheres and two-ball clumps.

Spheres

Three simulations (P, Q and R) were carried out on three samples with the same initial porosities of 0.37, all created using a particle friction coefficient of 0 during generation and at isotropic compaction. Upon completion of the isotropic compaction and prior to the cone penetrating the samples, the particle friction coefficients for the three samples were reset to 0.2, 0.5 and 1.0 respectively. An isotropic compressive stress of 100kPa was then maintained for all the samples. An isotropic compressive stress of 100kPa was used in these simulations because the tip resistance normalised by initial horizontal stress yielded approximately the same values as illustrated in Figure 4.26. Figure 4.27 shows that the ultimate tip resistance increases as the friction coefficient increases. The ultimate tip resistance of the sample with particle friction coefficient 0.2 is about 2MPa, increases to about 3MPa for the sample with particle friction coefficient of 0.5 and to about 4MPa for the sample with particle friction coefficient of 1.0.

It should be noted that in the DEM simulations there is an inter-relation between the parameters used, so changing one variable parameter may influence how another parameter affects the results. In contrasting, in the case of finite-element modelling changing one parameter will not affect the others and hence the results. In Figure

4.27 it can be seen that the scatter in the trend increases as the friction coefficient increases and this is because a sliding contact between two particles will generate an increased particle displacement or jump when the friction coefficient at contacts is increased, thereby inducing more fluctuations of the tip resistance curve. If the size of the particles is reduced, these jumps will decrease in amplitude. Whatever the size of the particles, any increase in the friction coefficient will amplify the fluctuations.

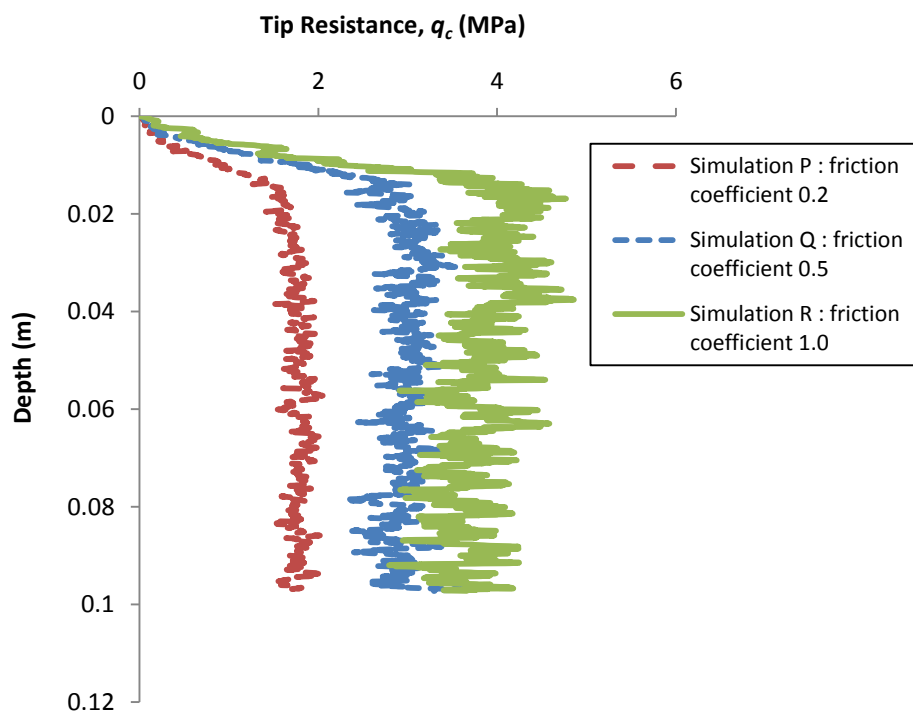


Figure 4.27 Influence of friction coefficient on tip resistance using sample of spheres

Two-ball clumps

The three simulations (P, Q and R) described above were repeated with some exceptions. Only the 1mm spheres next to the cone penetrometer were replaced with two-ball clumps (see Figure 4.17) of equivalent volume. The remaining layers (comprising 1.5,2,3 and 4 mm diameter spheres) in the chamber maintained as in the previous 5-tier simulations to save computational time. Therefore, three simulations

(S, T and U) were performed on the three new samples. Additionally, the initial porosity of the samples was measured after isotropic compaction to 100kPa with particle friction coefficient of 0 and it was found to be 0.32. Reduction in the sample porosities was due to the use of the clumps. Upon completion of the isotropic compaction and prior to cone penetrating the samples, the particle friction coefficients for the three samples were reset to 0.2, 0.5 and 1.0. Figure 4.28 shows the effect of particle friction coefficient on the tip resistance result. It can be seen that the ultimate tip resistance increases with increasing coefficient of friction. Whereas the ultimate tip resistance of the sample with particle friction coefficient 0.2 is about 3MPa, this value increased to about 5.75MPa for the sample with particle friction coefficient of 0.5 and to about 7MPa for the sample with particle friction coefficient of 1.0.

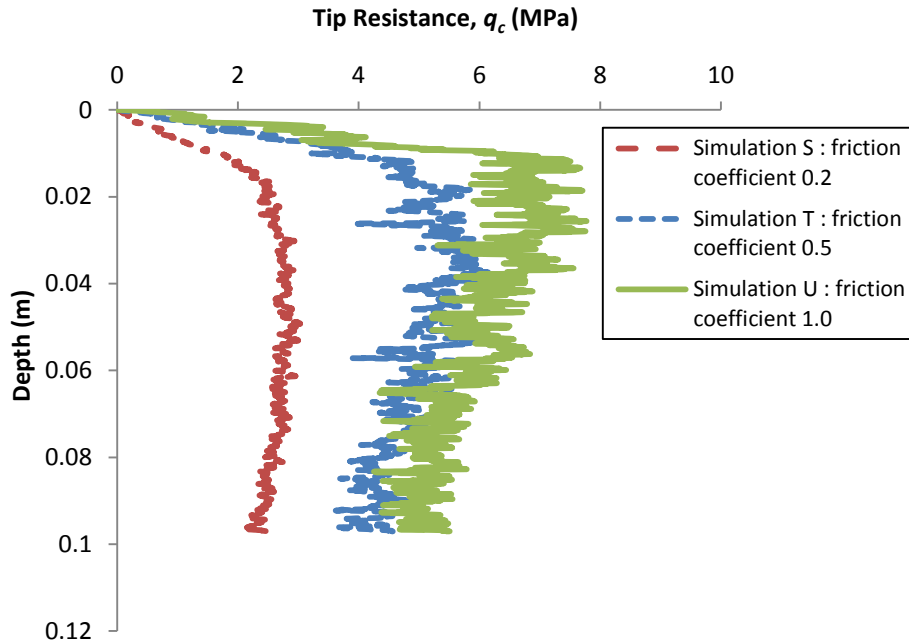


Figure 4.28 Influence of friction coefficient on tip resistance using sample of two-ball clump next to the cone

4.8.4 Effect of particle rotation

Several authors have introduced rolling resistance in to the particle contact law e.g. (Belheine et al., 2009) or have directly prohibited the particle rotation (Calvetti et al., 2003; Arroyo et al., 2011) in attempts to simulate the effect of particle shape on the mechanical behaviour of granular materials. With regards to the movement of a spherical particle, two scenarios are possible: free rotation and prohibited rotation.

To investigate the effect of prohibiting particle rotation on the tip resistance, two simulations (Q and V) were carried out. For both, the two samples had the same initial porosity 0.37 and isotropic compression stress of 100kPa. The particle friction coefficient for the two samples was 0 during generation and isotropic compaction; this was reset to 0.5 upon completion of the isotropic compaction and prior to cone penetration. During cone penetration the spheres of the first sample were allowed to rotate freely whereas those of the second sample were prohibited. From Figure 4.29 it can be seen that the ultimate tip resistance increased from about 3MPa for the sample with freely rotating particles to about 22MPa for the sample that prohibited particle rotation. This result is approximately in agreement with experimental data of Schnaid (1990) (see Figure 4.30) for dense Leighton Buzzard sand (of 89% relative density) having an isotropic stress of 100kPa. However, completely prohibiting rotation of spheres is not representative of reality and using clumps provides a better approximation to reality.

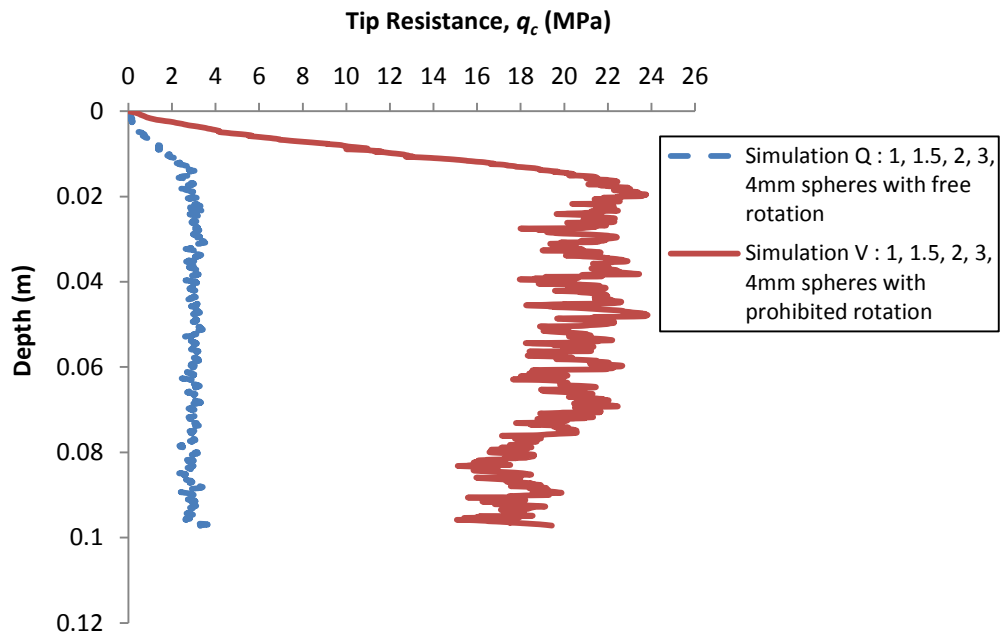


Figure 4.29 Influence of particle rotation on cone tip resistance

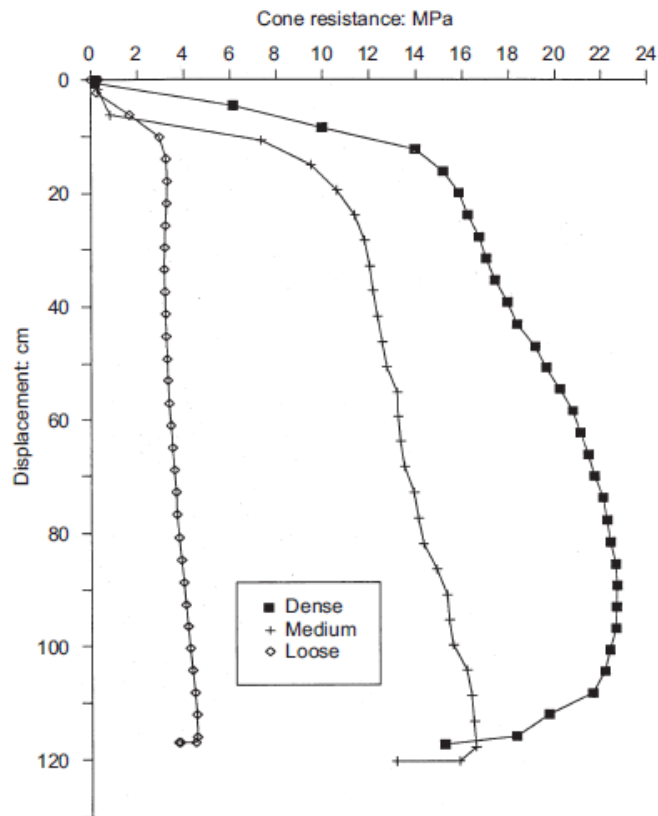


Figure 4.30 Influence of relative density on a profile of cone tip resistance against depth (Schnaid, 1990)

4.8.5 Effect of clump shape

In section 4.5 it was shown that the shape of particles influences cone tip resistance. This section examines further the effect of shape using different two-ball clumps having the same volume as the parent sphere (Figure 4.31) on cone tip resistance.



Figure 4.31(a) Single sphere. (b) Two-ball clump of equivalent volume (different size spheres). (c) Two-ball clump of equivalent volume (equal-sized spheres). (d) Two-ball clump of equivalent volume (equal-sized spheres, just touching).

Figure 4.31a shows the single or (parent) sphere, 1mm in diameter. Figure 4.31b shows a two-ball clump where the shape of clump comprises two overlapping spheres of different sizes. The radii are $R = 0.490\text{mm}$ and $r = 0.245\text{mm}$ for the larger and smaller spheres respectively and d is the distance between the centres of two spheres in each clump, such that $d = 2r$ and $r = 0.5R$. Figure 4.31c shows a two-ball clump where the shape of the clump comprises two overlap spheres of equal size. The radius $R = 0.420$ for both spheres and such that the centre of each is on the surface of the other (i.e $d=R$). Figure 4.31d shows a two-ball clump where the shape of clump is the same as in Figure 4.31c only with a relationship between d and R of $d = \frac{15}{8} R$ (just touching) and $R = 0.397\text{mm}$ for both spheres.

The first layer of spheres in the calibration chamber (i.e. nearest the cone penetrometer) were replaced with simple two-ball clumps, each having a volume equivalent to that of a 1mm diameter sphere. The clumps were each given a random

orientation before isotropic compression. The remaining layers (comprising 1.5,2,3 and 4 mm diameter spheres) in the chamber maintained their configuration as per previous 5-tier simulations to save computational time. An isotropic compressive stress of 300kPa was applied to the all samples. The particle friction coefficient for all samples was kept at zero during sample preparation and isotropic compaction to ensure that dense samples were achieved. The particle friction coefficient was then reset to 0.5 prior to cone penetration.

Table 4.4 shows the initial overall porosity for each sample. The porosities of the samples were calculated numerically using MATLAB.

Table 4.4 Sample initial overall porosities

Sample	Initial porosity
Spherical particles	0.37
Two-ball clumps (b)	0.34
Two-ball clumps (c)	0.32
Two-ball clumps (d)	0.37

It should be noted that due to the contribution to the mass in the overlapping region of the spheres in the first zone (next to the cone), the moment of inertia for a clump is not the same as that for a particle of the same shape and uniform density. Figure 4.32 compares the tip resistances of sample with individual spheres (simulation K) to the samples containing two-ball clumps (simulations W, X and Y) and confirms the initial hypothesis that the shape of two-ball clumps affects tip resistance. Key observations from the figure are: the ultimate tip resistance value increased from about 8MPa for single spheres to about 12MPa for the two-ball clump in Figure

4.31b, to about 15MPa for the two-ball clump in Figure 4.31c and to about 18MPa for the two-ball clump in Figure 4.31d.

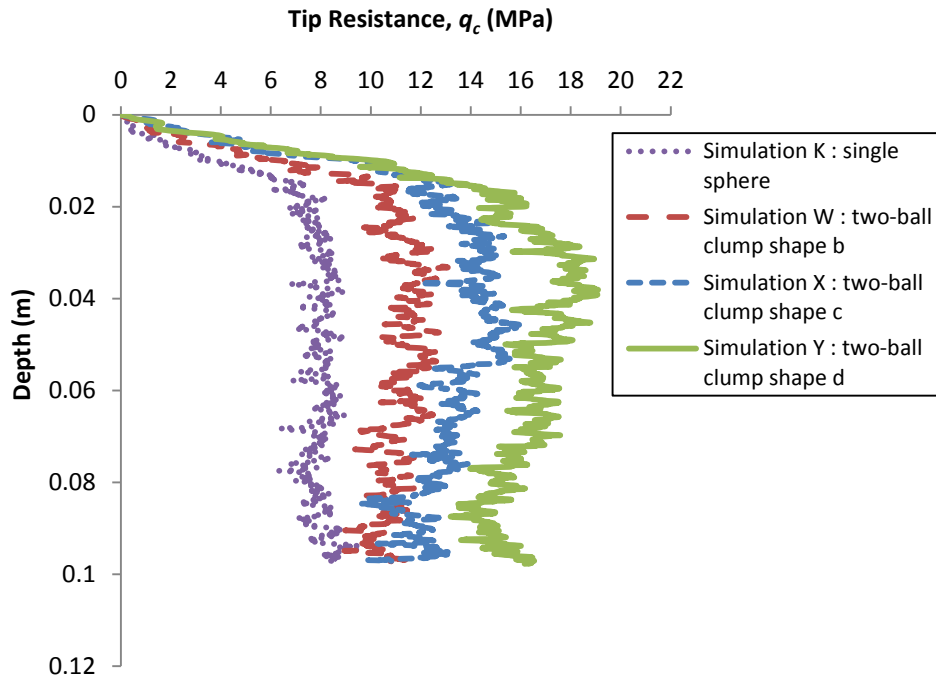


Figure 4.32 Tip resistance results for simulations K, W, X and Y

Tip resistance therefore increases with increasing clump angularity due to increased interlocking and rotational resistance. To simulate real granular material behaviour a more complicated particle shape similar to the real material under consideration is recommended, though this will increase computational time.

In Figure 4.32 the tip resistances for the two-ball clump samples are observed to decrease marginally at a cone penetration depth of about 0.04m. This is thought to have occurred as a result of prominent interlocking and dilation in the dense sample leading to high tip resistance as the cone penetrometer was installed but reducing slightly upon further advancement (i.e. from 0.04m onwards) of the cone into the sample.

To verify that this did result from the influence of sample density, the simulation was repeated using a medium sample for the two-ball clump in Figure 4.31c with initial porosity of 0.39 (simulation Z). Figure 4.33 shows no significant reduction of tip resistance over the measured depth in the medium sample (simulation Z) as in the dense sample (simulation X).

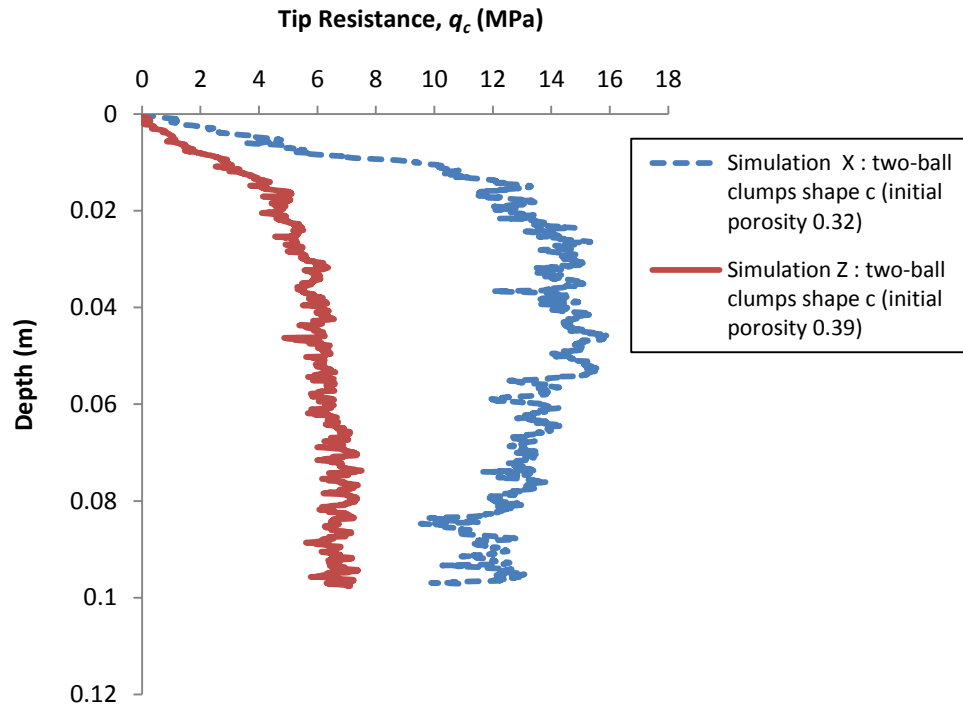


Figure 4.33 Tip resistance results for simulations X and Z

4.9 Contact force distributions

The contact force distributions were investigated by comparing the sample comprising only of spheres in direct contact with the cone penetrometer (simulation K) to the sample replaced with the two-ball clump in Figure 4.31c next to the cone penetrometer (simulation X).

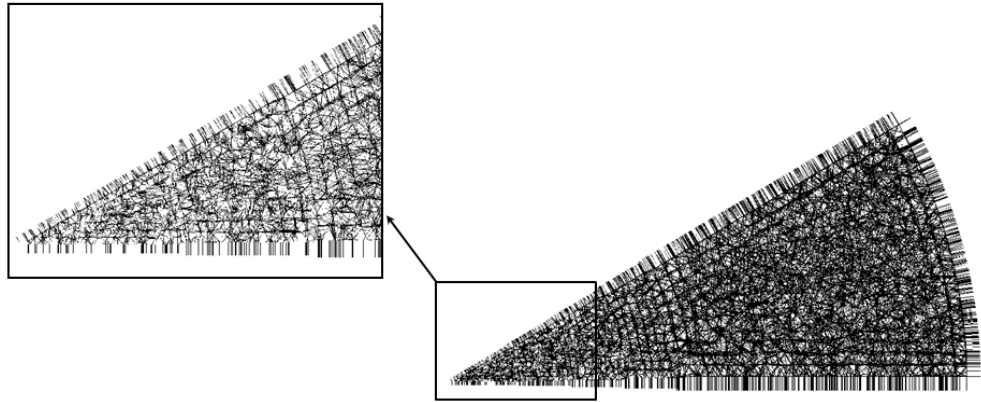
Figure 4.34 shows the contact forces within the sample before the cone was inserted for the samples comprising spheres and clumps respectively. Using identical scales for both samples, it can be observed that for the sample with clumps the magnitude of the mean contact forces is slightly decreased than the sample of spheres. This is due to the higher number of contacts per particle for the sample of two-ball clumps.

In Figure 4.35 the contact forces after cone insertion are shown at the same scale for the sample of spheres and sample containing clumps. It is evident that nearer the cone tip, contact forces are higher for both samples and lower at the other positions. However there is little observable difference between the magnitudes of the mean contact force for the sample of spheres and that including clumps. The maximum contact force and the number of contacts for the sample with clumps were slightly higher than that for the sample of spheres. The difference in the penetration depth obtained from the saved simulation files after a number of calculation cycles is due to the differences between the two samples. Figure 4.35 shows the situation where the samples have the closest penetration depths.

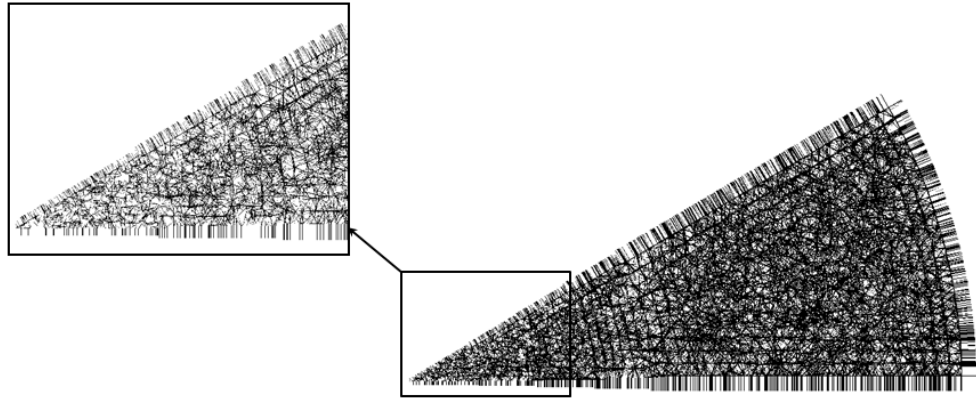
4.10 Displacement vector distributions

The same aforementioned samples (simulations K and X) were used to investigate the particle displacement vector distributions. Figure 4.36 shows at the same scale the particle displacement vectors upon inserting the cone into the sample of spheres and clumps. It is observed that the displacement tendency of the majority of particles near the cone tip and cone penetrometer is downwards and laterally for both samples. Moreover, the particle displacements at the cone tip and along the penetrometer shaft are larger than displacements observed at the other positions. The difference between

the sample of spheres and clumps can be attributed to the greater degree of interlocking provided by the clumps and increased rolling resistance.

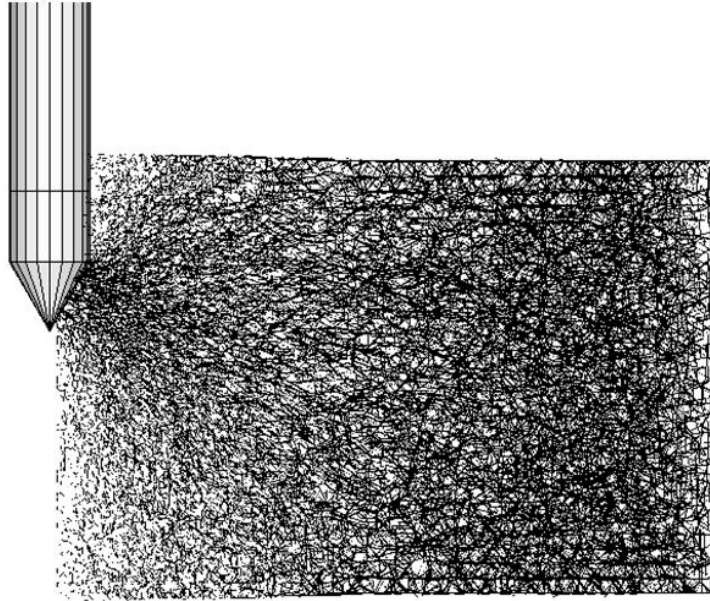


(a)

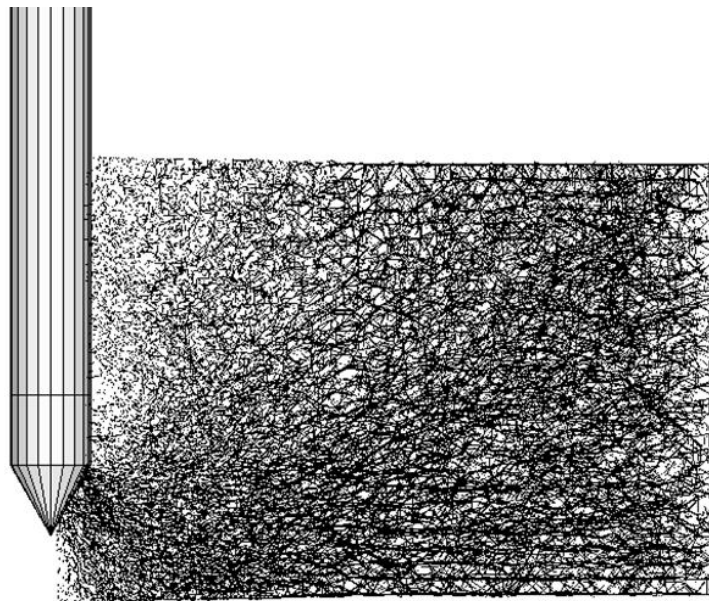


(b)

Figure 4.34 Contact forces before pushing the cone at the same scale of 0.001 for (a) spheres (maximum contact force=19.77N, mean contact force=1.35N, number of contacts=119228); (b) clumps (maximum contact force=23.42N, mean contact force=1.11N, number of contacts=145897)

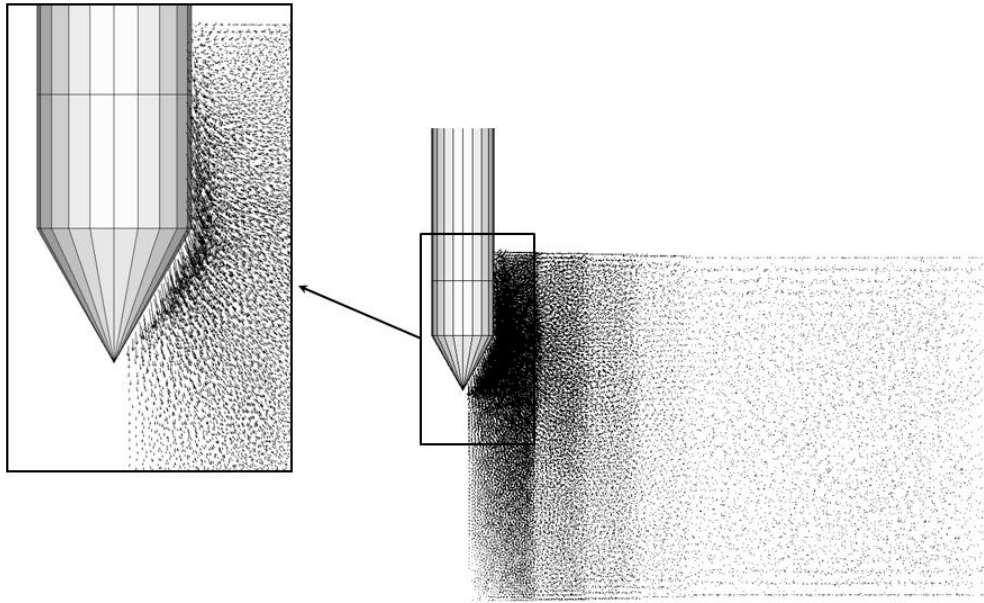


(a)

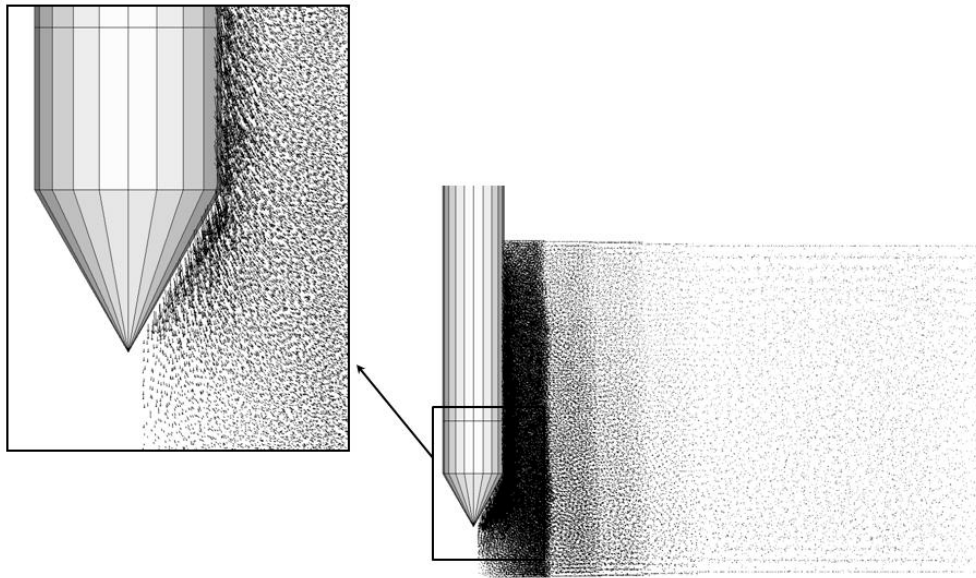


(b)

Figure 4.35 Contact forces after pushing the cone at the same scale of 0.001 for (a) spheres (maximum contact force=21.65N, mean contact force=1.95N, number of contacts=98054); (b) clumps (maximum contact force=24.41N, mean contact force=1.94N, number of contacts=100261)



(a)



(b)

Figure 4.36 Total displacement after pushing the cone at the same scale of 0.05 for (a) spheres (maximum displacement =24.35mm), (b) clumps (maximum displacement =56.35mm)

4.11 Conclusions

DEM was used in this study to simulate cone penetration tests in granular materials in the controlled environment of a calibration chamber. The particles were either spherical in shape or clumps comprising of two balls and were allowed to rotate freely. For simplicity a linear–elastic contact law was utilised. As axisymmetry was present in the simulation, only a quarter of the sample and penetrometer were initially analysed to reduce computational time. In addition to reducing the chamber height H , the ratio of chamber width D_c to cone diameter B was reduced to a value consistent with D_c/B of an experimental chamber for the following reasons:

- a) To enable the use of small particles in the numerical model to simulate real sand behaviour as closely as possible
- b) To increase the ratio between cone diameter and particle diameter B/d_{50} to a more realistic value
- c) To ensure that, during penetration, the cone tip remained in contact with an acceptable number of particles

A constant stress boundary condition (BC1) was applied and maintained during cone penetration using a servo-control mechanism. A novel technique of particle refinement was implemented in the simulations whereby small particles were generated near the cone penetrometer and larger ones further away to achieve a large number of small particles in contact with the cone tip and reduce computational time. The particles were graded in zones to ensure that the cone penetration resistance was approximately the same as would have been obtained if an entire chamber had been filled with small particles. 30 degree and 90 degree chamber segments comprising a

variety of particles zones were simulated. However, the 30 degree chamber segment was found to be more appropriate for the subsequent simulations as more acceptable number of particles next to the cone could be used, thereby reducing computation time.

Using a radius expansion method during sample preparation was found to reduce computational time significantly compared with the deposition and compaction method without affecting tip resistance too much. Furthermore, because the simulation is for a quasi-static process, giving constant mass to each particle size in the model was determined to be a key factor in reducing computational time compared with constant density, and almost the same tip resistance was obtained in both cases. A reduction in particle size next to the cone was found to increase cone tip resistance and decrease fluctuations in the tip resistance curve. The initial porosity, mean effective stress and particle friction coefficient were found to influence the tip resistance, with a reduction in initial porosity, an increase in particle friction coefficient and an increase in mean effective stress all leading to an increase in tip resistance. Moreover, prohibiting particle rotation was found to increase tip resistance significantly compared with free particle rotation and the ultimate tip resistance obtained from the DEM simulation with 1mm spheres next to the cone and prohibited particle rotation was shown to be in approximate agreement with available experimental data (Schnaid, 1990).

The effect of particle shape was initially examined in a 90° segment of the calibration chamber by replacing the whole spheres with simple two-ball clumps. This was found increase the cone penetration resistance three fold in comparison of using

single spheres. In a 30° segment of calibration chamber only the spheres next to the cone penetrometer were replaced with the two-ball clump to reduce computational time. The results show that using clumps gives a higher tip resistance compared with using single spheres and this resistance increased with increasing clump angularity due to increased interlocking and rotational resistance. Overall, compared to experimental results (Schnaid, 1990) of tip resistance as a function of depth the simulations undertaken in this investigation were found to be in correct form.

CHAPTER 5

DISCRETE ELEMENT MODELLING OF BIAXIAL TEST

5.1 Introduction

Granular materials such as sand are composed of discrete particles which exhibit very complex macroscopic mechanical characteristics when subjected to externally applied loads. The biaxial test is traditionally one of the most important laboratory tests for the determination of strength and stress-strain behaviour of soil and other granular materials. A biaxial flow consolidation test was developed by Peters and Leavell (1986) to determine axial and radial permeabilities of an anisotropic sample. From the theoretical relationship, they showed that anisotropy in stiffness has an important effect on the axial and radial permeabilities. Tatsuoka (1986) conducted drained plane strain compression tests on saturated samples of fine angular to sub-angular sand at confining pressures of up to 400kPa to study the strength and deformation characteristics of sand. The air-pluviation method was used to prepare the samples with changing the angle of the bedding plane δ to the σ'_1 -direction during plane strain compression tests from 0 to 90 degrees. The results showed that anisotropy is significant in the strength and deformation characteristics for both dense and loose samples.

Recently many researchers have succeeded in using DEM to simulate the behaviour of granular material. For example, Ni (2003) modelled a 3D numerical biaxial test with flexible boundaries using pairs of spheres bonded together with a high strength parallel bond to model soil particles. Similarly, through the 3D DEM of plane-strain biaxial compression tests, Geng (2010) investigated the mechanical response of cohesionless granular material under monotonic loading using spheres and two-ball clumps. Both sets of results by Ni (2003) and Geng (2010) compared well qualitatively with the results of traditional experimental methods. Additionally, they investigated the effect of different particle parameters such as particle shape and particle friction coefficient on the stress-strain behaviour. They found that the peak and ultimate shear strength and the overall dilation of the simulated sample increased with increasing the particle friction coefficient and the shape factor or when using two-ball clumps. Compaction of particles in 2D simulations of the biaxial compression test was discussed by Markauskas and Kaniuska (2006). Pena et al. (2008), using a packing of randomly generated polygonal particles, also simulated the biaxial test wherein the effects of initial density and interparticle coefficient of friction on the macro mechanical behaviour of a granular material were investigated. Their results showed identical void ratios to be achievable in samples at large strains, independent of their initial density.

In this chapter, 3D discrete element modelling was undertaken to explore the mechanical behaviour of granular material under biaxial test conditions with a view to capturing the essential macro behaviour of granular materials. A series of simulations was conducted to study the effects of sample initial porosity, confining pressure, particle friction coefficient and particle shape on the stress-strain

behaviour. The main purpose of the biaxial test simulations is to obtain continuum parameters to derive an analytical solution of q_c using a combined cylindrical-spherical cavity expansion method. The analytical solution of q_c obtained in Chapter 6 will be compared with some DEM simulation results for q_c reported in Chapter 4.

5.2 Modelling procedure and sample preparation

Simulation of the plane-strain compression tests was carried out with PFC^{3D} on samples that comprised of spheres or clumps. For simplicity, a linear-elastic contact law was selected for the simulations. The chamber model was prepared by generating six finite and frictionless rigid walls as sample boundaries to confine the single spheres or two-ball clumps (Figure 5.1). Around 13400 1mm diameter spheres were generated using the radius expansion method (see Section 4.6) and used for the formation of each sample in the simulations performed.

The dimensions of the sample modelled in the numerical biaxial test simulations were 56mm \times 28mm \times 7mm corresponding to the major (x), minor (y), and intermediate (z) principal stress axis respectively.

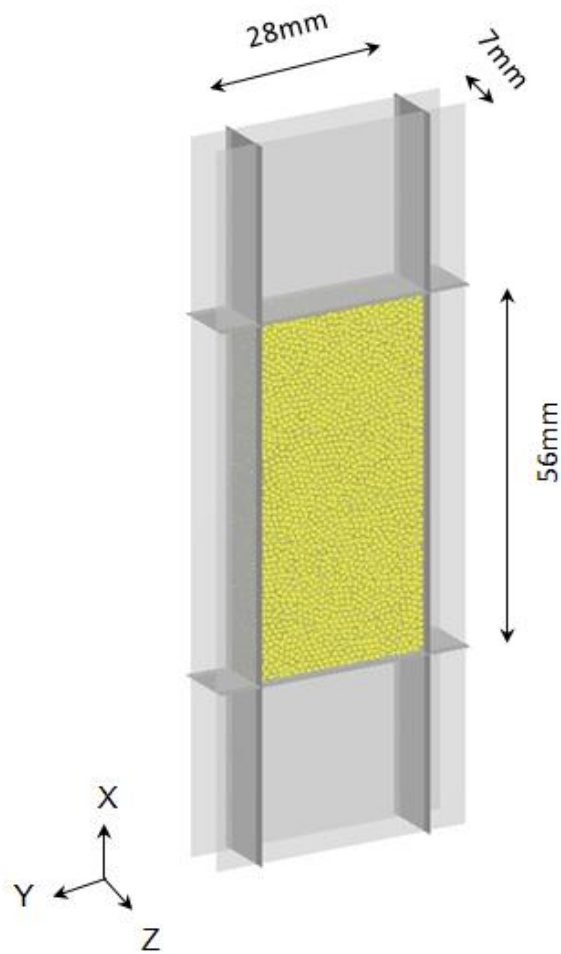


Figure 5.1 Sample for biaxial test simulation

Table 5.1 shows the particle and wall properties and this was maintained for all the simulations.

Table 5.1 The particle and wall properties for DEM simulations

Input parameter	Value
Particle and wall normal stiffness (k_n)	$5 \times 10^5 \text{N/m}$
Particle and wall shear stiffness (k_s)	$5 \times 10^5 \text{N/m}$
Particle density	2650kg/m^3
Particle friction coefficient	0.5
Chamber wall friction coefficient	0

After the sample was generated, the sample stress state was adjusted to an initial isotropic condition such that $\sigma_1 = \sigma_2 = \sigma_3 = 100\text{kPa}$. The stresses σ_1 (x-direction), σ_2 (z-direction) and σ_3 (y-direction) were calculated using the contact forces and the ball/wall contact areas. The stresses σ_1 and σ_3 are defined as the axial stress and confining stress respectively. After the sample had reached an initial pressure of 100kPa the velocities of the top and bottom walls (x-direction) were specified as 0.01m/s to simulate strain-controlled loading, while those of the left and right walls (y-direction) were controlled automatically by a servo-mechanism (see Appendix) to maintain a constant confining stress (Figure 5.2). The front and back walls (z-direction) were maintained in fixed positions. Table 5.2 shows a summary of all biaxial test simulations conducted in this study.

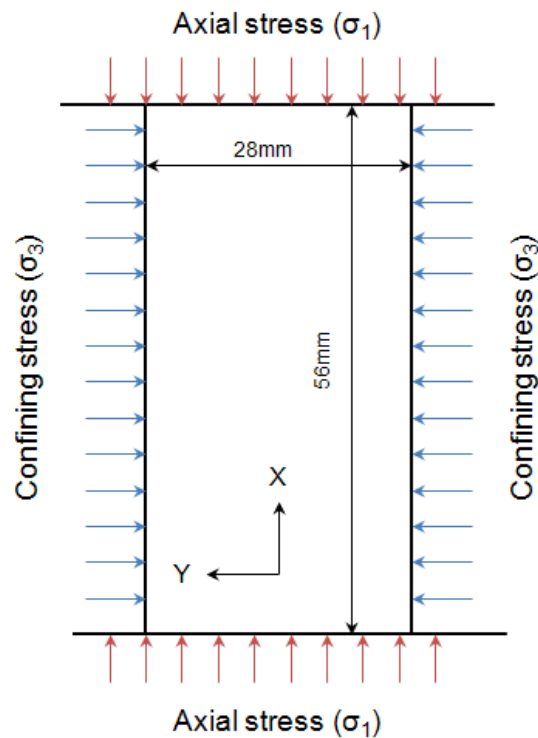


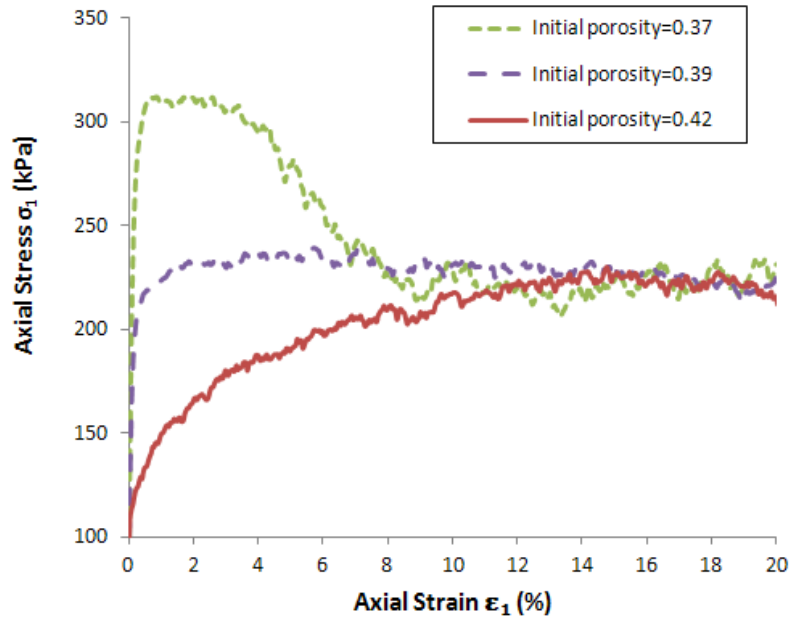
Figure 5.2 Schematic illustration of biaxial test

Table 5.2 Summary of biaxial test simulations

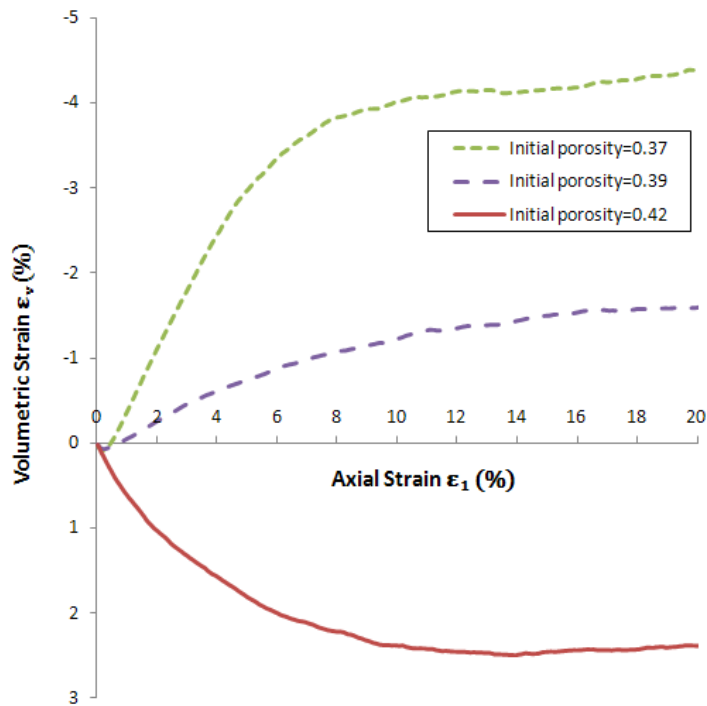
Simulation	Particle shape	Particle friction coefficient	Initial porosity	Confining stress σ'_3 (kPa)	ϕ'_{peak} (D)	ϕ'_{crit} (D)	Ψ_{max} (D)
BT1	Spheres	0.5	0.37	100	32	22	15
BT2	Spheres	0.5	0.39	100	24	22	3
BT3	Spheres	0.5	0.42	100	22	22	0
BT4	Spheres	0.5	0.37	200	33	20	14.5
BT5	Spheres	0.5	0.37	300	33	20	14
BT6	Two-ball clumps	0.5	0.37	100	53	32	30
BT7	Spheres	0.2	0.37	100	24	20	8
BT8	Spheres	1.0	0.37	100	36	22	18
BT9	Two-ball clumps	0.2	0.37	100	39	30	16
BT10	Two-ball clumps	1.0	0.37	100	62	32	39

5.3 Influence of initial sample porosity

Three simulation tests (BT1, BT2 and BT3) were carried out to investigate the effect of the initial sample porosity on the mechanical behaviour of granular material. Particle friction coefficients of 0, 0.15 and 0.5 were initially assigned to control the sample porosities during particle generation and isotropic compaction. This led to a porosity n for the three samples of 0.37 (dense), 0.39 (medium) and 0.42 (loose) respectively. Following the samples being subjected to isotropic compaction and prior to the shearing stage of the simulations, the particle friction coefficient of the first two samples was reset to 0.5. Each sample comprised around 13400 (1mm diameter sized) spheres that had been subjected to a confining stress of 100kPa. The effect of varying porosity on the mechanical behaviour of the granular material is shown in Figure 5.3 which compares axial stress against axial strain (Figure 5.3a) and volumetric strain against axial strain (Figure 5.3b) for the three simulations.



(a)



(b)

Figure 5.3 Axial stress and volumetric dilation for samples with different initial porosities: (a) Axial stress against axial strain (b) Volumetric strain against axial strain

In Figure 5.3a the peak axial stresses achieved are shown as varying from 310kPa for the sample with initial porosity 0.37 to 225kPa for the sample with initial porosity 0.42, corresponding to axial strains ranging from 2.0% to 15.0% respectively. However, for all three cases investigated the ultimate axial stress at 15.0% axial strain was about 225kPa (Figure 5.3a). Additionally, for dense sample the maximum angle of friction (ϕ'_{peak}) for the plane-strain condition was determined to be approximately 32° and was calculated from the peak stresses using Mohr circle of stress (Figure 5.4) as following:

$$\sin \phi'_{peak} = \frac{\sigma'_1 - \sigma'_3}{\sigma'_1 + \sigma'_3} \quad 5.1$$

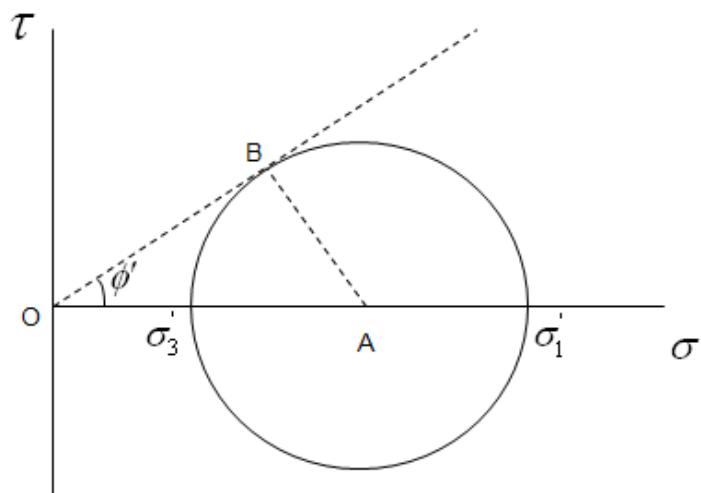


Figure 5.4 Mohr circle of stress

The plot of volumetric strain against axial strain (Figure 5.3b) shows that peak strength is related to the maximum rate of dilation. As peak strength normally corresponds to the maximum rate of dilation, a sample's angle of dilation (Ψ) is defined in terms of maximum and minimum principal strain increments $\delta\varepsilon_1$ and $\delta\varepsilon_3$. The dense sample had a maximum dilation angle (Ψ_{max}) at peak strength of approximately 15° compared with 0° for the loose sample. Additionally, all the simulations showed a dilation rate of about 0° beyond about 15.0% axial strain, indicating that critical state had been achieved. The maximum dilation angle was calculated in all instances using Mohr circle of strain increments as following:

$$\sin \Psi_{max} = \frac{\delta\varepsilon_1 + \delta\varepsilon_3}{\delta\varepsilon_1 - \delta\varepsilon_3} \quad 5.2$$

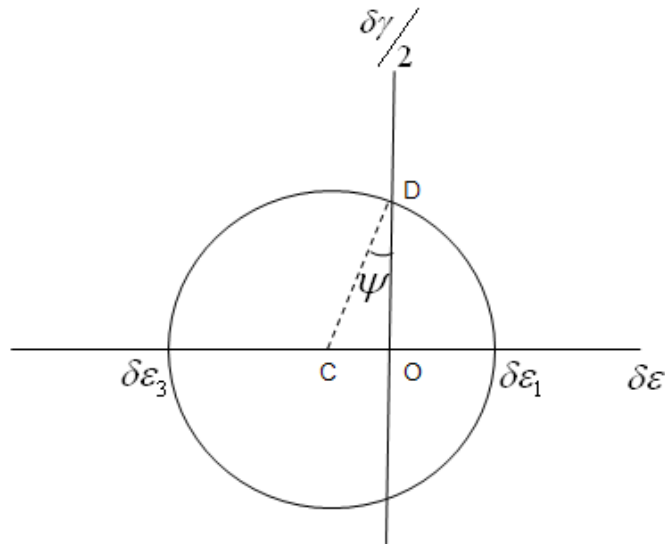
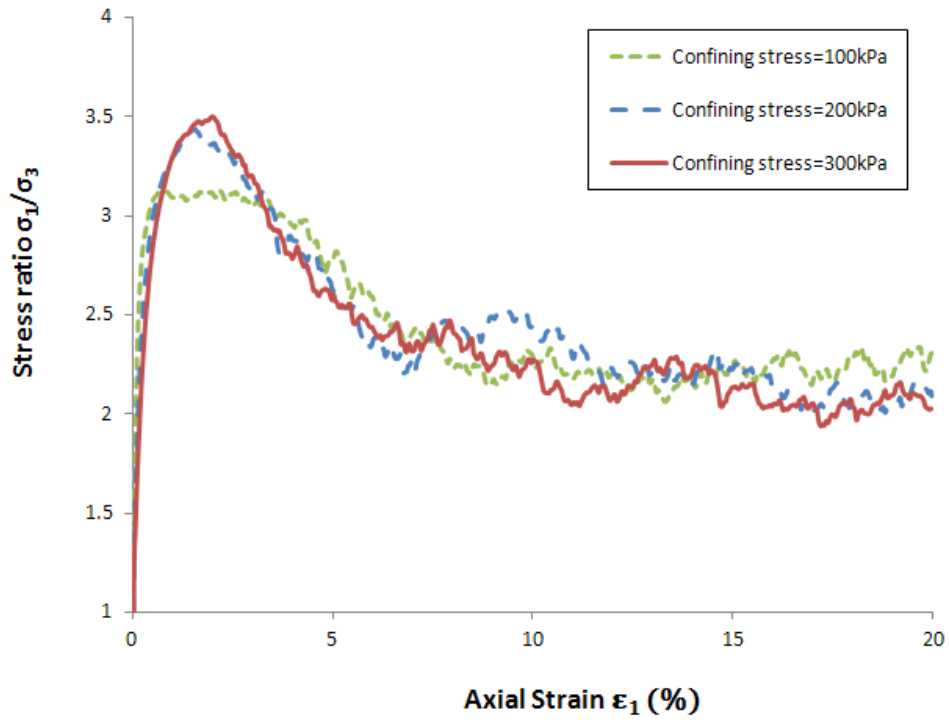


Figure 5.5 Mohr circle of strain increments

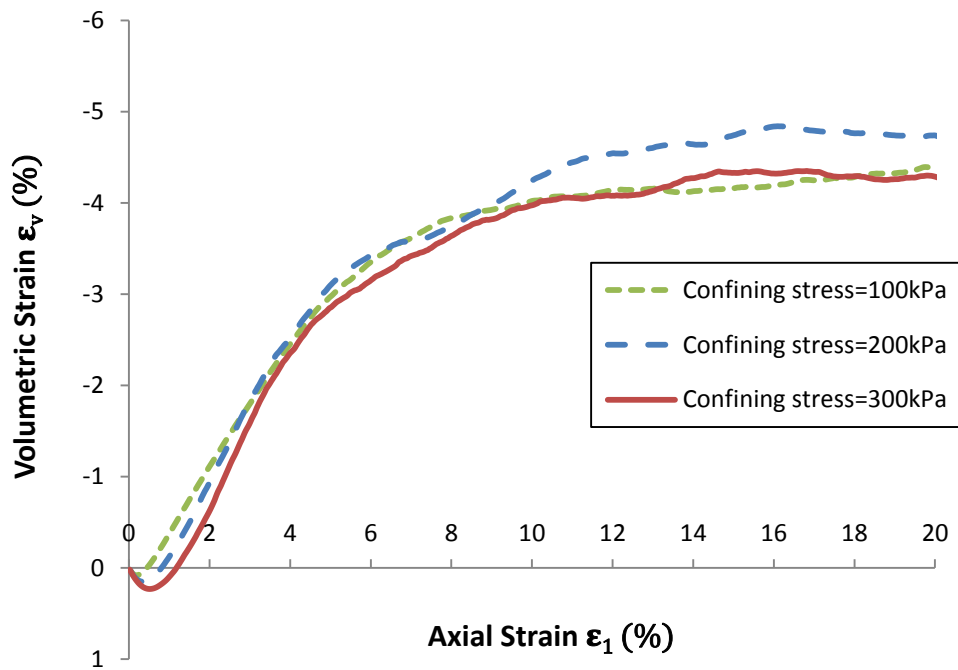
5.4 Influence of confining stress

It is widely reported that confining stress influences the stress-strain behaviour of granular materials. Wei-Feng et al. (2003) conducted triaxial tests on various granular soils to study the dilative behaviour. The results showed that dilation angles at low confining stress were much higher than theoretical values suggested by previous literature. Li (2006) performed two series of biaxial shearing tests with varying consolidation pressures to investigate the effect of the confining stress on the specimen response. The results showed that by increasing the confining stress, the specimen behaviour can change from a strain-hardening behaviour into a strain-softening one.

To investigate the effect of changing confining stress on the stress-strain behaviour, three biaxial test simulations (BT1, BT4 and BT5) were conducted on separate samples subjected to varying confining stress σ'_3 of 100kPa, 200kPa and 300kPa respectively. The initial porosity of all three samples comprising circa 13400 spheres was 0.37 and each sample had a particle friction coefficient of 0.5 at the shearing stage of the simulation. The effect of varying confining stress is shown Figure 5.6 where the outputs of the three simulations are illustrated and compared with regards to stress ratio (Figure 5.6a) and volumetric strain (Figure 5.6b).



(a)



(b)

Figure 5.6 Stress ratio and volumetric dilation for samples with different confining stress: (a) Stress ratio against axial strain (b) Volumetric strain against axial strain

In Figure 5.6a, stress ratio is plotted against axial strain for different confining stresses, it can be seen that there is not much difference in the peak stress ratio and the ultimate stress ratio (hence angle of friction) of the three samples at different confining stresses.

Also, from Figure 5.6b which shows volumetric strain against axial strain, it can be seen that there was an initial volumetric contraction which was followed by volumetric dilation. Additionally, it can be seen that there is little difference in the dilation of the three samples with increasing the confining stress and the values of the maximum angle of dilation are almost the same for the three samples. This is attributed to the absence of crushing in the model. In reality, at high stress levels crushing of particles could occur leading to reduced particle interlocking and hence reduced dilatancy.

5.5 Influence of particle shape

In order to investigate the effect of particle shape on the mechanical behaviour of granular materials, two simulations of the biaxial test (BT1 and BT6) were conducted on separate samples comprising spheres (1mm in diameter) and two-ball clumps each having a volume equivalent to that of the parent sphere. The shape of the clump is such that the two overlapping spheres are of equal size and such that the centre of each is on the surface of the other (i.e $d=R$) whereas $R=0.420\text{mm}$ is the radius for both spheres and d is the distance between the centres of two spheres in each clump. The aforementioned particle shapes for these simulations are shown in Figure 5.7 below.



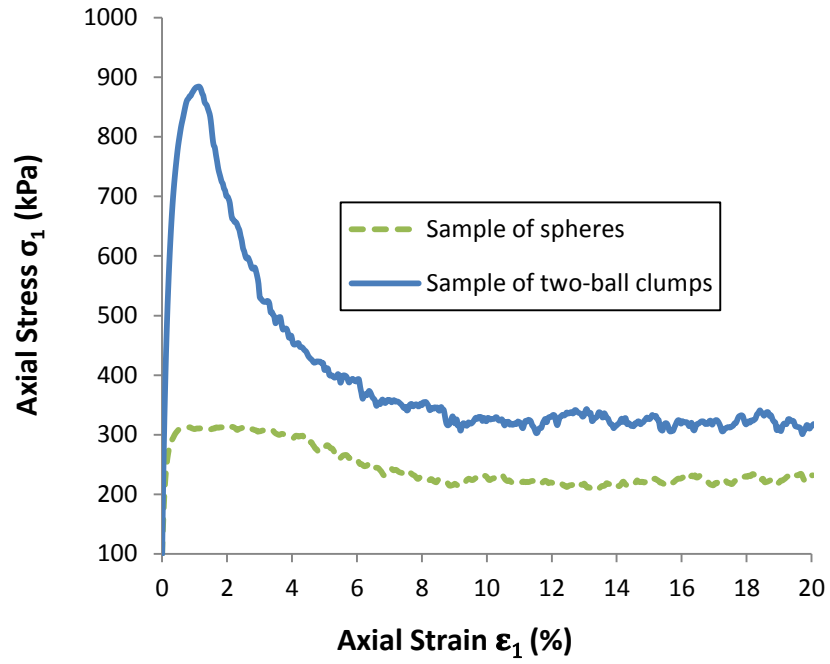
Figure 5.7 DEM of particle shape (a) Single sphere (b) Two-ball clumps of equivalent volume

The sample of spheres contained 13400 particles, whereas the sample of clumps comprised 26800 balls. Both samples were prepared to an initial porosity of 0.37 and subjected to a confining stress σ'_3 of 100kPa. Additionally, both had a friction coefficient of 0.5 at the shearing stage of the simulation.

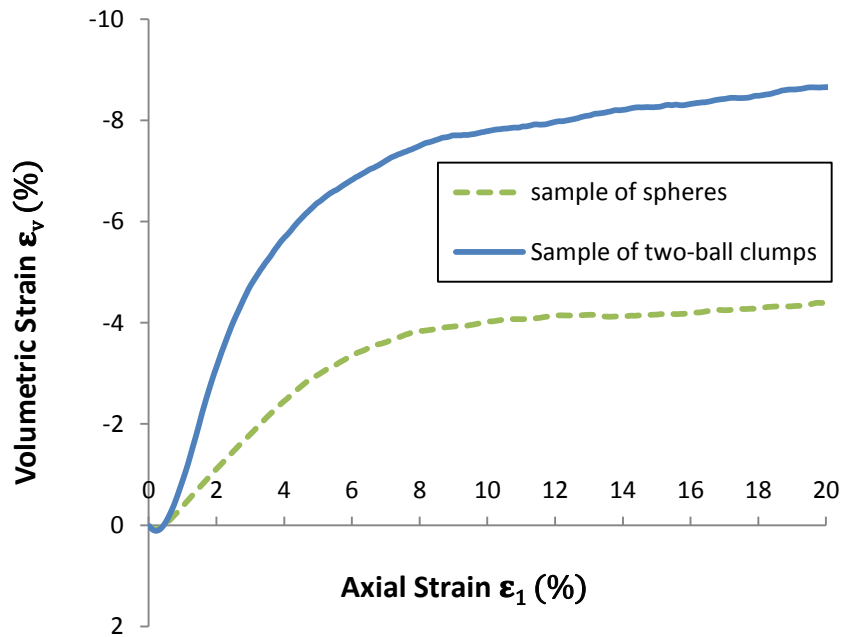
In Figure 5.8, axial stress and volumetric strain are plotted against axial strain for spheres and clumps. It is evident from Figure 5.8a that there is an increase in peak and ultimate axial stress as a consequence of changing the particle shape from a sphere to a two-ball clump. This behaviour is consistent with the creation of opportunity for interlocking and dilation (Mitchell, 1993). Figure 5.8a shows that using a sample of two-ball clumps results in a significantly higher peak stress of 880kPa in comparison to 310kPa for a sample of spheres. Consequently, this gives a higher peak friction angle (ϕ'_{peak}) for two-ball clumps of approximately 53° in comparison to a sample of spheres of approximately 32° . Furthermore, Figure 5.8a shows that the ultimate axial stress increased from 225kPa for a sample of spheres to about 325kPa for a sample of two-ball clumps. The increase in the peak and the ultimate axial stress for the sample of two-ball clumps is due to a considerable

degree of interlocking between particles which made it more difficult for the particles to rotate as compared to spheres.

With regards to Figure 5.8b it can be observed that the overall dilation of the sample during the simulation increased upon changing the particle shape from spheres to two-ball clumps. The volumetric strain increased by about 100% of its value (4%) when two-ball clumps were used. Consequently, this gives a higher value of maximum dilation angle (Ψ_{max}) for two-ball clumps of approximately 30° in comparison to a sample of spheres of approximately 15° . This indicates that the particle shape had a significant effect on the sample volume change, with increased dilatancy if particle shape is introduced.



(a)



(b)

Figure 5.8 Axial stress and volumetric dilation for samples with spheres and two-ball clumps:
(a) Axial stress against axial strain (b) Volumetric strain against axial strain

5.6 Influence of particle friction coefficient

Several researchers have shown that particle friction coefficient has a significant effect on the deformation behaviour of granular materials (Lee and Seed, 1967; Schanz and Vermeer, 1996). In this section, biaxial test simulations were conducted to investigate the effect of particle friction coefficient on the mechanical behaviour of granular materials using spheres and two-ball clumps.

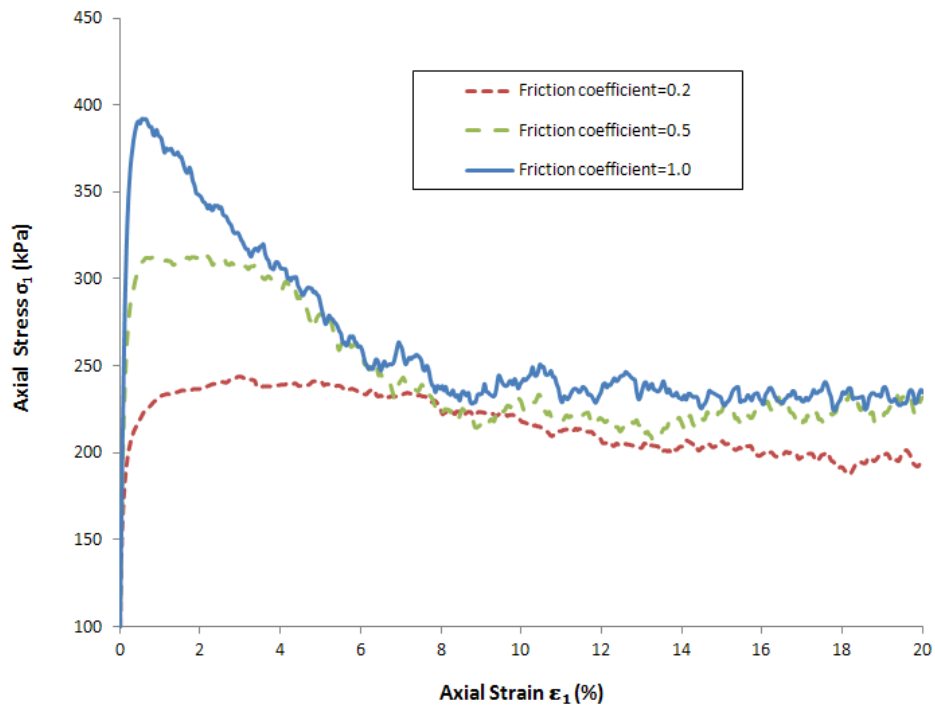
5.6.1 Spheres

Three biaxial test simulations (BT7, BT1 and BT8) were carried out on three samples with an initial porosity of 0.37, made possible by using a friction coefficient of 0 during particle generation and under isotropic compaction. The samples contained about 13400 particles were each subjected to a confining stress of 100kPa. At the shearing stage of the simulation the particle friction coefficients for the three samples were reset to 0.2, 0.5 and 1.0 respectively.

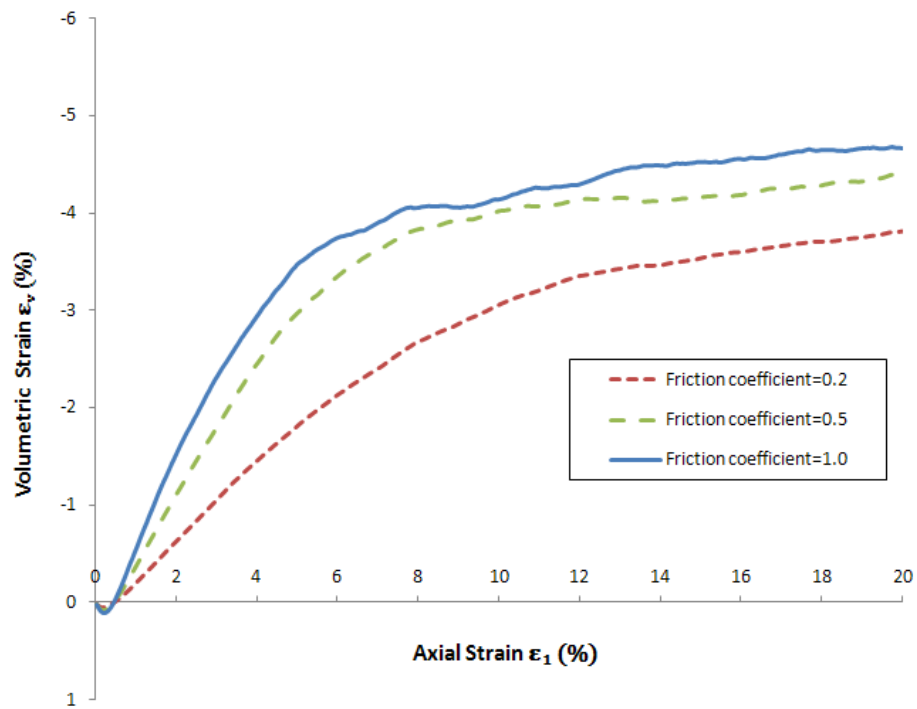
In Figure 5.9, varying the particle friction coefficient in the samples is shown to have a notable effect on peak axial stress and overall sample dilation at the end of the shearing process. The axial stress versus axial strain relationships of the samples using different friction coefficients are shown in Figure 5.9a. An examination of the respective stress-strain curves for each sample shows that increasing the particle friction coefficients resulted in progressively higher peak axial stresses. For the sample with a particle friction coefficient 0.2 the peak axial stress is about 240kPa; this value increased to about 310kPa for the sample with a friction coefficient of 0.5 and to about 390kPa for the sample with a friction coefficient of 1.0. However,

increasing the particle friction coefficient appeared to have very little notable influence on the ultimate stresses and hence the critical angle of friction of the three samples. This suggests that the critical angle of friction is independent of the particle friction coefficient, which is consistent with the results of (Skinner, 1969; Ni, 2003; Geng, 2010). However, increasing the particle friction coefficient might noticeably affect ultimate stress when particle size and particle shape are considered.

With regards to volumetric strain, Figure 5.9b shows that dilation increased when the friction coefficient increased. It is thought that when the particle friction coefficient is high, particles roll over rather than slide against other particles resulting in higher dilation (Skinner, 1969).



(a)



(b)

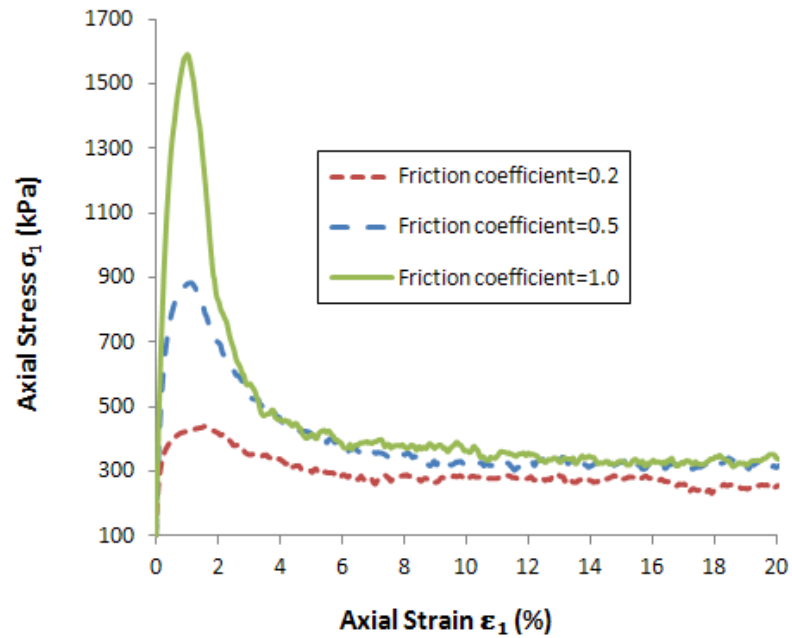
Figure 5.9 Axial stress and volumetric dilation for samples with spheres and different particle friction coefficients: (a) Axial stress against axial strain (b) Volumetric strain against axial strain

5.6.2 Two-ball clumps

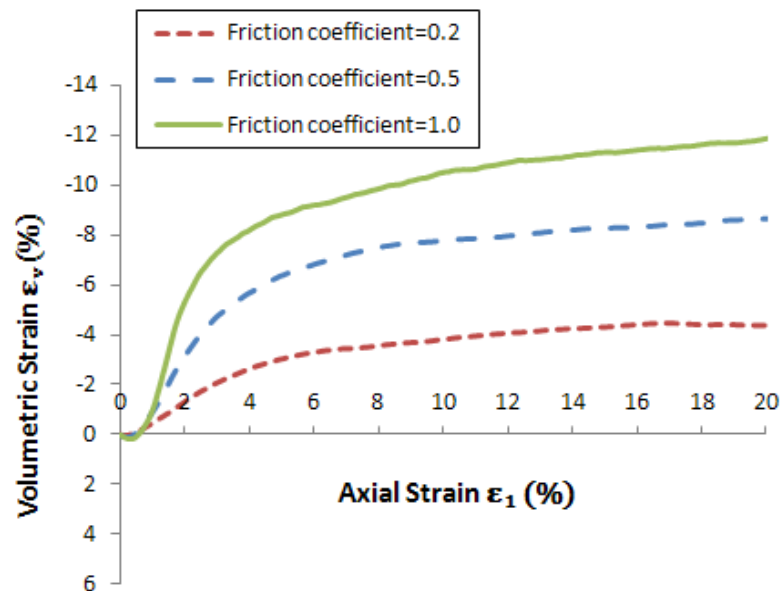
The individual spheres in the three previously examined samples (simulations BT7, BT1 and BT8) were replaced with two-ball clumps (Figure 5.7) of equivalent volume. As before, the samples were prepared to an initial porosity of 0.37 under a confining stress of 100kPa. In addition, identical particle friction coefficients were assigned to the three samples at the shearing stage of the simulation, and these are simulations BT9, BT6 and BT10. The effects of varying particle friction coefficients of the samples comprising two-ball clumps is seen in Figure 5.10 where it appears to have notably influenced the peak axial stress and the overall sample dilation at the end of shearing process. An inspection of the respective stress-strain curves shown in Figure 5.10a for each sample shows that increasing the particle friction coefficients resulted in progressively higher peak axial stresses. For the sample with a particle friction coefficient of 0.2, a peak axial stress of about 440kPa was recorded. This value increased to about 880kPa for the sample with friction coefficient of 0.5 and to about 1600kPa for the sample with friction coefficient of 1.0. Contrary to expectations, no significant change in the ultimate stress and critical angle of friction was evident for all three samples, possibly due to the use of particles with the same size of the simple shape clump.

From the axial strain-volumetric strain plot of Figure 5.10b it can be observed that the sample dilation increased when the friction coefficient increased. In general, the effect of particle friction coefficient for the sample containing two-ball clumps was found to be greater than for the sample containing only spheres. Whereas, the peak axial stress for the sample of spheres with particle friction coefficient 1.0 was about 390kPa; this value increased to about 1600kPa for the sample of two-ball clumps.

Also, the volumetric strain for the sample of spheres with particle friction coefficient of 1.0 was about 4.7%; this value increased to about 12% for the sample of two-ball clumps.



(a)



(b)

Figure 5.10 Axial stress and volumetric dilation for samples of two-ball clumps and different particle friction coefficients: (a) Axial stress against axial strain (b) Volumetric strain against axial strain

5.7 Conclusions

In this chapter, DEM was successfully implemented for the simulation of granular material behaviour in a plane-strain biaxial compression test. The stress-strain behaviour of cohesionless granular material under monotonic loading was studied and it was proven that several parameters have a significant effect on the soil stress-strain behaviour. Using different initial sample porosities was found to significantly influence peak strength and dilation. Peak and critical state stress ratio were found to be almost the same with increasing confining stress. In addition, there is not much difference in the overall dilation and the maximum angle of friction for samples subjected to increasing confining stresses as crushing had not been implemented. It has been shown that using a two-ball clump increases the peak and critical state angle of friction and dilation angle compared to using spheres. The two-ball clumps are thought to have provided a greater degree of particle interlock, thereby making it more difficult for particles to rotate. The peak friction angle and the maximum dilation angle for the samples of spheres and two-ball clumps increased when the particle friction coefficient was increased, with higher values recorded for the sample of two-ball clumps. However, the critical angle of friction was found to be independent of the particle friction coefficient when using spheres or two-ball clumps (higher values for the clumps – see Table 5.2). The simulation results are needed to obtain the parameters for the development of a constitutive model for the granular material. The results obtained from the simulations are also consistent with previous DEM results by Geng (2010) for investigating the effect of initial sample porosity, particle shape and particle friction coefficient on the mechanical behaviour of granular materials, lending further credibility to the methodology adopted.

CHAPTER 6

ANALYTICAL SOLUTION OF THE CPT AND COMPARISON WITH THE DEM SIMULATIONS

6.1 Introduction

Over the last few years, geotechnical researchers have made good progress in furthering understanding on the mechanics underlying cone penetration in cohesive soils. In contrast, progress has been slow in developing precise methods capable of analysing and predicting the behaviour of cohesionless soils subjected to cone penetration. This is mainly because of the dilatancy sand tends to exhibit when sheared, which is not the case when compared to the behaviour of undrained clay. Consequently, to gain further insight into the behaviour of sand during cone penetration, large laboratory chamber testing has been widely implemented (Parkin and Lunne, 1982; Houlsby and Hitchman, 1988; Been et al., 1987; Ghionna and Jamiolkowski, 1991) to establish empirical correlations between cone results and sand properties. Additionally, theories such as the bearing capacity theory (Durgunoglu and Mitchell, 1975) and cavity expansion theory (Vesic, 1977; Yu and Mitchell, 1998; Salgado et al., 1997) are widely applied in the analysis of deep cone penetration in sand.

Cone penetration testing of sand is assumed to occur under fully drained conditions and therefore the methods for analysis considered henceforth are those based on the

premise that excess pore pressures are not generated as a result of cone penetration. Friction angle is one of many soil parameters that can be determined from cone tip resistance in sand. In this regard, various correlations are often proposed with most of them based either on bearing capacity analysis or cavity expansion theory (Yu, 2004).

In this chapter, the continuum parameters obtained from biaxial test simulations (Chapter 5) are used to derive an analytical solution for cone tip resistance using a combined cylindrical-spherical cavity expansion method. The analytical solution will be compared with some DEM simulations of cone tip resistance reported in Chapter 4.

6.2 Cavity expansion method

The similarity between cavity expansion and cone penetration was first reported by Bishop et al. (1945) who noticed that the pressure required to create a deep hole in an elastic-plastic medium is proportional to that necessary to expand a cavity of the same volume under the same conditions. Their work was furthered by Yu and Mitchell (1996) and Yu and Mitchell (1998) who suggested that cone tip resistance could be related to cavity (mainly spherical cavities) limit pressures. They studied proposals offered (see Figure 6.1) by several researchers, including Landay and Johnston (1974) and Vesic (1977) and concluded that theoretical (analytical or numerical) limit pressure solutions for cavity expansion in soils were achievable.

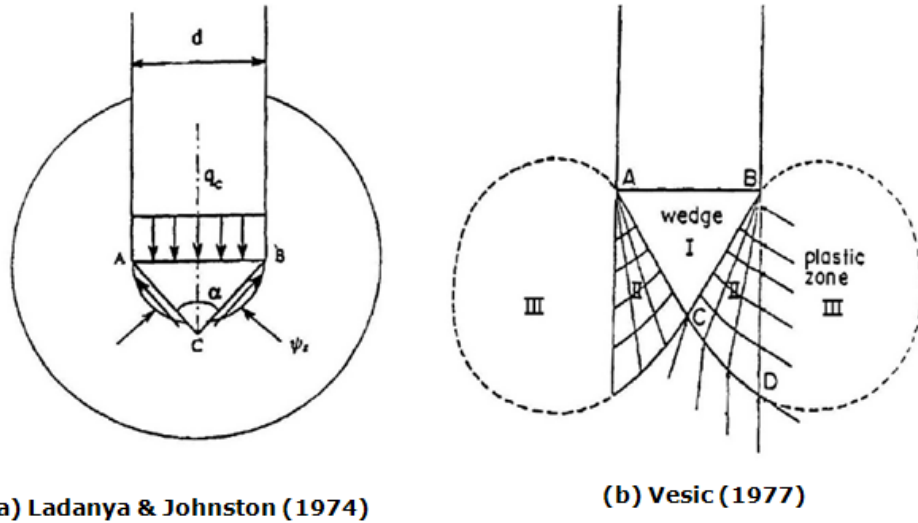


Figure 6.1 Mechanisms linking cone resistance with cavity limit pressures (Yu and Mitchell, 1998)

Vesic (1977) suggested that the cone tip resistance could be estimated from a spherical cavity limit pressure for the failure mechanism shown in Figure 6.1b. This assumption resulted in the proposal of a simple equation below for a cone factor N_q :

$$N_q = \left[\frac{1 + 2K_0}{3 - \sin \phi} \right] \exp \left[\left(\frac{\pi}{2} - \phi \right) \tan \phi \right] \tan^2 \left(\frac{\pi}{4} + \frac{\phi}{2} \right) (I_{rr})^n \quad 6.1$$

where

ϕ is the drained soil friction angle

K_0 is the coefficient of earth pressure at rest, given by equation 6.2

I_{rr} is the reduced rigidity index, given by equation 6.3

$$K_0 = \frac{\sigma'_{h0}}{\sigma'_{v0}} \quad 6.2$$

$$I_{rr} = I_s / (1 + I_s \epsilon_v) \quad 6.3$$

where

σ'_{h0} is the initial horizontal effective stress

σ'_{v0} is the initial vertical effective stress

ε_v is the average volumetric strain estimated in the plastic region during deformation

I_s is the rigidity index, given by equation 6.4

n is parameter, given by equation 6.5

$$I_s = G / (p'_0 \tan \phi) \quad 6.4$$

$$n = 4 \sin \phi / [3(1 + \sin \phi)] \quad 6.5$$

where

G is the shear modulus

p'_0 is the initial mean effective stress

After applying Vesic's approach to results stemming from a number of chamber tests, Mitchell and Keaveny (1986) proposed that cone tip resistances in sand could also be closely modelled for sands with low reduced rigidity indices (i.e. more compressible soils). However, it can be argued that as dilation was not considered in Vesic's correlation, this solution cannot be used to model cone penetration in medium dense to very dense sands where dilation is significant. Extending Vesic's method further, Salgado (1993) and Salgado et al. (1997) utilised stress rotation analysis to relate cone tip resistance to a cylindrical cavity limit pressure as illustrated in Figure 6.2.

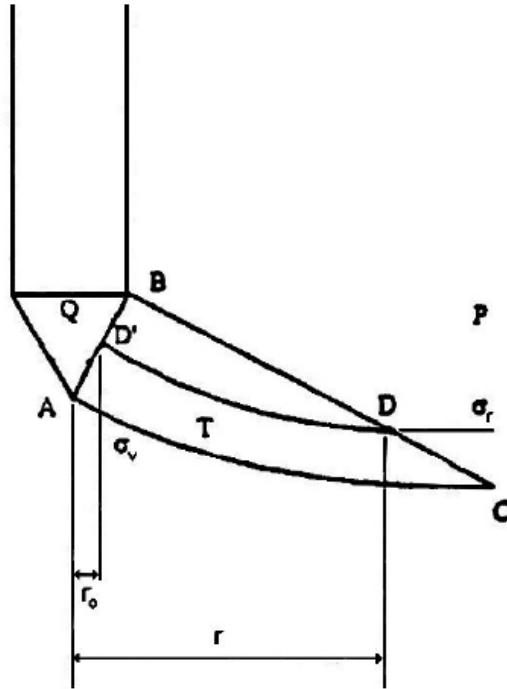


Figure 6.2 Linking cone resistance with cylindrical cavity limit pressure (Salgado, 1993)

Depending on a number of simplifying assumptions, cone resistance q'_c is linked to the effective cylindrical cavity limit pressure as follows:

$$q'_c = 2 \exp(\pi \tan \phi) \frac{[(1 + C)^{1+l} - (1 + l)C - 1]}{C^2 l (1 + l)} P'_{lc} \quad 6.6$$

where

P'_{lc} is the effective cylindrical cavity limit pressure

l is quantity determined numerically

C is parameter for a standard 60 degree cone, given by equation 6.7

$$C = \sqrt{3} \exp\left(\frac{\pi}{2} \tan \Psi\right) \quad 6.7$$

where

Ψ is the soil dilation angle

Using the theoretical correlations given by equations 6.6 and 6.7, Salgado et al. (1997) were able to predict measured cone resistances for a large number of cone penetration tests conducted in a large number of calibration chambers. They found the correlations to perform reasonably well, typically, predicting measured cone tip resistances within 30%.

6.3 Combined cylindrical-spherical cavity expansion method

As illustrated in the previous section (6.2), the cavity expansion method assumes that cone tip resistance is related through theoretical or semi-analytical considerations, to either spherical or cylindrical cavity limit pressure. This investigation uses a recently developed method (Yu, 2004) that combines the cylindrical and spherical cavity expansion solutions to estimate cone tip resistance. The novel proposal was implemented using the two-step approach described below:

- 1) Estimation of the size of the plastically deforming zone around the cone using the cylindrical cavity solution for the size of the plastic region.
- 2) Calculation of the cone tip resistance from the outputs in (1) and by using the spherical cavity expansion theory.

This method was encouraged by a recent finite element study of cone penetration in sand (Huang et al., 2004). They proposed that the plastic zone created behind the cone and around the shaft of a penetrometer is similar to that predicted by applying cylindrical cavity expansion theory. However, the shape of the elastic-plastic boundary around the cone tip and face is assumed to be circular or elliptical as shown in Figure 6.3.

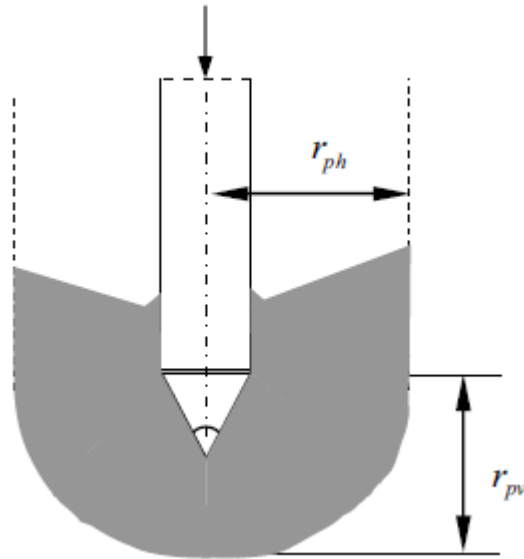


Figure 6.3 Plastic zone around a cone in sand (Huang et al., 2004)

By applying the above-mentioned assumption and using the cavity expansion solutions in Mohr-Coulomb materials, as derived by Yu (2000) and Yu and Carter (2002), cone tip resistance in a purely frictional soil can be obtained using the following expression:

$$\frac{q'_c}{p'_0} = \frac{3\alpha'}{2 + \alpha'} \left(F \frac{c}{a} \right)^{\frac{2(\alpha'-1)}{\alpha'}} \quad 6.8$$

where

F is the plastic zone shape factor and taken to be unity, in the event of a circular plastic zone around the cone (so that $r_{ph} = r_{pv}$) or otherwise less than 1.0. By applying more numerical studies, F is assumed to be between 0.7-0.8 (Yu, 2004).

The ratio $\frac{c}{a}$ is the relative size of the plastic zone generated as a result of expanding a cylindrical cavity from zero radius. This is determined using the simple non-linear equation for a purely frictional soil derived by Yu (2000):

$$1 = \gamma \left(\frac{c}{a}\right)^{\frac{\alpha'-1}{\alpha'}} + [2\delta - \gamma] \left(\frac{c}{a}\right)^{\frac{\beta'+1}{\beta'}} \quad 6.9$$

In which γ , δ , α' , β' , s' and x are constant derived parameters defined in equations 6.10 to 6.15 as follows:

$$\gamma = \frac{\alpha' \beta' s'}{\alpha' + \beta'} \quad 6.10$$

$$\delta = \frac{(\alpha' - 1)p'_0}{2(1 + \alpha')G} \quad 6.11$$

$$\alpha' = \frac{1 + \sin \phi}{1 - \sin \phi} \quad 6.12$$

$$\beta' = \frac{1 + \sin \Psi}{1 - \sin \Psi} \quad 6.13$$

$$s' = \frac{x(1 - \alpha')}{\alpha' \beta'} \quad 6.14$$

$$x = \frac{(1 - \nu)\alpha' p'_0}{((\alpha')^2 - 1)G} \left\{ \left[\beta' - \frac{\nu}{1 - \nu} \right] + \frac{1}{\alpha'} \left[1 - \frac{\nu \beta'}{1 - \nu} \right] \right\} \quad 6.15$$

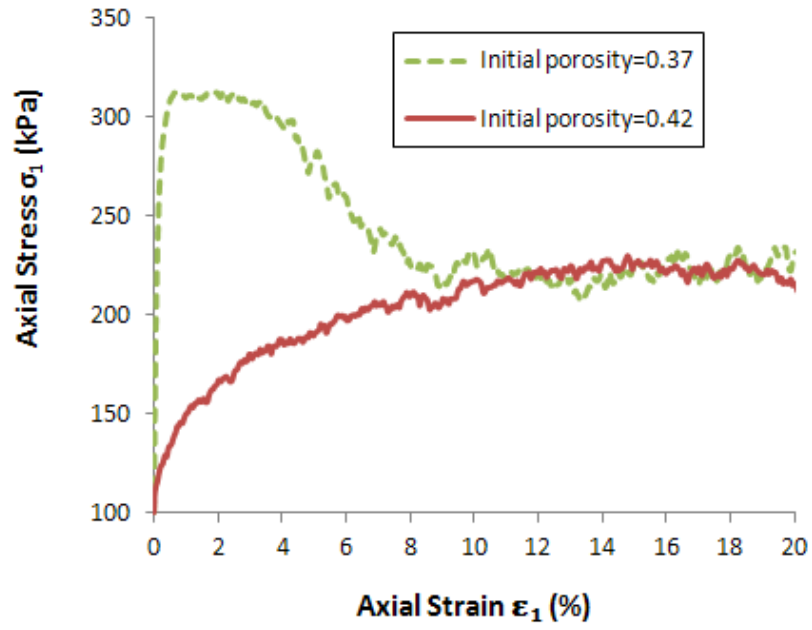
where

ν is the Poisson's ratio.

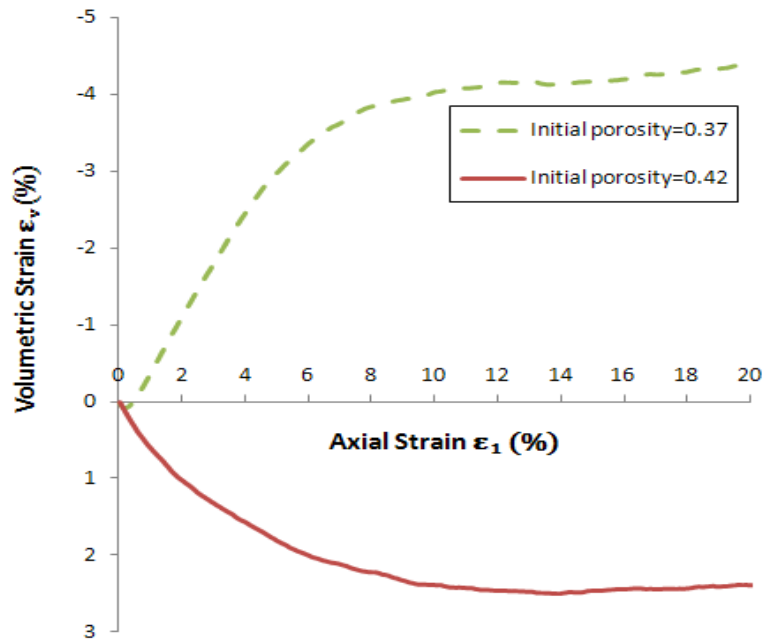
6.4 DEM simulation of biaxial and CPT tests

The DEM simulation of the biaxial test was illustrated in Chapter 5, where the effects of initial porosity, confining pressure, inter-particle coefficient of friction and particle shape on the macro-mechanical behaviour of granular material were successfully studied. Nevertheless, it should be noted that DEM simulation of the macro behaviour of granular materials is not a straight forward undertaking due to the complexity in selecting their micro-properties, which largely govern macro behaviour. These material properties were however required to develop the analytic CPT solution and to facilitate subsequent comparisons with DEM simulations of CPT, to which end the DEM simulations of the biaxial test were conducted. Identical particle parameters and initial conditions were utilised for both the biaxial test simulations and CPT simulations.

The modelling procedure and the sample preparation were the same as presented in Chapter 5. Two simulations were carried out on two samples comprising spheres of 1mm diameter size (the size that would be next to the cone in the most recent DEM simulations) and prepared with initial porosities of 0.37 (dense) and 0.42 (loose) respectively. Both samples were subjected to identical confining stresses of 100kPa. Figure 6.4 shows some of the salient aspects of stress-dilatancy behaviour of a granular assembly sheared biaxially for the two samples.



(a)



(b)

Figure 6.4 Axial stress and volumetric dilation for samples with two different initial porosities:
 (a) Axial stress against axial strain (b) Volumetric strain against axial strain

From the stress-strain curve of Figure 6.4a it is gleaned that dense sample experienced a peak axial stress of 310kPa at approximately 2% axial strain, and subsequent softening as the sand underwent dilations. On the other hand, the loose sample attained a maximum axial stress of 225kPa at approximately 15% axial strain. The relationship between volumetric strain and axial strain for the dense sample is characterised by an increase in its volume upon shearing as depicted in Figure 6.4b. The converse is true for the loose sample for which increasing the axial stress was accompanied by a reduction in volumetric strain.

The DEM simulation of the cone penetration test was discussed in detail in Chapter 4. The modelling procedure and the sample preparation were the same as presented in Chapter 4. Two simulations were carried out on two samples of spheres with particle configuration as in simulation K. Both samples were prepared with different initial porosity 0.37 (dens) and 0.42 (loose) respectively and subjected to identical isotropic stresses of 100kPa each. Figure 6.5 shows the effect of initial porosity had on tip resistance results. It can be clearly observed that the ultimate tip resistance of the sample with initial porosity 0.42 of about 1MPa increased to about 3MPa when the sample of reduced initial porosity 0.37 was investigated.

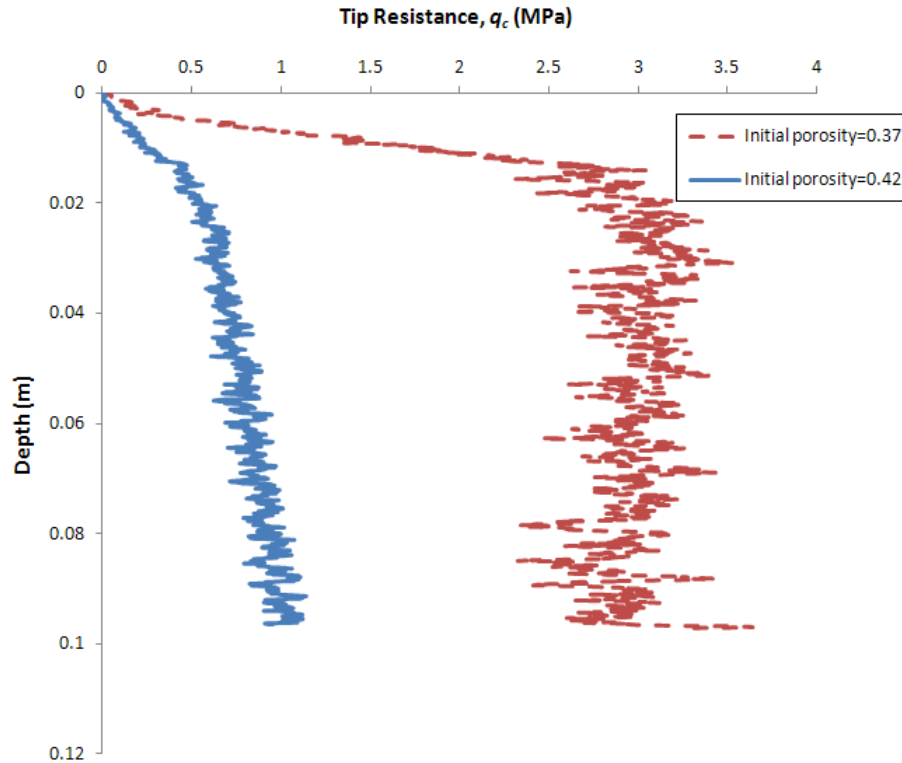


Figure 6.5 Influence of initial porosity on tip resistance under initial isotropic stresses of 100kPa

6.5 Analytical solution for CPT using a combined cylindrical-spherical cavity expansion method

It was previously mentioned that combining cylindrical and spherical cavity expansion solutions to estimate cone tip resistance occurs in two stages (see section 6.3). Theoretically the combined cylindrical-spherical cavity expansion solution is characterised by specific material properties. In order to determine these material properties for the analytical solutions sought, DEM simulations of biaxial tests were conducted as previously described (Section 6.4).

6.5.1 The procedure for obtaining an analytical CPT solution

Obtaining an analytical solution for CPT using combined cylindrical-spherical cavity expansion method required the determination of specific material properties. Firstly, the material properties E , ν , ϕ and Ψ were determined and the initial mean effective pressure p'_0 was known to be 100kPa. Secondly, the constant derived parameters: γ , δ , α' , β' , s' and x were determined as per equations (6.10 to 6.15). The ratio $\frac{c}{a}$ was then evaluated with equation 6.9 using a numerical programme (MATLAB). Finally, tip resistance q'_c was calculated using equation 6.8.

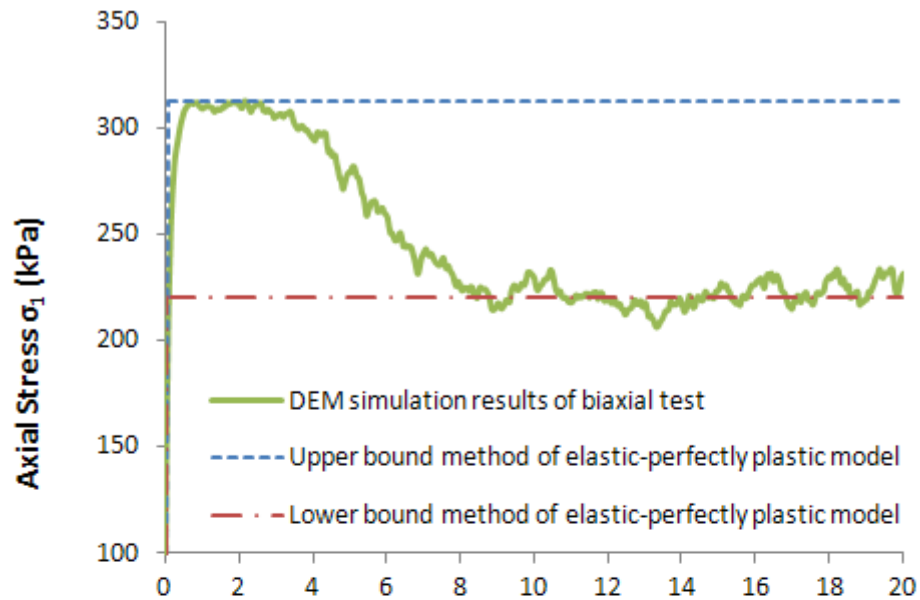
6.5.2 Results and discussion

The soil under consideration was assumed to be an isotropic dilatant elastic-perfectly plastic material that obeyed the Mohr-Coulomb yield criterion. It is not easy to fit the complete real stress-strain behaviour of sandy soil agreeably with a simple elastic-perfectly plastic model. Therefore, upper bound and lower bound solutions have been used to describe the investigated soil behaviour and it is assumed that its real stress-strain behaviour lies within these boundaries.

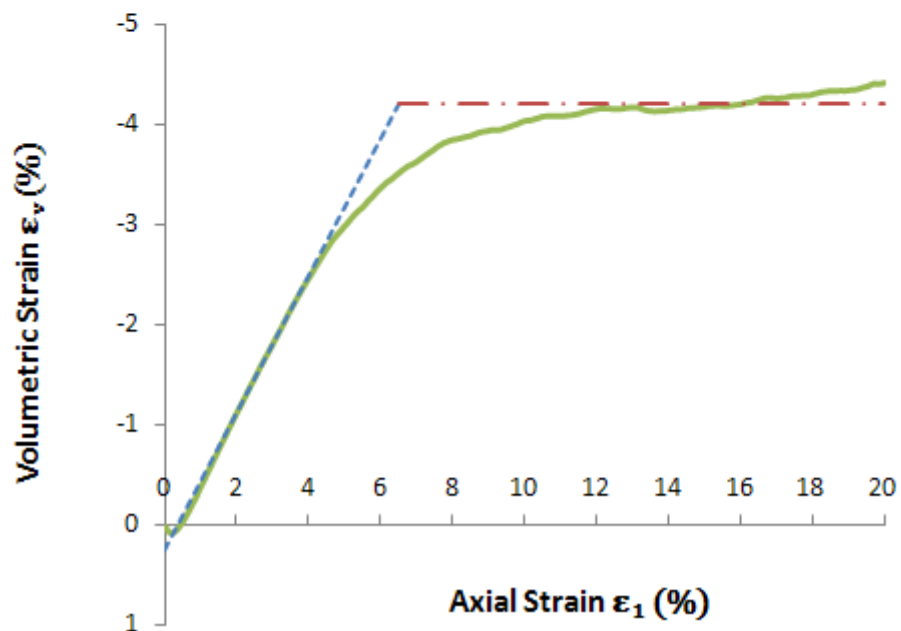
For the sample with initial porosity 0.37, the upper bound and lower bound are selected as elastic perfectly plastic model based on the biaxial test simulation results in Figure 6.4. These models are represented by two straight lines shown in Figure 6.6.

The upper bound in Figure 6.6a was coincided with the maximum axial stress and formed on the basis of the soil initial stiffness and peak axial stress value and used to calculate peak angle of friction. The lower bound was located where the critical axial

stress occurred and fixed with consideration to the soil initial stiffness and critical axial stress and used to calculate critical angle of friction. In Figure 6.6b the upper bound was used to calculate maximum angle of dilation which happened at peak axial stress, whereas the sample critical angle of dilation is zero at a critical state.



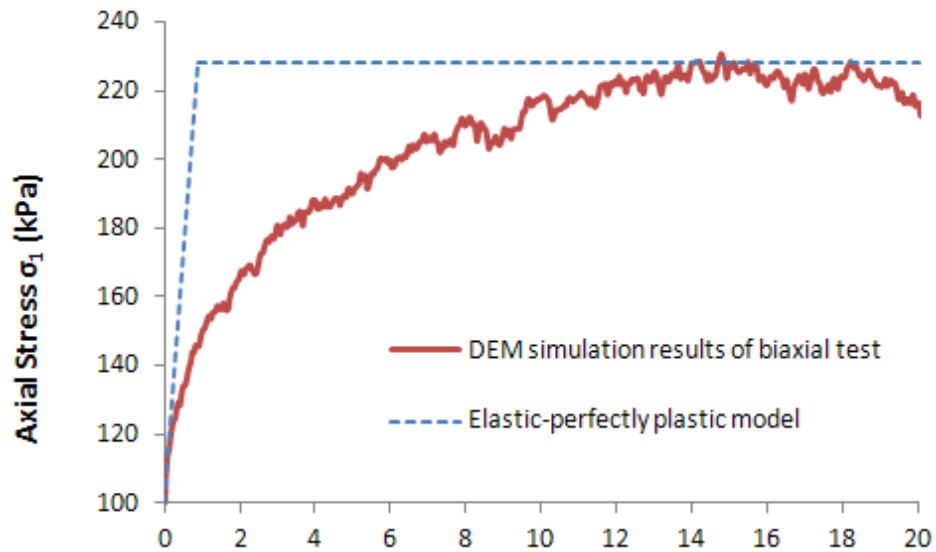
(a)



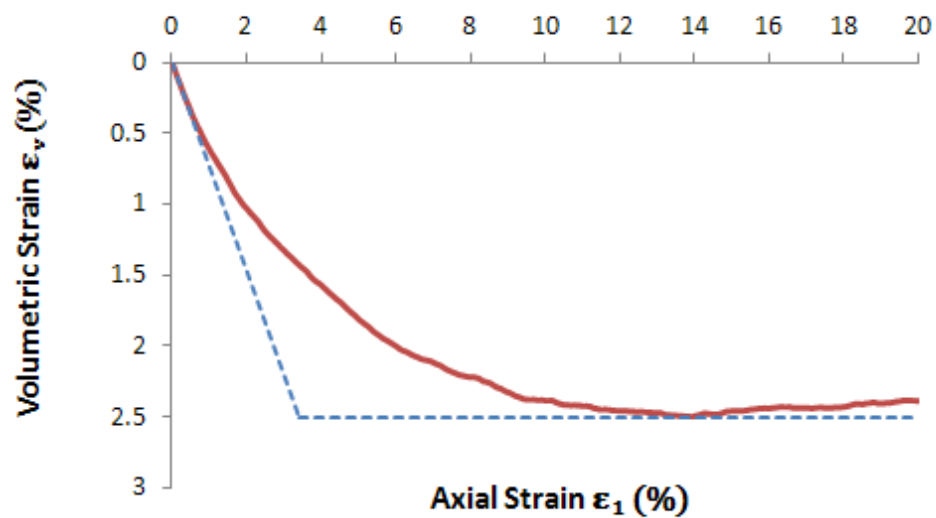
(b)

Figure 6.6 Upper and lower bounds for sample with initial porosity 0.37 in the DEM simulation

As no prior peak axial stress was observed for the sample with initial porosity 0.42 during shearing, only one elastic-perfectly plastic model was necessary. A single limit solution governed by the sample initial stiffness and peak (critical) axial stress value was formed as seen in Figure 6.7a and used to determine peak (critical) angle of friction, and the angle of dilation is zero (at critical state).



(a)



(b)

Figure 6.7 Elastic-perfectly plastic model for sample with initial porosity 0.42 in the DEM simulation

Other associated macroscale parameters of the granular material were also obtained from the following equations:

Young's modulus:

$$E = \frac{\delta\sigma_1}{\delta\varepsilon_1} \quad 6.16$$

Poisson's ratio:

$$\nu = -\frac{\delta\varepsilon_3}{\delta\varepsilon_1} \quad 6.17$$

It must be highlighted that the soil's Young's modulus was estimated from the unloading-reloading (hysteresis) loop in the elastic region of the axial stress-strain curve shown in Figure 6.8, while the Poisson's ratio was calculated from the initial axial-volumetric strain curve shown in Figure 6.9. The Young's modulus estimated from the initial curve was higher than that from unloading-reloading due to the effect of soil disturbance and using unloading-reloading loop will partially eliminate this effect and gives an appropriate Young's modulus value.

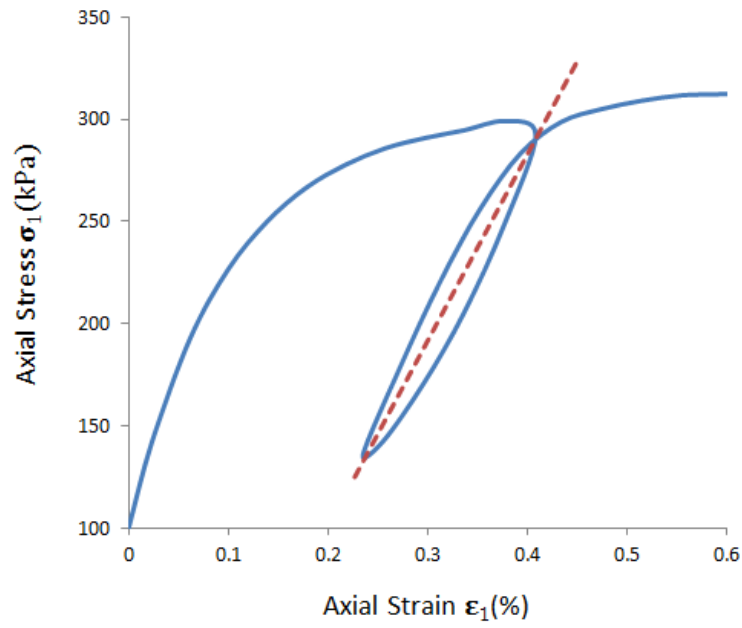


Figure 6.8 Young's modulus from axial stress-strain curve

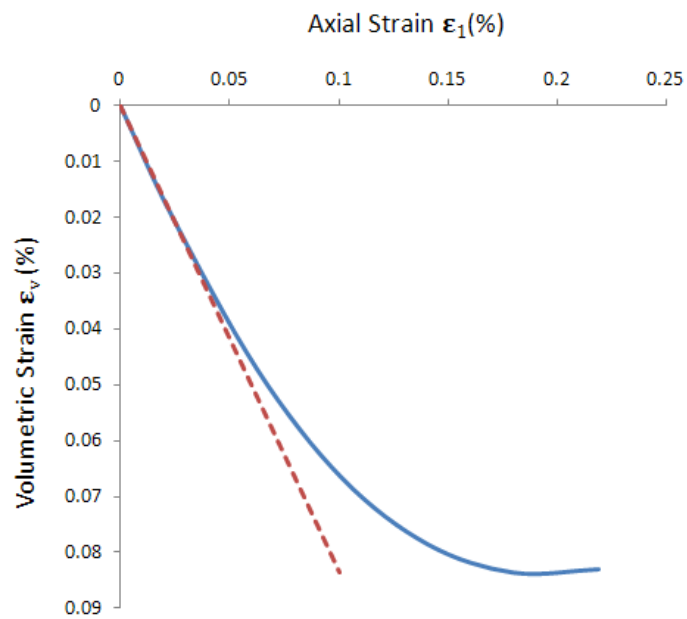


Figure 6.9 Poisson's ratio from axial-volumetric strain curve

Through the application of the above mentioned equations and the Mohr-Coulomb criterion, the material properties of each model considered were calculated, as shown in Table 6.1.

Table 6.1 The material properties for analytical solution of CPT and analytical and DEM tip resistance values

Model	Initial porosity	E (MPa)	ν	ϕ' (D)	Ψ (D)	p'_0 (kPa)	$\frac{c}{\bar{\alpha}}$	F	q'_c (MPa) Analytical	q'_c (MPa) DEM
U-D-S	0.37	62	0.2	32	15	100	40.4	1.0	31.2	3.0
U-D-S	0.37	62	0.2	32	15	100	40.4	0.7	19.1	3.0
U-D-S	0.37	62	0.2	32	15	100	40.4	0.5	12.0	3.0
L-D-S	0.37	62	0.2	22	0	100	21.5	1.0	4.4	3.0
L-D-S	0.37	62	0.2	22	0	100	21.5	0.7	3.0	3.0
L-D-S	0.37	62	0.2	22	0	100	21.5	0.5	2.1	3.0
E-L-S	0.42	20	0.2	22	0	100	12.2	1.0	2.4	1.0
E-L-S	0.42	20	0.2	22	0	100	12.2	0.7	1.6	1.0
E-L-S	0.42	20	0.2	22	0	100	12.2	0.5	1.1	1.0

U-D-S: Upper bound method of elastic-perfectly plastic model for sample consisting of spherical particles (dense sample with initial porosity=0.37)

L-D-S: Lower bound method of elastic-perfectly plastic model for sample consisting of spherical particles (dense sample with initial porosity=0.37)

E-L-S: Elastic-perfectly plastic model for sample consisting of spherical particles (loose sample with initial porosity=0.42)

6.5.3 Comparison of DEM results and analytical solutions

The results presented in Table 6.1 allow a comparison of the analytical solution results of CPT using a combined cylindrical-spherical cavity expansion method and DEM simulation results for a sample of spheres to be made. It can be seen that for the sample with initial porosity of 0.37, the upper bound solution led to an analytical tip resistance value of 31.2MPa for a plastic zone shape factor $F=1$. However, this

value decreased to 19.1MPa for $F=0.7$ and to 12.0MPa for $F=0.5$. On the other hand, when the lower bound solution was considered for the same sample, it resulted in an analytical tip resistance value of 4.4MPa for a plastic zone factor $F=1$, this value decreased to 3.0MPa for $F=0.7$ and to 2.1MPa for $F=0.5$. The 3MPa tip resistance as obtained from DEM simulation for the sample with initial porosity 0.37 falls in-between the upper bound and lower bound values of the analytical solutions for $F=0.5$.

For the sample with an initial porosity of 0.42, only one elastic-perfectly plastic model used to describe the soil behaviour, resulting in an analytical tip resistance value of 2.4MPa for a plastic zone factor $F=1$. However, this value decreased to 1.6MPa for $F=0.7$ and to 1.1MPa for $F=0.5$. In this regard, the tip resistance value of 1MPa obtained from DEM simulation for the sample with initial porosity 0.42 is consistent with the analytical solution for $F=0.5$ to within 10%.

Overall, the results suggest DEM can be used to simulate cone penetration tests in granular materials, and have shown reasonable agreement with theoretical analytical solutions. The process highlighted the important effect of plastic zone shape factor on the magnitude of tip resistance and a value for F of 0.5 gives an appropriate analytical tip resistance value compared with the numerical one.

6.6 Conclusions

This chapter examined DEM simulations of cone penetration tests in granular material. Through further simulations of biaxial tests, the properties of a cohesionless granular material were obtained from the resulting stress-strain curves. Analytical solutions to the cone penetration test were obtained from a combined cylindrical-spherical cavity expansion method that used the outputs of the biaxial test simulations. Advantages of the analytical approach were demonstrated and their outputs compared with DEM simulation of cone penetration tests. A comparison of the DEM simulation of tip resistance results to theoretical tip resistance results used in this study showed both approaches to be in good agreement.

The numerical simulations shed light on the mechanical behaviour of the granular materials under cone penetration on a micro to macro scale. On the other hand, the analytical method provided insight on granular material mechanical behaviour on a macro level. The DEM simulations have been shown to be capable of precisely capturing the macro scale response of a granular material subjected to cone penetration.

CHAPTER 7

DISCRETE ELEMENT MODELLING OF PARTICLE CRUSHING

7.1 Introduction

There are two methods for modelling particle crushing in DEM. The first approach treats each granular particle as a porous agglomerate built by bonding smaller particles with finite bond strengths (Robertson, 2000; Cheng et al., 2004; Lim and McDowell, 2005; Bolton et al., 2008). The second approach is to replace broken particles with an equivalent group of smaller fragments (Tsoungui et al., 1999; Lobo-Guerrero and Vallejo, 2005; Ben-Nun and Einav, 2010; McDowell and de Bono, 2013). Adopting the first approach, McDowell and Harireche (2002) used PFC^{3D} to simulate the breakage of silica sand with the crushable agglomerates particles. This research showed that the sand particle strengths followed the Weibull distribution, such that the correct average strength of agglomerates could be reproduced as a function of size and the correct statistical distribution of strengths could be produced for a given size. For the second approach, Lobo-Guerrero and Vallejo (2005) and (2007) utilised the PFC^{2D} program in the DEM of the penetration resistance of driven piles in an unbreakable granular material and a crushable granular material. Their results showed that a soil comprising weak granular particles has a lower penetration resistance than a similar soil composed of uncrushable particles. However, in their

model, mass is not conserved and so there is a loss of solid volume and an increase in void volume each time a particle breaks.

McDowell and de Bono (2013) have also applied PFC^{3D} to model one-dimensional compression in an oedometer for a large number of single particles, with conserving mass. They controlled particle crushing by the octahedral shear stress generated in individual particles due to the multiple contacts and a Weibull distribution of strengths. They investigated the effect of fragments distribution on the particle size distribution and the slope of the normal compression line and found the compression index is solely a function of the average strength of the particles as a function of size. In this chapter, the particle fracture mechanism adopted by McDowell and de Bono (2013) is applied to investigate particle crushing phenomena during cone penetration tests in a calibration chamber.

7.2 Modelling procedure

A 30° segment calibration chamber was filled with three zones of particles in ascending order of size away from the cone penetrometer to minimise the number of particles involved in the simulation and hence the computational time. Half the chamber (zone 1, 75 mm wide) was filled with 2 mm particles adjacent to the cone penetrometer and this was followed by zone 2, comprising a 20 mm band of 3 mm particles. The remainder of the chamber (zone 3, 55 mm wide) was filled with 4 mm particles as shown in Figure 7.1. The initial small particle size was chosen to be 2mm to reduce computational time as smaller particle sizes will be produced after breakage. The particles used were spheres and allowed to rotate freely. For simplicity a linear-elastic contact law was chosen for the simulations. The sample was

generated via radius expansion to an initial porosity 0.3543. All the particles were assigned a constant mass before and after they were crushed, in order to decrease computational time. An isotropic compression stress was applied to the sample before and during the penetration as described in Chapter 4. The cone penetrometer used in this simulation is also the same as described in Chapter 4.

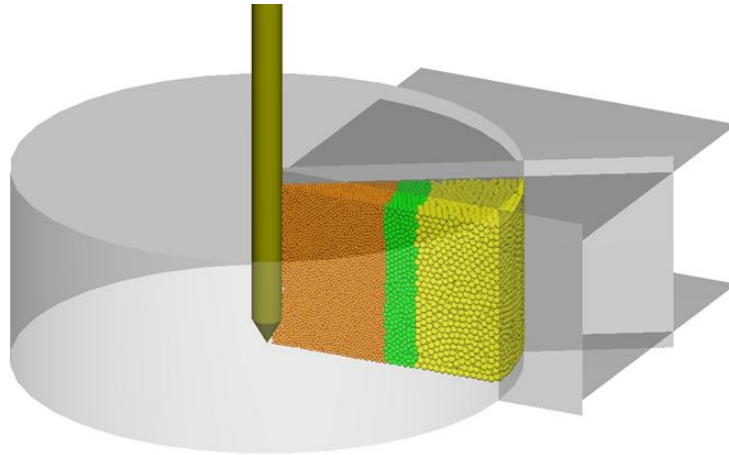


Figure 7.1 Calibration chamber model of 30° segment

In the modelling of particle breakage in the aforementioned manner, a decision was required to determine whether a particle in an aggregate subjected to multiple contacts would fracture or not. One option available was to use the stress tensor function in the PFC^{3D} programme to obtain the stress tensor for a single sphere as was used by McDowell and de Bono (2013). The method is also similar to those employed by Tsoungui et al. (1999) and Ben-Nun and Einav (2010), using discs.

Given that any particle subjected to a high hydrostatic stress is unlikely to break because it is loaded uniformly over its surface (McDowell and de Bono, 2013), it was considered unsuitable that mean stress should be used as the particle breakage criterion. Therefore, McDowell and de Bono (2013) decided to use the octahedral shear stress induced within each sphere as the breakage criterion, and this approach

is also adopted in this study. The octahedral stress in a particle is derived from its principal stresses, and is expressed as

$$q = \frac{1}{3} [(\sigma_1 - \sigma_2)^2 + (\sigma_2 - \sigma_3)^2 + (\sigma_1 - \sigma_3)^2]^{1/2} \quad 7.1$$

where

σ_1 is major principal stress in particle

σ_2 is intermediate principal stress in particle

σ_3 is minor principal stress in particle

McDowell and de Bono (2013) found that in PFC^{3D} for a sphere compressed diametrically between two walls, the value of q obtained using the above equation is equivalent to

$$q = 0.9 \frac{F}{d^2} \quad 7.2$$

Hence the q value in Equation 7.2 is proportional to the characteristic stress σ . Therefore, in view of McDowell and de Bono (2013), it was decided that for particles loaded under multiple contacts, any particle would break if the octahedral shear stress was greater than or equal to its strength, where the strengths of the particles follow a Weibull distribution of q values.

Golightly (1990) compressed different samples of carbonate and silica sands in an oedometer and the typical plots of void ratio against the logarithm of vertical effective stress are shown in Figure 7.2.

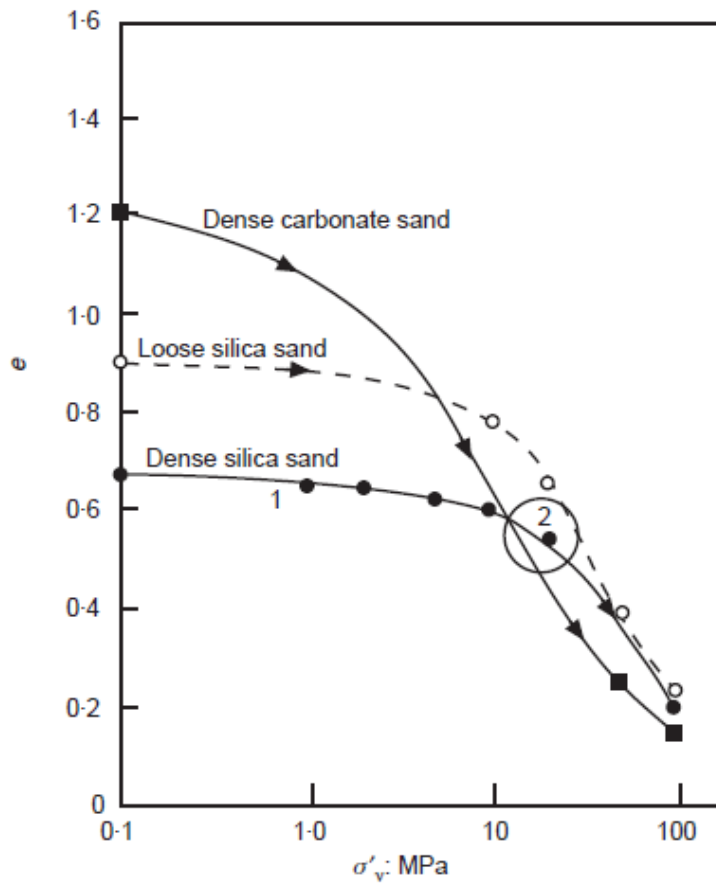


Figure 7.2 One-dimensional compression plots for carbonate and silica sands (Golightly, 1990)

The Weibull distribution of strengths assumed for the simulations for silica sand was taken from McDowell (2002), and is expressed by the Weibull modulus m , and the 37% tensile strength q_0 . Since the 37% tensile strength q_0 of silica sand for a 2mm particle size is 41.7MPa (McDowell, 2002), the 37% tensile strength q_0 for relatively weaker sand for particle size 2mm was estimated from the ratios of the yield stresses for the dense silica and carbonate sands in Figure 7.2 and chosen to be approximately 9MPa.

The size effects on the tensile strength of materials are described using Equation 2.12, and can be rewritten as:

$$q_0 \propto d^{-3/m}$$

7.3

assuming that bulk fracture dominates. Adopting the approach of McDowell and de Bono (2013) each sphere was allowed to split into two equal spheres with the same shape but without loss of mass and moving along the direction of the minor principal stress of the original parent sphere, when the value of q was greater than or equal to its Weibull strength. The result of this is that the new sphere fragments created in this manner possess sufficient overlap to be located within the boundary of the parent sphere, with the axis linking their centres aligned along the direction of the minor principal stress, as illustrated in Figure 7.3. However, this mechanism generates undesirable local pressure spikes due to the imposed elastic energy before particle separation (McDowell and de Bono, 2013). To release this artificial pressure and to maintain the stability of the sample, particle breakages for this specific aspect of the undertaken work were updated for the entire sample after a number of calculation cycles by checking the stresses on the walls were always at the desired value. The particle parameters used in these simulations are shown in Table 7.1.

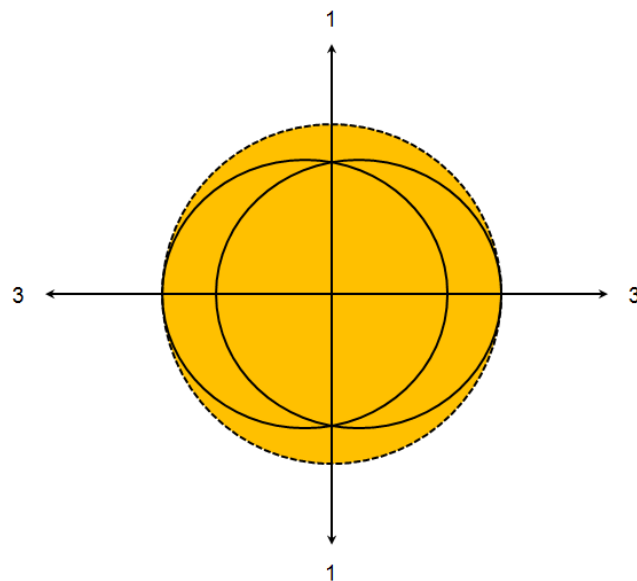


Figure 7.3 Mechanism of particle splitting into two particles of equal size, with mass conserved

Table 7.1 Parameters for DEM simulations of particle crushing

Setting	Units	value
Initial particle diameter, d_0	mm	2, 3, 4
Initial number of particles	-	33278
Initial porosity	-	0.3543
Particle normal stiffness	N/m	5×10^5
Particle shear stiffness	N/m	5×10^5
Particle friction coefficient	-	0.5

7.3 Results and discussion

To investigate the effect of particle crushing on the tip resistance results of silica sand, two simulations (A1 and B1) were carried out. A 300kPa isotropic confining stress was applied to the samples before and during the penetration. In the first simulation particle crushing was not allowed and in the second, particle crushing was allowed. In simulation B1, the Weibull modulus m was set to 3 and the material constant b to $-3/m = -1$. Figure 7.4 shows no marked difference between the ultimate tip resistance results for both simulations of about 6MPa. This is considered to be the consequence of the low degree of particle breakage (only three) in simulation B1 as illustrated in Figure 7.5. It shows that the silica sand particles were not subjected to significant crushing (if at all) in the cone penetration tests at this confining stress.

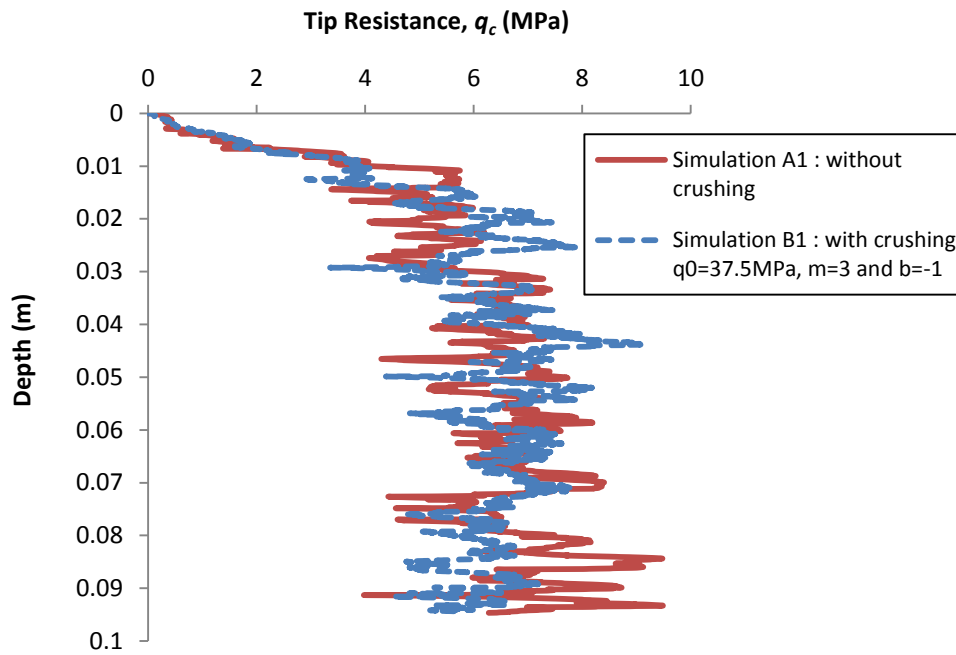


Figure 7.4 Tip resistance results for silica sand (simulations A1 and B1)

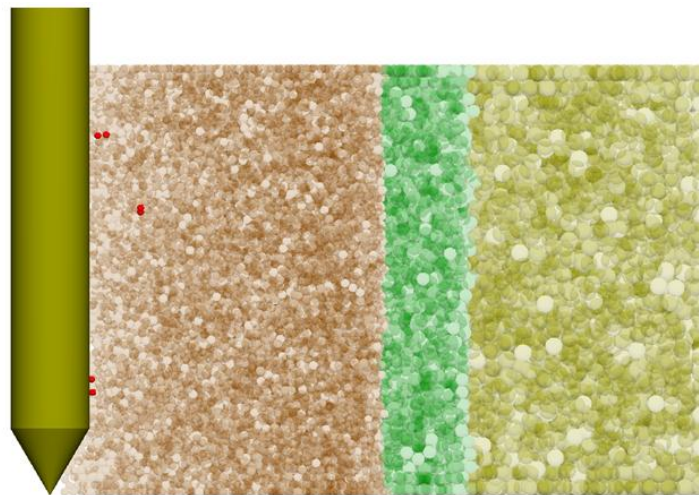


Figure 7.5 Particles breakage for silica sand (simulation B1: $q_0=37.5\text{MPa}$, $m=3$ and $b=-1$)

Similarly, to investigate the effect of particle crushing on the tip resistance results for relatively weaker sand and to decouple effects of statistical variability and size effect; three simulations (C1, D1 and E1) were conducted with isotropic confining

stress of 300kPa applied to the samples before and during the penetration. The three simulations were carried out with constituent particles having the same initial particle size d_0 and tensile strength q_0 , but different Weibull moduli m and material constants b .

In simulation C1, the Weibull modulus was set to 3 and b to -1. Figure 7.6 shows the extent of particle breakage; it is observed that the majority of the crushing during the cone penetration occurs near the cone penetrometer. This has been attributed to the particles in the immediate vicinity of the penetrometer having been subjected to high localised stresses compared with the remaining particles in other areas of the calibration chamber.

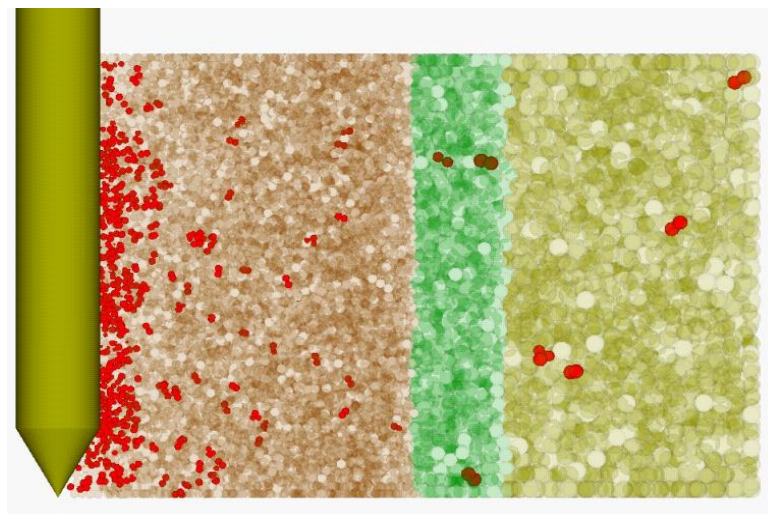


Figure 7.6 Particle breakage for relatively weaker sand (simulation C1 : $q_0=8\text{MPa}$, $m = 3$ and $b = -1$)

Figure 7.7 and Table 7.2 shows the number of particles broken in the three zones at different penetration depths for simulation C1. As expected the data shows that the most of the breakage occurred nearest to the cone penetrometer in zone 1 with only 3 and 7 particles broken in zones 2 and 3 respectively. Additionally, it can be seen that in zone 1 although fewer particles were crushed at shallow depths, this increased

considerably as the cone advanced. It should be noted that due to the considerable particle crushing, a significant number of particle fragments were produced, which slowed the simulation down significantly and the simulation eventually terminated when the cone reached a depth of 0.07m. To overcome this problem, the size of particles that were allowed to crush was limited to 0.01mm. Table 7.2 shows that the sample porosity increased slightly with increasing depth, which is believed to have occurred via a combination of crushing and rearrangement of unbroken particles as the cone advanced into the sample, consequently leading to a little decrease in cone tip resistance.

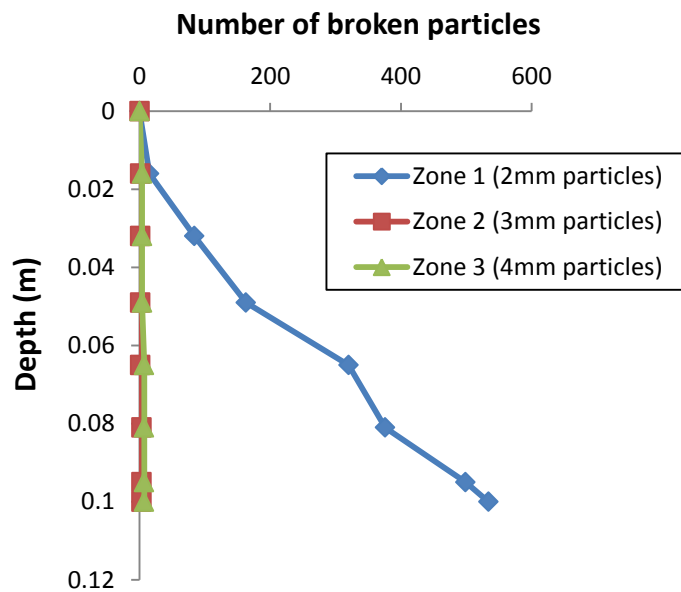


Figure 7.7 Number of broken particles for simulation C1 ($q_0=8\text{MPa}$, $m=3$ and $b=-1$)

Table 7.2 Number of broken particles and porosities for simulation C1

Penetration depth (m)	Number of broken particles			Porosity
	2mm	3mm	4mm	
0	0	0	0	0.3533
0.016	15	1	4	0.3533
0.032	84	1	4	0.3540
0.049	163	1	4	0.3549
0.065	320	1	7	0.3557
0.081	376	3	7	0.3559
0.095	499	3	7	0.3560
0.100	534	3	7	0.3569

It is known that reducing the Weibull modulus increases the variability in particle strengths for any given particle size and also governs the size effect according to Equation 7.3 if bulk fracture dominates. Therefore, for a Weibull modulus of 3 the distribution of strengths is quite narrow; this could be the reason why this simulation experienced noticeably late particle breakage. Selecting a Weibull modulus of, say 1.5 would increase the variability and also increase the size effect such that new fragments are statistically stronger for $b = -2$ than $b = -1$.

For simulation D1, Weibull modulus was set to 1.5 and b to -2. Figure 7.8 shows the particle breakage in simulation D1, while it can be seen that there are many particle breakages in the three zones.

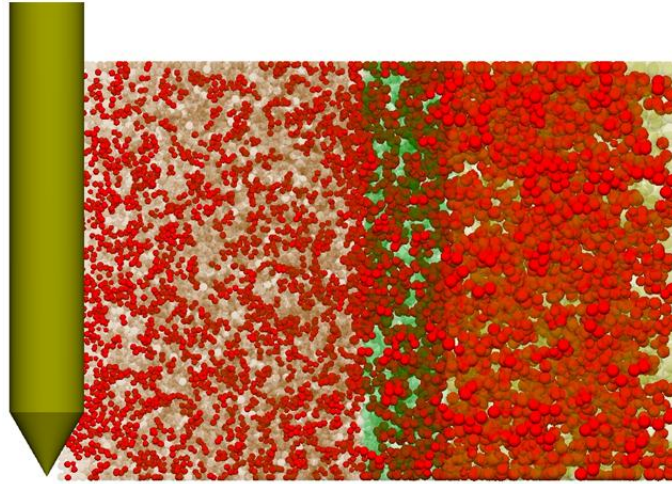


Figure 7.8 Particle breakage for relatively weaker sand (simulation D1: $q_0 = 8\text{MPa}$, $m = 1.5$ and $b = -2$)

Figure 7.9 and Table 7.3 show the number of broken particles in the three zones at different penetration depths for simulation D1. The data presented indicates that breakage occurred in all particle zones at shallow penetration depths. Almost all of the breakage in zones 2 and 3 occurred at shallow penetration depths. This was, however, not the case for zone 1 (next to the cone penetrometer) where particle breakage was recorded as having increased progressively in the same period as the cone advanced. Table 7.3 shows the evolution of the sample porosity over the full penetration depth achieved.

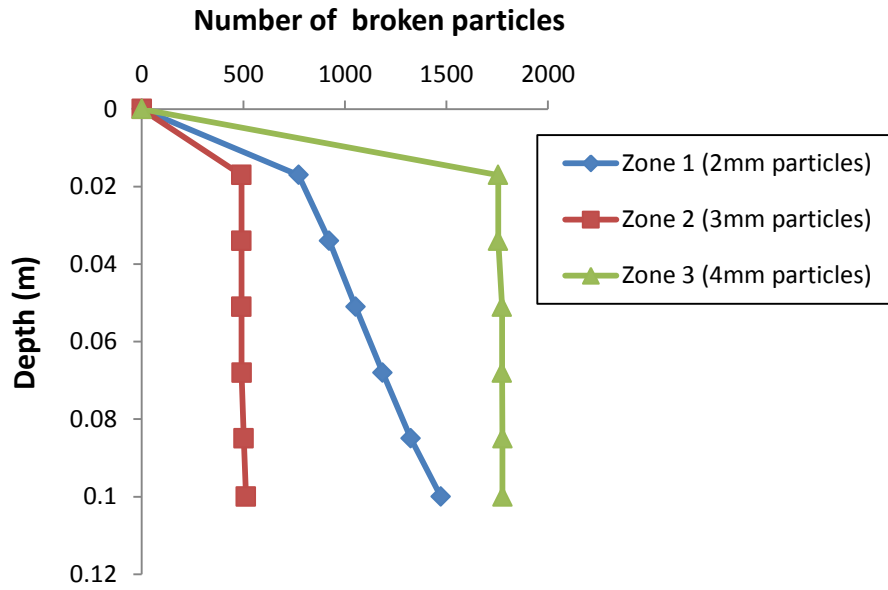


Figure 7.9 Number of broken particles for simulation D1 ($q_0=8\text{MPa}$, $m=1.5$ and $b=-2$)

Table 7.3 Number of broken particles and porosities for simulation D1

Penetration depth (m)	Number of breakage particles			Porosity
	2mm	3mm	4mm	
0	0	0	0	0.3533
0.017	772	491	1755	0.3711
0.034	923	491	1755	0.3719
0.051	1053	491	1774	0.3726
0.068	1186	492	1774	0.3732
0.085	1325	502	1776	0.3738
0.100	1437	513	1776	0.3741

Decreasing the Weibull modulus to 1.5 leads to more variation in particle strengths for any given particle size. In addition, the enhanced size effect on average strength with $b = -2$, means that the larger particles are much weaker, relative to the 2mm particles, for which the 37% strength is defined and is constant. This means that there is much breakage of the larger particles. The extent of particle breakage in zone 1 (2mm particles) confirms that there are fewer particle breakages in this zone where the particles are statistically stronger.

To clarify the effect of variability and size effect on the particle breakage separately, simulation E1 was conducted with $m = 3$ (as in simulation C1) but with $b = -2$. Figure 7.10 shows the particle crushing at the end of the simulation for the three particle zones. It can be seen that the majority of the crushing occurred in zone 3 (4mm particles).

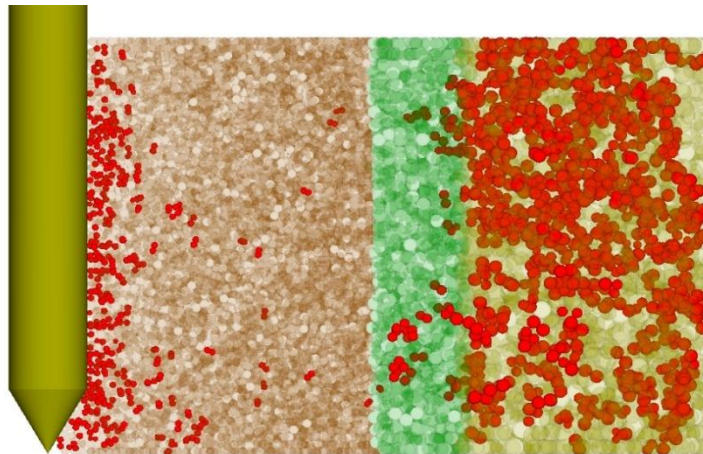


Figure 7.10 Particle breakage for relatively weaker sand (simulation E1 : $q_0 = 8\text{MPa}$, $m = 3$ and $b = -2$)

Figure 7.11 and Table 7.4 show the number of particles broken in the three zones at different penetration depths for simulation E1. The results presented show that at the beginning of the penetration a large number of particle breakages occurred in zone 3 followed by zone 2 and zone 1 respectively. It also can be seen that there was almost

no further particle breakage in zones 2 and 3 for the remainder of the simulation. This was, however, not the case for zone 1 (next to the cone penetrometer) where particle breakage was recorded as having increased gradually as the cone advanced. Furthermore, Table 7.4 shows that the sample porosity increased slightly with increasing penetration depth.

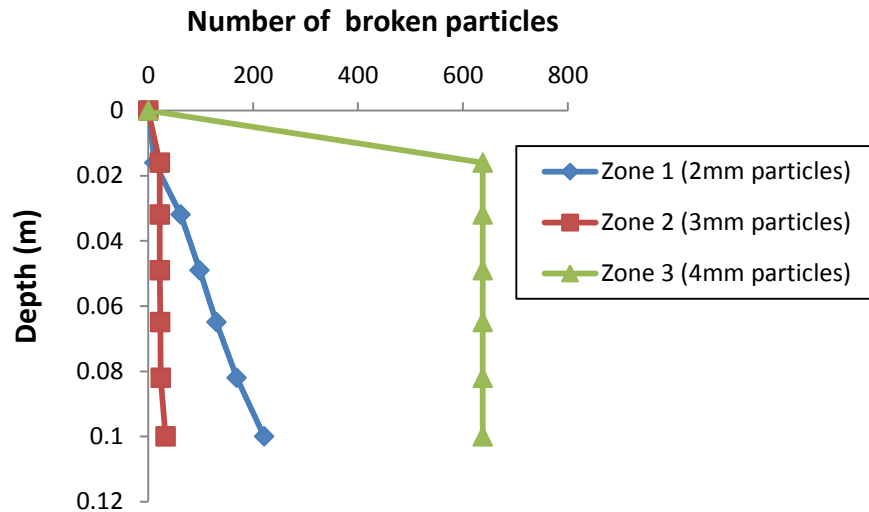


Figure 7.11 Number of broken particles for simulation E1 ($q_0=8\text{MPa}$, $m=3$ and $b=-2$)

Table 7.4 Number of broken particles and porosities for simulation E1

Penetration depth (m)	Number of broken particles			Porosity
	2mm	3mm	4mm	
0	0	0	0	0.3533
0.016	12	22	638	0.3602
0.032	62	22	638	0.3608
0.049	98	22	638	0.3617
0.065	130	23	638	0.3626
0.082	169	24	638	0.3632
0.100	221	33	638	0.3638

Selecting a b value of -2 for $m = 3$ increases the size effect and hence the larger particles become statistically weaker and this explains the large degree of crushing of the largest particle size (4mm). In addition, statistically stronger particles resulted from the breakages of the smaller particles, which resulted in fewer particle breakages in zone 1 (next to the cone) as the cone advanced - this is confirming that the large number of breakages in Figure 7.8 is due to the increase in the size effect and the wide variability in strengths.

Table 7.5 shows a summary of DEM simulations for investigating the effect of particle crushing on cone penetration tests in a calibration chamber.

Table 7.5 Summary of DEM simulations for investigating the effect of particle crushing on cone penetration tests

Simulation	Model type	Sand type	37% tensile strength, q_0 ($d_0=2\text{mm}$) (MPa)	Confining stresses (kPa)	Weibul modulus, m	Constant material, b
A1	Non-crushing model	-	-	300	-	-
B1	Crushing model	Silica sand	37.5	300	3	-1
C1	Crushing model	Relatively weaker sand	8.0	300	3	-1
D1	Crushing model	Relatively weaker sand	8.0	300	1.5	-2
E1	Crushing model	Relatively weaker sand	8.0	300	3	-2
F1	Non-crushing model	-	-	100	-	-
G1	Crushing model	Relatively weaker sand	8.0	100	3	-1
H1	Crushing model	Relatively weaker sand	8.0	100	1.5	-2
I1	Crushing model	Relatively weaker sand	8.0	100	3	-2

The tip resistance results for relatively weaker soil at confining stress of 300kPa for the three crushing models (simulations C1, D1 and E1) and the non-crushing model (simulation A1) are shown in Figure 7.12. Simulations C1 and E1 are shown to have experienced a slight decrease in the ultimate tip resistance compared to the non-crushing model (simulation A1). The decrease is viewed as the result of crushing of particles and migration of fragments into the pore spaces, inducing stress relaxation. For simulation D1 the ultimate tip resistance value decreased to about 4.5MPa compared to about 7MPa for the non-crushing model (simulation A1). The observed reduction in the ultimate tip resistance is believed to be due to the large number of breakages occurring in all three particle zones as a result of increasing the size effect and the variability in strengths. When the cone attained a depth of 0.05m and beyond, increasing particle breakage caused a progressive reduction in tip resistance until it reached a value of about 3MPa at the end of the simulation.

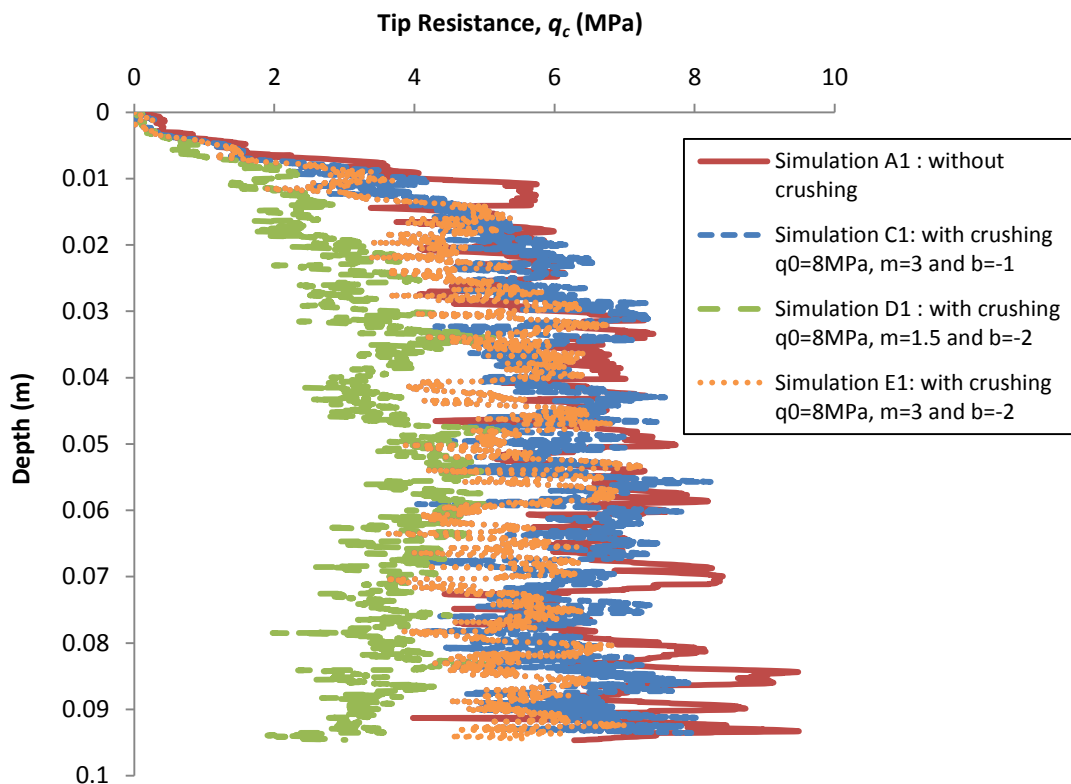


Figure 7.12 Tip resistance results for relatively weaker sand (simulations A1, C1, D1 and E1)

To examine the effect of confining stress on crushing and tip resistance for the relatively weaker sand the aforementioned simulations with confining stress 300kPa (A1, C1, D1 and E1) were repeated but with confining stress of 100kPa and these are simulations (F1, G1, H1 and I1). Figure 7.13 shows the particle crushing at the end of the simulation in the three particle zones for the simulations G1, H1 and I1.

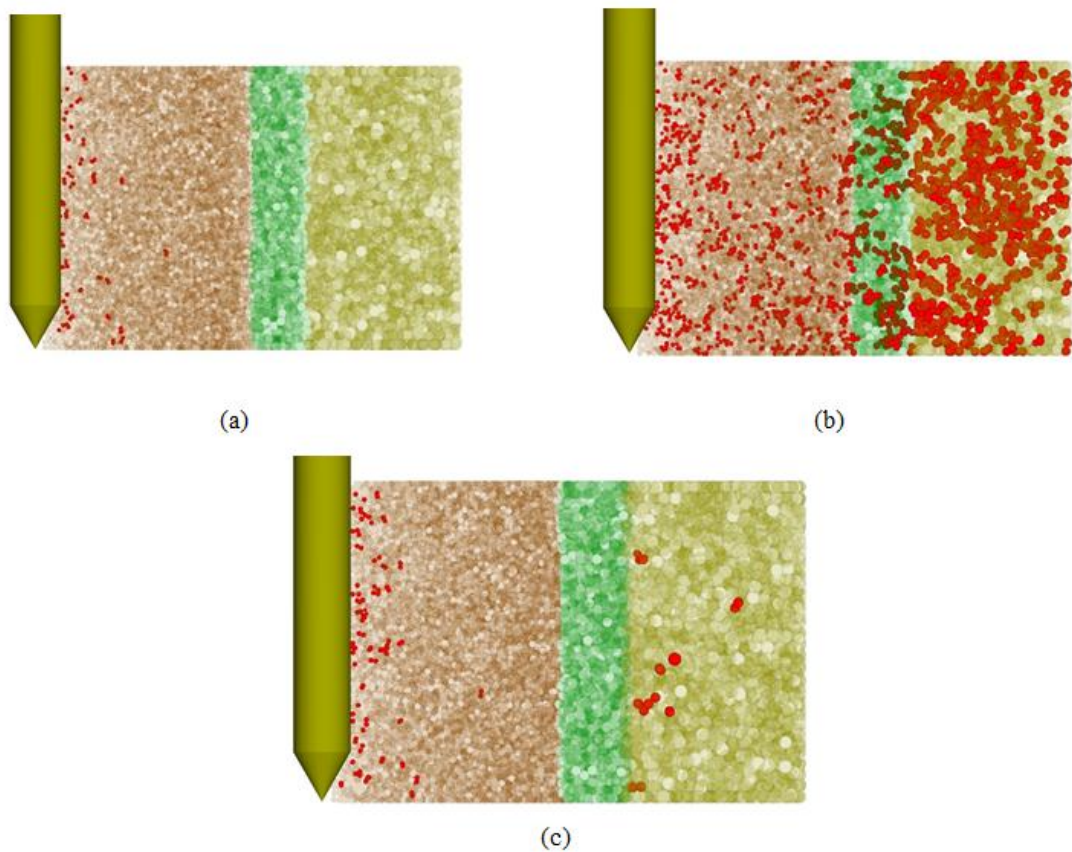


Figure 7.13 Particle breakage for relatively weaker sand at confining stress of 100kPa:

(a) Simulation G1: $q_0 = 8\text{MPa}$, $m = 3$ and $b = -1$

(b) Simulation H1: $q_0 = 8\text{MPa}$, $m = 1.5$ and $b = -2$

(c) Simulation I1: $q_0 = 8\text{MPa}$, $m = 3$ and $b = -2$

It can be seen that the particle crushing in the all zones for these simulations is less than those for simulations C1, D1 and E1. Figure 7.14 shows the tip resistance results

for relatively weaker sand at confining stress of 100kPa for the three crushing models (simulations G1, H1 and I1) and the non-crushing model (simulation F1).

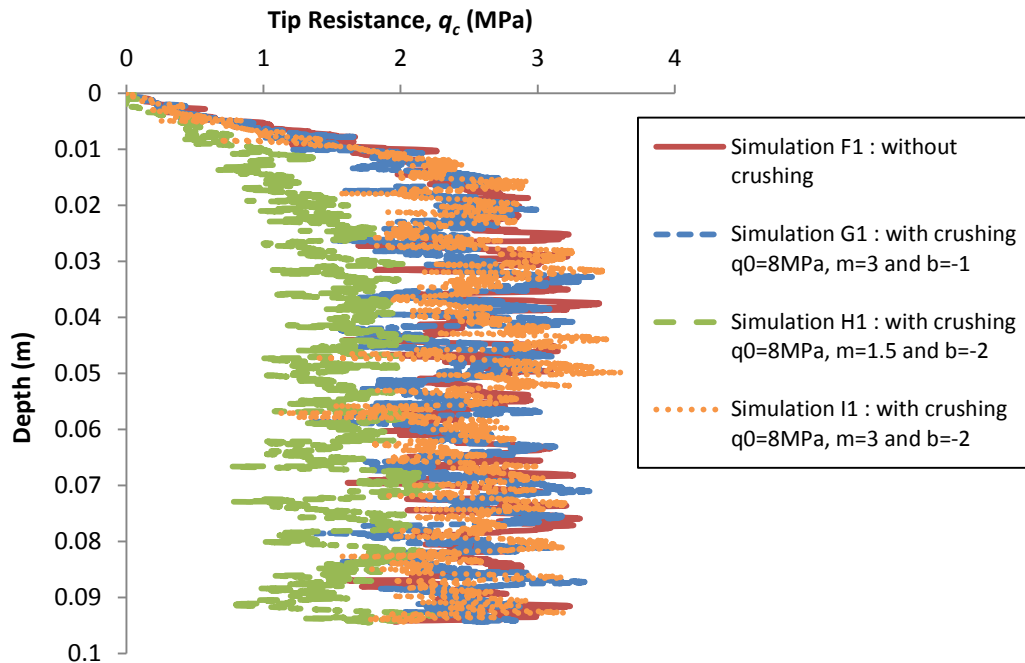


Figure 7.14 Tip resistance results for relatively weaker sand at confining stress of 100kPa (simulations F1, G1, H1 and I1)

Figure 7.15 shows a plot of normalised tip resistance by their initial horizontal stress q_c/σ_{ho} for these simulations. It can be seen that from Figure 7.15a for non-crushing model for simulations (F1 and A1) with confining stresses 100kPa and 300kPa respectively; the normalised tip resistance is almost the same for both simulations. However, from Figure 7.15b, Figure 7.15c and Figure 7.15d for the crushing models it can be seen that the normalised tip resistance decreases for simulations (C1, D1 and E1) with confining stresses 300kPa compared to the simulations (G1, H1 and I1) with confining stresses 100kPa. Therefore, increasing the confining stress lead to an increase in the particle crushing and a reduction in the normalised tip resistance.

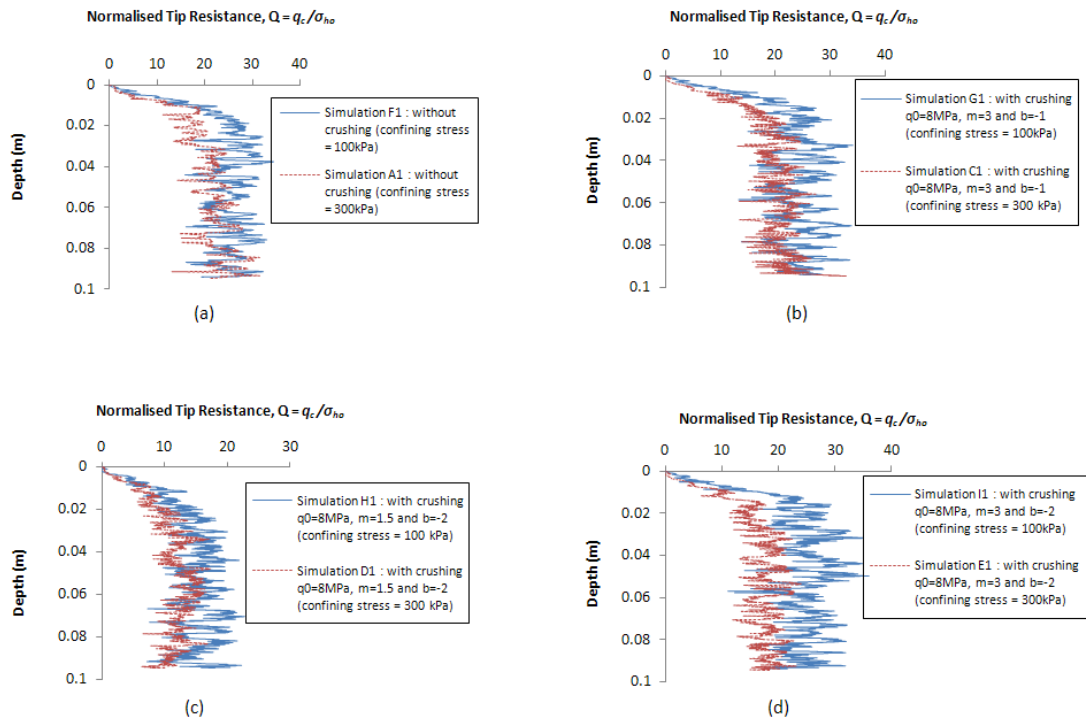


Figure 7.15 Normalised tip resistance ($Q = q_c / \sigma_{ho}$) for relatively weaker sand at different confining stresses

7.4 Conclusions

Discrete element modelling was used to simulate particle crushing during cone penetration tests in the three zones comprising initial particle sizes of 2, 3 and 4mm in a 30° segment of calibration chamber. Particle breakage was simulated by replacing a broken particle with two new equal-sized smaller particles, with conserving mass. Particle crushing was controlled by the octahedral shear stresses within the particles owing to their multiple contacts and a Weibull distribution of strengths. The results showed that for silica sand there was very little (or no) crushing near the cone penetrometer for the stress level applied and that the tip resistance is almost the same as for the non-crushing model.

It was found that for the relatively weaker sand samples of all crushing models the tip resistance decreased compared to the non-crushing model. Compared to the non-crushing model, the simulation with a 37% strength of 8MPa, a Weibull modulus $m = 3$ and size effect $b = -1$, the ultimate tip resistance decreased slightly. Some crushing was evident in the zone next to the cone penetrometer, with only a small number of particle breakages in the other zones. For the same Weibull modulus $m = 3$ and a stronger size effect with $b = -2$, the tip resistance dropped slightly. In this case, there was a reduction in particle breakage next to the penetrometer, because fragments are statistically stronger. However, there was more breakage in the zones further away due to the particles having lower average strengths with $b = -2$. For the same size effect $b = -2$ and a wider variability in strengths $m = 1.5$, there was a significant drop in tip resistance and extensive crushing in all the zones.

Normalised tip resistance was found to decrease as the confining stress increases and this is a result of increasing particle crushing. The particle refinement method has been proven to be a useful approach for simulating particle crushing during the cone penetration test for strong silica sand and relatively weaker sand (lower average strength), both with higher Weibull modulus ($m = 3$) and weaker size effect ($b = -1$); where crushing occurred only in the zone next to the cone penetrometer. However, it was not appropriate for the relatively weaker sand with higher Weibull modulus ($m = 3$) and stronger size effect ($b = -2$) or with lower Weibull modulus ($m = 1.5$) and stronger size effect ($b = -2$); where crushing occurred in all zones and because such extensive crushing far away from the cone is unrealistic and a feature of the larger particles having unrealistic strengths.

CHAPTER 8

CONCLUSIONS AND SUGGESTIONS FOR FUTURE RESEARCH

8.1 Summary and Conclusions

Cone penetration testing is a well established *in situ* soil test in geotechnical engineering because of its continuous data measurement capability and repeatability of output at relatively low cost. A three-dimensional discrete element method was used in this study to simulate cone penetration tests of granular materials in a calibration chamber. The particles were either spheres or two-ball clumps that were allowed to rotate freely. For simplicity a linear–elastic contact law was utilised. As the model to be analysed was axisymmetrical, only a quarter of the sample and penetrometer were initially analysed to reduce computational time. The chamber heights H and chamber widths D_c were reduced in order to increase the ratio of cone diameter to particle diameter B/d_{50} to a more realistic value and to ensure that during penetration, the cone tip remained in contact with an acceptable number of particles. The results showed that using chamber height and width of 100mm and 300mm respectively improved the computational time without significantly affecting tip resistance.

In order to increase the number of small particles in contact with the cone tip and to further reduce the computational time, a particle refinement method was

implemented in the simulations whereby small particles were generated near the cone penetrometer and larger ones further away. The particles were graded in zones to ensure that the cone penetration resistance was approximately the same as would have been obtained if an entire chamber had been filled with small particles. It was determined that simulating a sand-sized particle of 2 mm or 1.5mm near the cone penetrometer in the 90 degree chamber segment resulted in an unacceptably large number of particles and a long simulation time. A 30 degree chamber segment comprising five particle zones: 1, 1.5, 2, 3 and 4mm diameter spheres, with size increasing with distance from the cone was found to be more appropriate for the simulations conducted. Reducing the particle size next to the cone was found to increase cone tip resistance especially at shallow depths and decrease fluctuations in the tip resistance curve. However, compared to available experimental results of tip resistance as a function of depth, the simulations undertaken in this investigation were found to be of the correct form.

Using a radius expansion method during sample preparation was found to reduce computational time significantly with little impact on tip resistance compared with a deposition and compaction method. In addition, as the CPT test is a quasi-static process, it was found that the use of a constant particle mass, irrespective of particle size, led to a larger time-step and greater computational efficiency compared with using constant particle density. The tip resistance for both cases were found to be almost the same. The initial porosity, mean effective stress and particle friction coefficient were all found to influence the tip resistance. Reducing initial porosity and increasing particle friction coefficient all resulted in increasing tip resistance. Increasing mean effective stress was found to increase tip resistance if crushing is not

implemented. In addition, the effect of prohibiting particle rotation on tip resistance was investigated and was found to significantly increase tip resistance compared with freely rotating particles. The ultimate tip resistance obtained from the DEM simulation in a 30° chamber segment with 1mm spheres next to the cone and prohibited particle rotation is shown to be in approximate agreement with available experimental data. However, completely prohibiting rotation of particle spheres is not representative of reality and using clumps provides a better approximation to reality.

The effect of particle shape was examined in a 90° chamber segment by replacing the whole spheres with basic two-ball clumps, and also in a 30° segment chamber using two-ball clumps only next to the penetrometer to reduce computational time. The results show that using clumps gives a higher tip resistance compared to the use of single spheres and that this resistance increases with increasing clump angularity due to increased interlocking and rotational resistance.

DEM simulations of biaxial tests to study granular material behaviour were carried out. The stress-strain behaviour of cohesionless granular material under monotonic loading was studied and it was proven that several parameters have a significant effect on soil stress-strain behaviour. Suitable continuum parameters were obtained from the biaxial test simulations and used as inputs for an analytical cavity expansion solution for cone tip resistance. The analytical solution was based on continuum mechanics and a combined cylindrical-spherical cavity expansion method. A comparison of the DEM tip resistance to the analytical tip resistance results showed both methods to be in good agreement. It has been also shown that it is possible to

capture the essential feature of the mechanics of cone penetration in granular materials using DEM.

DEM was used to simulate particle crushing during cone penetration tests in three zones of a 30° segment calibration chamber. Particle breakage was simulated by replacing a broken particle with two new equi-sized smaller particles, while conserving mass. The results showed that for silica sand, very little crushing occurred near the cone penetrometer for the stress level applied and the tip resistance was almost the same as for the non-crushing model. In general, for the relatively weaker sand samples of all crushing models the tip resistance reduces compared to the non-crushing model. There was a considerable reduction in the tip resistance compared to the non-crushing model when the wider variability in strengths ($m = 1.5$) and stronger size effect ($b = -2$) were applied. This is due to the large number of breakages occurred in the all zones. Normalised tip resistance was found to decrease as the confining stress increases and this is as a result of increased particle crushing.

8.2 Suggestions for Further Research

The simulations carried out in this study used samples comprising single sand-sized particles graded in continuous zones. This was done to reduce the computational time of the simulations. It is possible to investigate the effect of the sand size distribution (near the cone penetrometer, for example) on tip resistance results for soil assembly.

Particle shape was found to significantly affect tip resistance and granular material response. The simulations carried out in this research focused on the use of simple shaped particles to reduce computational time. By using super computational power,

a future study could examine the influence of using more realistic particle shape models for better results since particle shape has been shown to be an important factor for tip resistance and granular material response.

For clumps to exist, it is necessary for spheres to overlap and due to the contribution to the mass in the overlapping region of the spheres, the moment of inertia for a clump is not the same as that for a particle of the same shape and uniform density. A method for producing clumps with uniform density and correct moment of inertia could be a subject of future research.

For simplicity and to reduce computational time, a linear elastic contact model with the same value for all particle size was used in this study. For different particle size the stiffness should be scaled to achieve a consistent material modulus. However, the contact mechanics between real particles is not so simple. Future work should examine the use of contact mechanics for real particles such as Hertzian contact mechanics, which provides a more accurate response for real soil.

The flexible membrane for the calibration chamber test and the biaxial test was simulated in this research using a rigid wall. Future study should develop an alternative method to model the real flexible boundary conditions. For example, it is possible to simulate a flexible membrane using a large number of bonded balls, albeit increasing computational time.

Due to the axisymmetry of the problem examined in this study and to reduce the calculation time, 90 and 30 degree calibration chamber segments were simulated.

Consequently, an extra two boundaries which do not otherwise exist in a full calibration chamber were generated. The real problem was not simulated because of the effect of these boundaries. A periodic boundary which could be used to simulate a large system by modelling a small part could be developed in the future to reduce boundary effects in the simulations.

A particle refinement method was used in this study to obtain a larger number of small particle sizes next to the cone penetrometer and to reduce computational time. However, this required the generation of numerous particles of different sizes in all zones and led to computational time inefficiency especially when clumps were utilised. It is proposed for future research to use a coupled numerical method to solve this problem. Two codes, Fast Lagrangian Analysis of Continua (FLAC), a finite difference code and Particle Flow Code (PFC), the discrete element code, can be coupled (Cai et al., 2007; Wang et al., 2010). Applying the FLAC/PFC coupled approach takes advantage of each modelling scheme and would at the same time reduce the demand for longer computational time. A large number of small particle sizes could be modelled next to the cone penetrometer using PFC and the particles further away could be modelled with FLAC.

To simulate particle crushing during cone penetration a particle refinement method comprising 2, 3 and 4mm particle sizes was used to reduce computational time. This method was found to be unsuitable for the relatively weaker sand with higher Weibull modulus ($m = 3$) and stronger size effect ($b = -2$) or with lower Weibull modulus ($m = 1.5$) and stronger size effect ($b = -2$); for which crushing occurred in all the zones. In the future, with improved computational power one initial particle size

may be used in the whole chamber, perhaps with clumps or agglomerates which model the real particle shape. Such a particle crushing model could also be used to simulate piled foundations in crushable soils.

This study has focused only on cone tip resistance and did not consider the effect of sleeve friction. Future research may simulate sleeve friction of cone penetrometer which is a common parameter used for soil classification.

REFERENCES

- ABDULLA, A. A. & KIOUSIS, P. D. (1997) Behavior of cemented sands—I. Testing. *International Journal for Numerical and Analytical Methods in Geomechanics*, 21, 533-547.
- ABU-FARSAKH, M., TUMAY, M. & VOYIADJIS, G. (2003) Numerical parametric study of piezocone penetration test in clays. *International Journal of Geomechanics*, 3, 170-181.
- AHMADI, M., BYRNE, P. & CAMPANELLA, R. (2005) Cone tip resistance in sand: modeling, verification, and applications. *Canadian geotechnical journal*, 42, 977-993.
- ARROYO, M., BUTLANSKA, J., GENS, A., CALVETTI, F. & JAMIOLKOWSKI, M. (2011) Cone penetration tests in a virtual calibration chamber. *Geotechnique*, 61, 525-531.
- BALDI, G., BELLOTTI, R., GHIONNA, V., JAMIOLKOWSKI, M. & PASQUALINI, E. (1982) Design parameters for sands from CPT. *Proc. Second Eur. Symp. on Penetration Testing*, AA Blakema, Rotterdam, The Netherlands, 425-432.
- BALDI, G., BELLOTTI, R., GHIONNA, V., JAMIOLKOWSKI, M. & PASQUALINI, E. (1986) Interpretation of CPTs and CPTUs; 2nd part: drained penetration of sands. *Proc. 4th Int. Geotech. Seminar: Field Instrumentation and In Situ Measurements*, Nanyang Technol. Univ., Singapore, 143-162.

BALIGH, M. M. (1985) Strain path method. *Journal of Geotechnical Engineering*, 111, 1108-1136.

BARDET, J. & PROUBET, J. (1992) Shear-band analysis in idealized granular material. *Journal of engineering mechanics*, 118, 397-415.

BARENTSEN, P. (1936) Short description of a field testing method with cone-shaped sounding apparatus. *Proceedings of the 1st International Conference on Soil Mechanics and Foundation Engineering*, 1, 6-10.

BATHURST, R. & ROTHENBURG, L. (1988) Micromechanical aspects of isotropic granular assemblies with linear contact interactions. *J. Appl. Mech.*, 55, 17-23.

BEEN, K., CROOKS, J. & ROTHENBURG, L. (1988) A critical appraisal of CPT calibration chamber tests. *Ruiter [145]*, 651-660.

BEEN, K., JEFFERIES, M., CROOKS, J. & ROTHENBURG, L. (1987) The cone penetration test in sands: part II, general inference of state. *Geotechnique*, 37.

BEGEMANN, H. (1953) Improved method of determining resistance to adhesion by sounding through a loose sleeve placed behind the cone. *Proceedings of the 3rd International Conference on Soil Mechanics and Foundation Engineering, ICSMFE, Zurich*, 1, 213-217., 16-27.

BEGEMANN, H. P. (1965) The friction jacket cone as an aid in determining the soil profile. *Proceedings of the 6th International Conference on Soil Mechanics and Foundation Engineering, Montreal*, 1, 17-20. .

- BEGEMANN, H. P. (1969) The Dutch Static Penetration Test with the Adhesion Jacket. *LGM Mededelingen*, 12, 69-100.
- BELHEINE, N., PLASSIARD, J.-P., DONZÀ, F.-V., DARVE, F. & SERIDI, A. (2009) Numerical simulation of drained triaxial test using 3D discrete element modeling. *Computers and Geotechnics*, 36, 320-331.
- BELLOTTI, R., BIZZI, G. & GHIONNA, V. (1982) Design, construction and use of a calibration chamber. *Proceedings of the 2nd European Symposium on Penetration Testing*, Amsterdam, 2, 439-446.
- BEN-NUN, O. & EINAV, I. (2010) The role of self-organization during confined comminution of granular materials. *Philosophical Transactions of the Royal Society A: Mathematical, Physical and Engineering Sciences*, 368, 231-247.
- BISHOP, A. W. (1954) Correspondence on shear characteristics of a saturated silt measured in triaxial compression. *Geotechnique*, 4, No.1, 43-45.
- BISHOP, R. F., HILL, R. & MOTT, N. F. (1945) The theory of indentation and hardness tests. . *Proceedings of Physics Society*, 57, 147-159.
- BOLTON, M. & GUI, M. (1993) The study of relative density and boundary effects for cone penetration tests in centrifuge. *EEC Science Contract SCI-CT91-0626 entitled Improvement of model testing in the geotechnical*.
- BOLTON, M., GUI, M., GARNIER, J., CORTE, J., BAGGE, G., LAUE, J. & RENZI, R. (1999) Centrifuge cone penetration tests in sand. *Geotechnique*, 49, 543-552.

BOLTON, M., NAKATA, Y. & CHENG, Y. (2008) Micro-and macro-mechanical behaviour of DEM crushable materials. *Geotechnique*, 58, 471-480.

BROMS, B. B. & FLODIN, N. (1988) History of Soil Penetration Testing. *Proceedings of the International Symposium on Penetration testing, Penetration Testing 1988, ISOPT-1, Orlando J. de Ruiter (ed.), Balkema, Rotterdam*, 1, 157-220.

BRUZZI, D. & BATTAGLIO, M. (1987) *Pore pressure measurements during cone penetration tests*, ISMES.

BUDHU, M. & WU, C. S. (1992) Numerical analysis of sampling disturbances in clay soils. *International journal for numerical and analytical methods in geomechanics*, 16, 467-492.

CAI, M., KAISER, P., MORIOKA, H., MINAMI, M., MAEJIMA, T., TASAKA, Y. & KUROSE, H. (2007) FLAC/PFC coupled numerical simulation of AE in large-scale underground excavations. *International Journal of Rock Mechanics and Mining Sciences*, 44, 550-564.

CALVETTI, F., NOVA, R., GARCIA-ROJO, R., HERRMANN, H. & MCNAMARA, S. (2005) Micro-macro relationships from DEM simulated element and in-situ tests. *Powders and Grains, 5th. International Conference on Micromechanics of Granular Media*, Stuttgart, 245-249.

CALVETTI, F., VIGGIANI, G. & TAMAGNINI, C. (2003) A numerical investigation of the incremental behavior of granular soils. *Rivista italiana di geotecnica*, 37, 11-29.

- CAMPANELLA, R., ROBERTSON, P. K. & GILLESPIE, D. (1983) Cone penetration testing in deltaic soils. *Canadian geotechnical journal*, 20, 23-35.
- CHAPMAN, G. (1974) A calibration chamber for field test equipment. *Proceedings, European Symp. Penetration Testing*, Stockholm, 2, 59-65.
- CHENG, Y., BOLTON, M. & NAKATA, Y. (2004) Crushing and plastic deformation of soils simulated using DEM. *Geotechnique*, 54, 131-141.
- CIVIDINI, A. & GIODA, G. (1988) A simplified analysis of pile penetration. Proc., 6th Int. Conf. on Numerical Methods in Geomechanics, 1988. Balkema, Rotterdam, Netherlands, 1043-1049.
- CLEARY, P. W. (2000) DEM simulation of industrial particle flows: case studies of dragline excavators, mixing in tumblers and centrifugal mills. *Powder Technology*, 109, 83-104.
- CLOUGH, G. W., RAD, N. S., BACHUS, R. C. & SITAR, N. (1981) Cemented sands under static loading. *Journal of the Geotechnical Engineering Division*, 107, 799-817.
- CUNDALL, P. (1988a) Computer simulations of dense sphere assemblies. *Micromechanics of granular materials*, 4, 113-123.
- CUNDALL, P. A. (1971) A computer model for simulating progressive, large-scale movements in blocky rock systems. *Proceedings of the Symposium of the International Society of Rock Mechanics, Nancy, France, Vol.1, Paper No.II -8*.
- CUNDALL, P. A. & HART, R. D. (1992) Numerical modelling of discontinua. *Engineering computations*, 9, 101-113.

- CUNDALL, P. A. & STRACK, O. D. (1979) A discrete numerical model for granular assemblies. *Geotechnique*, 29, 47-65.
- DE BORST, R. & VERMEER, P. A. (1982) Finite Element Analysis of Static Penetration Tests. *Proceedings of the 2nd European Symposium on Penetration Testing*, Amsterdam, Netherlands, 457-562. .
- DE RUITER, J. (1971) Electric penetrometer for site investigations. *Journal of the Soil Mechanics and Foundations Division*, 97, 457-472.
- DELUZARCHE, R. & CAMBOU, B. (2006) Discrete numerical modelling of rockfill dams. *International journal for numerical and analytical methods in geomechanics*, 30, 1075-1096.
- DOLBOW, J. & BELYTSCHKO, T. (1999) A finite element method for crack growth without remeshing. *Int. J. Numer. Meth. Engng*, 46, 131-150.
- DOUGLAS, B. J. & OLSEN, R. S. (1981) Soil classification using electric cone penetrometer. Cone Penetration Testing and Experience. *Proceedings of the ASCE National Convention*, American Society of Engineers (ASCE), St. Louis, 209-27.
- DURGUNOGLU, H. T. & MITCHELL, J. K. (1975) Static penetration resistance of soils. *Proceedings of the ASCE Specialty Conference on In-Situ Measurements of Soil Properties*, 1, 151-189.
- FAHEY, M. (1980) *A study of pressuremeter test in dense sand*. PhD thesis, Cambridge University, Cambridge, England.
- FAVIER, J., ABBASPOUR-FARD, M., KREMMER, M. & RAJI, A. (1999) Shape representation of axi-symmetrical, non-spherical particles in discrete element

simulation using multi-element model particles. *Engineering computations*, 16, 467-480.

GENG, Y. (2010) *Discrete element modelling of cavity expansion in granular materials*. PhD Thesis, University of Nottingham, Nottingham, UK.

GHIONNA, V. & JAMIOLKOWSKI, M. (1991) A critical appraisal of calibration chamber testing of sands. *Proceedings of the First International Symposium on Calibration Chamber Testing/ISOCCT1*, An-Bin Huang, Ed., Potsdam, New York, DTIC Document, 13-40.

GOLIGHTLY, C. R. (1990) *Engineering properties of carbonate sands.*, Ph.D. dissertation, Bradford University.

GRIFFITHS, D. (1982) Elasto-plastic analyses of deep foundations in cohesive soil. *International journal for numerical and analytical methods in geomechanics*, 6, 211-218.

GUI, M., BOLTON, M., GARNIER, J., CORTE, J., BAGGE, G., LAUE, J. & RENZI, R. (1998) Guidelines for cone penetration tests in sand. *Proceedings of the International Conference on Centrifuge Modelling (Centrifuge 98)*, Tokyo, Japan, 23-25.

HOLDEN, J. (1971) Laboratory research on static cone penetrometers. *University of Florida, Gainesville, Department of Civil Engineering, Internal Report, CE-SM-71-1*.

HOOMANS, B., KUIPERS, J. & VAN SWAAIJ, W. (2000) Granular dynamics simulation of segregation phenomena in bubbling gas-fluidised beds. *Powder Technology*, 109, 41-48.

- HOSSAIN, Z., INDRARATNA, B., DARVE, F. & THAKUR, P. (2007) DEM analysis of angular ballast breakage under cyclic loading. *Geomechanics and Geoengineering: An International Journal*, 2, 175-181.
- HOULSBY, G. & HITCHMAN, R. (1988) Calibration chamber tests of a cone penetrometer in sand. *Geotechnique*, 38, 39-44.
- HSU, H.-H. & HUANG, A.-B. (1999) Calibration of cone penetration test in sand. *PROCEEDINGS-NATIONAL SCIENCE COUNCIL REPUBLIC OF CHINA PART A PHYSICAL SCIENCE AND ENGINEERING*, 23, 579-590.
- HUANG, A.-B. & HSU, H.-H. (2005) Cone penetration tests under simulated field conditions. *Geotechnique*, 55, 345-354.
- HUANG, A.-B. & MA, M. Y. (1994) An analytical study of cone penetration tests in granular material. *Canadian geotechnical journal*, 31, 91-103.
- HUANG, A. & HSU, H. (2004) Advanced calibration chambers for cone penetration testing in cohesionless soils. In *ISC-2 geotechnical and geophysical site characterization* (Viana, A. & Mayne, P. W. (eds)). National Chiao Tung University: Millpress Science Publishers, pp. 147-166.
- HUANG, W., SHENG, D., SLOAN, S. & YU, H.-S. (2004) Finite element analysis of cone penetration in cohesionless soil. *Computers and Geotechnics*, 31, 517-528.
- INDRARATNA, B., IONESCU, D. & CHRISTIE, H. (1998) Shear behavior of railway ballast based on large-scale triaxial tests. *Journal of Geotechnical and Geoenvironmental Engineering*, 124, 439-449.

ISSMFE (1989) International reference test procedure for cone penetration test (CPT). *Report of the ISSMFE Technical Committee on Penetration Testing of soils-TC 16*. Linköping: Swedish Geotechnical Institute, 7,6-16.

ITASCA (2003) PFC3D Particle Flow Code in Three Dimensions Minnesota *Itasca Consulting Group, Inc*

IWASHITA, K. & ODA, M. (1998) Rolling resistance at contacts in simulation of shear band development by DEM. *Journal of engineering mechanics*, 124, 285-292.

JAMIOLKOWSKI, M., LADD, C. C., GERMAINE, J. T. & LANCELLOTTA, R. (1985) New developments in field and laboratory testing of soils. *Proceeding 11th International Conference on Soil Mechanics and Foundation Engineering*, San Francisco.

JAMIOLKOWSKI, M., PRESTI, D. L. & MANASSERO, M. (2004) Evaluation of relative density and shear strength of sands from CPT and DMT. ASCE.

JIANG, M., KONRAD, J. & LEROUEIL, S. (2003) An efficient technique for generating homogeneous specimens for DEM studies. *Computers and Geotechnics*, 30, 579-597.

JIANG, M., YU, H. S. & HARRIS, D. (2006) Discrete element modelling of deep penetration in granular soils. *International journal for numerical and analytical methods in geomechanics*, 30, 335-361.

KOLBUSZEWSKI, J. (1948) An experimental study of the maximum and minimum porosities of sands. *Proceedings of the Second International Conference on Soil Mechanics and Foundation Engineering*, 1, 158-165, 158-165.

- LACKENBY, J., INDRARATNA, B., MCDOWELL, G. & CHRISTIE, D. (2007) Effect of confining pressure on ballast degradation and deformation under cyclic triaxial loading. *Geotechnique* 57, No. 6, 527-536.
- LADANYI, B. (1963) Expansion of a cavity in a saturated clay medium. *Journal of the Soil Mechanics and Foundations Division*, 89, 127-161.
- LADANYI, B. & JOHNSTON, G. (1974) Behavior of circular footings and plate anchors embedded in permafrost. *Canadian geotechnical journal*, 11, 531-553.
- LEE, D.-M. (1992) *The angles of friction of granular fills*. PhD dissertation, University of Cambridge.
- LEE, K. L. & SEED, H. B. (1967) Drained strength characteristics of sands. *Journal of Soil Mechanics & Foundations Div.*
- LEVADOUX, J.-N. & BALIGH, M. M. (1986) Consolidation after undrained piezocone penetration. I: Prediction. *Journal of Geotechnical Engineering*, 112, 707-726.
- LI, X. (2006) *Micro-scale investigation on the quasi-static behavior of granular material*. PhD Thesis. The Hong Kong University of Science and Technology.
- LI, Y., XU, Y. & JIANG, S. (2009) DEM simulations and experiments of pebble flow with monosized spheres. *Powder Technology*, 193, 312-318.
- LIM, W. & MCDOWELL, G. (2005) Discrete element modelling of railway ballast. *Granular Matter*, 7, 19-29.

- LIN, X. & NG, T.-T. (1997) A three-dimensional discrete element model using arrays of ellipsoids. *Geotechnique*, 47, 319-329.
- LOBO-GUERRERO, S. & VALLEJO, L. (2005) Crushing a weak granular material: experimental numerical analyses. *Geotechnique*, 55, 243-249.
- LOBO-GUERRERO, S. & VALLEJO, L. E. (2007) Influence of pile shape and pile interaction on the crushable behavior of granular materials around driven piles: DEM analyses. *Granular Matter*, 9, 241-250.
- LU, M. (2008) *Discrete element modelling of railway ballast*. PhD thesis, University of Nottingham, Nottingham, UK.
- LU, M. & MCDOWELL, G. (2007) The importance of modelling ballast particle shape in the discrete element method. *Granular Matter*, 9, 69-80.
- LU, M. & MCDOWELL, G. (2010) Discrete element modelling of railway ballast under monotonic and cyclic triaxial loading. *Geotechnique*, 60, 459-467.
- LU, M. & MCDOWELL, G. R. (2008) Discrete element modelling of railway ballast under triaxial conditions. *Geomechanics and Geoengineering: An International Journal*, 3, 257-270.
- LUNNE, T. & CHRISTOPHERSEN, H. P. (1983) Interpretation of cone penetration data for offshore sands. *Proceedings of 15th Annual Offshore Technology Conference, Houston, Texas*, 181-192.
- LUNNE, T., ROBERTSON, P. & POWELL, J. (1997) Cone penetration testing in Geotechnical Practice. *Blackie Academic & Professional, New York*.

MARKAUSKAS, D. & KAÄ • IANAUSKAS, R. (2006) Compacting of particles for biaxial compression test by the discrete element method. *Journal of Civil Engineering and Management*, 12, 153-161.

MCDOWEL, G., LI, H. & LOWNDES, I. (2011) The importance of particle shape in discrete-element modelling of particle flow in a chute. *Geotech. Lett*, 1, 59-64.

MCDOWELL, G. (2002) On the yielding and plastic compression of sand. *Soils and foundations*, 42, 139-145.

MCDOWELL, G. & AMON, A. (2000) The application of Weibull statistics to the fracture of soil particles. *Soils and foundations*, 40, 133-141.

MCDOWELL, G. & BOLTON, M. (1998) On the micromechanics of crushable aggregates. *Geotechnique*, 48, 667-679.

MCDOWELL, G., BOLTON, M. & ROBERTSON, D. (1996) The fractal crushing of granular materials. *Journal of the Mechanics and Physics of Solids*, 44, 2079-2101.

MCDOWELL, G. & DE BONO, J. P. (2013) On the micro mechanics of one-dimensional normal compression. *Geotechnique*, 63.

MCDOWELL, G. & HARIRECHE, O. (2002) Discrete element modelling of soil particle fracture. *Geotechnique*, 52, 131-135.

MCDOWELL, G. R., LIM, W. L., COLLOP, A. C., ARMITAGE, R. & THOM, N. H. (2005) Laboratory simulation of train loading and tamping on ballast. *Proceedings of the Institution of Civil Engineers: Transport* 158, No. TR2, 89-95., 89-95.

MITCHELL, J. (1993) *Fundamentals of Soil Behavior*, John Wiley and Sons, Inc., New York.

MITCHELL, J. K. & BRANDON, T. L. (1998) Analysis and use of CPT in earthquake and environmental engineering. *Geotechnical site characterization*, 1, 69-98.

MITCHELL, J. K. & KEAVENY, J. M. (1986) Determining sand strength by cone penetrometer. *Use of In Situ Tests in Geotechnical Engineering (GSP 6)*, ASCE, 823-839.

MITCHELL, J. K. & SOGA, K. (2005) *Fundamentals of soil behavior*. John Wiley & Sons, New York.

NG, T. T. & DOBRY, R. (1992) A non linear numerical model for soil mechanics. *International journal for numerical and analytical methods in geomechanics*, 16, 247-263.

NI, Q. (2003) *Effect of Particle Properties and Boundary Conditions on Soil Shear Behavior: 3-D numerical simulations*. PhD Thesis, University of Southampton.

NORMAN, G. & SELIG, E. (1983) Ballast performance evaluation with box tests. *AREA Bul*, 692, 207-239.

ODA, M., KOISHIKAWA, I. & HIGUCHI, T. (1978) Experimental study of anisotropic shear strength of sand by plane strain test. *Soils and foundations*, 18, 25-38.

ONER, M. (1984) Analysis of fabric changes during cyclic loading of granular soils *Proc., 8th World Conf. Earthquake Engineering, San Francisco, Calif.*, 3, 55-62.

PARKIN, A. (1988) The calibration of cone penetrometers. *Proceedings of the 1st International Symposium on Penetration Testing, ISOPT-1, Orlando, FL, USA.* Elsevier, A91.

PARKIN, A. & LUNNE, T. (1982) Boundary effects in the laboratory calibration of a cone penetrometer for sand. *Norwegian Geotechnical Institute Publication.*

PENA, A., LIZCANO, A., ALONSO, M. & MARROQUIN, F. & HERRMANN, H. (2008) Biaxial test simulations using a packing of polygonal particles. *International journal for numerical and analytical methods in geomechanics*, 32, 143-160.

PETERS, J. F. & LEAVELL, D. A. (1986) A biaxial consolidation test for anisotropic soils. *Consolidation of Soils: Testing and Evaluation: a Symposium*, Astm International, 465.

ROBERTSON, D. (2000) *Numerical simulations of crushable aggregates*. Ph. D. dissertation, University of Cambridge.

ROBERTSON, P. (2009) Interpretation of cone penetration tests-a unified approach. *Canadian geotechnical journal*, 46, 1337-1355.

ROBERTSON, P. & WRIDE, C. (1998) Evaluating cyclic liquefaction potential using the cone penetration test. *Canadian geotechnical journal*, 35, 442-459.

ROBERTSON, P. K. (1986) In situ testing and its application to foundation engineering. *Canadian geotechnical journal*, 23, 573-594.

ROBERTSON, P. K. & CABAL, K. L. (2010) *Guide to Cone Penetration Testing for Geotechnical Engineering*. California: Gregg Drilling & Testing.

- ROBERTSON, P. K., CAMPANELLA, R., GILLESPIE, D. & GREIG, J. (1986) Use of piezometer cone data. Use of in situ tests in geotechnical engineering, ASCE, 1263-1280.
- ROBERTSON, P. K. & CAMPANELLA, R. G. (1983a) Interpretation of Cone Penetration Tests. Part I: Sand. *Canadian Geotechnical Journal*, 20(4) 718-733.
- ROBERTSON, P. K. & CAMPANELLA, R. G. (1983b) Interpretation of Cone Penetration Tests. Part II: Clay. *Canadian Geotechnical Journal*, 20(4), 734-745.
- ROBERTSON, P. K. & CAMPANELLA, R. G. (1986) Guidelines for the Use and Application of the CPT and CPTU. *Soil Mechanics series No. 105*, Department of Civil Engineering, The University of British Columbia, 187 p.
- ROTHENBURG, L. & BATHURST, R. (1992) Micromechanical features of granular assemblies with planar elliptical particles. *Geotechnique*, 42, 79-95.
- SAGASETA, C., WHITTLE, A. J. & SANTAGATA, M. (1998) Deformation Analysis of Shallow Penetration in Clay. *International Journal of Numerical and Analytical Methods in Geomechanics*, 21(10), 687 - 719.
- SALGADO, R. (1993) *Analysis of Penetration Resistance in Sands.*, PhD Thesis, University of California at Berkeley.
- SALGADO, R., MITCHELL, J. & JAMIOLKOWSKI, M. (1997) Cavity expansion and penetration resistance in sand. *Journal of Geotechnical and Geoenvironmental Engineering*, 123, 344-354.

- SALGADO, R., MITCHELL, J. & JAMIOLKOWSKI, M. (1998) Calibration chamber size effects on penetration resistance in sand. *Journal of Geotechnical and Geoenvironmental Engineering*, 124, 878-888.
- SANGLERAT, G. (1972) The penetration and soil exploration. Elsevier, Amsterdam.
- SANTAMARINA, J. & CHO, G. (2004) Soil behaviour: The role of particle shape. *Advances in geotechnical engineering: The skempton conference*, 604-617.
- SANTAMARINA, J. C., KLEIN, K. & FAM, M. (2001) Soils and waves. John Wiley and Sons Ltd, New York.
- SAZZAD, M. M. & ISLAM, M. S. (2008) Macro and micro mechanical responses of granular material under varying interparticle friction. *Journal of Civil Engineering (IEB)*, 36, 87-96.
- SCHANZ, T. & VERMEER, P. (1996) Angles of friction and dilatancy of sand. *Geotechnique*, 46, 145-152.
- SCHMERTMANN, J. (1976) An updated correlation between relative density, Dr, and Fugro-type electric cone bearing, qc. *Contract Report DACW*, 39-76.
- SCHNAID, F. (1990) *A study of the cone-pressuremeter test in sand*. PhD Thesis, University of Oxford, Oxford, UK.
- SCHNAID, F., PRIETTO, P. D. & CONSOLI, N. C. (2001) Characterization of cemented sand in triaxial compression. *Journal of Geotechnical and Geoenvironmental Engineering*, 127, 857-868.

- SKINNER, A. (1969) A note on the influence of interparticle friction on the shearing strength of a random assembly of spherical particles. *Geotechnique*, 19, 150-157.
- SUKUMAR, N. & BELYTSCHKO, T. (2000) Arbitrary branched and intersecting cracks with the extended finite element method. *Int. J. Numer. Meth. Engng*, 48, 1741-1760.
- SUSILA, E. & HRYCIW, R. D. (2003) Large displacement FEM modelling of the cone penetration test (CPT) in normally consolidated sand. *International journal for numerical and analytical methods in geomechanics*, 27, 585-602.
- TATSUOKA, F., SALAMOTO, M., KAWAMURA, T. AND FUKUSHIMA, S (1986) Strength and deformation characteristics of sand in plane strain compression at extremely low pressures. *Soils and Foundation*, 2, 65-84.
- TEH, C. & HOULSBY, G. (1991) An analytical study of the cone penetration test in clay. *Geotechnique*, 41, 17-34.
- TING, J. M., CORKUM, B. T., KAUFFMAN, C. R. & GRECO, C. (1989) Discrete numerical model for soil mechanics. *Journal of Geotechnical Engineering*, 115, 379-398.
- TING, J. M., MEACHUM, L. & ROWELL, J. D. (1995) Effect of particle shape on the strength and deformation mechanisms of ellipse-shaped granular assemblages. *Engineering computations*, 12, 99-108.
- TSOUNGUI, O., VALLET, D. & CHARMET, J.-C. (1999) Numerical model of crushing of grains inside two-dimensional granular materials. *Powder Technology*, 105, 190-198.

VESIC, A. (1963) Bearing capacity of deep foundations in sand. *Highway research record*, 39, 112-153.

VESIC, A. (1977) Design of pile foundations. *NCHRP synthesis of highway practice*.

VILLET, W. C. & MITCHELL, J. K. (1981) Cone resistance, relative density and friction angle. Cone penetration testing and experience, ASCE, 178-208.

WANG, J., WU, H., DENG, Y. & HUANG, L. (2010) Study of embankment reinforced mechanism based on discrete-continuous coupling calculation method. *Information Science and Engineering (ICISE), 2nd International Conference on, IEEE*, 4049-4052.

WANG, Y.-H. & LEUNG, S.-C. (2008) A particulate-scale investigation of cemented sand behavior. *Canadian geotechnical journal*, 45, 29-44.

WEI-FENG, L., CHIH-YING, L., JING-WEN, C. & KU, B.-H. (2003) Applications of dilative behavior in marine soil *Proceedings of The Thirteenth International Offshore and Polar Engineering Conference*, Honolulu, Hawaii, USA.

WEIBULL, W. (1951) A statistical distribution function of wide applicability. *Journal of applied mechanics*, 18, 293-297.

WILLSON, S. M. (1985) Finite Element Analysis of Piles and Penetrometers. PhD thesis, University of Manchester, UK.

YU, H.-S. (2000) *Cavity expansion methods in geomechanics*, Kluwer Academic Publishers, The Netherland.

YU, H.-S. (2004) In situ soil testing: from mechanics to interpretation. Proc. 2nd Int. Conf. on Site Characterization ISC, 3-38.

YU, H.-S. & CARTER, J. (2002) Rigorous similarity solutions for cavity expansion in cohesive-frictional soils. *International Journal of Geomechanics*, 2, 233-258.

YU, H.-S. & MITCHELL, J. K. (1998) Analysis of cone resistance: review of methods. *Journal of Geotechnical and Geoenvironmental Engineering*, 124, 140-149.

YU, H. -S. & MITCHELL, J. K. (1996) Analysis of cone resistance: a review of methods. *Research Report No. 142.09.1996.*, The University of Newcastle, NSW.

ZHANG, X. & VU-QUOC, L. (2000) Simulation of chute flow of soybeans using an improved tangential force–displacement model. *Mechanics of Materials*, 32, 115-129.

ZHANG, Y. & CUNDALL, P. A. (1986) Numerical simulation of slow deformation. *Proc., Symp. On the Mechanics of Particulate Media, 10th National Congress on Applied Mechanics, Austin, Tex.*

ZUIDBERG, H. M., SCHAAP, L. H. J. & BERINGEN, F. L. (1982) A penetrometer for simultaneous measuring of cone resistance, sleeve friction and dynamic pore pressure. *Proceeding of the 2nd European Symposium on Penetration Testing, ESOPT-11, Amsterdam, 2, 70-963.*

APPENDIX

Numerical Servo-Mechanism

A numerical servo-control mechanism was applied to reduce the difference between measured and required stresses (Itasca, 2003). The servo function was called once every cycle. Wall velocity was adjusted to make the measured stress closer to required stress and control the stress state. The wall velocity $\dot{u}^{(w)}$ was calculated from the following equation:

$$\dot{u}^{(w)} = G(\sigma^{measured} - \sigma^{required}) = G\Delta\sigma \quad A.1$$

where

G is the (gain) parameter that is estimated by the function get-gain

$\sigma^{measured}$ is the measured stress

$\sigma^{required}$ is the required stress

$\Delta\sigma$ is the difference between measured and required stresses

The maximum increment in wall force arising from wall movement in one timestep was calculated using the following equation

$$\Delta F^{(w)} = k_n^{(w)} N_c \dot{u}^{(w)} \Delta t \quad A.2$$

where

N_c is the number of contacts on the wall

$k_n^{(w)}$ is the average stiffness of these contacts

Hence, the change in mean wall stress $\Delta\sigma^{(w)}$ was calculated by the following expression:

$$\Delta\sigma^{(w)} = \frac{k_n^{(w)} N_c \dot{u}^{(w)} \Delta t}{A} \quad \text{A.3}$$

Where

A is the area of wall.

To achieve stability, the absolute value of the change in wall stress must be smaller than the absolute value of the difference between the measured stresses and required stresses. In practice, a relaxation factor (α) is used and the stability criteria can be expressed as:

$$|\Delta\sigma^{(w)}| < \alpha |\Delta\sigma| \quad \text{A.4}$$

When Equations A.1 and A.3 are substituted into Equation A.4, the stability criteria becomes:

$$\frac{k_n^{(w)} N_c G |\Delta\sigma| \Delta t}{A} < \alpha |\Delta\sigma| \quad \text{A.5}$$

where the (gain) parameter G can be determined by the following equation:

$$G = \frac{\alpha A}{k_n^{(w)} N_c \Delta t}$$

A.6

Therefore, the required stress can be achieved by adjusting the wall velocity using Equation A.1.